Influence of Nonlinear Hydrodynamic Response on the Fatigue Damage of a FOWT

R.S. Salih

Delft University of Technology

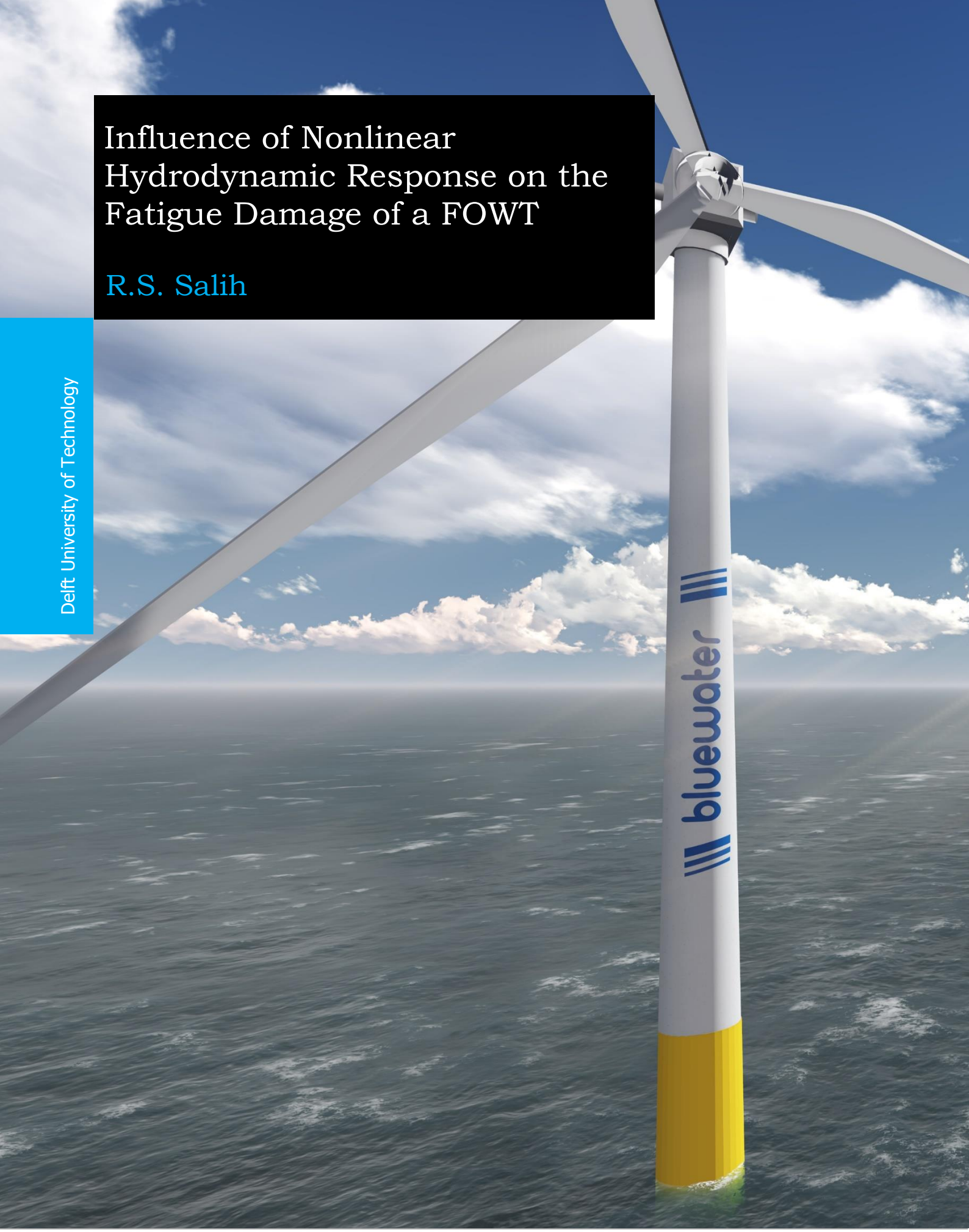

TU Delft Delft University of Technology

Challenge the future

This page is intentionally left blank

Influence of Nonlinear Hydrodynamic Response on the Fatigue Damage of a FOWT

Development of Method to Assess Hydrodynamic Nonlinear Response of a FOWT, Having Allowance for Platform-Turbine Coupling Effects and Combined Wind and Wave Loads

By

R.S. Salih
4155459

For obtaining the degree of

Master of Science
in Offshore and Dredging Engineering

at the Delft University of Technology,
to be defended publicly on Monday, May 28, 2018 at 1:00 PM.

Supervisor:	Prof.dr.ir. M.L. Kaminski,	TU Delft
Thesis committee:	Dr. A. A. Kana,	TU Delft
	Ir. P.S. van Lieshout,	TU Delft
	Dr.ir. C. van der Nat,	Bluewater

TU Delft

ACKNOWLEDGEMENTS

During my valuable adventure of graduating, I have been assisted by several kind and helpful colleagues at Bluewater, who all gave me the necessary inspiration at times when I needed it. I would, therefore, like to express my gratitude to Bluewater, for providing a very interesting graduation subject and the help and guidance during my graduation. Special thanks to my supervisor from Bluewater, Clemens van der Nat, who, with his broad knowledge and experience and critical judgment, has directed me on the right path at crucial moments.

I would also like to thank my supervisor and also committee chairman Mirek Kaminski for proposing the thesis topic and answering my questions during progress meetings. And the other committee members, Paula van Lieshout and Austin Kana, I thank wholeheartedly for their flexibility and willingness to assist me in the final stages.

Lastly, I would like to express my profound gratitude and appreciation to, perhaps the most influential person, my mother, Shewbo.

PREFACE

"It can scarcely be denied that the supreme goal of all theory is to make the irreducible basic elements as simple and as few as possible without having to surrender the adequate representation of a single datum of experience."

Albert Einstein
(14 March 1879 - 18 April 1955)

ABSTRACT

A method has been developed with which the rigid-body motions, stress and fatigue damage response of a TLP-type FOWT are determined in time domain, with the aim of assessing the influence of non-linear hydrodynamic response on the fatigue damage. The dynamics are described by means of a system of coupled 6DOF-EoMs and solved in Matlab, after which the validity of the method is confirmed by means of validation and verification using OrcaFlex models.

Subsequently, a method has been proposed to linearize the dynamics of the developed model. For linearization of quadratic damping, three different methods have been proposed, after which the best performing method is determined by means of a comparative study. Subsequently, using the fully linearized model, the difference in long-term damage w.r.t. the nonlinear model is calculated and the influence of multiaxiality is investigated.

The results have shown that the linear approach is suitable for approximation of long-term fatigue damage in hotspots that are located in the connections between the central column and the pontoons of the TLP. However, in hotspots with relatively low stress response, the long-term damage is underestimated by 48% due to the high sensitivity of the damage to differences in the stress response. Finally, the presence of multiaxiality and non-proportionality has been demonstrated for a number of hotspots and during both operational and extreme conditions.

.

TABLE OF CONTENTS

LIST OF ABBREVIATIONS

FOWT	Floating Offshore Wind Turbine
CAPEX	Capital Expenditures
TLP	Tension Leg Platform
TLPWT	Tension Leg platform Wind Turbine
CoG	Centre of Gravity
CoB	Centre of Buoyancy
FPSO	Floating Production, Storage and Offloading
FSO	Floating Storage and Offloading
SPM	Single Point Mooring
DFOWDC	Dounreay Floating Offshore Wind Deployment Centre
RNA	Rotor Nacelle- Assembly
FD	Frequency Domain
TD	Time Domain
VIV	Vortex Induced Vibrations
FEM	Finite Element Method
FEA	Finite Element Analysis
EoM	Equation of Motion
DoF	Degree of Freedom
ULS	Ultimate Limit State
MSL	Mean Sea Level
CFD	Computational Fluid Dynamics
RAO	Response Amplitude Operator
PSD	Power Spectral Density
FLS	Fatigue Limit State
HCF	High Cycle Fatigue
CWM	Cubic Weighted Mean

LIST OF FIGURES

LIST OF TABLES

1
INTRODUCTION

1.1 Background

1.1.1 Renewable Energy

Unsurprisingly, the main resources of world energy supply are currently still non-renewable resources such as oil, gas and coal. Over the past few decades, politics, science and society are increasingly concerned with the question: "What if the non-renewable sources run out?". As concluded in *Energy Policy*, an international journal dealing with implications regarding energy supply, if the world continues to consume petroleum products at the rates of 2006, the oil, gas and coal reserves will last another 40, 70 and 200 years, respectively [1]. The global economy has become aware that the trend towards renewable sources is inevitable, which has resulted in a 71% growth of EU's green energy production between 2005 and 2015 [2]. Related to these developments are the Paris Agreements at the end of 2016, where 195 countries agreed on many policies for limiting global warming, as a result further strengthening the political drive towards renewable resources.

1.1.2 Offshore Wind Energy

Compared to other renewable resources, the offshore wind energy sector has showed a remarkable growth in the past decade (Figure 1-1). With roughly 13 gigawatts worth of offshore wind turbines installed in the region surrounding the North Sea, the transition from fossil fuels to renewable energy resources seems to be accelerating. The market is slowly blooming and more

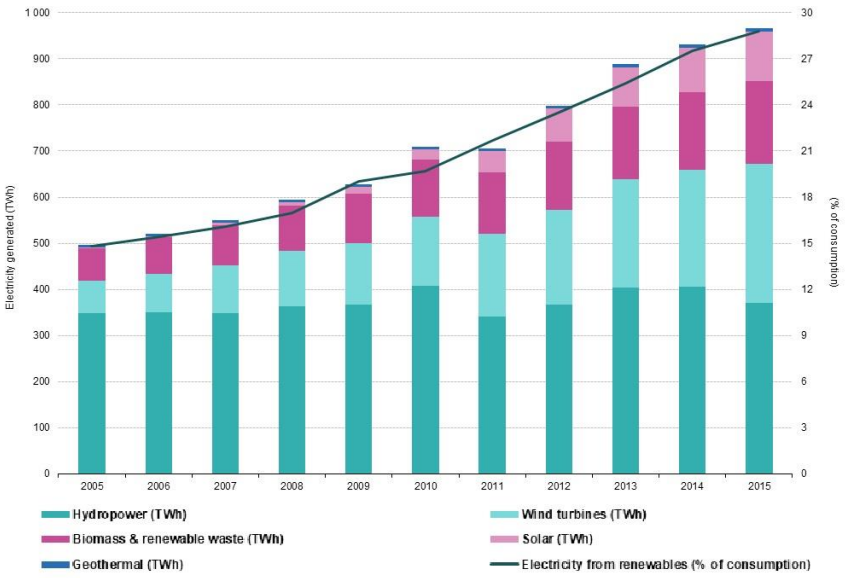

Figure 1-1: Renewable Energy Recourses [2]

and more investors and offshore companies are eager to capitalize on the opportunities of offshore wind turbines.

1.1.3 Floating Offshore Wind Turbines

Although bottom founded offshore structures have become a well-known concept after decades of experience and numerous bottom fixed offshore wind turbines have been installed, Floating Offshore Wind Turbines (FOWTs) are still relatively new and unevolved. Areas close to shore are often shallow and therefore more suitable for wind turbines supported by bottom founded structures, whereas deeper waters usually require floating platforms to keep the concept profitable. Compared to bottom fixed turbines, FOWTs are often designed larger, more complex and therefore require more Capital Expenditures (CAPEX). However, at larger water depths with harsher environments, higher wind speeds are available and a larger power supply can be achieved. This is well illustrated in Figure 1-2, where today's FOWTs are usually applicable to water depths from around 60m, with the expectation that future systems will be scaled up to more than 8MW. These prospects imply that the transition into deeper waters will make bottom fixed applications increasingly unattractive.

The cost-effectiveness of a floating solution depends on the type of support structure, which is chosen based on local external conditions and technical and practical requirements. As shown in Figure 1-3, floating support structures applied to FOWTs are generally subdivided into three main categories: TLPs, Spar Buoys and Barges. The distinction between the support types is primarily based on their stabilization technique. The Tension Leg Platform (TLP) is fully stabilized by excessive buoyancy, counteracted by tensioned tendons. Spar buoys achieve rotational stability by applying ballast to shift the Centre of Gravity (CoG) at a point below the Centre of Buoyancy (CoB), a concept that normally requires water depths of 100m or more. The barge type platform owes its stability to a combination of buoyancy, catenary (slack) mooring lines and large water piercing area to obtain rotational stability. Although this type is applicable to shallower waters (50m+), it requires a relatively large mooring footprint.

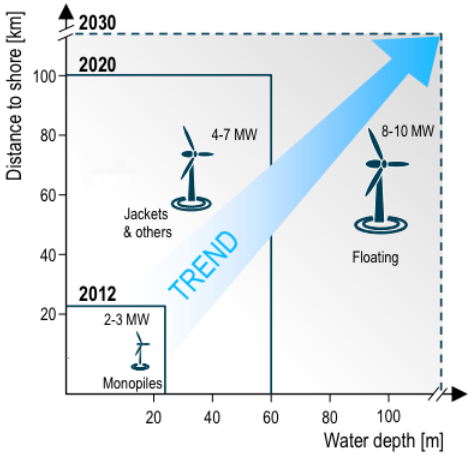

Figure 1-2: Trend in FOWTs [92]

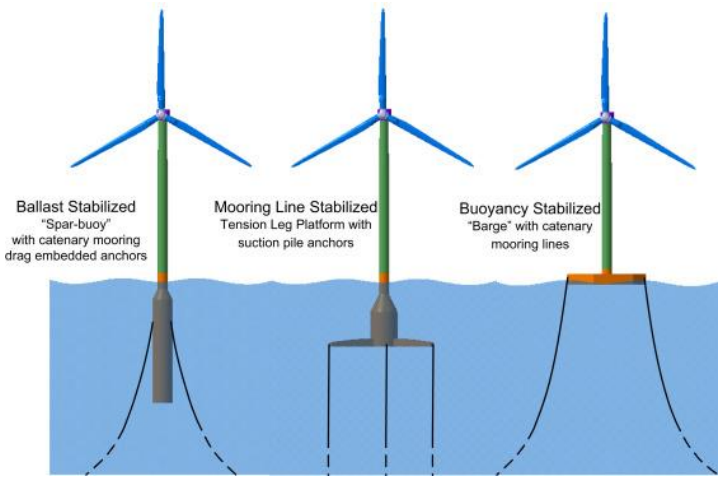

Figure 1-3: Support Structures for FOWTs [91]

1.2 Motivation

1.2.1 WindFlo Project

As an extension to its leading experience in developing and delivering FPSOs, FSOs and SPM systems, Bluewater is currently exploring the possibilities of offshore wind energy. While prominent offshore wind development companies have already established a strong position in the bottom fixed wind industry, now the focus tends to shift more towards FOWTs and deeper waters. Bottom-fixed specialists are generally pre-occupied with bottom founded projects at shallow-water sites and have no intention to get involved in floating wind. This provides a good opportunity for Bluewater's project development team to utilize its experience in the floating offshore technology and gain a significant position in the wind energy industry.

In this context, project *"WindFlo"* was initiated by Bluewater with the aim to acquire the permits of the Dounreay demonstration project, which is set to take place at the Dounreay Floating Offshore Wind Deployment Centre (DFOWDC), in the remainder referred to as the "Dounreay site". The area is exposed to extremely harsh environments, making it suitable for developers to demonstrate their innovative and cost-effective solutions. The permits will be granted by the Scottish Government to the lowest bidder who meets all the technical and economical requirements: a 5MW FOWT-design with an operational life span of at least 25 years and minimal overall costs.

The floating offshore wind test facility, depicted in Figure 1-4, is located at roughly 9km from the North Coast of Scotland and is between 69 to 103m deep. The local environment is characterised by its high waves and currents, with a 50-year significant wave height of 11.35m and 1-year current speed of 1.28ms^{-1} (at MSL). This and other site specific meteorological and oceanographic data, as provided by Renewable Energy Systems Ltd [3], will be used in the remainder of this research.

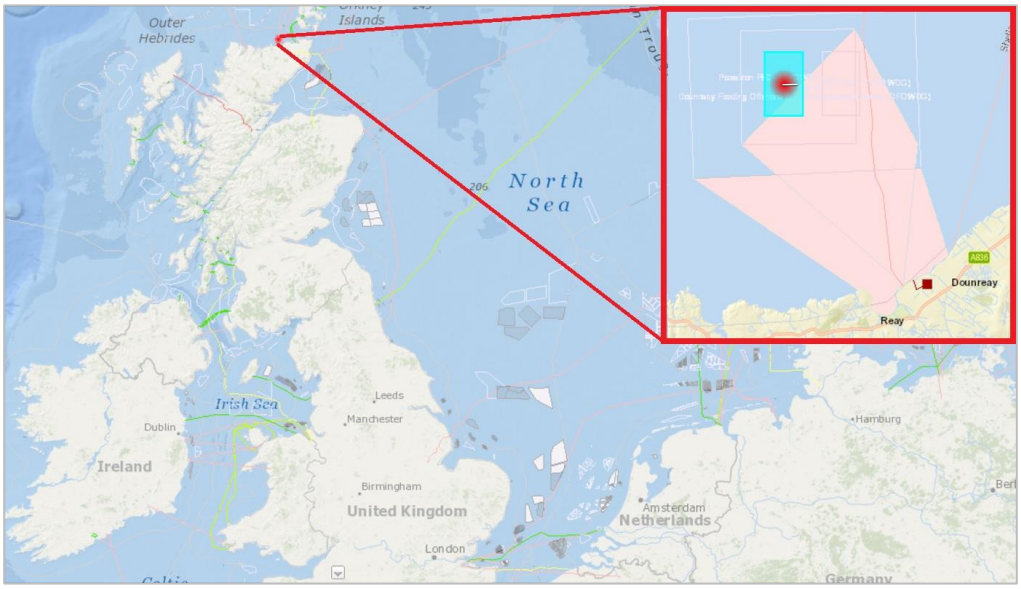

Figure 1-4: Location Dounreay-Site

1.2.2 The Tension Leg Platform

Since the structural design of wind turbines is often based on vibration requirements, in order to minimize adjustments and reinforcements to the turbine, the support system needs to match bottom-fixed support structures as much as possible. This is well achieved with the application of a taut mooring system, which is only possible for tension leg platform wind turbines (TLPWTs). Another defining TLP characteristic is its relatively low material weight and light tendons, resulting in relatively low CAPEX of the platform and mooring lines [4]. In view of these benefits, the floater type that has been chosen is the TLP.

General Overview of TLPWTs

This offshore platform type is a well-known concept that that has been widely applied for oil and gas exploration during the past three decades. The overall configuration of the TLP is identical for both applications in the oil and gas industry and FOWTs: a buoyant, submerged body stabilized by pre-tensioned mooring lines that are attached to the seabed. Pretension in the mooring lines arises from excessive buoyancy, which restricts the vertical and rotational motions considerably and can be designed to control the TLP's dynamic properties.

Conventional TLPs designed for FOWTs can be subdivided into two categories, depending on the distribution of buoyancy along the platform. In both cases, the turbine tower is supported by the transition piece, a cylindrical shaped central column. The most common TLPWT is the mono-column (or sea star) type, which consists of multiple buoyant pontoons attached to the central column. Truss type TLPs apply the principle of braced units to transfer the forces from the central column to the mooring lines. The truss and mono-column type TLPs are shown in Figure 1-5. Different configurations of the mono-column type can be obtained by varying the pontoon- and central column characteristics, as shown Figure 1-6.

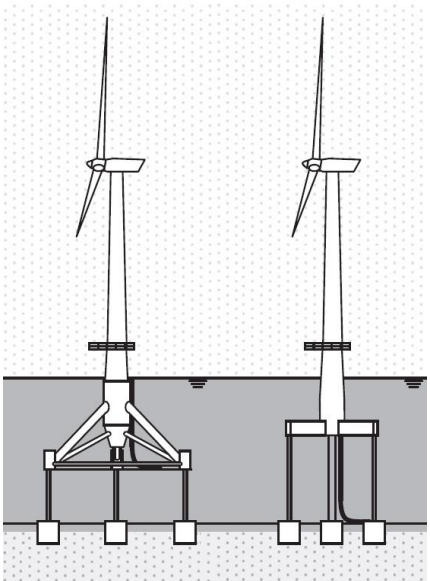

Figure 1-5: Truss (left) and mono-column (right) TLP

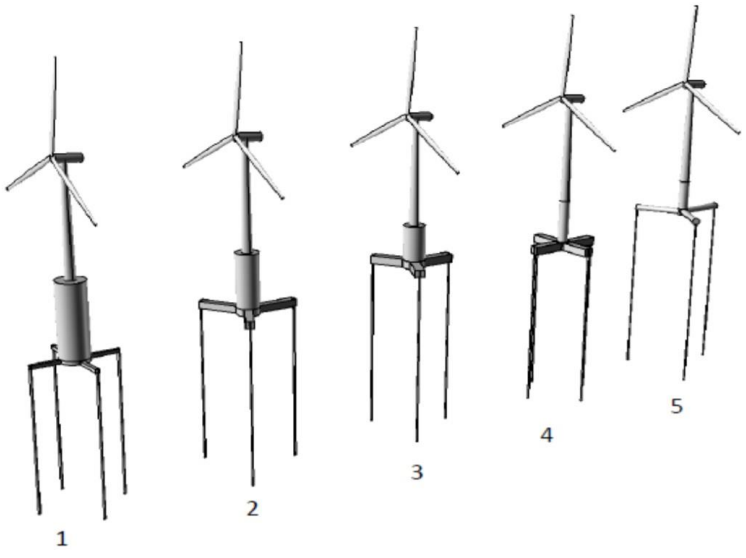

Figure 1-6: Mono-column designs [90]

Hybrid forms of TLPs have also been developed, using principles of other platforms types combined with taut mooring lines. Tension leg semi-submersible variants are obtained when the water-plane area of the TLP substructure is large compared to conventional TLPWTs, where the water surface is only penetrated by the central column. An example of this concept is Gicon's Windfloat design, shown in Figure 1-7. Another hybrid variant is the tension leg spar, where the spar-buoy platform is stabilized by taut lines, as depicted in Figure 1-8. For further reading on TLPWTs and a complete overview of all concepts currently under development, it is referred to Carbon Trust's publication on the state of the floating wind industry and technology [4].

1.2.3 Characteristics of the TLP

Fatigue Sensitivity

Generally, the main feature of the TLP is associated with are its relatively high vertical and rotational stiffness, which is both its main strength and drawback. Although highly beneficial from turbine cost point of view, restricting the vertical and rotational vibrations will cause relatively large mooring induced internal stresses. In order to obtain small motion amplitudes, either the mooring stiffness must be large, or the hydrodynamic damping must be large. Hydrodynamic damping in TLP structures is almost entirely due to viscous friction, which depends, among other parameters, on the relative velocity with respect to the water. Since most DOFs are limited, significant velocity amplitudes cannot occur. As a result, damping in TLPs is often small, especially for the vertical translations and rotations in the vertical plane. Therefore, increasing the mooring stiffness is the only way to obtain small motions.

This means that small elongations of the tendons, caused by excitation in any of the DOFs, will induce large mooring forces. Since the turbine tower and TLP arms are unsupported for the most part, external forces and mooring loads can locally cause large bending moments. Internal stresses that arise from this, combined with often highly dynamic and multidirectional environmental loading, make the TLP structure particularly sensitive to fatigue damage.

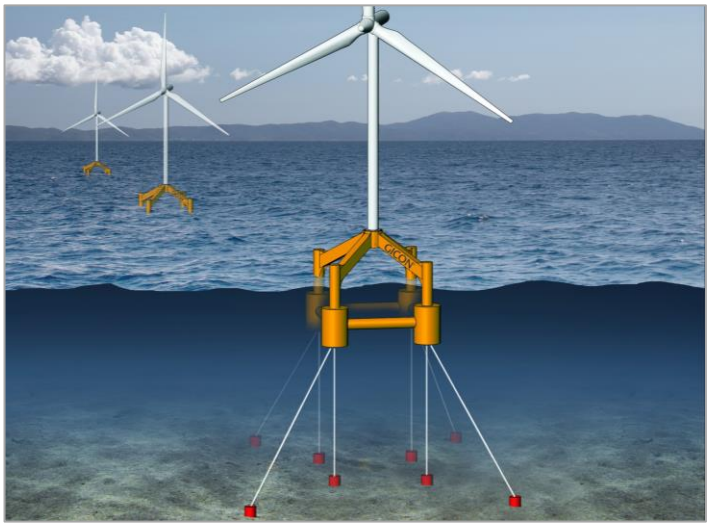

Figure 1-7: Tension Leg Semi-Sub [93]

Figure 1-8: Tension Leg Spar [94]

Risk of Resonating Motions

It is expected that in harsh environments such as the Dounreay-site, the FOWT will be exposed to considerable cyclic loading as a result of wind and waves. Interaction between environmental forces and various parts of the structure creates a complex interplay of dynamic influences, in which vibrations of different sections caused by external forces can amplify or diminish each other. Engineering practice has shown that in order to mitigate cyclic loading and therefore fatigue damage of TLPs, the risk of resonance phenomena must be minimized. This is achieved by minimizing the overlap between natural frequencies and excitation frequencies, or by incorporating sufficient damping in the system.

To illustrate the importance of damping, consider the Dynamic Amplification Factor (DAF) of a 1-DOF mass-spring-dashpot system, as shown in Figure 1-9. The DAF, which is simply the ratio between the dynamic and quasi-static response, shows that the magnitude of damping has a significant effect on the response in the resonance region. As mentioned before, typical TLPs experience weak damping in the roll, pitch and heave motions. As a result, if one of these DOFs resonate, the motion and stress response amplitudes can amplify to extremely large values.

On the other hand, minimizing the overlap between natural frequencies and excitation frequencies is a rather cumbersome task for the designer. Figure 1-10 illustrates the typical yearly extreme wind and wave spectrum at the Dounreay-site, along with a number of typical natural frequencies that are important for dynamic analyses of TLPWTs[1]. From this figure, typical peak wave frequencies are roughly 3 times the surge/sway natural frequencies. Based on the graph in Figure 1-9, it follows that the surge and sway natural frequencies are in the inertia dominated region, which is typically achieved through application of relatively heavy and large structural composition.

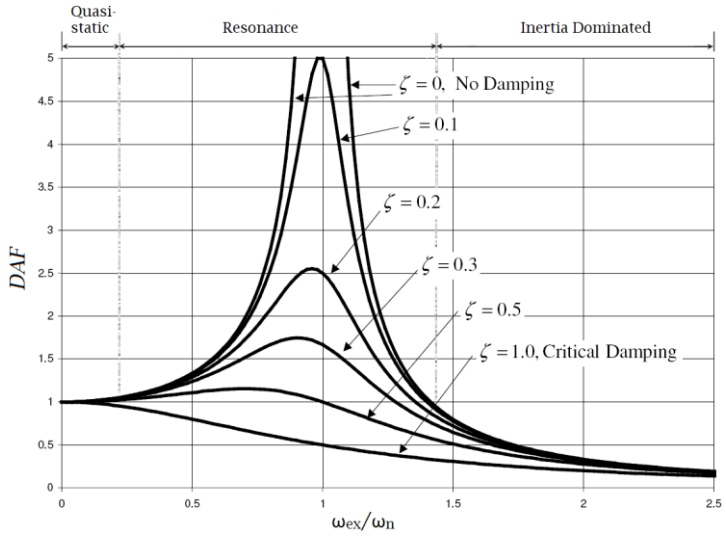

Figure 1-9: Dynamic Amplification Factor

[1] First rotor frequencies (1P), blade passing frequencies (3P) and tower height (for determining reference wind speed) are based on NREL reference turbine. Typical TLP natural frequencies are adopted from the design specification report of the WindStar TLP, a mono-column type concept that has been developed for supporting the NREL turbine [73].

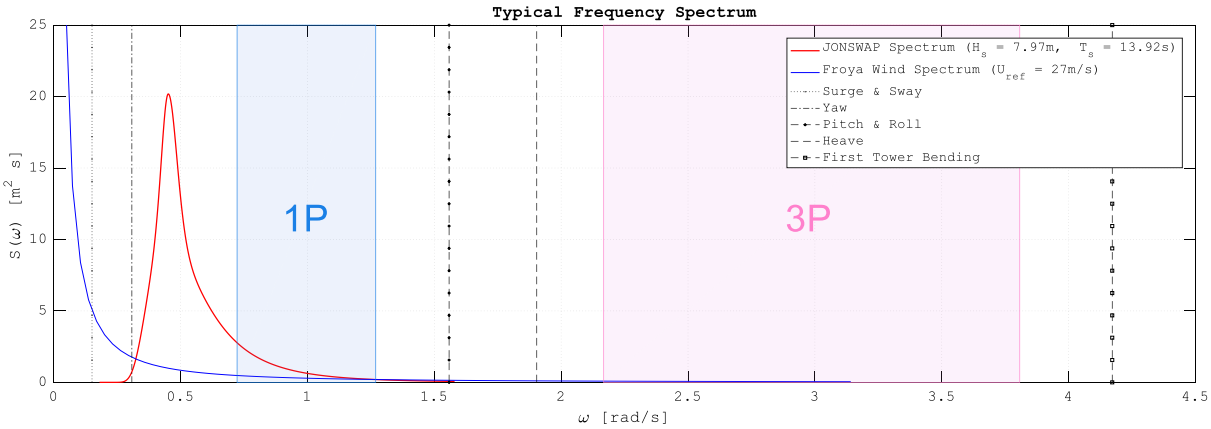

Figure 1-10: Typical Frequency Spectrum

Nonetheless, the 5MW WindFlo design is only considered economically feasible if the total structural weight of the platform is limited to 1000 tonnes, which has proven a major challenge as weight reduction results in a shift of the surge, sway and yaw natural frequencies towards the wave resonance region. In conclusion, weight reduction could amplify motions and shorten the structural lifespan significantly if the associated fatigue loads are not predicted properly.

1.2.4 The WindFlo Solution

The WindFlo concept is an all-steel mono-column type TLP with three rectangular shaped pontoons, as illustrated in Figure 1-11. The central column, also called the transition piece, is a hollow, cylindrical shaped unit, connecting the TLP arms (pontoons) with the turbine tower. Detailed two-dimensional representation of the structure is given in Appendix A, along with a description of relevant design parameters.

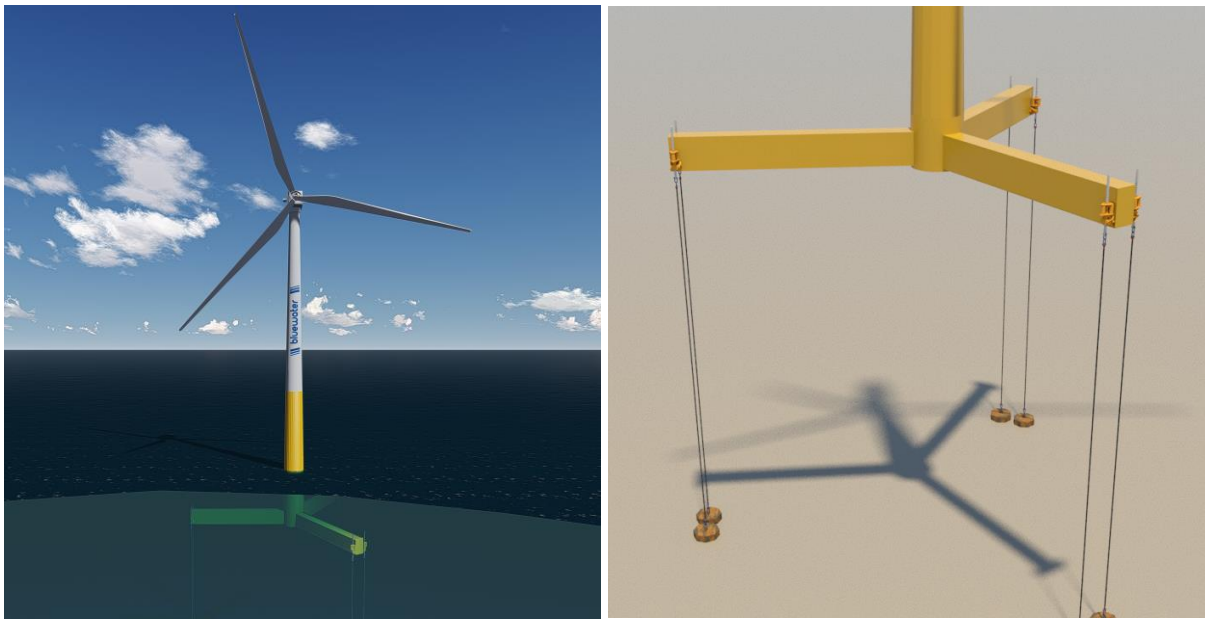

(a) (b)

Figure 1-11: 3D View of WindFlo TLP Including (a) and Excluding (b) Turbine

1.3 Problem Statement

1.3.1 Research Problem 1 - Adequacy of Frequency Domain

Due to uncertainties and stochastic nature in loading and resistance parameters, fatigue damage analyses require a long-term damage extrapolation technique. For linear systems with stationary loading conditions, the long-term fatigue damage calculation is usually carried out using Frequency Domain (FD) stochastic analyses such as the energy spectrum approach. This approach assumes that any stationary Gaussian process (external loads and internal stress response) can be represented by an infinite number of harmonic components. To make use of this approach, all nonlinear effects must either be linearized or completely disregarded.

Consequently, if nonlinear effects govern the dynamic response, the linear FD approach could fail to provide sufficient accuracy in determining the fatigue lifetime. An important feature of fatigue damage in welded steel joints is that, by approximation, the number of stress cycles until fatigue failure is characterized by the stress range to the power 3. In such case, if stresses are underestimated with, for example, 10%, the fatigue lifetime is overestimated with at least 33%.

Depending on the exact structural characteristics and loading conditions, the following nonlinear effects may play a significant role in TLPWTs:

- Nonlinear hydrodynamic forces;
- Nonlinear turbine loads;
- Nonlinear mooring effects;
- Structural (elastic) resonance and hydro-elasticity;
- Multiaxial Fatigue.

If the FD approach proves to be inadequate, the only alternative to long-term damage analysis is the Time Domain (TD) approach, which involves time integration of the Equations of Motion (EoMs) and evaluation of the internal stress state at each time step. To obtain reliable statistics, TD simulations require sufficient length and need to be carried out for all relevant sea states and loading conditions. This is a highly time consuming and costly procedure and is avoided when possible. Since it is not possible to judge in advance to what extent nonlinear influences will play a role, it is desirable to investigate to what extent the TD approach is necessary.

1.3.2 Research Problem 2 - Absence of Simple and Transparent Models

Determining the accuracy of the FD fatigue approach requires a concept-specific stress prediction method that makes it possible to compare the results of a nonlinear model with results from a linear model. The non-linear model must incorporate all relevant phenomena with an adequate level of accuracy. And the linear model must be obtained from the nonlinear model, by linearizing the nonlinear effects in a mathematically and physically correct manner. This implies that the nonlinear model must provide the possibility to adjust the mathematical description of the

system's dynamics and associated external forces. The usefulness of the nonlinear model is assessed on the basis of two requirements [5], being:

i. Level of detail

Level of detail is defined as the amount of phenomena and interdependencies that is incorporated within the model. A model with lower level of detail tends to be less complex and has a smaller chance for errors, but it is also less suitable for solving more complex problems. The exact opposite is true for models with higher detail level. Finding the appropriate level of detail includes determining what physical phenomena need to be incorporated and what can be disregarded, i.e. correct conceptualisation of the problem.

ii. Level of accuracy

Level of accuracy is the extent to which the framework of mathematical formulae and underlying theory predict the real system behaviour, i.e. how the modelled phenomena resemble the actual physics. Higher level of accuracy improves the validity of results but often undermines the ease with which the results can be interpreted. An appropriate level of accuracy is obtained when, for each individual phenomenon, the proper amount of computational and modelling effort is made to embody the physics behind the phenomena.

1.4 Research Objectives and Questions

1.4.1 Research Objective

The main research objective is to identify and assess the influence of nonlinearities on the adequacy of linear methods for calculation of fatigue damage of the WindFlo TLP.

In order to do this, a methodology must be developed that is capable of addressing the influence of nonlinearities on the dynamic response of the floater and the corresponding fatigue loads, using computational models specifically designed for the WindFlo TLP. In order to capture the influence of nonlinearities, the complete nonlinear model must be linearized, after which results from both models are compared in time domain. This implies that the nonlinear model must be adjustable and easy to interpret, yet without disregarding any important aspects that may influence the fatigue damage prediction.

1.4.2 Research Questions

The main research question can be formulated as:

"Given a TLPWT, what is the simplest approach of combining wind and wave loads to determine the influence of nonlinear hydrodynamic response on the governing fatigue damage, taking into account the platform-turbine coupling effects?"

The main research question is subdivided in a number of sub-questions in accordance to the research problems specified in section 1.3. Sub-questions 1 and 2 are meant to assess, respectively, the level of detail and level of accuracy of the developed, analytical model. Sub-questions 3 and 4 deal with aspects that examine the adequacy of linear approach for fatigue damage calculations.

1. *What physical phenomena play a key role in the determination of the dynamics and associated fatigue forces of the WindFlo TLP?*
2. *What is the minimum level of accuracy needed to embody the physics of the WindFlo TLP and how can these effects be implemented in a dynamic motion analysis?*
3. *What is the influence of system linearization on the stress and fatigue damage response at the governing hotspots?*
4. *What is the extent to which multi-axial fatigue loading occurs at the governing hotspots?*

1.5 Research Plan

1.5.1 Scope of Work

The focus in the present work will primarily be placed on nonlinearities related to the behaviour of the floater and its interaction with the turbine and mooring lines, as illustrated in Figure 1-12. This entails providing clear mathematical descriptions of all forces acting on these structural components, consisting of hydrostatics, hydrodynamics, mooring interaction and turbine loads. The system's motion and stress response are calculated by means of a computational model, specifically developed to evaluate the influence of nonlinearities. This model, in the remainder referred to as "the analytical model", is developed in Matlab and solved in time domain.

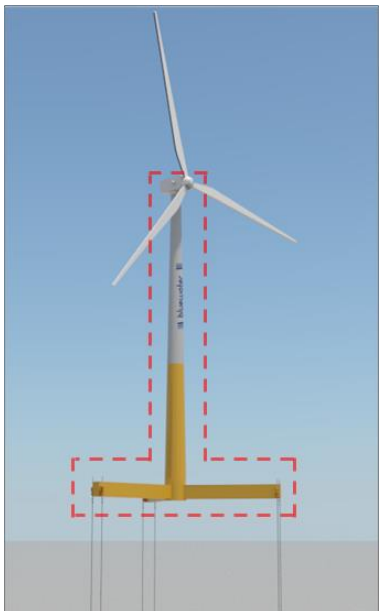

Figure 1-12: Structural Scope

The current study does not tackle any design considerations, nor does it consider any advanced rotor dynamics or effects of the turbine control system. The influence of ringing, springing, snap loads and VIVs will be discussed briefly, but these effects classify as design constraints and are therefore outside the scope of this thesis. Moreover, the problem of flexibility could not incorporated in the model within the time frame of this project. A direct consequence is that the influence of possible nonlinearities due to turbine or TLP deformations could not be captured within the linearization methodology. The influence of flexibility on the fatigue load response is addressed in a separate analysis, using existing coupled hydrodynamic and structural analysis software. Although advanced rotor dynamics is omitted, the model will account for coupled platform-turbine aerodynamics based on one-dimensional momentum theory including a closed-form approximation of the control system, with the possibility to incorporate more advanced turbine dynamics in follow-up studies.

1.5.2 Approach

Although this thesis involves several iterative processes that do not allow for a strictly phased approach, for the sake of clarity, the activities are grouped into a number of main phases. These consist of (1) a preparatory literature review, (2) development and validation of simulation models and (3) investigation of the influence of linearized dynamics. A summary of activities in each phase is listed below and a schematic overview of phase 2 and 3 is presented in Figure 1-13.

Phase 1: Literature Review

Prior to the development and analysis of the TLP's motion and stress response, a comprehensive literature study is carried out to gain clear understanding of relevant theory in the dynamics of TLPWTs and corresponding fatigue loads. The following topics are further explored:

- Underlying principle theories in hydromechanics, structural dynamics, structural mechanics and fatigue damage calculation;
- Theory and research on nonlinearities in TLPWTs;
- State of the art motion and stress computation tools for TLPWTs;
- Validated data regarding the dynamics of a reference TLPWTs.

Phase 2: Development and Validation of Simulation Model

During this phase, the dynamic model is developed in Matlab [6] by means of an iterative, step-by-step, development-validation process. This process is characterised by the following steps:

1. The first step is to establish an appropriate numerical model in Matlab for predicting the three-dimensional motions of a reference TLPWT with predetermined, validated data. The analytical model is built up in a step-wise manner and successively validated using motion analyses in OrcaFlex [7]. Geometrical and dynamic properties of the reference

TLPWT are based on publicly accessible conference reports and possible shortcomings in data are determined by means of a reverse engineering approach;

2. The analytical model is applied to the WindFlo TLP and extended to incorporate automated meshing, stochastic wind and wave generation and postprocessing of the stress and fatigue damage response at the governing structural hotspots.
3. Using an OrcaFlex model of the WindFlo TLP, the motion and stress response of the analytical model are verified and the influence of flexibility is investigated.

Phase 3: Influence of Linearized Dynamics

During the third and finally phase, the analytical model of the WindFlo TLP is linearized and the influence of nonlinearities are investigated by comparing the long-term fatigue damage and motion- and stress response with results of the nonlinear analytical model. The optimal linearization method is found by investigating multiple methods and determining their accuracy of each predicting the fatigue damage. Additionally, the importance of multi-axiality is investigated by establishing the principal stress directions and investigating degree of non-proportionality between normal and shear stress response.

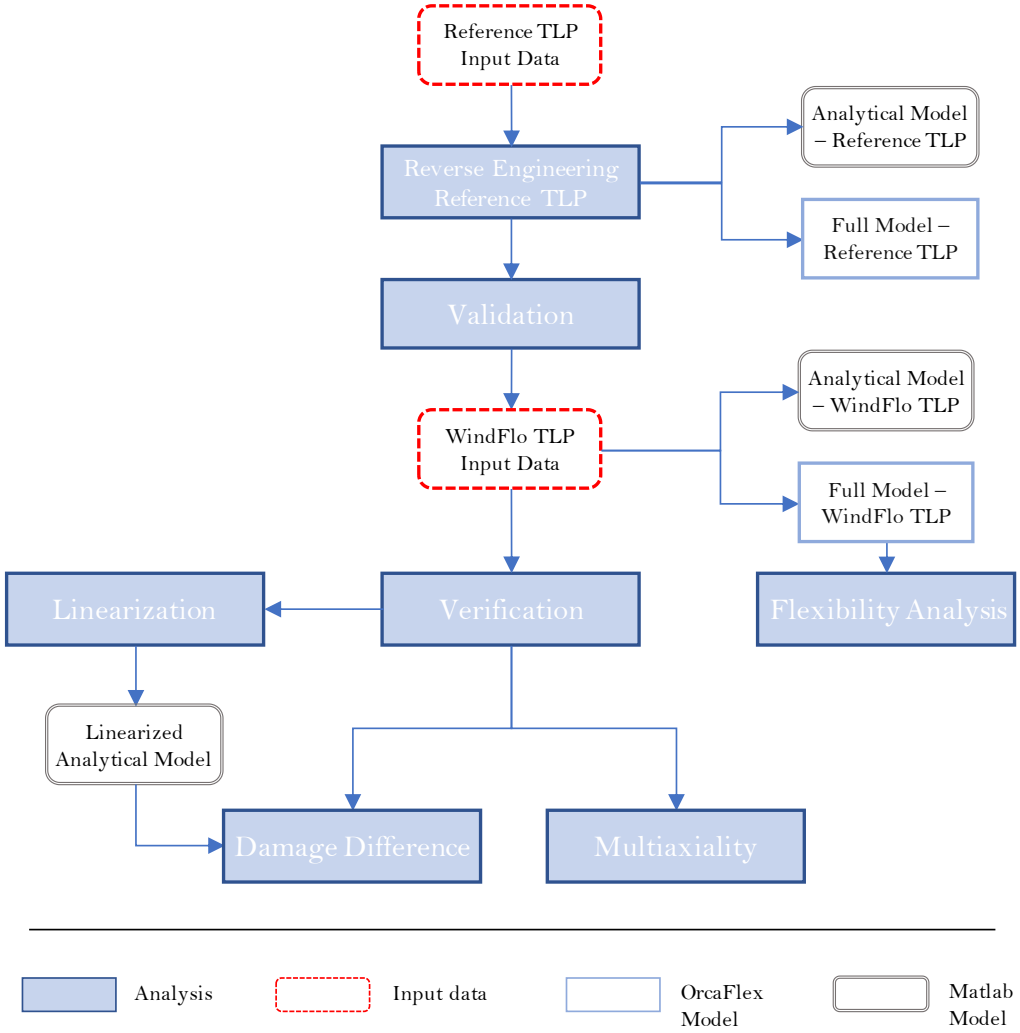

Figure 1-13: Schematic Overview of Research Approach

1.5.3 Thesis Outline

Chapter 1: Introduction

The research motivation, problem definition and composition of research goals and research questions are discussed in this chapter.

Chapter 2: Literature Review

Relevant theoretical background, current studies, available experimental data and computational simulation methods regarding TLPWTs are treated in this chapter. The chapter is finalized with conclusions and identification of the knowledge gap.

Chapter 3: Model Development

In this chapter, the application of theories to establish the mathematical description of the dynamics and structural analysis of the WindFlo TLP is described, including assumptions and ranges of applicability. The numerical application of the mathematical model and the detailed set-up of the numerical model is also discussed, including an evaluation of the numerical aspects of the solver. The final part of this chapter discusses the verification with OrcaFlex and a quantification of the influence of flexibility.

Chapter 4: Model Validation

The methodologies and results regarding the validation of the analytical model is discussed, which is conducted based on a reference TLPWT with predetermined properties and experimental data. This chapter also includes the reverse engineering approach and validation of the OrcaFlex model.

Chapter 5: Linearization

This chapter describes the theoretical and computational approach of linearizing the nonlinear dynamic system of the WindFlo TLP. The chapter concludes with the long-term fatigue damage difference between the nonlinear and linearized model.

Chapter 6: Conclusions and Recommendations

Based on results from earlier chapters, conclusions will be drawn on the performance of the developed model, the influence of nonlinearities and importance of multi-axiality, followed by a number of recommendations for further investigations.

2
LITERATURE REVIEW

The following chapter provides an overview of underlying principle theories in motion- and fatigue analyses and of TLPWTs, as well as the current state of the art regarding research and development of fatigue assessment methods. The focus will be primarily on the nonlinear effects that are typically encountered and their influence on the accuracy of linearized methods. Commonly accepted theories and methods can be recapitulated by reviewing the provided sources where the principles are explained in detail.

2.1 Hydromechanics

2.1.1 Wave Theories

One of the most important aspects in determining the fatigue lifetime of floating structures is the wave environment. In the most general case, ocean waves propagate as disturbances of water with non-uniform density in non-stationary directions while interacting with itself, the seabed, the wind and currents. This problem is mathematically too complex to solve and therefore, various linear and nonlinear approximation theories are derived based on specific assumptions and range of validity. Elaborate descriptions of these wave theories and the corresponding water particle kinematics are provided by Holthuijsen [8], with further elaboration on the higher order Stokes waves, Dean's Stream Function theory and Fenton's cnoidal theory in [9].

2.1.2 Hydrostatic and Hydrodynamic Forces

According to theory on offshore hydromechanics, as described by Journée [10], the general form of the total hydrostatic and -dynamic forces acting on a floating structure can be split into four parts, consisting of:

- *Incident wave forces,* caused by surface pressures on a fixed body subjected to approaching waves;
- *Diffracting wave forces*, due to the deflection of incoming waves caused by the presence of a fixed body;
- *Radiation forces*, due to radiated waves caused by oscillations of the body in still water;
- *Hydrostatic forces*, due to buoyancy of a submerged body in still water.

Although hydrostatic and incident wave forces may contain nonlinearities, such as quadratic drag, these forces can often be approximated without sophisticated solution techniques. For example, the empirically derived Morison equation is commonly used to determine wave loading

on slender structures. On the other hand, diffraction and radiation forces can only be determined by solving the diffraction and radiation potential, respectively. The solution to these force components contain nonlinear terms and require numerical diffraction software to solve them in TD.

2.1.3 Importance of Radiation and Diffraction Forces

The importance of implementing potential forces for TLPWTs has been studied extensively by Bachynski and Moan [11], where Morison-based motion response was compared with results using first and second order potential flow. Up to 10% higher tendon forces were found using the potential flow model in extreme conditions, while in operational conditions the results were almost identical. This was believed to be a consequence of high frequency wave forces, which led to increased pitch/bending resonance. It was also observed that for large diameter pontoons in wave frequencies near the natural frequency, the Morison equation gave unrealistic pitch/bending predictions, leading to a maximum mooring stress overprediction of 30% compared to the potential flow model. In a different study, Wehmeyer et al. [12] proved that when the TLPWT is exposed to irregular waves, depending on the geometry, second order diffraction forces could become important. The hydrodynamic damping was in all cases dominated by the nonlinear viscous contribution.

2.1.4 Second Order Wave Response

First and second order wave harmonics induce wave forces proportional to the wave amplitude and wave amplitude squared, respectively. First order wave forces are characterized by response frequencies that correspond with those of the first order harmonics, i.e. a linear relationship between wave- and response frequencies. Second order wave forces involve energy transfer from waves to structure motions at frequencies that do *not* correspond with those of the first order harmonics, i.e. there is no linear relationship between wave- and response frequencies [13]. Response to these forces may arise in the form of:

- *Mean drift forces*, constant force components that are proportional to the wave amplitude squared, causing a constant off-set of the structure;
- *Low frequency drift forces*, secondary wave forces caused by wave components at frequencies equal to the difference of two harmonic wave components with frequencies close to one another. The result is slow varying oscillations at frequencies much lower than the governing wave frequencies;
- *Sum-frequency wave forces,* secondary wave forces caused by wave components at frequencies equal to the sum of two harmonic wave components. The result is oscillations at frequencies much higher than the governing wave frequencies.

Nonlinear low frequency drift forces are implicitly incorporated by accounting for the instantaneous position of the platform when solving the structure's response to irregular waves, as determined by Kamirinad et al. [14]. The same technique is applied by Chandrasekaran & Jain [15] to account for mean (static) drift forces, for both regular and irregular waves. It was also observed that the method to extrapolate wave kinematics above Mean Sea Level (MSL) influenced the mean drift forces, which is a secondary nonlinear effect.

2.1.5 Sub- and Super-Harmonic Response

When waves remain (nearly) harmonic for a certain minimum duration, a steady state resonant response can build up at frequencies above or below the excitation frequency ω_{ex}. If resonance occurs at integer n multiples of the excitation frequency ($f_{super,n} = \omega_{ex} n$), the response is called a super-harmonic response. Sub-harmonic resonance occurs at fracture multiples of the excitation frequency ($f_{sub,n} = \omega_{ex}/n$). Yang et al. [16] showed that, for certain dynamic systems, super-harmonic resonance may even occur at non-integer multiples of the wave frequency.

This effect can only emerge for nonlinear dynamic systems with small damping and natural frequencies near the sub- or super-harmonic frequencies. Moreover, in irregular waves, harmonic wave propagation almost never lasts long enough to cause such effects [10]. It is nevertheless recommended by the DNV [17] to consider the super-harmonic excitations for TLPs, as they may cause resonance the heave, roll and pitch response.

2.2 Turbine Dynamics

2.2.1 Wind Forces

The wind environment exerts forces on the turbine primarily in the form of thrust loads and aerodynamic drag. According to one-dimensional momentum theory, thrust and aerodynamic drag forces have similar mathematical approximations as hydrodynamic drag, i.e. quadratic dependence on the flow velocity [18]. Wind turbulence, however, is highly stochastic and chaotic of nature and can therefore induce nonlinear forces and moments on the turbine. Time series of stochastic wind turbulence is often predicated using approximation methods such as the von Karman [19], Kaimal [20] and Frøya [21] model.

2.2.2 Nonlinear Turbine-Platform Interaction

During operating conditions, wind turbines can transmit several secondary nonlinear vibrations onto the platform. For example:

1. *The active blade pitch control system*, which induces secondary vibrations that are implicitly dependent on the aerodynamic forces acting on the blades [22], [23];
2. *Gyroscopic moments,* generated by interactions between the rotating blades with coupled nacelle-platform motions [24];

3. *Tower flexibility;*
4. *Misaligned wind and wave excitation.*

FOWTs compensate for variations in thrust-induced moments by actively pitching the blades and de-powering the turbine. This control system algorithm is used to maintain constant power but produces highly dynamic vibrations. Lupton [25] investigated the accuracy of linearized control system dynamics of FOWTs and found that the results were inaccurate near rated wind speeds, conditions in which fatigue damage is usually governing. Near rated wind speed, both the pitch and variable speed controllers are active, causing highly nonlinear interactions between both control systems. The mismatch was believed to be caused by this effect.

The importance of gyroscopic moments was investigated by Jensen [26], concluding that its main effects, being torsional shear stresses at tower base, are usually negligible for the tower stress response. Matha et al. [27] developed a comprehensive tool for TLPWTs that accounts for hydrodynamic loads, nonlinear aerodynamics, gyroscopic effects and tower flexibility. A study case was investigated based on the NREL 5MW turbine, comparing the flexible-tower nonlinear results with a fully rigid nonlinear model and a fully rigid linear model. The most noticeable difference was found between the flexible model and rigid models, where in the flexible model, the tower-bending flexibility caused a shift of the pitch RAO peaks towards lower frequencies.

Influence of misaligned wind and waves on the motions and fatigue damage in FOWTs was investigated by Bachynski et al. [28]. They concluded that in operational conditions, the low-frequency horizontal motions increase for increasing misalignment while the axial stress induced fatigue damage at tower base was reduced. The major contribution to the fatigue loads at tower base were due to blade passing vibrations.

2.3 Mooring System

2.3.1 Quasi-Static Mooring Forces

The relationship between the quasi-static mooring forces and platform displacements becomes nonlinear after a certain offset from its equilibrium position. An effect that is typically caused by large horizontal platform displacements is the set-down effect, causing coupling between the horizontal and vertical displacement [29]. Asymmetric mooring line configurations or mooring lines under a static angle often cause nonlinear response, even for small displacements. These phenomena are visualized in Figure 2-1 and Figure 2-2.

Realistic mathematical representation of TLP restoring forces was derived by Senjanovic et al. [30] and Tabeshpour & Shoghi [31], incorporating the nonlinear set-down effects. It was observed that in case of large mean offset due to, for example, currents or mean drift forces, the TLP's motions experience a hardening effect. Nonlinearity in mooring forces may also lead to changes in the eigenfrequencies of the system. Bapat & Sprinivasan [32] demonstrated that, for

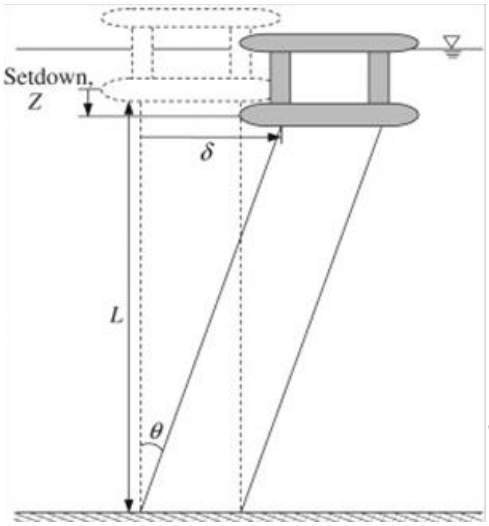

Figure 2-1: Set-Down Effect

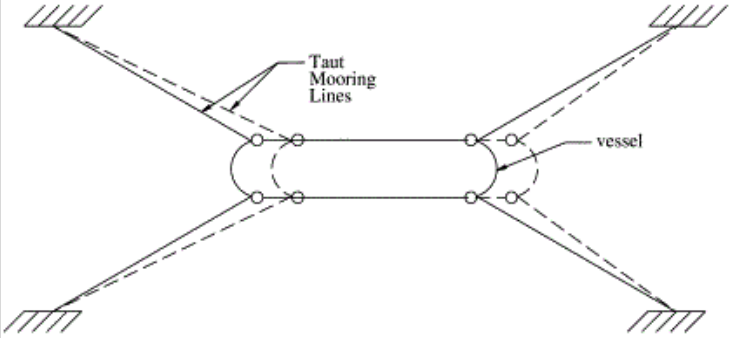

Figure 2-2: Inclined Mooring Lines (Top View)

a TLP with given harmonic excitation, the natural period of the horizontal motion decreases if the static deflection is not negligible compared to the oscillation amplitudes.

2.3.2 Snap Loads and Mooring Dynamics

Snap loads are high-peaked impact forces caused by sudden reactivation of line tension after slacking momentarily. Mooring dynamics (vibrations), caused by inertial effects of the mooring lines, are included in FLS analyses when resonance with waves or currents are expected. A study by Hall et al. [33], focussing on the differences in dynamic and quasi-static based modelling on of TLPWT mooring lines, showed that the quasi-static model started to exhibit small errors in the tower-base load predictions in the case of extreme conditions and minimal aerodynamic damping. Mooring load discrepancies remained under 1% as long as snap loads did not occur. Hsu et al. [34] showed that, indeed, impact forces caused by snap loads can cause mooring stress peaks up to 68% larger than the cyclic non-snap maxima.

Mooring dynamics of TLPs mostly involve Vortex Induced Vibrations (VIVs), which may influence the tendons' fatigue sensitivity if the mooring natural frequency is close to the vortex shedding frequency [17]. Surprisingly few studies have been performed on the sensitivity of TLPWTs to these effects. An interesting example, though not specifically applicable to TLPWTs, is Stabile's [35] linearized method for calculation of VIVs in offshore structures. Based on experimental validation, it was observed that the model was accurate in predicting the amplitude and oscillations for at least a number of flow velocities.

2.4 Flexibility Induced Nonlinearities

2.4.1 Ringing and Springing

Various nonlinear resonance phenomena arise when the natural frequency of a structural vibration mode is in the vicinity a first- or second order excitation frequency. For TLPs, the most important ones are:

- *Ringing*, a transient elastic response in the vertical (heave) and/or pitch-bending mode at frequencies much higher than the governing wave frequencies;
- *Springing*, a steady-state resonant response (in the same modes as ringing) to high frequency wave loads;

Bachynski & Moan [36] investigated the sensitivity of a TLPWT to ringing response. This study showed the fatigue sensitivity due to ringing response to be particularly important for structures with coupled pitch/tower-bending natural period of 3 to 4s. Aerodynamic damping from the turbine showed to be important whereas the hydrodynamic drag was insignificant. Shen et al. [37] and Matsui et al. [38] performed a similar study on springing response, which showed a highly nonlinear dependency on the wave height and was also influenced by quadratic drag forces. Again, aerodynamic loads had a damping effect on the structural vibrations.

2.4.2 Hydroelasticity

The motion response is directly influenced by the instantaneous position, velocity and acceleration of the structure with respect to the surrounding water and air flow. At the same time, the hydro- and aerodynamic loads causing the structure to deform are also dependent on the instantaneous position, velocity and acceleration. This implicit relationship, illustrated in Figure 2-3, is called hydroelasticity and causes a nonlinear coupling between external and internal loads [39]. When global deformations in the support structure or turbine become large and external forces are purely based on rigid body motions, hydro-elastic response could affect the accuracy of the solutions.

Hydroelasticity has not been investigated extensively for FOWTs, with only two studies that are considered to be relevant. A study by Kamirinad et al. [14] determined that, for a tension leg spar, the hydro-elastic response caused structural damping in the surge and pitch motions while

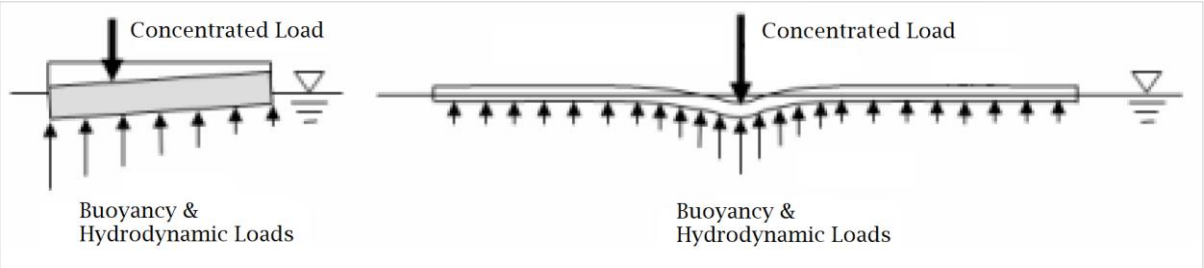

Figure 2-3: Conventional Fluid-Structure Interaction (Left) and Hydroelasticity (Right)

tendon forces were only influenced in case of heave resonance. And Finn's [40] Morison-based Finite Element Analysis showed that if the first elastic natural frequency of the FOWT, which is often the pitch/tower-bending mode, is below 5 times the wave peak frequency, hydroelasticity should be included.

2.5 Fatigue Damage

2.5.1 Calculation Methods

Fundamentals of fatigue damage calculations and damage mechanisms in marine and steel structures are explained by Schijve [41], Radaj [42], Lassen [43] and den Besten [44]. The three-part series by Hartsuijker [45] gives an extensive overview of all theories in the field of applied mechanics and structural analysis, which can be used for stress analyses. Depending on the required accuracy of the fatigue loads, one can make use of three stress calculation techniques, being the nominal, hotspot and notch stress concept. The most straightforward method is the nominal stress concept, which is based on elasticity theory and ignores all local stress concentrations. In other words, it uses the initial cross-sectional area without accounting for any geometrical discontinuities, local stiffness variations or plastic deformations. The hotspot stress method includes local stiffness induced stress concentrations and the notch stress method also accounts for the presence of the weld. In any case, the maximum principal stress is generally chosen for calculation of fatigue damage.

Stress-based fatigue damage methodologies are either based on stress cycle counting in TD or spectral analysis in FD. Using the stress cycle counting method, one can apply the Palmgren-Miner rule to determine the fatigue damage accumulation during the period of the time series. In the case of spectral analysis, the stress response is formulated in terms of frequency dependent, harmonic stress amplitudes. As a result, the complete sea-state characterisation is directly converted from wave- and wind spectra into stress energy spectra by means of Response Amplitude Operators (RAOs). From the stress energy spectra, the long-term fatigue damage accumulation is calculated directly.

2.5.2 Multiaxial Fatigue

A fairly new concept in the field of fatigue damage is the principle of multiaxial fatigue damage estimation, which is fatigue damage due to combined normal and shear stress components. In case of non-proportional loading, which is the occurrence of out-of-phase normal and shear stresses, the principal stress direction varies in time. This makes it impossible to characterize the fatigue damage by a single stress state [46]. Since conventional damage accumulation methodologies are based on a constant stress direction, non-proportional loading poses additional difficulties.

There are several enhanced methods and codes that are developed to account for multiaxial fatigue damage calculations, of which the vast majority have not been experimentally validated (see for example [47] - [53]). The most commonly applied multiaxial fatigue damage methods are summarized by Marin [54] and Lieshout et al. [55], with the most notable method being the Path Dependent Maximum Range Method (PDMR). This approach was formulated by Dong et al. [56] and verified based on existing multiaxial fatigue data. Lieshout et al. observed large discrepancies in results between different methods and proposed experimental testing under non-proportional multiaxial load for validation, refinement or the development of existing and new methods. Contrary to assumptions in DNV standards, in which disregarding multiaxiality is considered as conservatism [17], Lieshout et al. concluded that, in case of non-proportional multiaxiality, application of uniaxial-based approach can lead to non-conservative results. Non-proportional loading is represented by out-of-phase normal and shear stresses.

2.6 Computational Modelling

2.6.1 State of the Art Modelling Software

Dynamic and fatigue analyses of a TLPWT can be performed using pre-established techniques and software tools. The highest possible accuracy and detail level is obtained when modelling the full range of hydro- and aeromechanics by application of the Navier-Stokes equations, implemented in a CFD-based software. However, when long simulations are required and complex problems need to be solved, this is computationally too expensive. For this reason, various simplified motion and stress simulation methods have been developed, each with a specific application area and solved with different software.

An overview of 19 different FOWT motion and stress analysis methods and their capabilities are listed and reviewed in a comparison study performed by Robertson et al. [57]. Although the assessments of the methods were based on application to a semi-sub FOWT, it nevertheless provides a good representation of the methods currently applied. The considered methods can evaluate the linear and nonlinear hydro- and aerodynamics of FOWTs including mooring line dynamics and structural deformations. The latter are analysed dynamically or quasi-statically using modal analysis, multibody approach (rigid or flexible body discretisation), in FEA or a combination of multiple techniques. Turbine aerodynamics are usually modelled using Blade Element Momentum (BEM)-theory, with an external function to simulate the turbine control system in parallel [58].

For the specific application on TLPWTs, motion and stress analyses are performed using similar techniques as described above. Examples of these methodologies are presented by [59], [60] and [61], all incorporating nonlinear wave and wind loading including flexibility and control system vibrations.

2.6.2 Linear vs Nonlinear Modelling Methods

A dynamic system is called nonlinear when the system's dependent variables (positions, velocities, accelerations) consist of mathematically nonlinear functions or when the mass, damping or stiffness matrix is non-symmetric [62]. Linearization of nonlinear dynamic systems is often performed using the small perturbation method, which approximates the nonlinear solution around an equilibrium point under the assumption of small disturbances [63]. General theories on structural dynamics, including formulation of equations of motion (EoMs) and solution methods of linear and nonlinear dynamic systems is described by Metrikine et al. [64].

Jonkman [65] developed a TD simulation model based on Airy wave theory to calculate the linear wave radiation and diffraction combined with nonlinear turbine aerodynamics, after which the results were compared to fully linear FD simulations. Even after linearization of the mooring forces, the pitch motion RAOs were incomparable, which was believed to be caused by the pitch motions being dominated by nonlinear aerodynamics. The adequacy of FD methods for TLPWTs was also investigated by Bachynski & Moan [66], by comparing fully nonlinear TD simulations with FD results. They found that the FD approach was merely usable for predicting trends in motions and mooring forces but failed to accurately assess the designs' motion performance. In a similar study, Kvittem & Moan [67] developed a rigid-body FD method to assess the fatigue damage of a semi-sub FOWT, using superposition of decoupled wind and wave response. Compared to results from a fully flexible, nonlinear TD model with coupled wind and wave excitation, the short-term tower base fatigue damage was underestimated by 0-60%. This was due to (1) disregarding tower flexibility, (2) lost nonlinear aerodynamic loads and (3) decoupling of the wind and wave excitations.

2.6.3 OrcaFlex Software

A pre-established and validated modelling tool that has been used in this thesis for validation, verification and assessment of flexibility influences is OrcaFlex, a hydrodynamic software capable of performing coupled nonlinear, three-dimensional TD and linear FD analyses of rigid and flexible multi-bodies in (non)linear waves. The most important properties regarding modelling, analyses and numerical properties of solution techniques are summarized below. For detailed information, it is referred to the OrcaFlex Manual [7].

Object Types

Models are composed of 8 types of objects, all with distinct dynamic, structural and computational properties. The two types of objects used in this thesis are:

- *6D Buoys* – Rigid bodies with motions in 6 DOFs around its local CoG/CoB, calculated based on hydromechanical loads (Morison's equation), aerodynamic loads (friction), applied user-defined loads and contact loads. This object type is further subdivided in lumped buoys (abstract geometry), spar buoys (cylinder with local z-axis along longitudinal axis) and towed fish (cylinder with local z-axis along lateral axis).

- *Lines* – Flexible linear elements, modelled as lumped masses connected with massless springs. Geometrical, sectional and structural properties are all defined by the user. Pre-defined properties of a number of flexible materials are provided in the Line Type Wizard.

Computation Methods

Prior to motion analyses, the system's static equilibrium is determined, including the mooring line static positions and the system's natural modes. Dynamic analyses in FD are based on a linearized system, performed using the small perturbation technique combined with an iterative algorithm to linearize quadratic drag forces. The TD approach is limited to fully nonlinear dynamics, based on numerical integration of the EoMs.

Numerical Aspects

Analyses in TD are performed with an explicit or implicit integration scheme, both using a constant, user-defined time step size. The explicit solver is based on the semi-implicit Euler method, which is a more accurate and robust version of the forward Euler method. The implicit solver (Generalized Alpha method) also includes pre-programmed numerical damping to minimize non-physical high frequency response.

2.7 Experimental Validation

2.7.1 Available Scale Test Data

Once the computational model is developed in Matlab, the validity of the model needs to be confirmed based on experimentally derived data. Since such data was not yet available for the WindFlo TLP, an investigation is conducted to assemble relevant scale test data with which the model can be validated. Three different scale test results of TLPWTs have been made public, being the SBM TLP [68], Gicon's hybrid semi-sub TLP [69] and the Iberdrola TLP [70].

Based on the provided data, it has become clear that SBM's TLP is the only reliable option to validate the model. The dynamic properties of Gicon's hybrid TLP (Figure 1-7) are expected to differ too much from the WindFlo mono-column TLP to serve as a reliable validation basis, as the physics behind the dynamic model is based on the behaviour of the WindFlo TLP. Although the Iberdrola TLP-geometry seems to match the WindFlo TLP more, insufficient data was provided to be able to apply the analytical model to this TLPWT.

2.7.2 SBM TLP

SBM's truss type TLPWT consists of three outer buoys and a middle buoy, connected with a braced system in an equilateral-shaped arrangement (Figure 2-4). The support structure is designed to support the NREL5MW turbine at 80m water depth [71], validated with 1:40 scale experimental testing (Figure 2-5). Technical properties and scale test results are obtained from the OMAE2016 [68] and OTC2016 [72] conference paper, made public by SBM.

Figure 2-4: SBM 3D TLP Geometry [68]

Figure 2-5: SBM TLP Scale Model [68]

Technical Properties

The bracing system are subdivided in primary elements, with the purpose of transferring global loads, and secondary elements, to minimize the buckling length of primary parts. Mooring lines are connected to each side buoy and consist of standard offshore grade mooring chain. Great emphasis is placed on the vertical configuration of the mooring lines, which is characterized by the fact that the extension of the lines intersect at an imaginary point just above nacelle height. This arrangement causes a compliant mechanism in roll and pitch, resulting in negligible horizontal nacelle velocities and the subsequent application of a turbine control system that is almost identical to those of land-based turbines. Technical properties of the platform are listed in Table 2-1. A number of notable design related statements are summarized below:

- The bracing assembly is designed similar to jacket structure designs;
- The bracing system is designed to participate in the overall buoyancy of the platform;
- The transition piece in the platform is derived from swivel stacks employed in taut-moored FPSOs, which weight up to 300t;
- The middle buoy is fully buoyant during all conditions and the side buoys may be partially filled with ballast water during operational conditions;
- During operational conditions, platform elements penetrating the water surface are limited to the bracing and transition piece;
- Hydrostatic stability during towing operation, which is conducted after integration of the turbine, is ensured without the use of stabilization auxiliary;
- The tower wall thickness of the NREL5MW turbine is adjusted to meet specific design requirements.

Table 2-1: Technical Properties SBM TLP

Parameter	Unit	Value
Floater radius (from centre to chain connector)	m	45
Floater height (from keel to tower flange)	m	35
Displacement (operating)	t	2200
Bundle pretension	kN	1560
Draft at {operating, towing, load-out} conditions	m	25, 6.4, 4.3
GM (towing)	m	41.2
Hub height w.r.t. MSL	m	85
Tower length	m	74
Tower connection height w.r.t. MSL	m	10
Rotor plane diameter	m	132
Tower mass	t	222
RNA mass	t	300
Max. thrust force	kN	720
Natural period sway/roll (rigid)	s	46.8
Natural period surge/pitch (rigid)	s	45.0
Natural period yaw (rigid)	s	25.1
Natural period heave (structural)	s	2.5

2.8 Conclusions and Knowledge Gap

2.8.1 Studies and Experiments on Dynamics and Fatigue of TLPWTs

Existing studies on nonlinearities of FOWTs are strongly focused on a specific design or with emphasis on a particular phenomenon, using solution methods that often offer little transparency. Quantitative results and observations regarding the effects of nonlinearities should, therefore, not be seen as a guideline to draw conclusions for the WindFlo TLP but serve only as a preliminary assessment of the importance of such influences. With this in mind, the following hypotheses can be formulated with regard to the calculation of fatigue damage of TLPWTs:

- The accuracy of wave theories is mostly governed by local met-ocean characteristics, and even with application of the linear wave theory, hydrodynamic radiation and potential forces may still arise, making the hydrodynamic problem too complex to solve with closed-form expressions such as the Morison equation. It is not possible to state in advance whether such inaccuracies will overestimate or underestimate results;

- In the case of narrow banded wave distribution, the irregular wave regime will approximate a harmonic wave field, with the result that super-harmonic frequencies can resonate with the weakly damped heave, roll and pitch motions;
- Structural vibrations of the turbine are especially important when there is a risk of resonance of the pitch and roll motions of the platform, as these are strongly coupled to the bending vibrations of the tower;
- The combination of stochastic wind regime and highly nonlinear blade control systems makes it difficult to obtain accurate linearized aerodynamic response of the turbine;
- Gyroscopic moments and wind-wave misalignments have proven to be of secondary importance for the fatigue damage of TLPWTs;
- Mooring loads are well approximated using quasi-static approach, provided that snap loads do not occur.

The extent to which fatigue life of TLPWTs is influenced by control system vibrations, mooring line VIVs, hydroelasticity and multi-axial fatigue have not been sufficiently investigated to form any hypotheses. Moreover, studies on differences between linear and non-linear modelling methods provided insufficient insight into the exact physics behind the observations. It is, therefore, not possible to confirm to what extent these aspects affect the reliability of linear approximation methods for fatigue damage of TLPWTs. Experimental data concerning the dynamics and fatigue damage of TLPWTs is scarce, where most of the available data is either incomplete or unsuitable for validation purposes. Although the available data is limited and incomplete, SBM's TLP has been considered as the best option to validate the dynamic model. As a result, shortcomings in information have to be estimated on the basis of the available data.

2.8.2 Computational Solution Methods

Several existing methods and simulation tools are available to model the WindFlo TLP, in which all relevant nonlinearities are included and the most sophisticated dynamics and fatigue modelling is applied. The problem is that the complexity level of such elaborate models has a certain lower limit, so that it is often not possible to model a simple representation of the FOWT dynamics.

There are also a number of hydrodynamic software tools that offer the possibility to simulate the internal stress response in TD or FD. However, these tools are either not applicable to TLPWTs or designed as black-box tools. Such tools do not offer the possibility to make conceptual changes and adjust the mathematical descriptions behind the solver. This makes it impossible to isolate the influence of nonlinear phenomena and adjust or linearize terms. This statement has proved equally valid for OrcaFlex. The main characteristics of the modelling and solution methods of OrcaFlex have been investigated, which has led to the conviction that the tool is versatile in solution and postprocessing techniques but is very limited in adjustments of underlying mathematical descriptions.

3
MODEL DEVELOPMENT

The following chapter deals with the development of the computational model, including the theoretical basis for describing the system's dynamics with corresponding assumptions and ranges of validity. This is followed by the numerical implementation of the EoMs and the postprocessing methods to evaluate the stress and fatigue damage response.

3.1 Rigid Body Dynamics

3.1.1 Definition of Degrees of Freedom

The platform's three dimensional rigid-body motions are computed in time domain by numerically solving the coupled 6DOF-EoMs. The six degrees of freedom are defined as Surge (η_1), Sway (η_2), Heave (η_3), Roll (η_4), Pitch (η_5) and Yaw (η_6). It is assumed that the kinematics of the structure are independent of the location of the reference point at which the EoMs are solved; in this case, the reference point is chosen at the Centre of Gravity (CoG) of the structure. The positive directions of these motions w.r.t. the CoG is visualized in Figure 3-1.

3.1.2 Axis Conventions

To describe the platform's motions and position in space, it is made use of three types of cartesian coordinate systems. Each axis convention is described below, with a visual representation in Figure 3-2.

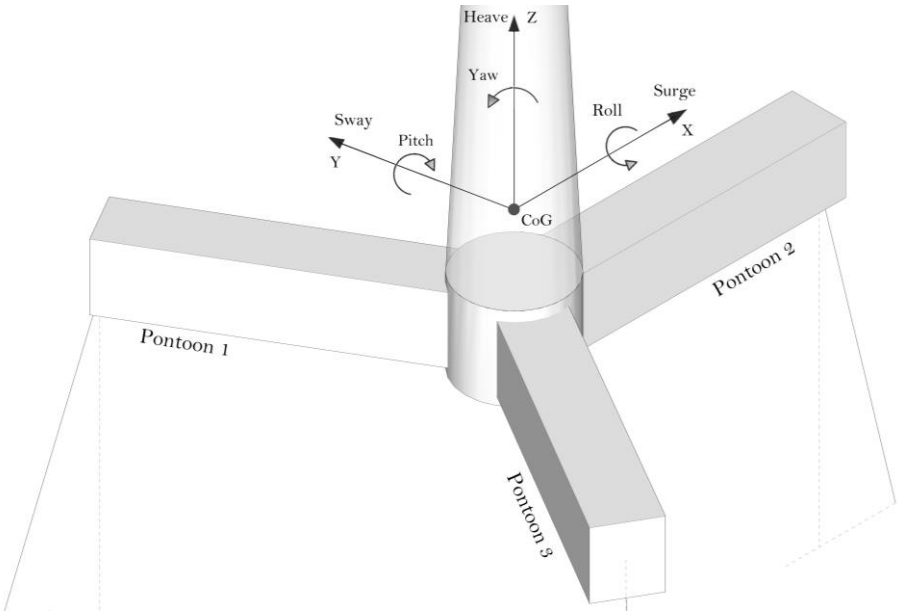

Figure 3-1: Definition of Degrees of Freedom

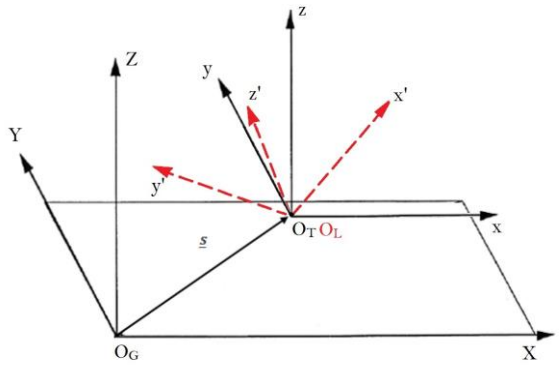

Figure 3-2: Axis Conventions

Earth-bound Global Coordinate System

The earth-bound global coordinate frame O_GXYZ has its origin O_G at the static position of the CoG. All motions and positions within this axis convention are defined in an *inertial* frame of reference, relative to the *static* origin O_G.

Translational Local Coordinate System

The translational local coordinate frame $O_T$xyz has its origin O_T at the non-rotating, displaced position of the CoG, resulting from only the translational displacements $\underline{s} = [\eta_1 \quad \eta_2 \quad \eta_3]^T$. Since all motions and positions within this axis convention are relative to an origin that is *accelerated* in the translational DOFs, objects experience no translational motions.

Body-Bound Local Coordinate Systems

The local body-bound coordinate frame O_Lx'y'z' has its origin O_L at the instantaneous position of the CoG. All motions and positions within this axis convention are defined in a *non-inertial* frame of reference, relative to an origin O_L that is *accelerated* in all DOFs. Since the origin is accelerated together with the platform, motions seem absent when viewed from O_L. Note that any other non-inertial coordinate frame can be created by positioning the origin of this coordinate frame at an arbitrary point on the structure.

3.1.3 Rotation Matrix

In linear algebra, a rotation matrix is defined as a matrix whose multiplication with any vector rotates the vector while preserving its length. Under the condition that only rigid bodies and non-rotating reference frames are considered, the rotated position of a point can be described by the product of a rotation matrix $\boldsymbol{R}$ with the cartesian coordinates of that point. By using this property, the shifted coordinates of a point due to rotational displacements can be described in the $O_T$xyz frame according to Equation [3-1].

$$\underline{p} = [x_P \quad y_P \quad z_P]^T = \boldsymbol{R} \cdot \underline{p}' \qquad [3\text{-}1]$$

where $\underline{p}' = [x_P' \quad y_P' \quad z_P']^T$ is the coordinate vector of a point in the O_Lx'y'z' frame.

The total rotation matrix $\boldsymbol{R}$ is, according to Euler's rotation theorem, the matrix multiplication of the three elemental rotation matrices that describe rotations around the axes of the coordinate system. The total rotation matrix is different for different sequences in which the elemental rotation matrices are multiplied. The yaw-pitch-roll sequence is utilized in this thesis, as illustrated in Figure 3-3.

The elemental rotation matrices for roll, pitch and yaw w.r.t. the translational local coordinate frame $O_T$xyz are given in Equation [3-2], [3-3] and [3-4], respectively. The total rotation matrix is shown in Equation [3-5].

$$\boldsymbol{R}_x = \begin{bmatrix} 1 & 0 & 0 \\ 0 & \mathrm{c}(\eta_4) & -\mathrm{s}(\eta_4) \\ 0 & \mathrm{s}(\eta_4) & \mathrm{c}(\eta_4) \end{bmatrix} \quad [3\text{-}2]$$

$$\boldsymbol{R}_y = \begin{bmatrix} \mathrm{c}(\eta_5) & 0 & \mathrm{s}(\eta_5) \\ 0 & 1 & 0 \\ -\mathrm{s}(\eta_5) & 0 & \mathrm{c}(\eta_5) \end{bmatrix} \quad [3\text{-}3]$$

$$\boldsymbol{R}_z = \begin{bmatrix} \mathrm{c}(\eta_6) & -\mathrm{s}(\eta_6) & 0 \\ \mathrm{s}(\eta_6) & \mathrm{c}(\eta_6) & 0 \\ 0 & 0 & 1 \end{bmatrix} \quad [3\text{-}4]$$

$$\boldsymbol{R} = \boldsymbol{R}_z \cdot \boldsymbol{R}_y \cdot \boldsymbol{R}_x = \begin{bmatrix} \mathrm{c}(\eta_6)\mathrm{c}(\eta_5) & \mathrm{c}(\eta_6)\mathrm{s}(\eta_5)\mathrm{s}(\eta_4) - \mathrm{s}(\eta_6)\mathrm{c}(\eta_4) & \mathrm{s}(\eta_6)\mathrm{s}(\eta_4) + \mathrm{c}(\eta_6)\mathrm{s}(\eta_5)\mathrm{c}(\eta_4) \\ \mathrm{s}(\eta_6)\mathrm{c}(\eta_5) & \mathrm{s}(\eta_6)\mathrm{s}(\eta_5)\mathrm{s}(\eta_4) + \mathrm{c}(\eta_6)\mathrm{c}(\eta_4) & \mathrm{s}(\eta_6)\mathrm{s}(\eta_5)\mathrm{c}(\eta_4) - \mathrm{c}(\eta_6)\mathrm{s}(\eta_4) \\ -\mathrm{s}(\eta_5) & \mathrm{c}(\eta_5)\mathrm{s}(\eta_4) & \mathrm{c}(\eta_5)\mathrm{c}(\eta_4) \end{bmatrix} \quad [3\text{-}5]$$

where c and s are shortened notations for cosine and sine, respectively.

Similar to the translation of coordinates due to rotations about $O_T$xyz, angular motions also induce translational motions. The translational velocities $\underline{\dot{p}}$ and accelerations $\underline{\ddot{p}}$ due to angular velocities and accelerations about $O_T$xyz can be determined by resp. multiplying the first and second time-derivative of $\boldsymbol{R}$ with $\underline{p'}$, as shown in Equation [3-6] and [3-7]. Here, the single and double dot above the variables symbolize the first and second time derivative, respectively.

$$\underline{\dot{p}} = [\dot{x}_P \quad \dot{y}_P \quad \dot{z}_P]^T = \dot{\boldsymbol{R}} \cdot \underline{p'} \quad [3\text{-}6]$$

$$\underline{\ddot{p}} = [\ddot{x}_P \quad \ddot{y}_P \quad \ddot{z}_P]^T = \ddot{\boldsymbol{R}} \cdot \underline{p'} \quad [3\text{-}7]$$

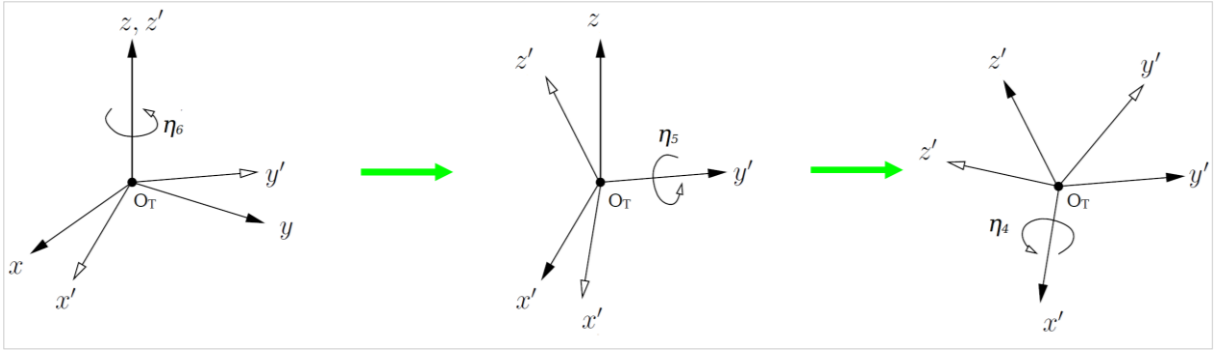

Figure 3-3: Elemental Rotation in Yaw, Pitch and Roll (From Left to Right)

The first and second time derivatives of $\boldsymbol{R}$, depicted in resp. Equations [3-8] and [3-9], are determined according to the chain rule.

$$\dot{\boldsymbol{R}} = \frac{\partial \boldsymbol{R}}{\partial t} = \frac{\partial \boldsymbol{R}}{\partial \eta_4}\dot{\eta}_4 + \frac{\partial \boldsymbol{R}}{\partial \eta_5}\dot{\eta}_5 + \frac{\partial \boldsymbol{R}}{\partial \eta_6}\dot{\eta}_6 \quad [3\text{-}8]$$

$$\ddot{\boldsymbol{R}} = \frac{\partial^2 \boldsymbol{R}}{\partial t^2} = \frac{\partial \dot{\boldsymbol{R}}}{\partial \eta_4}\dot{\eta}_4 + \frac{\partial \dot{\boldsymbol{R}}}{\partial \eta_5}\dot{\eta}_5 + \frac{\partial \dot{\boldsymbol{R}}}{\partial \eta_6}\dot{\eta}_6 + \frac{\partial \dot{\boldsymbol{R}}}{\partial \dot{\eta}_4}\ddot{\eta}_4 + \frac{\partial \dot{\boldsymbol{R}}}{\partial \dot{\eta}_5}\ddot{\eta}_5 + \frac{\partial \boldsymbol{R}}{\partial \dot{\eta}_6}\ddot{\eta}_6 \quad [3\text{-}9]$$

3.1.4 Coordinate Transformations

To obtain positions and motions in the earth-bound global coordinate frame $O_G XYZ$, one must transform the positions and motions from $O_T xyz$ back to $O_G XYZ$. This is done according to the expressions in Equation [3-10], [3-11] and [3-12].

$$\underline{P} = \underline{p} + \underline{s} = \boldsymbol{R} \cdot \underline{p}' + [\eta_1 \quad \eta_2 \quad \eta_3]^T \quad [3\text{-}10]$$

$$\underline{\dot{P}} = \underline{\dot{p}} + \underline{\dot{s}} = \dot{\boldsymbol{R}} \cdot \underline{p}' + [\dot{\eta}_1 \quad \dot{\eta}_2 \quad \dot{\eta}_3]^T \quad [3\text{-}11]$$

$$\underline{\ddot{P}} = \underline{\ddot{p}} + \underline{\ddot{s}} = \ddot{\boldsymbol{R}} \cdot \underline{p}' + [\ddot{\eta}_1 \quad \ddot{\eta}_2 \quad \ddot{\eta}_3]^T \quad [3\text{-}12]$$

In the remainder of this report, coordinates or motion vectors denoted with a capital letter imply that it is defined w.r.t. the global coordinate frame, whereas small letters and letters with a single quotation mark are coordinates or motions in the translational and local coordinate frame, respectively. It is also worth mentioning that transformations from global to local axes is performed in a similar manner as described above, but by multiplication with the inverse of $\boldsymbol{R}$.

3.1.5 Formulation of EoMs

The complete nonlinear EoMs for the coupled platform and wind turbine are derived according to Newton's second law. Translational DOFs (1 to 3) are solved in the earth-bound global coordinate system whereas the rotational DOFs (4 to 6) are computed around the instantaneous CoG, i.e. the translational local coordinate system (illustrated in Figure 3-4). The general form of the EoM is shown in Equation [3-13].

$$\boldsymbol{M}\underline{\ddot{\eta}} = \underline{f_{ext}} + \underline{f_{moor}} \quad [3\text{-}13]$$

where $\boldsymbol{M}$ is the mass matrix, $\underline{f_{ext}}$ is the total external force vector and $\underline{f_{moor}}$ is the mooring force vector.

The total external force vector is a summation of the hydrostatic force vector $\underline{f_{stat}}$, the hydrodynamic force vector $\underline{f_{hyd}}$ and the turbine induced force vector $\underline{f_{turb}}$, as shown in Equation [3-14]. Each of these terms will be discussed in the following sections.

$$\underline{f_{ext}} = \underline{f_{stat}} + \underline{f_{hyd}} + \underline{f_{turb}} \quad [3\text{-}14]$$

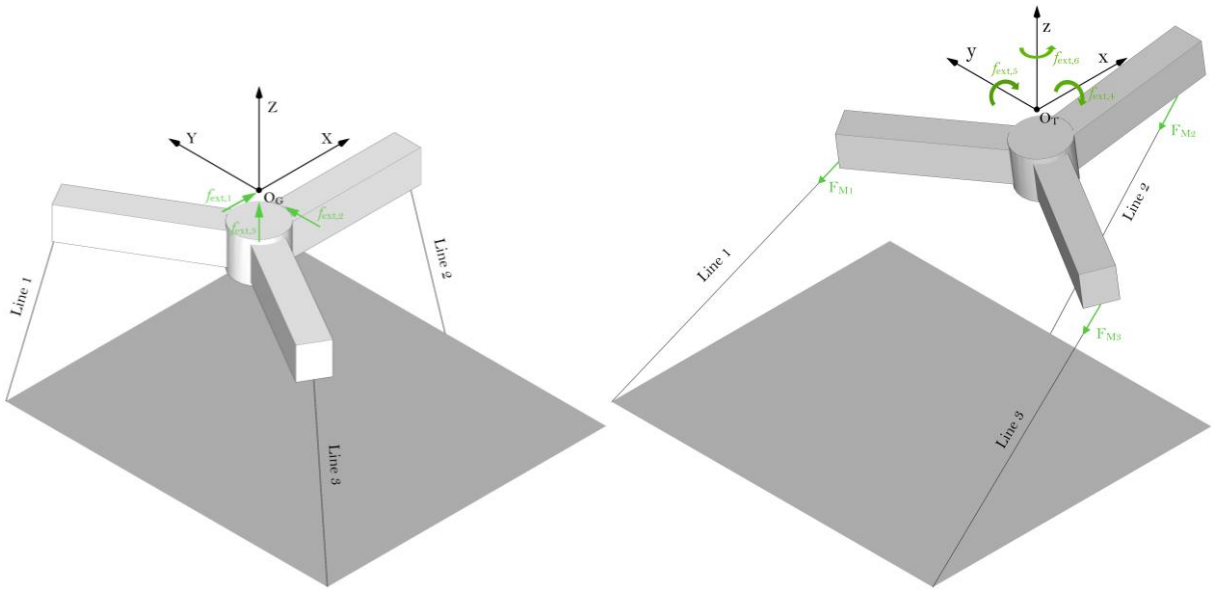

(a) (b)

Figure 3-4: Definition of Loads in the Global (a) and Translational (b) Axis Frame

3.1.6 Structural Mass Matrix

Since the reference point of the EoMs (O_G) is chosen at the CoG, inertial forces are considered fully decoupled and therefore the structural mass matrix is a 6x6 diagonal matrix, as shown in Equation [3-15]. Note that the mass of all structural components (thus the position of CoG) is considered time independent and mass density is assumed constant throughout the whole structure. The complete calculations of mass moments of inertia are shown in Appendix B.

$$\boldsymbol{M} = \begin{bmatrix} m & 0 & 0 & 0 & 0 & 0 \\ 0 & m & 0 & 0 & 0 & 0 \\ 0 & 0 & m & 0 & 0 & 0 \\ 0 & 0 & 0 & I_{XX} & 0 & 0 \\ 0 & 0 & 0 & 0 & I_{YY} & 0 \\ 0 & 0 & 0 & 0 & 0 & I_{ZZ} \end{bmatrix} \quad [3\text{-}15]$$

where m is the total structural mass including wind turbine and mooring lines and I_{ii} is the mass moments of inertia about the i-axis of the earth-bound global coordinate system.

3.2 Hydromechanical Loads

3.2.1 Selecting the Appropriate Wave Theory

As mentioned in Chapter 2, there are several wave theories for describing the wave kinematics. The regions of applicability for each of these wave theories is depicted in Figure 3-5, depending on the wave height H, water depth h, wave period T and wave length λ. Nonlinearities in waves primarily occur during extreme wave conditions in which the wave steepness becomes increasingly large. Hence, linear wave theory is only accurate for small ratios of wave height to wave length and intermediate or deep-water waves.

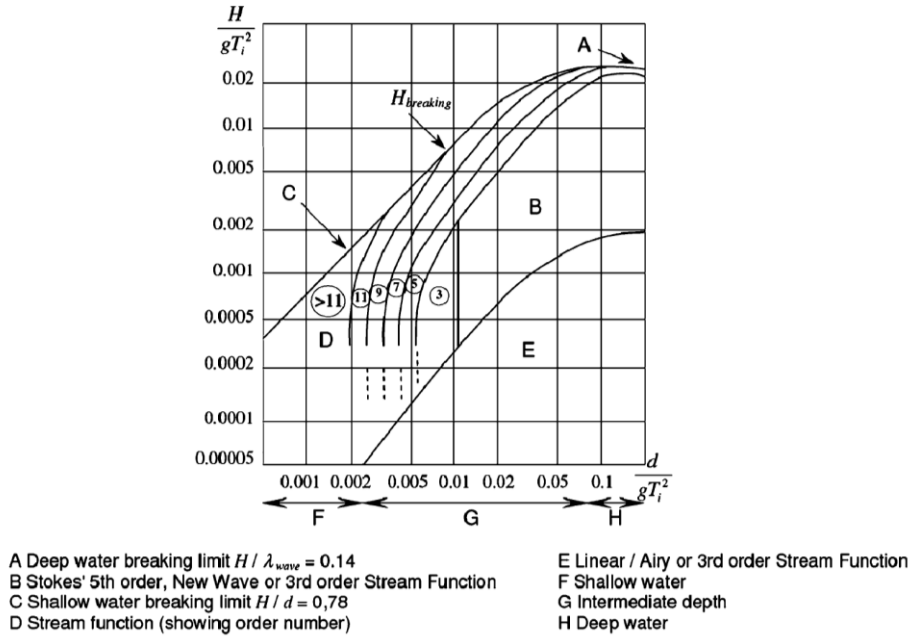

Figure 3-5: Ranges of Applicability of Wave Theories [96]

Using Figure 3-5 and site specific met-ocean data [3], it can be reasoned whether nonlinear wave theories are important. Based on long term and short-term wave data, consisting of wave heights and wave periods, it is determined in what region of the graph in Figure 3-5 each data point is located (see Appendix E). From these analyses, the following conclusions were drawn:

1. The water depth to wave length ratio is always large enough ($d/\lambda > 1/20$) so that the water depth is classified as either "deep" or "intermediate";
2. Based on significant wave heights and wave periods, approximately 66% of all sea states lie within the region of applicability for linear wave theory.

Although these conclusions seem to suggest that application of higher order Stokes waves are more appropriate, based on the TLP geometry and loading conditions considered in this thesis, it is nevertheless deemed acceptable to approximate the wave kinematics using linear wave theory. The reasoning is as follows.

The precise wave form and orbital motions, as described by higher order wave theories, are mostly important for predicting extreme events such as green water effects and wave impact loads on large surfaces [73]. Green water effects do not apply to the WindFlo TLP and the possibility of wave slamming is considered a design issue and is therefore not treated in this thesis. In addition, the nonlinear description of wave kinematics is most influential where the wave kinematics are at maximum, namely around the mean sea level (MSL). However, the structural area that is exposed to surface waves is relatively small (only the central column). On the other hand, the draft is designed such, that platform elements with significant dimensions (the pontoons) are located at a water depth where differences between linear and nonlinear wave kinematics are, due to its exponential decrease with water depth, likely to be minimal.

Finally, it should be borne in mind that, in this section, the applicability of linear wave theory was based on the significant wave height of each sea state. This parameter is defined as the average wave height corresponding to the highest $^1/_3$ of the waves, which means that within sea states marked as "not applicable", still $^2/_3$ of the waves could be accurately described with linear wave theory. From a fatigue damage point of view, mainly the moderate wave conditions are important, in which (significant) wave heights are relatively small. In that regard, the 66% applicability of linear wave theory can be considered as a relatively conservative estimate.

3.2.2 Wave Kinematics

Based on linear wave theory, the irregular wave field, generated by winds blowing over the (fully developed) sea surface, is approximated as a linear summation of an infinite number of harmonic wave components, each with a random wave height, wave period and phase. Under the assumption that the flow is two-dimensional and wave and current directions are constant in time, the surface elevation can be described as in Equation [3-16].

See Figure 3-6 for an illustration of the terms. The horizontal and vertical water particle *velocities* are described in Equation [3-17] and [3-18], respectively. The horizontal and vertical water particle *accelerations* are shown in Equation [3-19] and [3-20], respectively.

$$\xi(X,Y,t) = \sum_{i=1}^{N_{wave}} a_i \cdot c_i(X,Y,t) \quad [3\text{-}16]$$

$$\dot{\xi}_h(X,Y,Z,t) = \sum_{i=1}^{N_{wave}} \omega_i a_i \cdot \frac{\cosh\left(k_i \cdot \left(d + z_{hyd}\right)\right)}{\sinh(k_i d)} \cdot c_i(X,Y,t) \quad [3\text{-}17]$$

$$\dot{\xi}_v(X,Y,Z,t) = \sum_{i=1}^{N_{wave}} \omega_i a_i \cdot \frac{\sinh\left(k_i \cdot \left(d + z_{hyd}\right)\right)}{\sinh(k_i d)} \cdot s_i(X,Y,t) \quad [3\text{-}18]$$

$$\ddot{\xi}_h(X,Y,Z,t) = \sum_{i=1}^{N_{wave}} \omega_i^2 a_i \cdot \frac{\cosh\left(k_i \cdot \left(d + z_{hyd}\right)\right)}{\sinh(k_i d)} \cdot s_i(X,Y,t) \quad [3\text{-}19]$$

$$\ddot{\xi}_v(X,Y,Z,t) = \sum_{i=1}^{N_{wave}} -\omega_i^2 a_i \cdot \frac{\sinh\left(k_i \cdot \left(d + z_{hyd}\right)\right)}{\sinh(k_i d)} \cdot c_i(X,Y,t) \quad [3\text{-}20]$$

where:

- $c_i(X,Y,t) = \cos(k_i \cdot (cos(\mu_{wave}) \cdot X + sin(\mu_{wave}) \cdot Y) - \omega_i t + \varepsilon_i)$;
- $s_i(X,Y,t) = \sin(k_i \cdot (cos(\mu_{wave}) \cdot X + sin(\mu_{wave}) \cdot Y) - \omega_i t + \varepsilon_i)$;
- a_i is the wave amplitude of wave component i [m];
- $\omega_i = 2\pi/T$ is the wave frequency of wave component i [rads^{-1}];
- $k_i = 2\pi/\lambda$ is the wave number of wave component i [m];
- ε_i is the random phase of wave component i, uniformly distributed within $[-\pi, \pi]$;
- μ_{wave} is the wave direction w.r.t. the X-axis [rad];
- d is the water depth [m];
- N_{wave} is the total number of wave components [-];

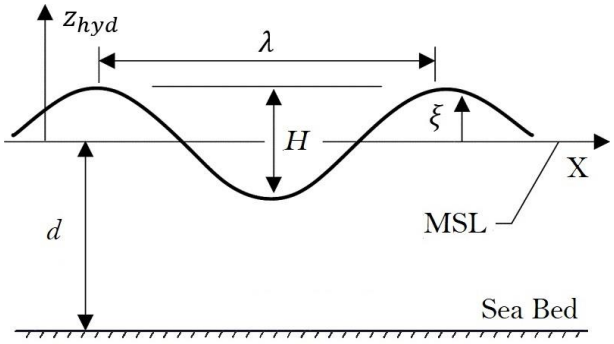

Figure 3-6: Definitions of Wave Characteristics

It is worth mentioning that the wave kinematic formulations require a fixed coordinate frame with an origin at MSL, which is not the case since the fixed global coordinate system has its origin at the CoG. Therefore, the input z-coordinate is adjusted to mimic an origin at MSL, as shown in Equation [3-21].

$$z_{hyd} = Z - T_{mean} - \xi(X,Y,t) + KG \qquad [3\text{-}21]$$

where T_{mean} is the average draft and KG is the distance from keel to CoG.

For description of the site-specific wave spectrum $S(\omega)$, including calculations of wave component frequencies ω_i, amplitudes a_i and random phases ε_i, it is referred to Appendix .

3.2.3 Wave Surface Extrapolation

An important drawback of the linear wave theory is its limitation to predict water particle kinematics at the instantaneous water level (above the MSL). This is a direct consequence of the hyperbolic tangents in the definitions of the wave kinematics, leading to unrealistically large values when the vertical coordinate z_{hyd} becomes positive. A technique that is often applied to overcome this limitation is the Wheeler stretching method, which is essentially a linear shift of z_{hyd} such that its range is from $-d$ to 0. To apply this method, the variable z_{hyd} in Equations [3-17] to [3-20] must be replaced by the expression in Equation [3-22].

$$z_{hyd}^{w} = d \cdot \frac{d + z_{hyd}}{d + \xi(X,Y,t)} - d \qquad [3\text{-}22]$$

3.2.4 Hydrodynamic Loads

As mentioned before, the hydrodynamic forces consist of incident wave forces, diffraction and radiation forces. As a rule, diffraction and radiation forces are disregarded if the characteristic length scale D of the structural is smaller than $^1/_6$ of the shortest wavelength. By taking the diameter of the centre column D_{mid} as the characteristic length scale (characteristic length scale of the pontoons is smaller) and considering the shortest individual waves ($H = 0.25$m and $T =$1.5s, see Appendix D.2), it has been found that diffraction forces are negligible ($\pi D/\lambda \leq 0.136$). The complete region of expected wave force types is depicted in Figure 3-7.

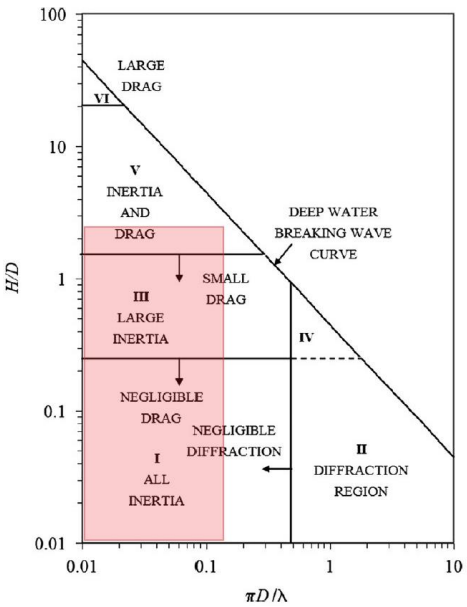

Figure 3-7: Regions of Wave Forces (Red Area is Applicable to the WindFlo TLP)

Incident wave forces are a result of dynamic pressure variation between both ends of the structure, which is directly derived from water particle kinematics and do not require the velocity potential. In two-dimensional flows, the net hydrodynamic pressure can be represented by a force per unit length dF_{hyd} (Figure 3-8). According to Morison's equation, the total hydrodynamic force vector acting on a cylinder with diameter D can be calculated by integrating dF_{hyd} over a length unit s representing its submerged portion.

Since the dimensions of the structure are small compared to the wave length and water depth, the integration can be approximated by an average hydrodynamic pressure across the body surface. The resulting hydrodynamic forces in the direction of the global axes are then calculated using Equation [3-23]. An illustration for this two-dimensional case is shown in Figure 3-9.

$$\underline{F}_{hyd} = \rho_w \cdot V \cdot \left(\dot{\underline{U}} + \underline{C}_a \circ \left(\dot{\underline{U}} - \ddot{\underline{P}}\right)\right) + \frac{\rho_w}{2} \cdot \underline{C}_D \circ \underline{A}_D \circ \left(\underline{U} - \dot{\underline{P}}\right) \circ \left|\underline{U} - \dot{\underline{P}}\right| \qquad [3\text{-}23]$$

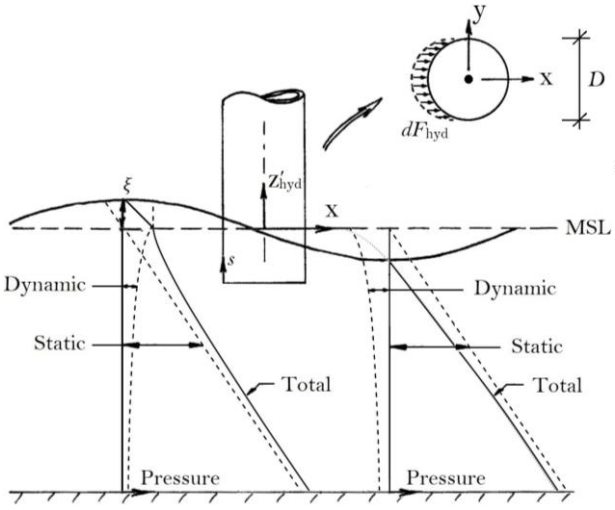

Figure 3-8: Wave Forces in 2D Flow

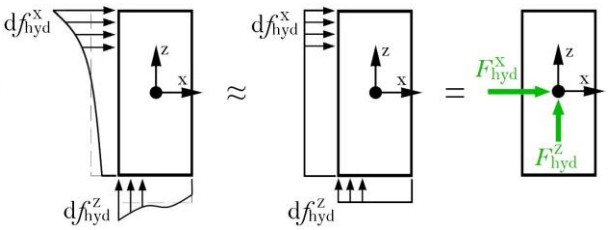

Figure 3-9: Hydrodynamic Loads Approximation

where

- $\rho_w = 1025\text{kgm}^{-1}$ is the water density;
- V is the instantaneous submerged volume;
- $\underline{P}$, $\dot{\underline{P}}$ and $\ddot{\underline{P}}$ are the structure's coordinates, velocities and accelerations in the global axis frame, respectively;
- $\underline{C}_D$ and $\underline{C}_a$ are resp. the hydrodynamic drag and added mass coefficients for motions in the direction of the global axes. Their values are assumed equal for horizontal motions (along X and Y axes) and independent of wave frequencies and water depth;
- $\underline{A}_D$ are the body surface areas in the planes perpendicular to the global axes;
- $\underline{U}$ are the water particle velocities, defined as the summation of the power law-based current velocity [74] and wave particle velocities, as shown in Equations [3-24];
- $\dot{\underline{U}}$ are the water particle accelerations, obtained using [3-25];
- The symbol $\circ$ stands for element-wise multiplication.

$$\underline{U} = \begin{bmatrix}\cos(\mu_{cur})\\ \sin(\mu_{cur})\\ 0\end{bmatrix} \cdot \left(U_{cur,sb} + \left(U_{cur,MSL} - U_{cur,sb}\right) \cdot \left(\frac{z_{hyd}}{d} + 1\right)^{\alpha}\right) + \begin{bmatrix}\dot{\xi}_h(\underline{P},t) \cdot \cos(\mu_{wave})\\ \dot{\xi}_h(\underline{P},t) \cdot \sin(\mu_{wave})\\ \dot{\xi}_v(\underline{P},t)\end{bmatrix} \quad [3\text{-}24]$$

$$\dot{\underline{U}} = \begin{bmatrix}\ddot{\xi}_h(\underline{P},t) \cdot \cos(\mu_{wave})\\ \ddot{\xi}_h(\underline{P},t) \cdot \sin(\mu_{wave})\\ \ddot{\xi}_v(\underline{P},t)\end{bmatrix} \quad [3\text{-}25]$$

where $U_{cur,sb}$ and $U_{cur,MSL}$ are the current velocities at resp. seabed and water plane, μ_{cur} and μ_{wave} are resp. the current and wave flow angle w.r.t. the X-axis and $\alpha = \frac{1}{9}$ is the power exponent.

3.2.5 Hydrostatic Loads

At non-zero roll and pitch angles, freely floating structures experience static restoring moments due to unbalanced hydrostatic buoyancy forces. According to the Scribanti formula [10], for roll and pitch angles up to $15°$, the hydrostatic roll and pitch restoring moments can be calculated using Equations [3-26] and [3-27], respectively. Vertical buoyancy forces F_B are calculated using Equation [3-28]. Figure 3-10 illustrates the variables for pitch restoring moments. The same mechanics are applicable to hydrostatic roll restoring moments.

$$M_B^x = -\rho_w g(V_0 + \Delta V) \cdot \left(KB_{var} + \frac{I_t}{V_0 + \Delta V}\left(1 + \frac{1}{2}\tan(\eta_4)^2\right) - KG\right) \cdot \sin(\eta_4) \quad [3\text{-}26]$$

$$M_B^y = -\rho_w g(V_0 + \Delta V) \cdot \left(KB_{var} + \frac{I_t}{V_0 + \Delta V}\left(1 + \frac{1}{2}\tan(\eta_5)^2\right) - KG\right) \cdot \sin(\eta_5) \quad [3\text{-}27]$$

$$F_B = \rho_w g(V_0 + \Delta V) \quad [3\text{-}28]$$

where

- g is the gravitational acceleration (9.81ms^{-2});
- V_0 is the submerged volume at equilibrium state and;
- $I_t = \frac{\pi}{64} D_{mid,wp}^4$ is the second moment of area at water plane, as a function of the centre column diameter at water plane $D_{mid,wp}$.

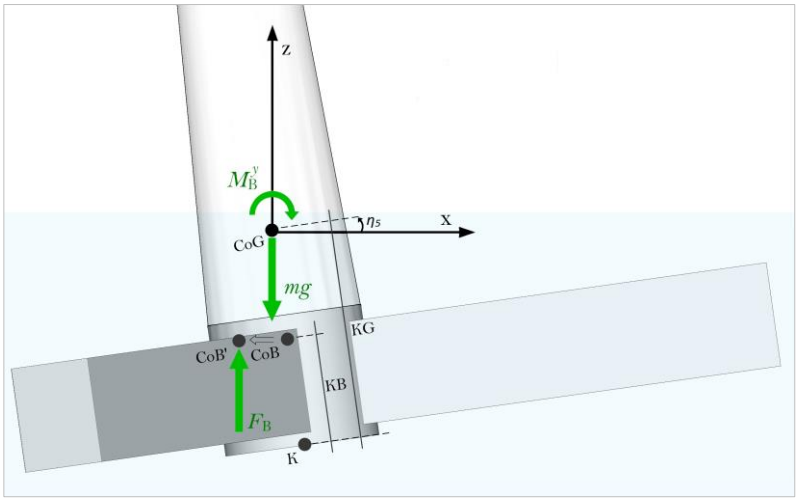

Figure 3-10: Definition of Hydrostatic Loads

The time-varying submerged volume ΔV and the instantaneous distance from keel level K to the CoB of the structure KB_{var} are determined using the expressions in Equation [3-29] and [3-30], respectively.

$$\Delta V = A_{wp} \cdot (\xi(\eta_1, \eta_2, t) - \eta_3) \quad [3\text{-}29]$$

$$KB_{var} = \left(V_0 \cdot KB_0 + \frac{\Delta V^2}{2A_{wp}} \right) \cdot (V_0 + \Delta V)^{-1} \quad [3\text{-}30]$$

where KB_0 is distance from keel level K to the CoB of the structure at equilibrium.

3.3 Mooring Loads

3.3.1 Quasi-static Displacements

Mooring loads are essentially axial stresses caused by elongation of the mooring lines as a result of the platform's motions. As shown in Figure 3-11, the elongation of a mooring line (denoted with subscript i) is based on the earth-bound coordinates of:

- The static position of its anchor point at seabed $\underline{SB}_i = [X_{SB,i} \quad Y_{SB,i} \quad Z_{SB,i}]^T$;
- The static position of the line connector[2] $\underline{P}_{0,i} = [X_{0,i} \quad Y_{0,i} \quad Z_{0.i}]^T$;
- The instantaneous position of the line connector $\underline{P}_{new,i} = [X_{new,i} \quad Y_{new,i} \quad Z_{new,i}]^T$.

The latter vector is the summation of the translational motions $\underline{s}$ and the rotation-induced displacements $\underline{p}_{new,i}$, as shown in Equation [3-31].

$$\underline{P}_{new,i} = \underline{s} + \underline{p}_{new,i} \quad [3\text{-}31]$$

where $\underline{p}_{new,i}$ is determined according to Equation [3-32].

[2] Connections between the mooring lines and platform.

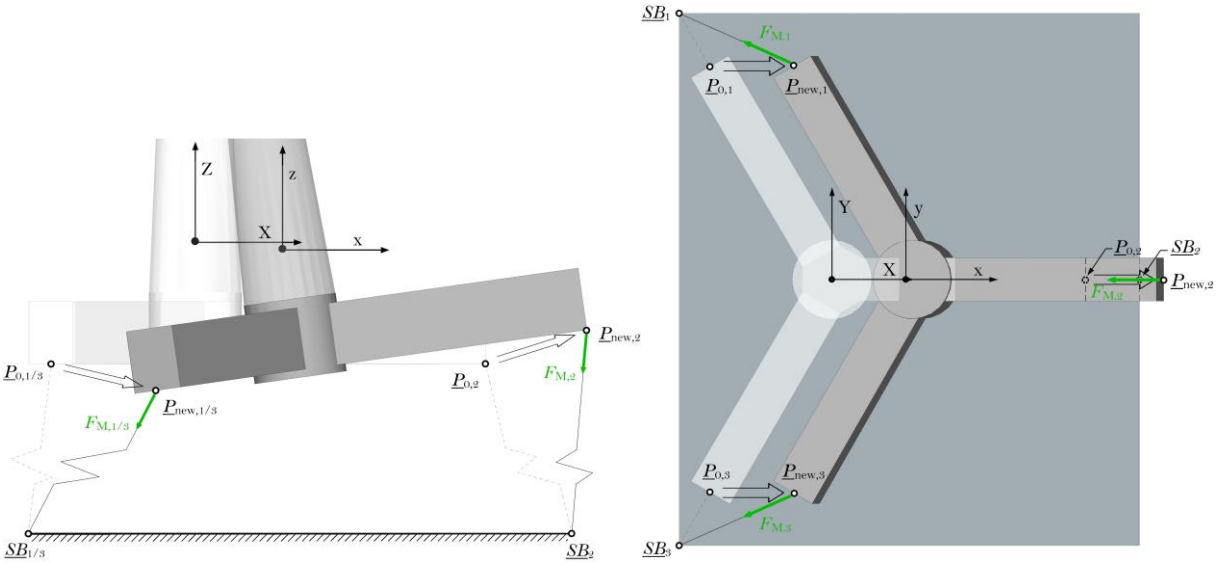

(a) (b)

Figure 3-11: Definition of Coordinate and Displacement Vectors for Calculation of Mooring Loads

$$\underline{p}_{new,i} = [x_{new,i} \quad y_{new,i} \quad z_{new,i}]^T = \boldsymbol{R} \cdot \underline{P}_{0,i} \qquad [3\text{-}32]$$

The mathematical formulations of the static and instantaneous line lengths are derived from the vector lengths spanning from seabed to the static and instantaneous position of the mooring line connector, respectively. The expressions for the static and instantaneous line lengths are shown in Equations [3-33] and [3-34], respectively. See Appendix B for the geometry-dependent description of the static vectors $\underline{SB}_i$ and $\underline{P}_{0,i}$.

$$L_{0,i} = \left|\underline{SB}_i - \underline{P}_{0,i}\right| = \sqrt{\left(X_{SB,i} - X_{0,i}\right)^2 + \left(Y_{SB,i} - Y_{0,i}\right)^2 + \left(Z_{SB,i} - Z_{0.i}\right)^2} \qquad [3\text{-}33]$$

$$L_{new,i} = \left|\underline{SB}_i - \underline{P}_{new,i}\right| = \sqrt{\left(X_{SB,i} - X_{new,i}\right)^2 + \left(Y_{SB,i} - Y_{new,i}\right)^2 + \left(Z_{SB,i} - Z_{new,i}\right)^2} \qquad [3\text{-}34]$$

3.3.2 Formulation of Mooring Forces

Provided that the mooring line elongations remain in the elastic region and the stress-strain relationship is linear in the elastic region, the three-dimensional mooring force vectors can be calculated using Equation [3-35]. Note that this expression is based on the assumption that the initial pretension is equal in all mooring lines and hydrodynamic forces on the lines are negligible.

$$\underline{F}_{M_i} = \left[F_{M_i}^X \quad F_{M_i}^Y \quad F_{M_i}^Z\right]^T = \left(\frac{L_{new,i} - L_{0,i}}{L_{0,i}} \cdot EA_{moor} + \frac{F_B - mg}{3 \cdot \hat{L}_i^Z}\right) \cdot \underline{\hat{L}}_i \qquad [3\text{-}35]$$

in which EA_{moor} is the mooring line axial stiffness and the unit vector $\underline{\hat{L}}_i$ describes the direction of mooring line i in the global axes by normalizing the vector $\underline{P}_{new,i} - \underline{SB}_i$:

$$\underline{\hat{L}}_i = [\hat{L}_i^X \quad \hat{L}_i^Y \quad \hat{L}_i^Z]^T = \frac{\underline{P}_{new,i} - \underline{SB}_i}{L_{new,i}} \qquad [3\text{-}36]$$

3.4 Turbine Loads

3.4.1 Introduction

Turbine loads are subdivided in three categories: aerodynamic friction, thrust forces and gyroscopic moments. In survival conditions, the wind turbine is in non-operating state and therefore wind loads are limited to aerodynamics drag forces. In operational conditions, rotations of the rotors will also induce thrust forces and gyroscopic moments.

The aerodynamic friction and thrust forces are described according to the one-dimensional momentum theory, also known as the actuator disk theory. The idea behind this theory is that the rotor plane can be represented as an infinitely thin disk, subjected to a uniform wind flow. As illustrated in Figure 3-12, the rotors extract energy from the wind flow as the wind stream passes the rotor plane, causing a constant pressure discontinuity across the surface of the disk. This pressure drop is then translated into the thrust force, assuming there is no friction involved along the disk. The assumption of constant pressure across rotor plane is that it cannot capture yaw moments due to misaligned of the wind stream w.r.t the normal axis of the rotor plane, since it requires two-dimensional pressure variation across the disk area. This would also require three-dimensional air flow, which has not been incorporated in the wind speed model.

3.4.2 Wind Regime

The wind speed model that is used to simulate wind disturbances is considered as a superposition of a time-invariant component $u_{w,a}$ and a fluctuating turbulent component $u_{turb}(t)$.

$$u_w(t) = u_{w,a} + u_{turb}(t) \qquad [3\text{-}37]$$

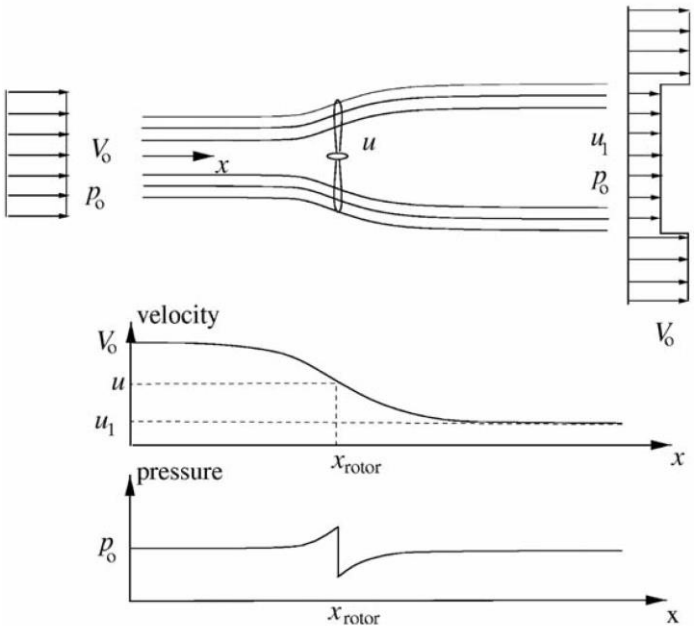

Figure 3-12: Principles of One-Dimensional Momentum Theory [97]

The turbulence model is derived on the basis of the superposition principle, as was introduced in section 3.2.2 for modelling of irregular waves. The time series of the wind turbulence is constructed according to Equation [3-38], in which the frequency dependent amplitudes $u_{turb,j}$ are determined based on site specific power spectral density (PSD) function of the wind velocity $S_{turb}(\omega)$. Met-ocean studies at the Dounreay site [3] show that the Frøya PSD is the most suiting for representation of the local wind conditions. As an example, realization of the wind turbulence for a mean wind speed of 15.5ms^{-1} is plotted in Figure 3-13. Further description of the Frøya spectrum and construction of the wind turbulence time series is presented in Appendix C.

$$u_{turb}(t) = \sum_{j=1}^{N_{turb}} u_{turb,j} \cdot \sin\left(\omega_{turb,j} \cdot t + \varepsilon_{turb}\right) \quad [3\text{-}38]$$

$$u_{turb,j} = \sqrt{2S_{turb}(\omega_j) \cdot \Delta\omega_{turb}} \quad [3\text{-}39]$$

where ε_{turb} is a random phase angle uniformly distributed between $-\pi$ and π and $\Delta\omega_{turb}$ is the frequency resolution.

Since the time series of the wind speed is only a realization at a single point in space, the model must be enhanced to account for the wind speed variability in the vertical axis. This type of spatial distribution of wind is called wind shear and leads to a wind speed pattern similar to Figure 3-14. The mean and fluctuating wind velocities can be vertically extrapolated from a single point using the Frøya wind profile model, a method proposed in the Dounreay met-ocean studies [3] and recommended by DNV [75]. The formula is shown in Equation [3-40]. The vertical coordinate w.r.t. the instantaneous sea level z_w can be expressed in terms of the global Z-axis, as shown in Equation [3-41].

$$\tilde{u}_w(z_w, t) = u_w(t) \cdot \left(1 + 5.73 \cdot 10^{-2} \cdot \sqrt{1 + 0.148 \cdot |u_w(t)|} \cdot \ln\frac{z_w}{H}\right) \quad [3\text{-}40]$$

$$z_w = Z - T_{mean} - \xi(\eta_1, \eta_2, t) + KG \quad [3\text{-}41]$$

where $H = 80$m is the height above MSL at which the mean wind speed $u_{w,a}$ was measured.

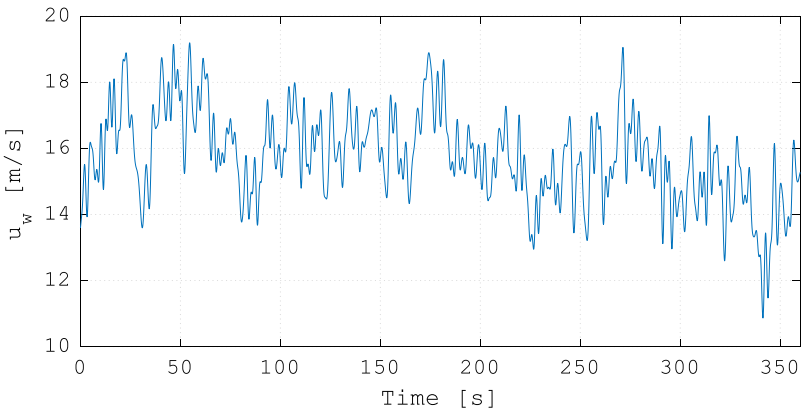

Figure 3-13: Realization of 360s Turbulent Wind Velocity

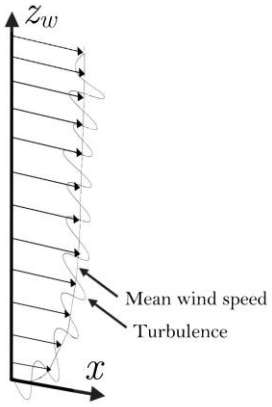

Figure 3-14: Turbulent Wind Shear Model

3.4.3 Tower Friction Forces

The one-dimensional momentum theory treats aerodynamic friction forces in a similar way as in Morison's equation for hydrodynamic drag, as shown in Equation [3-42]. The wind velocity in the direction of the global axes is calculated using Equation [3-43].

$$\underline{F}_{aero} = \frac{1}{2}\rho_a \cdot \underline{C}_{D,t} \circ \underline{A}_t \circ \left(\underline{U}_w - \underline{\dot{P}}\right) \circ \left|\underline{U}_w - \underline{\dot{P}}\right| \quad [3\text{-}42]$$

$$\underline{U}_w = \begin{bmatrix} \cos(\mu_{wind}) \\ \sin(\mu_{wind}) \\ 0 \end{bmatrix} \cdot \tilde{u}_w(z_{w,}, t) \quad [3\text{-}43]$$

where

- $\rho_a = 1.237\text{kgm}^{-3}$ is the average air density at 80m above MSL;
- $\underline{C}_{D,t}$ is the aerodynamic friction coefficient of the tower;
- $\underline{A}_t$ are the incident drag areas of the tower;
- μ_{wind} is the wind angle w.r.t. the global X-axis. Note: the platform's orientation is chosen such, that the positive direction of the global X-axis is equal to the governing wind direction. Therefore, its value is always zero ($\mu_{wind} = 0°$).

3.4.4 Rotor Plane Forces

Depending on the average wind speed at nacelle height, the turbine will generate thrust forces during operational conditions while in parked conditions, rotor plane forces are limited to aerodynamic friction of the rotor blades. Suppose that U_{out} is the wind speed at which the turbine is shut down, then the wind-induced RNA forces can be described as in Equation [3-44]. The cut-out speed is a predetermined turbine specification, which, for this study, is based on the NREL 5MW turbine ($U_{out} = 25\text{ms}^{-1}$).

$$\underline{F}_{RNA} = \begin{cases} \underline{F}_{RNA,ex} & u_{w,a} \geq U_{out} \\ \underline{F}_{RNA,op} & u_{w,a} < U_{out} \end{cases} \quad [3\text{-}44]$$

where $\underline{F}_{RNA,ex}$ and $\underline{F}_{RNA,op}$ are the turbine force vector during extreme and operational conditions, respectively.

Extreme Conditions

Aerodynamic drag forces acting on the RNA can be calculated using the expression in Equation [3-45]. The relative wind velocity at the instantaneous position of the RNA is calculated in the global direction according to Equation [3-46] and aerodynamic properties of the RNA can be found in Table A - 2 in Appendix A.

$$\underline{F}_{RNA,ex} = \frac{1}{2}\rho_a \cdot C_{D,RNA} \circ \underline{A}_{RNA} \circ \left(\underline{U}_{w,RNA} - \underline{\dot{P}}_{RNA}\right) \circ \left|\underline{U}_{w,RNA} - \underline{\dot{P}}_{RNA}\right| \quad [3\text{-}45]$$

$$\underline{U}_{w,RNA} = \begin{bmatrix} \cos(\mu_{wind}) \\ \sin(\mu_{wind}) \\ 0 \end{bmatrix} \cdot \tilde{u}_w(z_{w,RNA}, t) \quad [3\text{-}46]$$

where

- $\underline{A}_{RNA} = \boldsymbol{R} \cdot \begin{bmatrix} A^X_{RNA,ex} & 0 & 0 \end{bmatrix}^T$ are the drag areas in parked conditions, corrected with the rotation matrix to account for platform-wind stream misalignment;
- $C_{D,RNA}$ is the drag constant of the RNA in parked conditions;
- $\underline{\dot{P}}_{RNA}$ is the RNA rigid-body velocity in the global axis frame.

Operational Conditions

During operational conditions, thrust forces are generated by wind-induced pressures on the rotor plane. As a result, its orientation is always perpendicular to the rotor plane, which means that the direction of the thrust force depends on the motions of the TLP. This is visualized in Figure 3-15. Since the EoMs are formulated in the global coordinate frame, the RNA forces are calculated as the components of the thrust force in the global coordinate system. The conversion of local thrust force to global RNA forces is performed using Equation [3-47] and the thrust force F_T is determined according to Equation [3-48].

$$\underline{F}_{RNA,op} = \boldsymbol{R} \cdot [F_T \quad 0 \quad 0]^T \tag{3-47}$$

$$F_T = \frac{1}{2}\rho_a \cdot C_T \cdot A^X_{RNA,op} \cdot u^{x'}_{RNA} \cdot |u^{x'}_{RNA}| \tag{3-48}$$

where $A^X_{RNA,op} = \frac{\pi}{4} D^2_{RNA}$ is the swept area of the RNA during operational condition and C_T is the thrust coefficient, which can be found in Table A - 4.

The thrust force depends on the velocity term $u^{x'}_{RNA}$, which represents the component normal to the rotor plane. Since the motions of the TLP can cause instantaneous misalignments with the wind stream (Figure 3-15), the wind direction must be transformed from the global axis frame to components in the body axes of the rotor plane. This conversion is performed using the inverse of the rotation matrix, as shown in Equation [3-49].

$$\underline{u}'_{RNA} = \begin{bmatrix} u^{x'}_{RNA} & u^{y'}_{RNA} & u^{z'}_{RNA} \end{bmatrix}^T = \boldsymbol{R}^{-1} \cdot \left(\underline{U}_{w,RNA} - \underline{\dot{P}}_{RNA}\right) \tag{3-49}$$

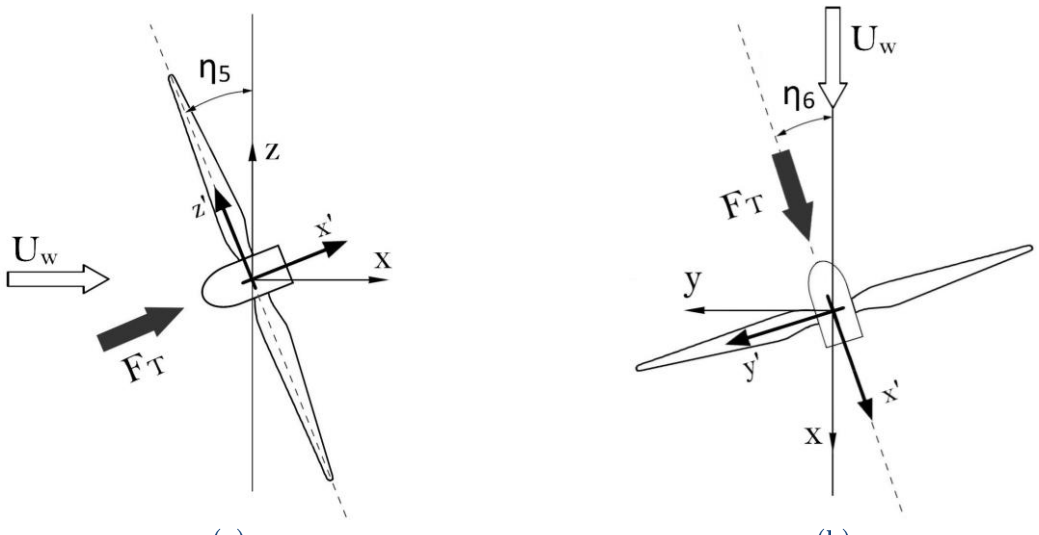

(a) (b)

Figure 3-15: RNA-Wind Stream Misalignments due to Pitch (a) and Yaw (b) Motions

3.4.5 Gyroscopic Moments

When a body that is spinning around an axis is rotated about another axis, due to the principle of conservation of angular momentum, a secondary rotational motion arises around the third axis. This so-called gyroscopic effect introduces moments around the axes perpendicular to the spinning axis when the turbine is in operation and the rotor plane experiences rotational motions around its yaw or pitch (tilt) angle. This is visualized in Figure 3-16.

Assuming the turbine operates with a constant rotational speed Ω and the rotor plane has a polar moment of inertia around its spinning axis of I_{disk}, the gyroscopic moment around its local tilt (y') and yaw (z') axis can be described using Equation [3-50].

Analogous to thrust forces, gyroscopic moments are a result of forces acting on the rotor plane in its local body-fixed axes. Therefore, yaw and pitch (tilt) motions of the rotor plane, as well as the corresponding gyroscopic moments must be described in the local body-fixed axis of the rotor plane. The local angular velocities that introduce gyroscopic moments depend on the global rotational velocities through the matrix operation that is shown in Equation [3-51]. It is referred to Appendix for the calculation of the rotor plane polar moment of inertia.

$$\underline{M'}_{gyro} = I_{disk} \cdot \Omega \cdot \begin{bmatrix} 0 \\ \omega^{z'} \\ -\omega^{y'} \end{bmatrix} \quad [3\text{-}50]$$

$$\underline{\omega} = [\omega^{x'} \quad \omega^{y'} \quad \omega^{z'}]^{\mathrm{T}} = \boldsymbol{R}^{-1} \cdot [\dot{\eta}_4 \quad \dot{\eta}_5 \quad \dot{\eta}_6] \quad [3\text{-}51]$$

Again, similar to thrust forces, the gyroscopic moments about the local body-fixed axes are transformed into moments about the translational axes. This is done using Equation [3-52].

$$\underline{M}_{gyro} = \boldsymbol{R} \cdot \underline{M'}_{gyro} \quad [3\text{-}52]$$

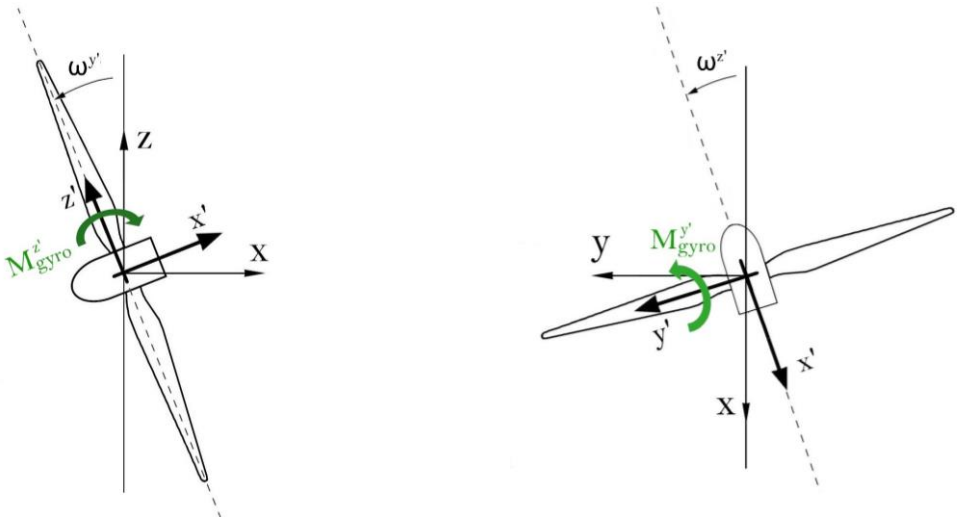

(a) (b)

Figure 3-16: Gyroscopic Moments During to Tilt (a) and Yaw (b) Motions of the RNA

3.5 Numerical Implementation

3.5.1 Introduction

In previous sections, the general form of the EoMs and the corresponding force terms were formulated. The current section deals with the numerical implementation of the EoMs in Matlab and the associated solution and postprocessing methodologies. A schematic representation of the composition of numerical functions and scripts for solving the system's motions and sectional stresses is presented in Figure 3-17, with brief explanations on each component given below.

Main Script

- "*P*" and "ICs" are structure arrays, containing resp. input properties and the initial conditions stored within the fields of the array.
- "Wave Generator" and "Wind Generator" are algorithms that generate the irregular wave and stochastic wind velocity distribution, as introduced in resp. Sections 3.2 and 3.4.
- "Geometry Discretization" is an algorithm that discretises the geometry, which is explained in Section 3.5.2.
- "ODE Solver" is a discrete, numerical time integration scheme that solves the complete set of EoMs, including all time- and motion dependent parameters, using a built-in Matlab solver. The numerical implementation of the force vectors is explained in Section 3.5.3 and properties of the solver are discussed in Section 3.6.
- "Numerical Differentiator" calculates the accelerations from the velocities by means of numerical differentiation, as shown in Equation [3-53]. This is necessary because the solver only generates the system variables and their first time derivatives as output.

$$\underline{\ddot{\eta}}(t = t_i) = \frac{\underline{\dot{\eta}}(t = t_{i+1}) - \underline{\dot{\eta}}(t = t_i)}{t_{i+1} - t_i} \qquad [3\text{-}53]$$

where i is the time step.

Postprocessor

- "EoMs" the numerical descriptions of the EoMs, directly duplicated from the formulations in "ODE Solver".
- "Motions to Forces" uses the structure's potions and kinematics in time to reproduce all force terms that constitute the EoMs. These force terms are used to calculate the sectional forces at a number of structural details.
- "Stress Calculator" uses the sectional forces and hydrostatic pressures to determine the sectional stresses. Based on the sectional stresses, the principal stresses and corresponding principal stress directions are calculated.
- "Damage Calculator" uses a stress counting algorithm to determine the stress range distribution of the governing principal stress and corresponding fatigue damage. The complete postprocessing approach is explained in section 3.7.

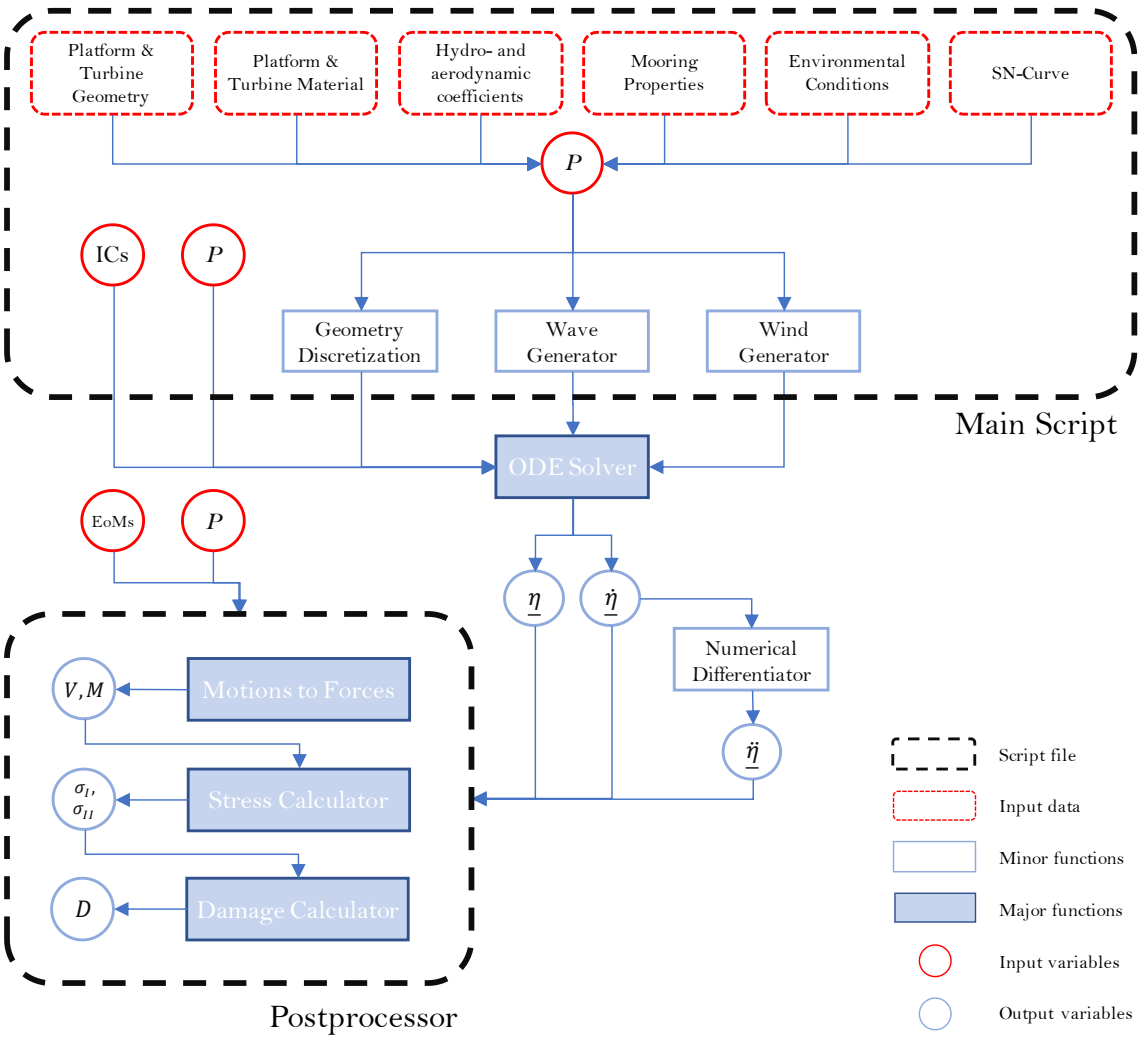

Figure 3-17: Arrangement of Matlab Scripts and Functions

3.5.2 Discretization of Geometry

Application of numerical methods for solving dynamic systems is often limited to discrete time-integration of the system variables as well as spatial integration of pressures. Although the Morison equation already takes into account the spatial estimation of hydrodynamic pressures by assuming a two-dimensional flow, this approximation is only valid for a structure with negligible dimensions. Since the TLP dimensions are not necessarily small w.r.t. the waves and water depth, the kinematics of the structure and water particles can show large variations at different locations of the structure. Therefore, to obtain accurate results, the forces must be calculated at discretized segments of the geometry.

Discretization of the geometry is performed parametrically by dividing each pontoon into N_{box} segments and the tower in N_{tower} segments. Each of these segments are represented as concentrated masses, located in the CoG of the respective body. Similarly, the submerged volumes of all pontoon segments are represented as point volumes, concentrated in the CoB of the respective body. The submerged portion of the central column is divided into three parts and

the RNA is presented as a single concentrated mass. The resulting geometry consists of $3{\cdot}N_{box}{+}N_{tower}{+}4$ bodies, each experiencing concentrated forces in the global axis directions.

This procedure has been demonstrated in Figure 3-18a, where the CoB/CoG positions of the pontoon segments are denoted with blue dots, tower segment CoGs are denoted with red dots and the RNA CoG is shown as a green dot. For clarity, the number of pontoon and tower segments, N_{box} and N_{tower}, are taken as 6 and 4, respectively.

The parts in the vicinity of the water surface are exposed to water level fluctuations and therefore have time-varying submerged volume, vertical positioning of CoB and hydro- and aerodynamic drag area. This is included by setting the upper boundary of the topmost submerged segment of the central column equal to the instantaneous water level. The lower boundary is fixed and chosen in such a way that the body always remains submerged, with the aim of avoiding numerical contact problems and conditional statements. It should be noted that the (wind) drag area of the tower segment just above the water surface is also affected by water level fluctuations.

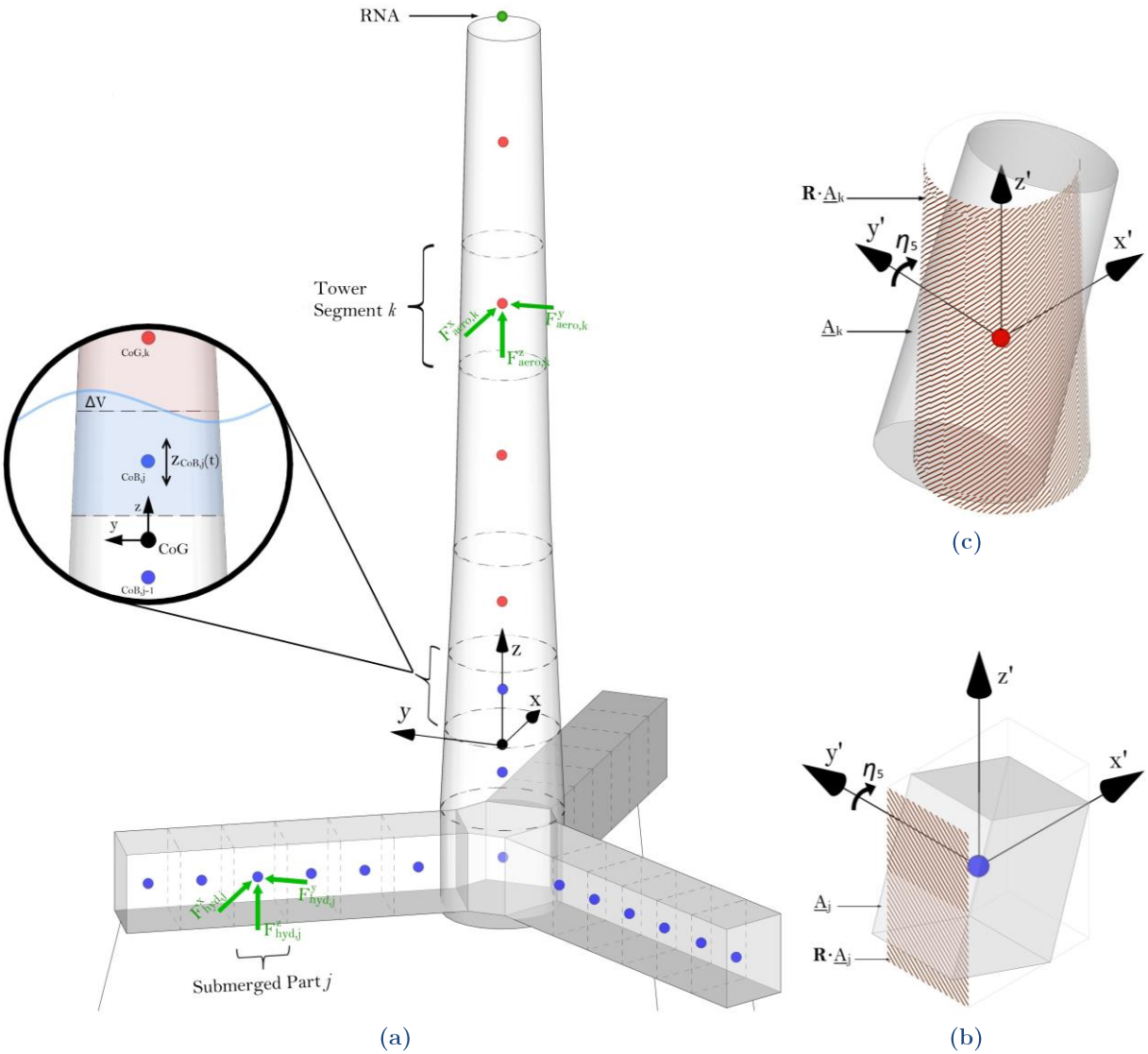

Figure 3-18: Discretization of the TLP Geometry

Table 3-1: Discretized Properties of Sub-Bodies

Part	Parameter	Symbol	Range
Submerged Segments	Displaced Volumes	V_j	$j = 1 \dots 3N_{box} + 3$
	Static Drag Areas	$\underline{A}_j$	
	Instantaneous Drag Areas	$\boldsymbol{R} \cdot \underline{A}_j$	
	Hydrodynamic Drag and Added Mass Coefficients	$\{\underline{C}_{D,j}, \underline{C}_{a,j}\}$	
	Coordinates of CoBs/CoGs in the Translational Coordinate Frame	$\underline{p}_j$	
	Coordinates, Velocities and Accelerations of CoBs/CoGs in the Global Coordinate Frame	$\{\underline{P}_j, \dot{\underline{P}}_j, \ddot{\underline{P}}_j\}$	
Tower Segments	Static Drag Areas	$\underline{A}_k$	$k = 1 \dots N_{tower}$
	Instantaneous Drag Areas	$\boldsymbol{R} \cdot \underline{A}_k$	
	Aerodynamic Drag Coefficients	$\underline{C}_{D,k}$	
	Coordinates of CoGs in the Translational Coordinate Frame	$\underline{p}_k$	
	Coordinates, Velocities and Accelerations of CoGs w.r.t. the Global Coordinate Frame	$\{\underline{P}_k, \dot{\underline{P}}_k, \ddot{\underline{P}}_k\}$	

Table 3-1 presents the system of symbols that have been devised to assign the discretized properties of the subparts. The instantaneous drag areas are defined as the drag area in the static state, corrected with $\boldsymbol{R}$ to incorporate the orientation of the body with respect to the hydro and aerodynamic flow direction. See Figure 3-18b and Figure 3-18c for an illustration of the instantaneous orientation of the pontoon and tower segment, respectively. For the complete mathematical description of the discretization algorithm, it is referred to Appendix C.

3.5.3 Numerical Implementation of Force Vectors

Discretizing the geometry in smaller segments results in the hydro- and aerodynamic forces having to be calculated in each of the sub-bodies. This was done by determining the required hydro- and aerodynamic properties of each body. In this section, the mathematical formulae, as were introduced in Sections 3.2, 3.3 and 3.4, will be applied to determine the forces acting on each separate body. The following sub-sections will deal with each loading type separately.

Hydrodynamic Loads

Hydrodynamic forces acting on a submerged segment are calculated at the instantaneous position of the CoB/CoG by substituting the segment-specific properties into the Morison equation (Equation [3-23]). The resulting expression is shown in Equation [3-54].

$$\underline{F}_{hyd,j} = \rho_w \cdot V_j \cdot \left(\dot{\underline{U}}_j + \underline{C}_{a,j} \circ \left(\dot{\underline{U}}_j - \ddot{\underline{P}}_j\right)\right) + \frac{\rho_w}{2} \cdot \underline{C}_{D,j} \circ \left[\boldsymbol{R} \cdot \underline{A}_j\right] \circ \left(\underline{U}_j - \dot{\underline{P}}_j\right) \circ \left|\underline{U}_j - \dot{\underline{P}}_j\right| \quad [3\text{-}54]$$

where $\underline{U}_j = \underline{U}\big|_{\underline{P} = \underline{P}_j}$ and $\dot{\underline{U}}_j = \dot{\underline{U}}\big|_{\underline{P} = \underline{P}_j}$.

The total hydrodynamic force and moment vector $\underline{f}_{hyd}$ acting on the complete structure is calculated by superposing the contribution of all submerged bodies, according to Equation [3-55].

$$\underline{f}_{hyd} = \sum_{j=1}^{3N_{box}+3} \begin{bmatrix} \underline{F}_{hyd,j} \\ \underline{p}_j \times \underline{F}_{hyd,j} \end{bmatrix} \quad [3\text{-}55]$$

where the symbol × denotes the cross product.

Hydrostatic Loads

The hydrostatic loads, as derived in section 3.2.5, do not require any spatial integration and can therefore be implemented numerically without discretization. The total hydrostatic load vector $\underline{f}_{stat}$ can be determined according to Equation [3-56].

$$\underline{f}_{stat} = \begin{bmatrix} 0 & 0 & F_B - mg & M_B^x & M_B^y & 0 \end{bmatrix}^T \quad [3\text{-}56]$$

Mooring Loads

The mooring loads, as derived in section 3.3, do not require any spatial integration and can therefore be implemented numerically without discretization. The mooring force vector $\underline{f}_{moor}$ is, as shown in Equation [3-57], the summation of the mooring forces of each line and their moments about the translational coordinate frame.

$$\underline{f}_{moor} = -\sum_{i=1}^{N_M} \begin{bmatrix} \underline{F}_{M_i} \\ \underline{p}_{new,i} \times \underline{F}_{M_i} \end{bmatrix} \quad [3\text{-}57]$$

where $N_M = 3$ is the number of mooring lines.

Tower Friction Forces

Aerodynamic friction forces acting on a dry segment of the tower are calculated at the instantaneous position of the CoG by substituting the segment-specific properties into Equation [3-42]. The resulting expression is shown in Equation [3-58].

$$\underline{F}_{aero,k} = \frac{1}{2}\rho_a \cdot \underline{C}_{D,k} \circ \left[\boldsymbol{R} \cdot \underline{A}_k\right] \circ \left(\underline{U}_{w,k} - \dot{\underline{P}}_k\right) \circ \left|\underline{U}_{w,k} - \dot{\underline{P}}_k\right| \quad [3\text{-}58]$$

where $\underline{U}_{w,k} = \underline{U}_w\big|_{\underline{P} = \underline{P}_k}$.

Total Turbine Load Vector

Thrust and aerodynamic friction forces acting on the RNA as well as gyroscopic moments, as derived in resp. sections 3.4.4 and 3.4.5, do not require any spatial integration and can therefore be implemented numerically without discretization. The total turbine load vector, consisting of all forces and moments acting on the complete turbine, is established by superposing the forces and moments on each turbine segment plus the contribution from the RNA. The resulting expression is shown in Equation [3-59].

$$\underline{f}_{turb} = \begin{bmatrix} zeros(3,1) \\ \underline{M}_{gyro} \end{bmatrix} + \begin{bmatrix} \underline{F}_{RNA} \\ \underline{p}_{RNA} \times \underline{F}_{RNA} \end{bmatrix} + \sum_{k=1}^{N_{tower}} \begin{bmatrix} \underline{F}_{aero,k} \\ \underline{p}_k \times \underline{F}_{aero,k} \end{bmatrix} \quad [3\text{-}59]$$

where $\underline{p}_{RNA} = [x_{RNA} \quad y_{RNA} \quad z_{RNA}]^T$ are the CoG coordinates of the RNA in the translational coordinate frame.

3.6 Matlab ODE Solver

3.6.1 Implementation

Numerical ordinary differential equation (ODE) solvers consist of an algorithm that iteratively searches for solution estimates at discrete time steps using a certain numerical scheme. The error w.r.t. the exact solution depends on the mathematical properties of the numerical method and the computational suitability of the solver with regards to the EoMs. he EoMs considered in this problem are characterized as second order ODEs with certain initial conditions, i.e. an initial value problem with multiple dependent variables and their first and second derivatives with respect to time. Matlab built-in ODE solvers are only capable of solving first order ODEs, which have the form as shown in Equation [3-60].

$$\frac{\partial y}{\partial t} = f(t, y) \quad [3\text{-}60]$$

Higher order ODEs must therefore be rewritten to obtain an equivalent system of first order ODEs. The method of rewriting higher order ODEs to a first order equivalent system is done using generic substitutions. As an example, consider the following generic problem of a second order ODE with dependent variable vector $\underline{x}$, as shown in Equation [3-61].

$$\boldsymbol{M}\underline{\ddot{x}} + \boldsymbol{C}\underline{\dot{x}} + \boldsymbol{K}\underline{x} = \underline{F}(t) \quad [3\text{-}61]$$

where $\boldsymbol{M}$, $\boldsymbol{C}$ and $\boldsymbol{K}$ are the system's mass, damping and stiffness matrix, respectively. Vector $\underline{F}(t)$ consists of all remaining terms that do not contain any of the dependent variables.

To be able to solve this (or any) ODE numerically, one must subdivide the simulation time t_{end} in N time steps with each a duration of Δt. The vector $\underline{x}$ and its time derivatives must be rewritten as new sets of vectors with a maximum order time derivative of 1, in order to transform the system into a 1st order ODE. The following convention is used to perform this procedure.

$$\underline{q}_i = \begin{bmatrix} \underline{x}_i \\ \underline{\dot{x}}_i \end{bmatrix} \quad [3\text{-}62]$$

$$\underline{\dot{q}}_i = \begin{bmatrix} \underline{\dot{x}}_i \\ \underline{\ddot{x}}_i \end{bmatrix} = \begin{bmatrix} \underline{\dot{x}}_i \\ \boldsymbol{M^{-1}} * \left(-\boldsymbol{C}\underline{\dot{x}}_i - \boldsymbol{K}\underline{x}_i + \underline{F}(t) \right) \end{bmatrix} = \begin{bmatrix} \underline{\dot{x}}_i \\ \boldsymbol{M^{-1}} * \underline{F}_{rhs}(t, \underline{x}_i, \underline{\dot{x}}_i) \end{bmatrix} \quad [3\text{-}63]$$

where $\underline{x}_i$ is the solution during the i^{th} time step and $\underline{\dot{x}}_i$ is the time derivative during that time step. Note that the vector $\underline{\ddot{x}}_i$ can be rewritten using the EoMs.

Using this convention, the EoMs can be written as a function of $\underline{q_i}$ and $\underline{\dot{q}_i}$ instead of $\underline{x_i}$, $\underline{\dot{x}_i}$ and $\underline{\ddot{x}_i}$. The problem becomes a 1st order ODE with initial conditions $\underline{q_0}$, which can be solved using one of the ODE solvers. The conditions at each consecutive time step are approximated based on the conditions at a number of previous time steps, possibly including the current time step. The end result is the vector $\underline{q_i}$, containing the solutions for the variables and their first time derivative during each time step. The accelerations can be calculated after the simulation is completed, using $\underline{q_i}$ and the EoMs.

3.6.2 Solver Characteristics

There are 8 built-in ODE solvers in Matlab, composed of algorithms that are based on various numerical solution schemes. Depending on the algorithm used in the solver, each solver may have unique characteristics. In this section, the main solver characteristics are described for the solvers that are considered in this report, being the ODE45, ODE113, ODE23t and ODE15s.

A list of the solvers, underlying numerical methods and their order of local truncation error is depicted in Table 3-2. For a more extensive elaboration on solver properties and clarification of the terminology, it is referred to Appendix F.

Table 3-2: Main Properties of Four Matlab ODE Solvers

Solver	Method classification	Method	Problem	ε	Step size
ODE45	Runge-Kutta (RK4)	Dormand-Prince algorithm	Non-stiff	4 - 5	Variable
ODE113	Linear multi-step	Adams–Bashforth–Moulton	Non-stiff	Variable	Variable
ODE23t	Linear multi-step	Trapezoidal rule	Stiff	3	Variable
ODE15s	Linear multi-step	Backward differentiation formulas	Stiff	1 - 5	Variable

The ODE45 solver

This code is based on the Dormand-Prince algorithm, which is a pair of single-step explicit Runge-Kutta methods. The basis for this algorithm is the classical Runga-Kutta method, which is discussed in Appendix E.4. In contrast to the classical Runga-Kutta method, the Dormand-Prince algorithm uses six intermediate evaluations between each adjacent time instants. By doing so, the algorithm calculates both the 4th and 5th order approximations of the solution, after which the difference is calculated. This local error estimation enables an efficient way of varying the time step size per step. The ODE45 is recommended as a first try for solving non-stiff problems.

The ODE113 solver

This solver is based on the Adams-Bashforth-Moulton algorithm, which is a combination of the explicit Adams-Bashforth method and the implicit Adams-Moulton method. As discussed, both methods are classified as linear multi-step methods. In this code, the Predict–Evaluate–Correct–Evaluate (PECE) mode is applied, which is basically a predictor-corrector algorithm with additional steps to refine the accuracy of the estimated curvature. The ODE113 is preferred when solving non-stiff problems and it is often more efficient than ODE45 since it is a variable step and variable order solver.

The ODE23t solver

The ODE23t code is based on the trapezoidal rule with a free interpolant, a second-order implicit linear-multistep method. Implementation of a free interpolant implies that the code produces a continuous curve rather than discrete solutions only on specific points. The solver excludes numerical damping and works relatively efficient in case of stiff problems with lower accuracy requirements.

The ODE15s solver

If the results obtained by ODE45 proofs to be unsatisfactory, it is recommended to try ODE15s. This code is based on the BFDs. This method uses polynomial interpolation, i.e. continuous piece-wise polynomial functions that approximate the solution throughout the complete interval between two consecutive time steps. This solver is often preferred as first try when solving stiff problems. It uses local truncation errors of order 1 to 5, combined with a variable step mechanism.

3.6.3 Compatibility with the EoMs

To investigate the compatibility of the different ODE-solvers to the dynamics of the TLP, the platform's equilibrium state is computed in response to zero external loads, initial conditions of zero and no damping. Naturally, all result should be zero, i.e. no motions in any of the DOFs. However, since the system is undamped, small numerical errors could increase in time. This shows the sensitivity of the applied ODE solver to numerical errors and indicates whether the problem can be defined as stiff or non-stiff.

Results of the vertical motions, shown in Figure 3-19, indicate that the non-stiff solvers require much longer computation time than the stiff solvers. Stiff solvers show less rapid variation in the solutions compared to the non-stiff solvers, which implies that the problem is stiff (see Appendix E.6 for explanation on numerical stiffness). Moreover, since the ODE15s uses variable order error estimation, both the local as well as the global errors are an order smaller than the errors in ODE23t. The error accumulation is better visible for the non-stiff solvers. The errors for these solvers are 10 orders higher than errors of stiff solvers. Errors for ODE113 are higher than errors for ODE45, since the trapezium rule has a 3^{rd} order local truncation error while Dormand-Prince algorithm has a 4^{th} to 5^{th} order local truncation error. It should also be noted that Matlab uses

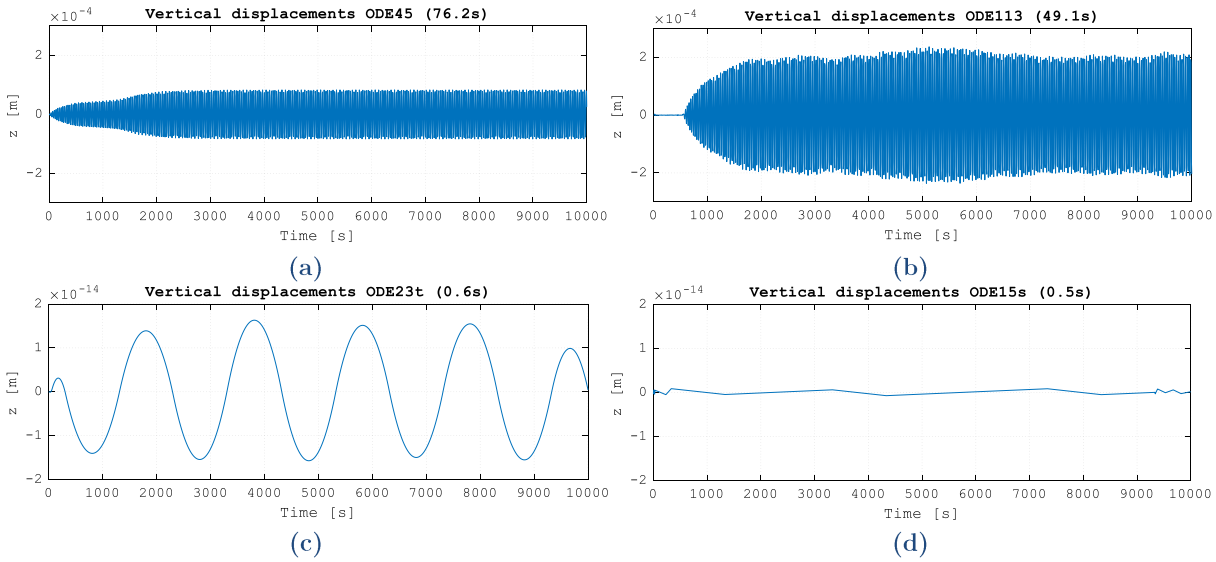

Figure 3-19: Simulations of White Noise to Test Efficiency of Solvers

double-precision numbers as default, which means that the upper bound of the relative error due to rounding, the so-called machine epsilon, is 2.2204e-16. This means that numbers are stored with roughly 15-16 digits of precision. The smallest solution values were found for ODE15s and were of order 10^{-15}, which means these values may have been influenced by rounding errors. This could explain the non-harmonic shape of the solution. Solutions of other solvers were at least of order 10^{-14} and are therefore not expected to be influenced by rounding errors.

From this exercise, it has been shown that both in terms of computational efficiency as well as global error accumulation, the stiff solvers ODE23t and ODE15s are preferable for solving the current problem.

3.7 Structural and Fatigue Analysis

3.7.1 Identification of Hotspots

After solving the time history of positions and kinematics of the structure, a postprocessing module is added to the model to extract the sectional forces and corresponding sectional stresses and fatigue damage at a number of structural details. These details are determined based on Finite Element Analysis (FEA), performed in Ansys using a pre-established model[3]. The FEM model is merely used to detect the location of stress concentrations that arise from a typical quasi-static loading case. Due to the large pretension in the mooring lines, loads acting on the pontoons are dominated by mooring restoring forces, which is always nearly vertical. Therefore, the load case is simplified to a pure vertical load at the location of the pontoon ends.

As shown in Figure 3-20, stress concentrations occur at the welded connections near the transition piece, where the top plate of the pontoons are attached to the centre column of the

[3] Provided by Bluewater on November 3, 2017.

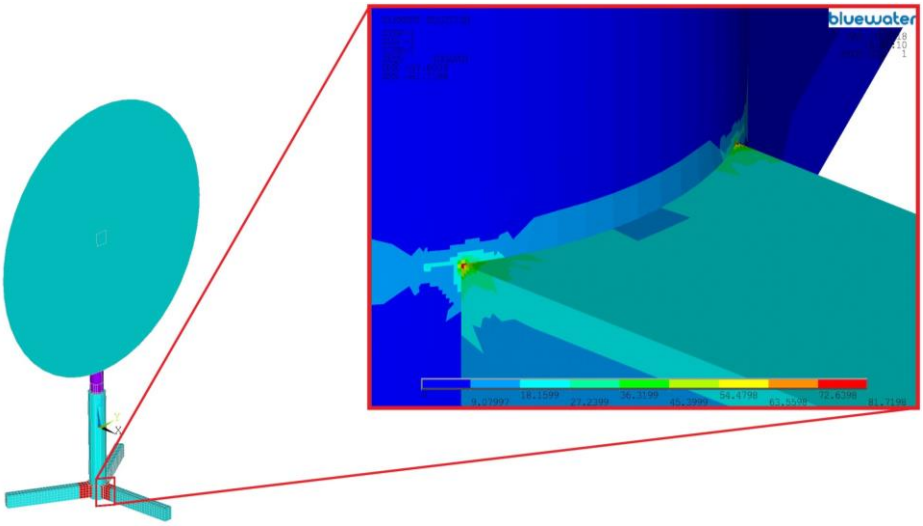

Figure 3-20: Hotspot Locations (FEM Results)

TLP. Due to discontinuities in the spatial distribution of the geometric stiffness, the stress path deflects towards the stiffer regions at these locations, resulting in stress concentrations.

The subsequent cross-sectional positions, considered for the fatigue analysis, are located on the cut-sections of the structural component that is isolated by cutting off the pontoons in the planes next to the welds and by considering only the part of the central column just below the weld seam. This structural element, in the remainder referred to as "the mid-section", contains the hotspots in the top plates of the pontoons and the corresponding points in the section of the central column. For completeness, the points in the middle of the weld seams that connect the pontoon top-plates to the central column (between the hotpots) are included as well. The resulting 6 pairs of locations have been defined as illustrated in Figure 3-21 and Figure 3-22. The sectional and material properties of the cross sections are listed in Appendix A.

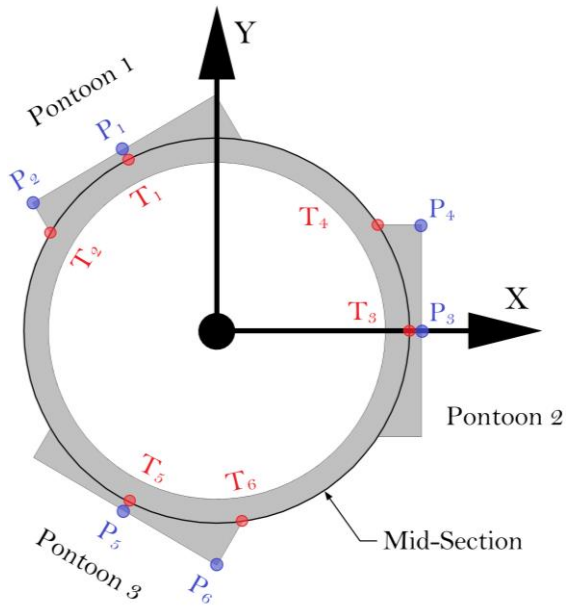

Figure 3-21: Hotspot Locations - Top View

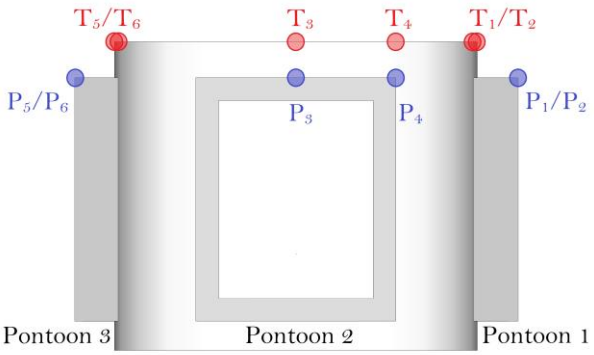

Figure 3-22: Hotspot Locations - Side View

3.7.2 Sectional Forces

The dynamic model calculates all forces based on the instantaneous positions, orientations and kinematics at designated points w.r.t. the global coordinate frame. The resulting framework of loads is expressed in terms of time dependent force vectors, acting on all points of the structure. Variations in the magnitude and direction of these force vectors are embedded within the time-dependent magnitudes of the X, Y and Z– components. These force components are subtracted from their points of application on the oscillating body and applied to the same points including dynamic and static gravitational loads, while the structure is kept stationary. Hence, the structural model is created. For clarification, the cross-sectional forces in top view (pontoon 2) are shown in Figure 3-23 and the cross-sectional forces in side view (pontoon 1 and central column) are illustrated in Figure 3-24, including the definitions of the local axis systems. The detailed derivations of the sectional forces are presented in Appendix F.

Provided that deformations remain small enough to not affect the hydro- and aerodynamic forces (i.e. negligible hydro-elastic response), the dynamic and structural model are equivalent in terms of physical representability. The only difference is the frame of reference in which the forces are observed: the dynamic model is based on an inertial reference frame, while the structural model uses a non-inertial frame of reference. The validity of negligible hydroelasticity is verified using a separate analysis in OrcaFlex (see Paragraph 3.9).

It is also important to note that the hydrostatics and mooring loads in the dynamic model were implicitly subjected to a number of simplifications, which have negligible influence on the dynamics but may lead to underestimation of the cross-sectional forces if the same simplifications are applied to the structural model. Therefore, the following features have been added to the structural model to determine the sectional forces more accurately:

Hydrostatic Pressures

In the dynamic model, the influence of hydrostatic pressures was simplified as a concentrated buoyancy force and restoring moments about the X and Y axes, all acting in the CoG of the total structure. The structural model takes the effect of hydrostatic hull pressures into account by distributing horizontal and vertical hydrostatic pressures based on instantaneous drafts of each submerged component (Figure 3-23 and Figure 3-24). The horizontal and vertical pressures acting on the pontoons are calculated using resp. Equations [3-64] and [3-65]. The horizontal and vertical pressures on the mid-section are calculated with resp. Equations [3-66] and [3-67].

$$P_{h,j} = \rho g z_{CoB,j} \quad [3\text{-}64]$$

$$P_{v,j} = \frac{g \cdot (\rho V_{box} - m_{box})}{L_{box} W_{box}} \quad [3\text{-}65]$$

$$P_{h,mid} = \rho g z_{CoB,mid} \quad [3\text{-}66]$$

$$P_{v,mid} = g \cdot \frac{\rho \cdot (V_{mid} + V_{trans}) - (m_{tot} - 3m_{box})}{\frac{1}{4}\pi D_{mid}^2} \quad [3\text{-}67]$$

where $j = 1 \ldots 3$ is the pontoon number, subscript *"box"* represents a property of the pontoon structure, subscript *"mid"* represents mid-section properties and $z_{CoB,j}$ and $z_{CoB,mid}$ are the vertical CoB positions of pontoon j and mid-section w.r.t. the water level, respectively.

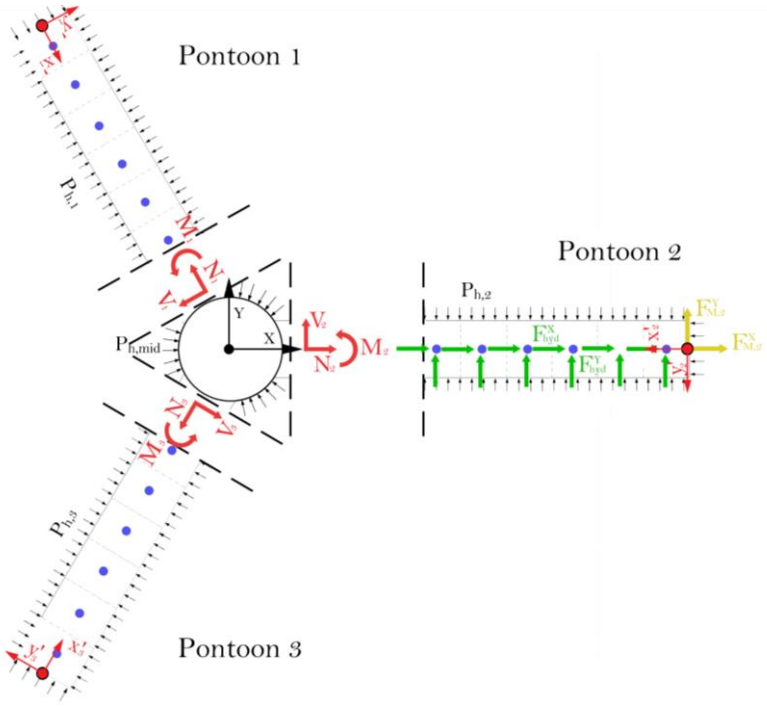

Figure 3-23: Cross-Sectional Forces - Top View

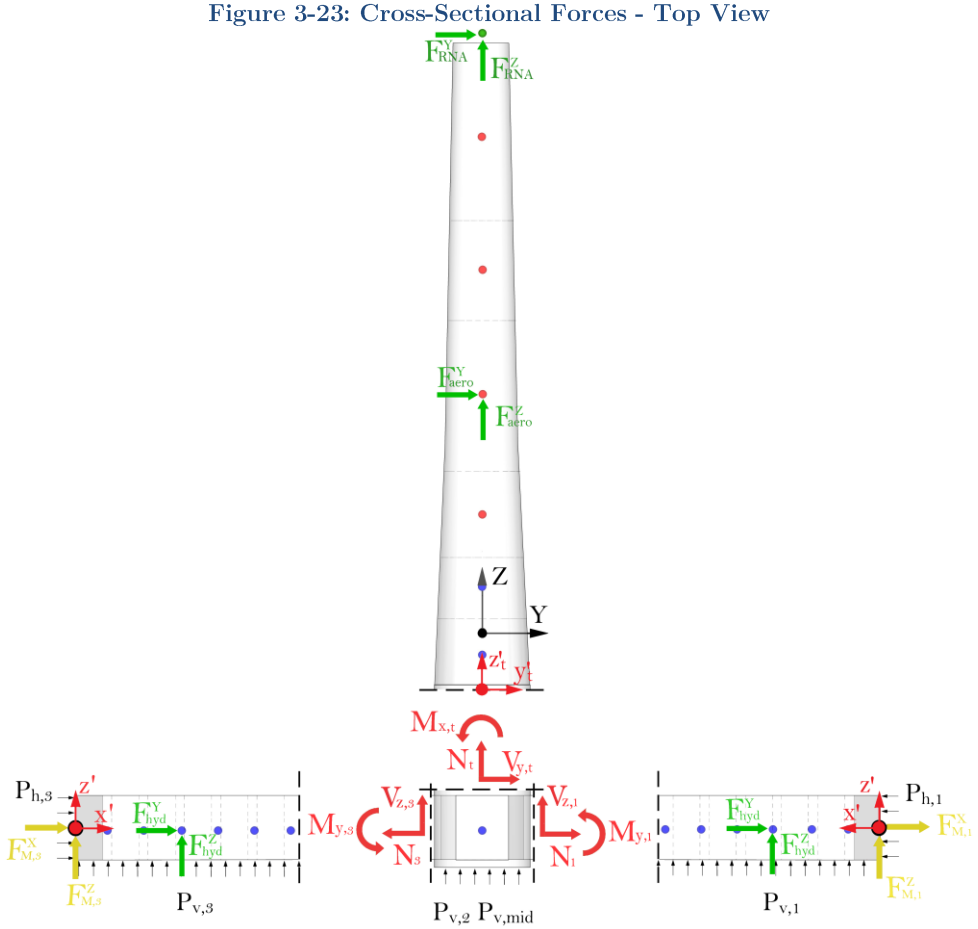

Figure 3-24: Cross-Sectional Forces - Side View

Mooring Induced Torsion

In the dynamic model, mooring lines were represented as single lines, connected to the pontoon-ends at a parametrically defined height along the centroidal axis. Thus, each pontoon experienced mooring forces in the form of a single vector. In reality, the mooring system consists of pairs of double mooring lines per pontoon, connected to the side plates of the pontoon ends (see Figure 3-25). Modelling double mooring lines induces torsion in the pontoons, resulting from asymmetric vertical loading from the mooring line pairs and from the vertical eccentricity of the horizontal forces w.r.t. the centroid of the pontoon (See Figure 3-26 and Figure 3-27).

The latter is a relatively simple mechanism; the derivation of this force can be found in Appendix F. To derive the torsional moment due to asymmetric mooring loads, consider an arbitrary rotation of the pontoon surface around its centroid, denoted with θ. This rotation causes a vertical shift u, as illustrated in Figure 3-27. Due to the vertical shift, an additional mooring force ΔF arises in each line, which gives rise to the torsion couple M_T according to Equation [3-68].

$$M_T = \Delta F \cdot W_{box} \quad [3\text{-}68]$$

where

$$\Delta F = \frac{u}{L_0} \cdot \frac{EA}{2} \quad [3\text{-}69]$$

$$u = \theta \cdot \frac{W_{box}}{2} \quad [3\text{-}70]$$

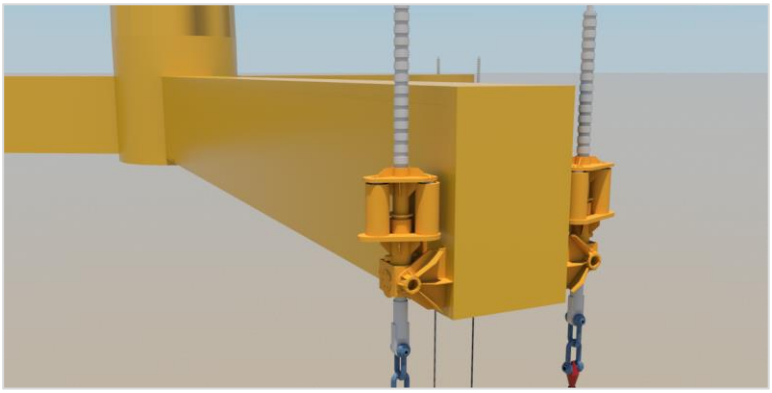

Figure 3-25: Mooring Line -Pontoon Connection

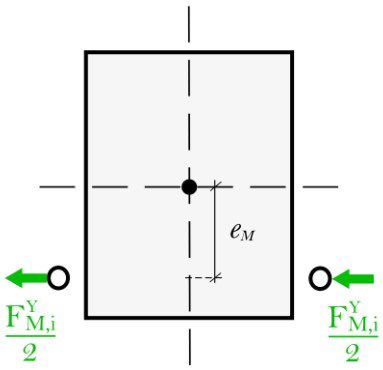

Figure 3-26: Torsion due to Eccentric Loading

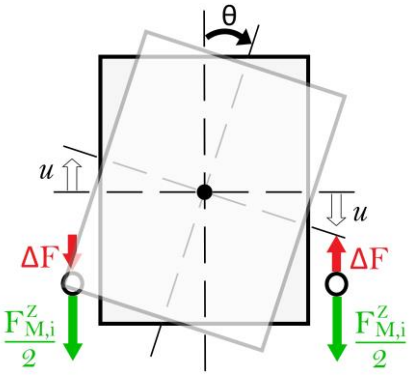

Figure 3-27: Torsion due to Asymmetric Loading

By formulating the torsional stiffness K_t as the division of the torsional moment by the rotation θ, the torsional stiffness can be found as shown in Equation [3-71].

$$K_t = \frac{M_T}{\theta} = \left(\frac{W_{box}}{2}\right)^2 \frac{EA}{L_0} \qquad [3\text{-}71]$$

Derivation of the torsional stiffness was performed on the basis of the following assumptions:

- Rotation amplitudes of the pontoons about their local x-axis (longitudinal axis) are small, such that: $\sin(\theta) = \theta$. This assumption is reasonable as θ depends on the roll η_4 and pitch η_5 motions, which are typically smaller than 2 degrees (verified based on results in Paragraph 3.8);
- The torsional stiffness of the pontoon structure itself is large enough to assume that no torsional deformations (i.e. torsional moments) arise from the small rotations θ. For closed box structures such as the pontoons, this assumption is considered reasonable;
- Elongations of the mooring lines caused by global motions are negligible, meaning the instantaneous line length is equal to the static line length: $L_i(t) = L_0 + \Delta L_i(t) \approx L_0$. Due to the large stiffness of the mooring lines, this assumption is also permissible;
- Mooring lines are assumed vertical (zero static angle), which is a slightly conservative assumption as it implies that u is completely undertaken by elongation of the lines. In reality, as the lines are under a slight angle, a smaller portion of u causes elongations.

3.7.3 Nominal Stress Response

The stress state in each specified location is defined based on elastic theory, according to the three-dimensional stress tensors in the pontoons and central column, as shown in resp. Figure 3-28 and Figure 3-29. The corresponding cross-sectional properties are presented in Appendix A and for a more detailed formulation of stresses, it is referred to Appendix F.

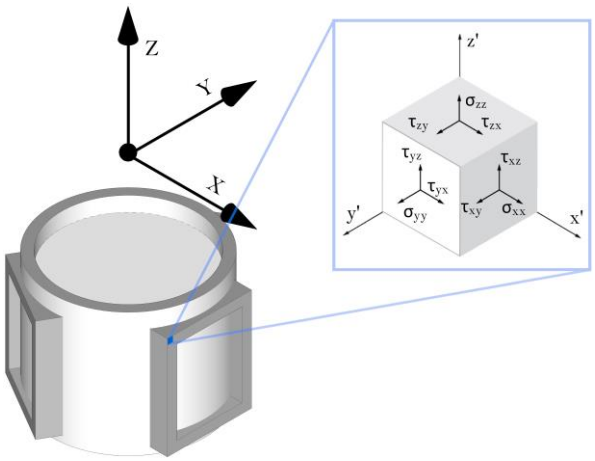

Figure 3-28: Pontoon Sectional Stresses

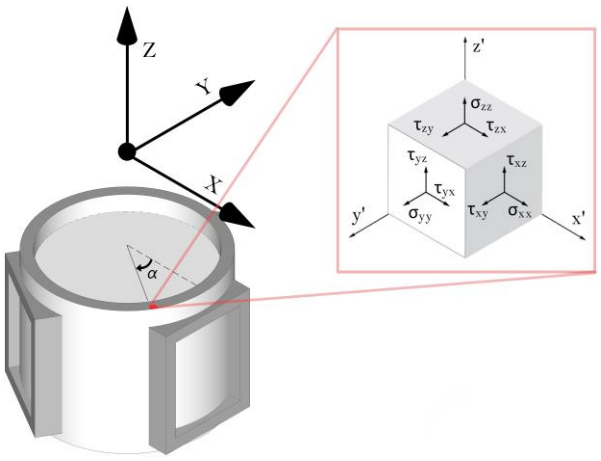

Figure 3-29: Central Column Sectional Stresses

Pontoon Sectional Stresses

Normal stresses in the local x- and y- direction of pontoon j are obtained using Equation [3-72] and [3-73], respectively. Shear stresses in the y-direction of pontoon j, in the plane normal the x-axis, is calculated with Equation [3-74]. All other stress components are negligible and therefore omitted. The first and second principal stresses in pontoon j are obtained according to Mohr's circle, as shown in Equations [3-75] and [3-76], respectively.

$$\sigma_{xx,j} = \frac{N_j}{A^x_{s,box}} + \frac{M_{z,j} \cdot y_{max}}{I_{z,box}} + \frac{M_{y,j}}{I_{y,box}} \cdot \frac{H_{box}}{2} \quad [3\text{-}72]$$

$$\sigma_{yy,j} = P_{h,j} \cdot \frac{H_{box} L_{box}}{A^y_{s,box}} \quad [3\text{-}73]$$

$$\tau_{xy,j} = \frac{V_{z,j} Q_z}{I_{z,box} \cdot t_{top}} + \frac{V_{y,j} Q_y}{I_{y,box} \cdot t_{top}} + \frac{M_{x,j}}{2A_{in,box} \cdot t_{top}} \quad [3\text{-}74]$$

$$\sigma_{I,j} = \frac{\sigma_{xx,j} + \sigma_{yy,j}}{2} + \frac{1}{2}\sqrt{\left(\sigma_{xx,j} - \sigma_{yy,j}\right)^2 + 4\tau^2_{xy,j}} \quad [3\text{-}75]$$

$$\sigma_{II,j} = \frac{\sigma_{xx,j} + \sigma_{yy,j}}{2} - \frac{1}{2}\sqrt{\left(\sigma_{xx,j} - \sigma_{yy,j}\right)^2 + 4\tau^2_{xy,j}} \quad [3\text{-}76]$$

where:

- $\{N_j,\ V_{y,j},\ V_{z,j},\ M_{x,j},\ M_{y,j}\ M_{z,j}\}$ are the cross-sectional forces in pontoon j;
- $A^x_{s,box}$ and $A^y_{s,box}$ are the cross-sectional areas of pontoon j in the cross sections normal to the local x and y-axis, respectively;
- y_{max} is the cross-sectional position in the local y-axis where the stress is calculated;
- Q_z and Q_y are resp. the first moments of the area along the z- and y-axis, between the location where the shear stress is being calculated and the centroid of the cross-section;
- $A_{in,box}$ is the enclosed area of the pontoon cross-section normal to the local x-axis.

Central Column Sectional Stresses

Normal stresses in the local z- and y-direction are obtained using Equation [3-77] and [3-78], respectively. The latter component is fully caused by the *hoop stress*, which occurs in pressurized bodies with closed circular cross sections. The sectional shear stress in the y-direction, on the plane normal the z-axis, is calculated with Equation [3-79]. All other stress components are negligible and therefore omitted. The first and second principal stresses are obtained using Equation [3-80] and [3-81], respectively.

$$\sigma_{zz,t} = \frac{N_t}{A_{s,t}} + \frac{M_{x,t}}{I_{x,t}} \cdot \frac{D_{mid}}{2} \cdot \cos(\alpha) - \frac{M_{y,t}}{I_{y,t}} \cdot \frac{D_{mid}}{2} \cdot \sin(\alpha) \quad [3\text{-}77]$$

$$\sigma_{yy,t} = P_{h,mid} \cdot \left(\frac{D^2_{mid} + D^2_{mid,in}}{D^2_{mid} - D^2_{mid,in}}\right) \quad [3\text{-}78]$$

$$\tau_{zy,t} = \frac{2 \cdot V_{x,t} \cdot \sin(\alpha)}{\pi D_{mid} t_{mid}} + \frac{2 \cdot V_{y,t} \cdot \cos(\alpha)}{\pi D_{mid} t_{mid}} + \frac{M_{z,t}}{J_t} \cdot \frac{D_{mid}}{2} \quad [3\text{-}79]$$

$$\sigma_{I,t} = \frac{\sigma_{zz,t} + \sigma_{yy,t}}{2} + \frac{1}{2}\sqrt{\left(\sigma_{zz,t} - \sigma_{yy,t}\right)^2 + 4\tau^2_{zy,t}} \quad [3\text{-}80]$$

$$\sigma_{II,t} = \frac{\sigma_{zz,t} + \sigma_{yy,t}}{2} - \frac{1}{2}\sqrt{\left(\sigma_{zz,t} - \sigma_{yy,t}\right)^2 + 4\tau_{zy,t}^2} \quad [3\text{-}81]$$

where:

- $\{N_t,\ V_{y,t},\ V_{z,t},\ M_{x,t},\ M_{y,t}\ M_{z,t}\}$ are the cross-sectional forces in the central column;
- $A_{s,t}$ is the cross-sectional area of the central column;
- α is the cross-sectional angle w.r.t. the local x-axis where the stress is calculated;
- $D_{mid,in} = D_{mid} - 2t_{mid}$ is the inner diameter of the central column (see Appendix A);
- J_t is the second polar moment of area, given in Appendix A.

3.7.4 Fatigue Damage Calculation

Short term fatigue damage is calculated using the SN-curve approach and linear damage accumulation is based on the Palmgren-Miner rule, as shown in Equation [3-82].

$$D = \sum_{i=1}^{M} \frac{n_i}{N_i} \quad [3\text{-}82]$$

where M is the total number of stress ranges in the signal, n_i is the number of occurrence of a stress range S_i and N_i is the constant amplitude fatigue limit, corresponding to S_i.

Implementation of SN-Curve

The general expression with which the number of cycles to failure N_i can be calculated, based on the stress range and properties of the SN-curve, is presented in Equation [3-83]. The double-sloped SN-curve consists of two regions that are characterized by their negative inverse slopes m_i and fatigue strength parameters C_i, separated with a known transition value of the stress range. Since the fatigue strength of welded joints depends on the local plate thickness, DNV [75] recommends to correct the actual stress range S_i with a dimensionless number that accounts for the ratio of the local plate thickness t to the reference thickness t_{ref} for which the SN-curve is designed. This is done according to Equation [3-84].

$$N_i = \frac{C_i}{\left(\tilde{S}_i\right)^{m_i}} \quad [3\text{-}83]$$

$$\tilde{S}_i = S_i \cdot \left(t/t_{ref}\right)^k \quad [3\text{-}84]$$

where k is the thickness exponent.

According to DNV, for fully penetrated, butt welded joints with load carrying welds and principal stresses that are calculated with the nominal stress approach and exhibit angles up to 30° w.r.t. the normal line of the weld seam, the appropriate SN-curve is classified as the *F*-curve. The corresponding reference thickness (for joints other than tubulars) is 25mm, $k = 0.25$ and the values of m_i and C_i are shown in Equation [3-85] and [3-86], respectively.

$$m_i = \begin{cases} 3, & \tilde{S}_i \geq 65.8\text{MPa} \\ 5, & \tilde{S}_i < 65.8\text{MPa} \end{cases} \quad [3\text{-}85]$$

$$C_i = \begin{cases} 10^{11.455}, & \tilde{S}_i \geq 65.8\text{MPa} \\ 10^{15.091}, & \tilde{S}_i < 65.8\text{MPa} \end{cases} \quad [3\text{-}86]$$

To be able to utilize a single load parameter to construct the stress ranges and calculate the fatigue damage, the direction of the principal stress signal is retained throughout the time series over which the damage is calculated. This implies each stress range signal is based on either the first or second principal stress, depending on which has the greatest absolute mean value.

Rain-Flow Counting Algorithm

The procedure of transforming the stress time-history to discretized stress ranges is performed using a Matlab built-in rainflow counting algorithm, which is developed according to ATSM standards [76]. The principles of the method are visualized in Figure 3-30 and summarized below:

1. Peak-valley filtering: For fatigue damage calculations, only the maxima and minima of the stress signal are relevant, as these data points determine the reversals in the stress slope. Therefore, intermediate data points between maxima and minima are removed.
2. Stress range quantification: The peak-valley filtered stress response is rearranged to start with the highest peak, after which the following peaks and valleys are matched to form closed hysteresis loops. Unclosed hysteresis loops are included as half-cycles, i.e. inducing half the damage of a full cycle.
3. Binning: Stress ranges are divided into fixed discrete bins, often visualized by means of stress range histograms. The determined stress ranges are mapped to the centres of each bin, enabling efficient counting procedures. If this step is omitted, all stress ranges are considered individually and the number of occurrence of each stress range n_i becomes 1.

It should be born in mind that the combined application of the rain-flow counting method with linear damage accumulation approach does not take influences of mean stresses and stress range sequences into account, which are secondary effects that may affect the fatigue damage.

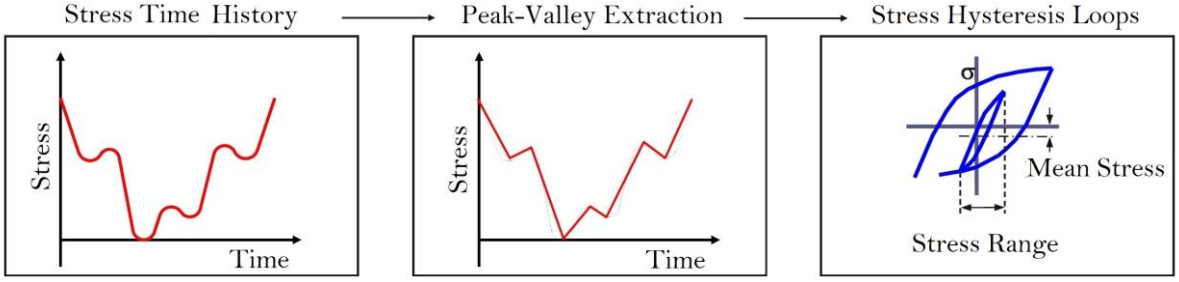

Figure 3-30: Rainflow Counting Algorithm

3.8 Model Verification

3.8.1 Introduction

This paragraph is aimed to assess the correctness of the numerical implementation and postprocessing techniques, based on numerical verification using OrcaFlex simulations. In the first sub-section, a method is proposed to determine the appropriate mesh size of the pontoon and tower segments. The subsequent sub-sections deal with the applied OrcaFlex model, the external conditions and simulation results that were used to compare the model outputs.

3.8.2 Appropriate Mesh Size

As explained in section 3.5, the TLP pontoons and turbine tower are subdivided in smaller segments in order to obtain more accurate hydro- and aerodynamic force distribution. In this section, the number of pontoon segments N_{box} and tower segments N_{tower} are determined by means of a mesh convergence test. Since convergence is purely based on the number of pontoon and tower segments, the turbine is, for the sake of simplicity, assumed non-operational.

The sea state (Table 3-3) is chosen such, that the fatigue damage is in the high cycle fatigue (HCF) range and therefore induce a fifth order dependency between damage and stress. This creates a high sensitivity of damage to hydrodynamic forces, implying that relatively large damage differences will occur as a result of mesh variations.

Table 3-3: Environmental Conditions Used for Convergence Test

Parameter	Symbol	Value
Significant wave height	H_s	1.25m
Spectral peak period	T_p	5.5s
Wave direction w.r.t. X-axis	μ_{wave}	90°
Current velocity at Water Plane	$U_{cur,wp}$	1.28ms^{-1}
Current velocity at Seabed	$U_{cur,sb}$	0ms^{-1}
Current direction w.r.t. X-axis	μ_{cur}	180°
Mean wind velocity	$u_{w,a}$	15.5ms^{-1}
Wind direction w.r.t. X-axis	μ_{wind}	0°

Convergence criteria are based on 300s simulations of the highest principal stress at a governing hotspot location and the corresponding damage response. The stress criterion is formulated as the normalized root mean squared error (RMSE) between results of two adjacent simulations, as shown in Equation [3-87]. The damage criterion is defined as the subsequent difference in damage w.r.t. the damage for 1 segment, as shown in Equation [3-88]. Convergence is reached when the stress convergence value reaches 0.05 and the damage criterion is converged to 0.10. The results for N_{box} and N_{tower}, as shown in resp. Figure 3-31 and Figure 3-32, indicate that the appropriate number for both N_{box} and N_{tower} is 4.

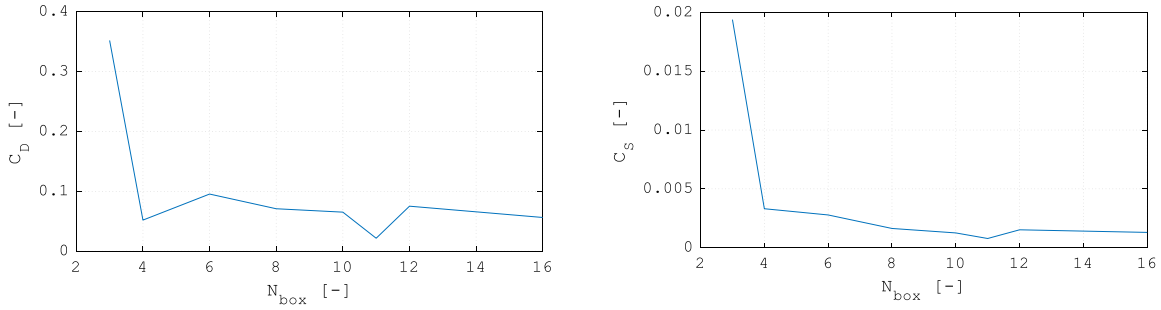

(a) (b)

Figure 3-31: Convergence Test of N_{box} Based on Damage (a) and Principal Stress (b)

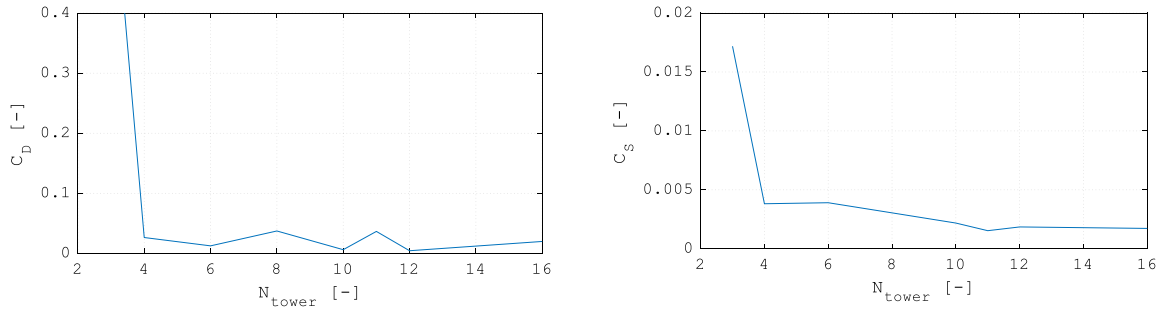

(a) (b)

Figure 3-32: Convergence Test of N_{tower} Based on Damage (a) and Principal Stress (b)

$$c_{S,j} = \frac{\mathrm{RMS}(\sigma_{j-1} - \sigma_j)}{\max(\sigma_j) - \min(\sigma_j)} \quad [3\text{-}87]$$

$$c_{D,j} = \frac{|D_{j-1} - D_j|}{D_1} \quad [3\text{-}88]$$

where σ_j is the first principal stress response at convergence step j and RMS denotes the root mean square function: $\mathrm{RMS}(x) = \sqrt{\frac{1}{N}\sum_{n=1}^{N}|x_n|^2}$.

3.8.3 OrcaFlex Model

Verification is performed using the motion and stress response in a fully rigid model of the WindFlo TLPWT in OrcaFlex (Figure 3-33). The natural periods of all DOFs are depicted in Table 3-4 and the natural modes are visualized in Figure G - 1, Appendix G.

The pontoons, turbine tower, transition piece and mid-section are all modelled as hollow spar buoy elements. The mooring lines are modelled as line elements, the RNA is represented by a lumped buoy and lumped buoys with negligible properties are attached to the pontoon ends to vary the position of the mooring line connection along the cross section. The pontoons are each divided in 4 segments with equivalent diameters (5.6m) to match the displaced volumes. The tower is divided in 40 segments in order to model the tapered tower shape as a series of cylinders with varying diameter. Based on the mesh size analysis in the previous section, applying larger numbers of segments does not induce errors larger than 0.5% in the stress response.

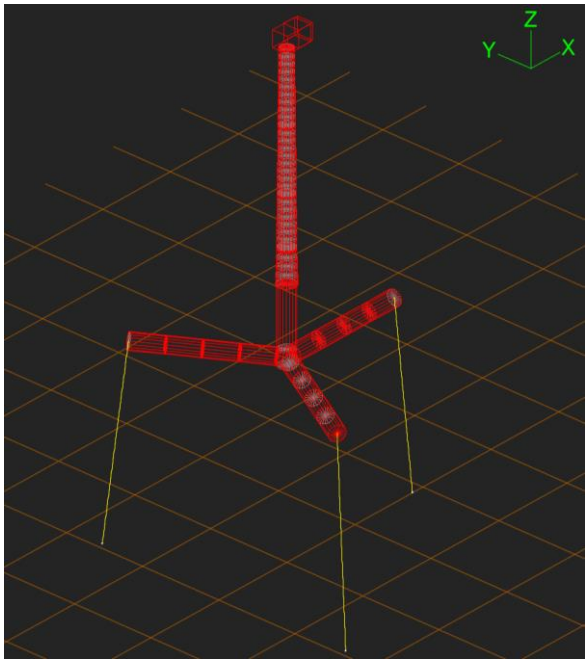

Figure 3-33: WindFlo TLP in OrcaFlex (Fully Rigid)

Table 3-4: WindFlo Rigid Body Natural Periods

	Natural Period (s)	
DOF	Matlab	OrcaFlex
Surge	35.2	35.0
Sway	35.2	35.0
Heave	1.7	1.7
Roll	2.2	1.7
Pitch	2.2	1.7
Yaw	13.3	14.1

3.8.4 Verification Approach

The verification approach is based on 250s simulations in regular waves, combined with misaligned currents. Waves and currents are based on extreme conditions, so that inconsistencies in results are easier to detect. Generation of interactive thrust forces, gyroscopic moments and the distribution of wind velocities in space and time according to the Frøya method need detailed programming, as these effects are not included in OrcaFlex by default.

In general, the verification of aerodynamics is a relatively extensive operation that must be performed in a suitable (BEM-based) software. Due to time constraints, this analysis could not be included. Verification of aerodynamics is, therefore, based on a static thrust force that is applied to the RNA in the direction negative of the X-axis (normal to the rotor plane). The implicit assumption is that the wind regime method, as proposed in the met-ocean data, has been validated and is correctly implemented. Table 3-5 depicts a summary of the applied environmental conditions.

Table 3-5: Conditions Used for Verification Analysis

Parameter	Symbol	Value
Wave height	H_{wave}	11.35m
Wave period	T_{wave}	12.40s
Wave direction w.r.t. X-axis	μ_{wave}	30°
Current velocity at Water Plane	$U_{cur,wp}$	1.28ms^{-1}
Current velocity at Seabed	$U_{cur,sb}$	0ms^{-1}
Current direction w.r.t. X-axis	μ_{cur}	0°
Static Thrust Force	F_T	1500kN

Motions outputs are generated at the CoG of the structure and since OrcaFlex is not able to output stress response for rigid body elements, the stresses are calculated using sectional force outputs at the cross-sections in the pontoons and mid-section. The errors in motions, mooring loads and sectional stresses are expressed in terms of normalized Root Mean Squared Errors (RMSEs), defined as in Equation [3-89]. Calculation of the errors were based on steady state conditions, in order to omit possible errors due to non-physical start-up phenomena.

$$\varepsilon = \frac{\mathrm{RMS}(x_{OF} - x_{ML})}{\max(x_{OF}) - \min(x_{OF})} \qquad [3\text{-}89]$$

where x_{OF} and x_{ML} are simulation results obtained from OrcaFlex and Matlab, respectively.

The stress response is verified according to the following considerations:

- Hydrostatics-induced stresses could not be included in OrcaFlex. For the verification analysis, this effect has been omitted in the analytical model as well.
- The mooring system is in the analytical and full model represented by a single line per pontoon, as it could not be confirmed in advance whether rigid elements in OrcaFlex are capable of transferring torsional moments. Analyses to reaffirm this effect and the influence of double mooring lines on the dynamic response has been omitted due to time constraints. Therefore, for the verification analysis, the effect of shear stresses due to asymmetric mooring loads have not been included.
- Torsional stresses in the pontoons due to mooring line eccentricity is included by assuming that the mooring lines are connected to the bottom of the pontoon ends.
- Since the OrcaFlex model uses an unspecified and non-adjustable numerical damping parameter, in order to achieve better correspondence in the transient response region, each DoF of the analytical model is equipped with a linear damping term consisting of 3% of its respective critical damping. This value was found on the basis of minimum RMSEs of the transient motion response w.r.t. OrcaFlex results.

3.8.5 Results and Conclusions

The resulting RMSEs and corresponding average amplitudes are presented in Table 3-6 and visual comparisons of simulation results is presented in Appendix G. The motion RMSEs are expressed as the average RMSE of all DOFs and the stress RMSEs are expressed as the average RMSE of all six hotspot locations in the {pontoon, mid-section} cross sections. Principal stress errors are calculated by substituting the sectional stresses in Equations [3-75] and [3-76], after which the RMSEs are calculated according to Equation [3-89].

Interpretation of the results should be done with the understanding that the RMSE is largely dominated by differences in mean and phase shifts between the two signals, which accumulates errors throughout the simulation. With regard to fatigue damage, however, it is more important that the stress amplitudes are determined as accurately as possible. Since this requirement is met (see Appendix G.4 and G.5), RMSEs are assumed to be mainly influenced by the above-mentioned causes and are therefore deemed acceptable under less stringent requirements.

The motion-, mooring load- and normal stress RMSEs, for instance, remain below 9% and are therefore considered acceptable. The shear stresses contain relatively large errors but are nevertheless considered acceptable, as the amplitudes of the shear stresses are negligible compared to the normal stresses (see Appendix G). Compared to the first principal stress at the pontoon cross sections, the errors in the second principal stress are relatively large. This is due to a relatively large contribution of shear stresses, as the average amplitude of the second principal stress (9.6MPa) is much smaller than the first principal stress (97MPa). However, since fatigue damage is based on the largest principal stress (i.e. either first or second, depending on which has greater mean value), the error in damage is are hardly affected by errors in the shear stress.

Table 3-6: Errors w.r.t. Results in OrcaFlex

Parameter	Error (%)
Displacements	5.9
Velocities	3.8
Accelerations	6.7
Mooring Loads	6.8
Normal Stress in the Pontoons	7.8
Normal Stress in the Mid-Section	8.6
Shear Stress in the Pontoons	18.1
Shear Stress in the Mid-Section	16.8
First Principle Stress in the Pontoons	7.8
First Principle Stress in the Mid-Section	11.7
Second Principle Stress in the Pontoons	19.5
Second Principle Stress in the Mid-Section	12.0

3.9 Flexibility Analysis

3.9.1 Introduction

The following section deals with the influence of structural flexibility on the external loads and stress response. Time domain simulations and spectral analyses are performed using OrcaFlex models and validated with linear Euler Beam theory. The first objective is to verify whether structural deformations are coupled with the external forces acting on the system (hydroelasticity). The second objective is to obtain a qualitative assessment of the influence of structural vibrations on the fatigue damage.

3.9.2 OrcaFlex Models

The OrcaFlex model that is described in the previous section (Figure 3-33) is used as a basis to perform the flexibility analysis. This model is adjusted in order to obtain a semi-rigid and fully flexible model. The semi-rigid model (Figure 3-34a) is obtained by modelling the tower as a line element with varying stiffness and its connection with the transition piece as a rotational spring.

The fully flexible model (Figure 3-34b) is obtained by replacing the rigid pontoons in the semi-rigid model with line elements with stiffness and connection stiffness with the mid-section. The main properties of each OrcaFlex model are summarized in Table 3-7. The three-dimensional stiffness vectors of the pontoons and tower, as well as the rotational spring constants are detailed in Appendix A.

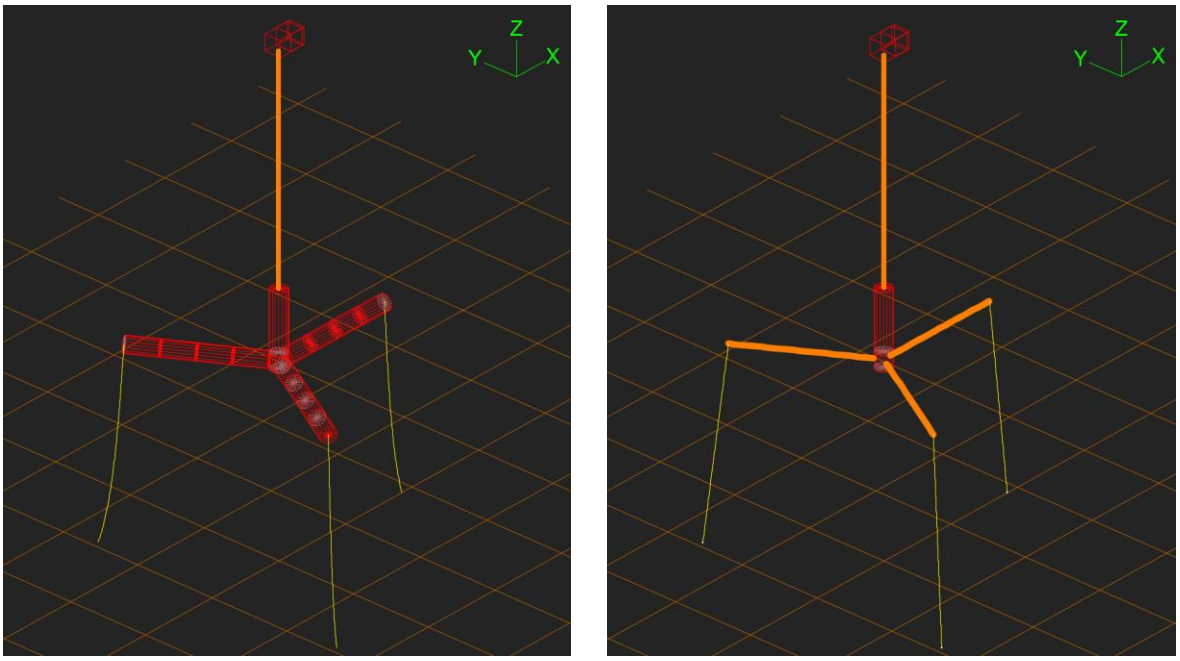

(a) (b)

Figure 3-34: Semi-Rigid (a) and Fully Flexible (b) OrcaFlex Model of WindFlo TLP

Table 3-7: Characteristics of OrcaFlex Models used in Flexibility Analysis

	Tower		Pontoon	
Model	Bending Stiffness	Connection Stiffness	Bending Stiffness	Connection Stiffness
Fully Rigid	Rigid	Rigid	Rigid	Rigid
Semi-Rigid	Flexible	Flexible	Rigid	Rigid
Fully Flexible	Flexible	Flexible	Flexible	Flexible

3.9.3 Methodology

Time history simulations of displacements, mooring loads and sectional stresses are computed based on regular waves, stationary currents and static thrust force (Table 3-8). Waves, current velocities and static thrust force are based on extreme conditions, with the aim of maximizing influences of flexibility. The OrcaFlex output parameters that are analysed are described below:

1. Time history of motions at RNA level and outer end of pontoon 2, mooring loads in line 2 and axial stresses in hotspot locations P_3 and T_3. Since OrcaFlex is only able to output the stress response for line elements, the sectional stress response at cross-sections of rigid elements is calculated by postprocessing sectional force outputs.
2. Spectral density of the axial stresses at P_3 and T_3 and at the corresponding cross-sectional locations at the tower top (connection with RNA) and pontoon tip (outer end). The aim is to characterize the vibration behaviour of the structural elements in terms of frequencies and determine the vibration frequencies that are directly transmitted. By comparing the natural frequencies of the structural elements, possible resonance vibrations can be detected.

Tower and pontoon deflections are determined by subtracting the rigid body displacements from the total displacements, as shown in Equations [3-90] and [3-91], respectively. As the displacements are defined w.r.t. the global coordinate system, the differences in displacements are corrected for the inclination angles of the tower and pontoons w.r.t. the longitudinal axes

Table 3-8: Conditions Used for Flexibility Analysis

Parameter	Symbol	Value
Wave height	H_s	11.35m
Wave period	T_p	12.00s
Wave direction w.r.t. X-axis	μ_{wave}	0°
Current velocity at Water Plane	$U_{cur,wp}$	1.28ms^{-1}
Current velocity at Seabed	$U_{cur,sb}$	0ms^{-1}
Current direction w.r.t. X-axis	μ_{cur}	0°
Static Thrust Force	F_T	1500kN

(see Figure 3-35). Note that for the tower deflections, the total (flexible) displacements are based on the semi-rigid model, to only capture the deflection of the tower.

$$u_t = \frac{X_{t,semi} - X_{t,rigid}}{\cos(\alpha_t)} \quad [3\text{-}90]$$

$$u_p = \frac{Z_{p,flex} - Z_{p,rigid}}{\cos(\alpha_p)} \quad [3\text{-}91]$$

where:

- $X_{t,semi}$ and $X_{t,rigid}$ are the time history of the X-coordinate of the RNA using the semi-rigid and fully rigid model, respectively.
- $Z_{p,flex}$ and $Z_{p,rigid}$ are the time history of the Z-coordinate of the pontoon ends using the fully flexible and fully rigid model, respectively.
- α_t and α_p are the inclination angles at the tower tip and pontoon tip.

Deflections obtained from OrcaFlex are validated using the analytical expression for the tip deflection of a prismatic cantilever beam with length L, under a single point load F_0 at its end:

$$u_{beam} = \frac{F_0 L^3}{3EI} \quad [3\text{-}92]$$

where EI the out-of-plane bending stiffness of the prismatic beam.

This expression can be readily applied to the pontoons by substituting the mooring load pretension as static point load ($F_0 = F_{pre}/3$) and its given length and bending stiffness. In case of the tower, the thrust force is substituted as the point load ($F_0 = F_{pre}/3$) and the tower length as L. However, since the diameter and wall thickness of the tower varies along the longitudinal axis, the second moment of area varies as well. The tower's equivalent (prismatic-beam) bending stiffness $EI_{eq,t}$ is obtained by solving the Euler-Bernoulli differential equations and equating the corresponding maximum deflection to the expression in Equation [3-92] (see Appendix H.1 for the derivation).

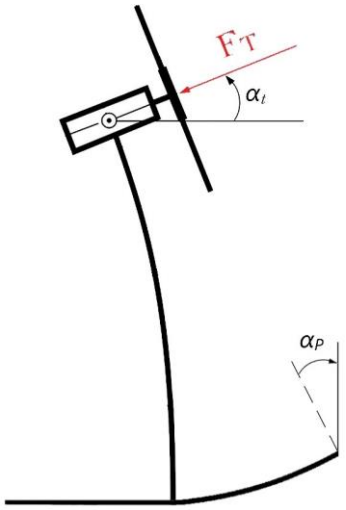

Figure 3-35: Definitions used in OrcaFlex Model

Finally, the following considerations should be born in mind regarding the proposed methodology:

- Pontoon deflections in the remaining directions (x' and y') are not considered as the vertical component of the mooring loads are much larger than the horizontal components due to the pretension. Therefore, the bending moment around local y-axes are governing;
- Due to symmetrical cross section of the tower, tower deflections around both horizontal axes are considered similar. Therefore, only deflections around the y-axis is analysed.
- As concluded in Section 3.8, the shear stress amplitudes are small compared to the normal stresses. Therefore, only normal stresses are considered.

3.9.4 Results and Conclusions

The time domain response of the deflections, mooring loads and axial stresses are presented in Figure 3-36 and a quantitative assessment of the influence of deformations on mooring loads and stress response is summarized in Table 3-9. Here, the constant ε_u is defined as the ratio between the mean deflections from OrcaFlex $\mathbf{mean}(u)$ and the equivalent beam deflection u_{beam}. The ratio r_u is defined as the ratio between the tip deflections and the rigid-body displacements ($r_u = u/x_{rigid}$). The amplitude ratios are defined as the ratio between the average response amplitudes from the fully flexible and fully rigid model.

Figure 3-37 and Figure 3-38 depict, respectively, the stress spectral densities at hotspots P_3 and T_3, including the spectral densities at the pontoon and tower free end and the natural frequencies of the flexible model (up to 5Hz). Since the axial stresses at the hotspots are magnitudes larger than the stress amplitudes at the free ends of the tower and pontoons, the stress spectral densities are normalized by dividing the output by their maximum value. An additional comparison between the fully flexible and semi-rigid model is given in Appendix H.2.

Table 3-9: Influence of Flexibility Based on TD Analyses

	$\mathbf{mean}(u_{OrcaFlex})$	u_{beam}	ε_u	$\mathbf{mean}(r_u)$	$\mathbf{max}(r_u)$
Tower	0.43m	0.42m	1.024	0.060	0.082
Pontoon	0.25m	0.24m	1.042	0.155	0.218
	Amplitude Ratios				
Mooring Loads	1.051				
Axial Stresses at P_3	1.106				
Axial Stresses at T_3	1.234				

Time Domain Analyses

The analytically derived tip deflections correspond well with the numerical values. Since the simulations were based on extreme conditions, the influence of flexibility on tower deflections and mooring force amplitudes are conservative and therefore considered insignificant. Although the pontoon deformations are considerable (22% of rigid displacements), since there are no phase shifts between the mooring load response from the flexible and rigid model, the results indicate that quasi-static deformations do not influence the external loads.

Compared to the fully rigid model, the flexible model shows larger stress amplitudes at both considered hotspots. The influence of flexibility is most noticeable at time instants where maximum displacements occur, which is also when the acceleration is at its maximum (double derivative of sinusoid). When large accelerations occur, flexible structures experience additional inertia forces caused by dynamic deformations. This causes an increase of the mooring load and stress peaks compared to the (semi-)rigid model. This effect is most prominent for the tower deflection due to the relatively large length of the tower and the presence of the RNA mass at the free end of the tower. It is less noticeable for the pontoons as they are largely restrained by the mooring lines. This is once again confirmed as the semi-rigid model demonstrates mooring loads and stress response that are almost identical for the fully rigid model, indicating that the influence of the pontoon stiffness is small.

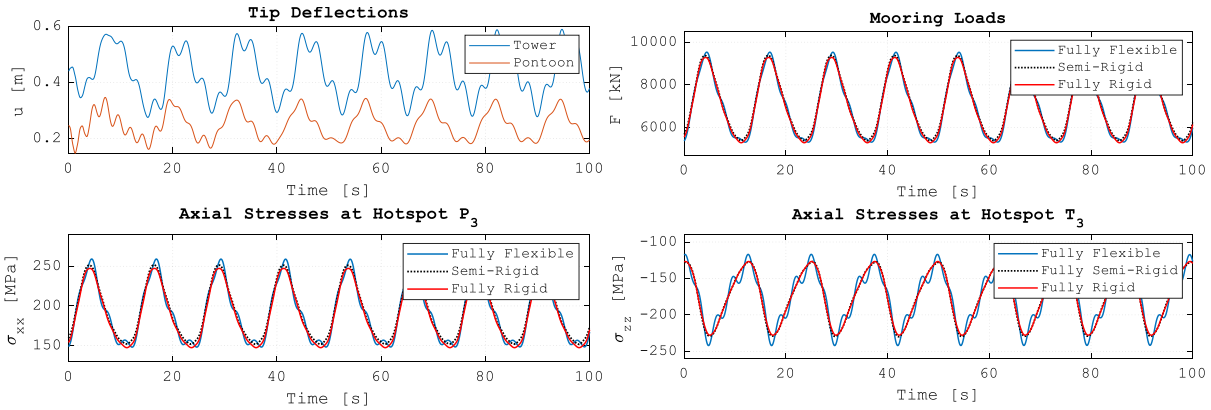

Figure 3-36: Flexibility Analysis - Time Domain Results

Spectral Analyses

The area of under the spectral density graphs at the frequency of the wave (Appendix H.2) comprises of 93% and 88% of the total area for the stress response at, respectively, hotspots P_3 and T_3. In other words, almost all output energy is at the same frequency as the input, which implies that the stress response is nearly linear. In terms of frequencies, at hotspots P_3 and T_3, the only peak frequencies that demonstrate a clear relation with a natural mode are the peaks at 0.32Hz, 0.43Hz and 1.80Hz. The remaining peaks are all found at integers of the wave frequency, which is an indication of super-harmonic excitation.

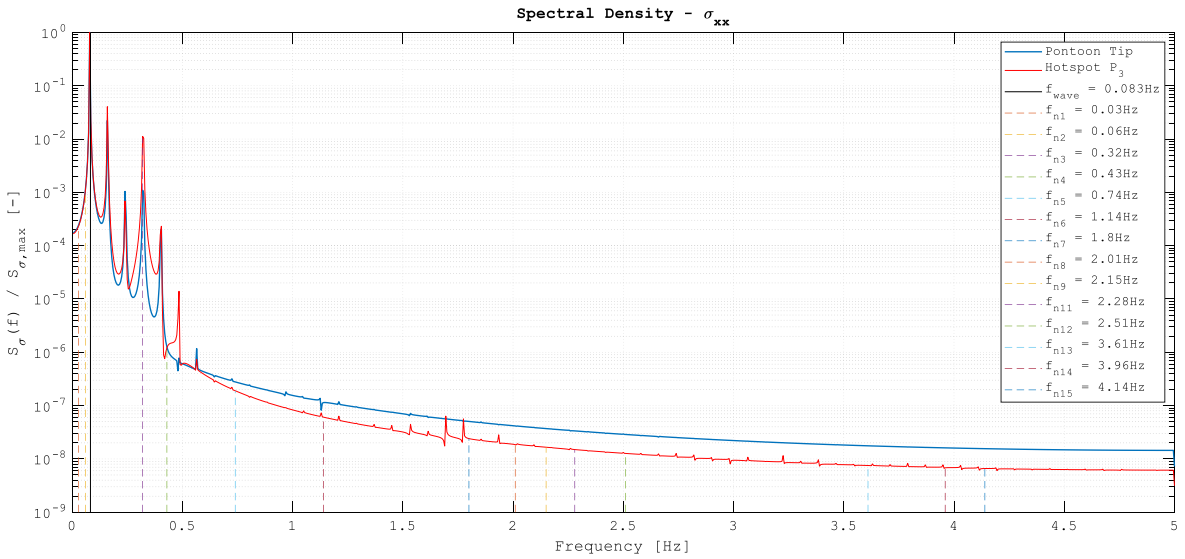

Figure 3-37: Stress Spectral Density at Hotspot P_3 and Pontoon Tip

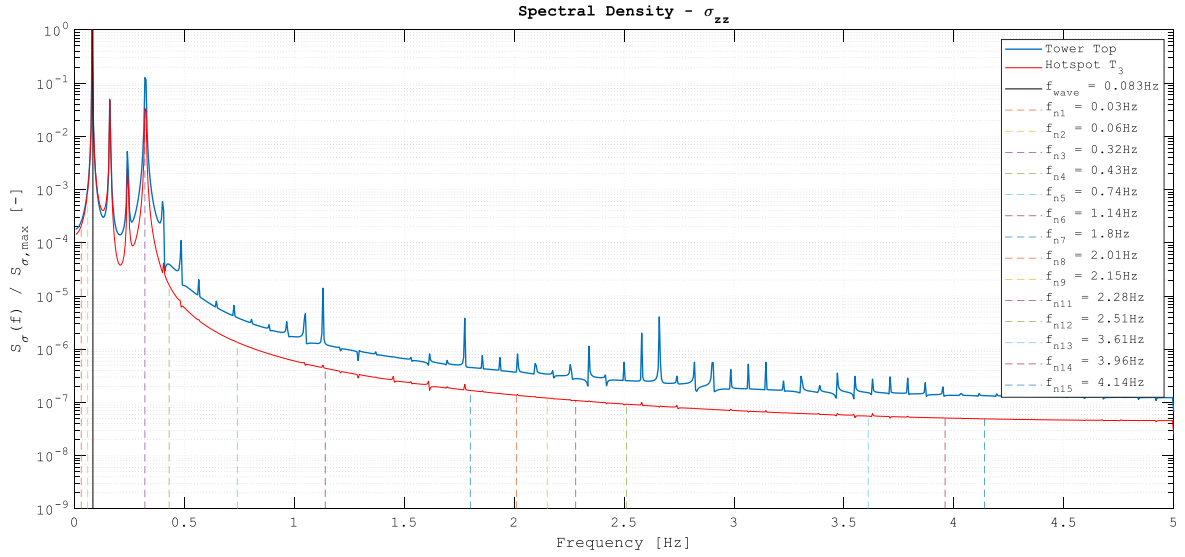

Figure 3-38: Stress Spectral Density at Hotspot T_3 and Tower Top

Compared to the stress spectral density at hotspot T_3, the response at the tower top shows notably more peaks high frequencies, which are mainly caused by inertial loads of the RNA and the rotational spring stiffness of tower-transition piece connection. Due to redistribution of energy into smaller vibration frequencies (<0.4Hz), a large contribution of these high frequency stress variations are not directly transmitted to hotspot T_3.

By comparing results from the fully flexible and semi-rigid model (see Appendix G), it was also observed that the stress response at hotspot T_3 is more sensitive to stiffness variations than stresses at P_3. When modelling the pontoons and their connections as fully rigid, more stress frequency peaks arise at hotspot T_3, indicating that applying rigid pontoons increases stresses in the HCF range. The reason for this behaviour is relatively straightforward; increasing the material stiffness of a structural element causes a shift of its (structural) natural frequencies towards higher frequencies.

Conclusions

Based on observations in the time domain analyses, it can be concluded that the flexibility of the tower can exert considerable influence on the stress amplitudes, while the pontoon flexibility has negligible influence. According to spectral analyses, the tower stiffness has a significant influence on the stress variations in the central column, whereas the response at the pontoon cross-sections do not show any correlation with structural vibrations.

Therefore, in regards to the applicability of fully rigid body dynamics for fatigue assessment, it is expected that the hotspots at the pontoon cross-sections are not significantly influenced by flexibility while the fatigue damage at the mid-section may be influenced if structural modes of the tower are amplified.

3.9.5 Discussion

Validation of the tower and pontoon deflections were according to Euler-Bernoulli beam theory, based on a fully clamped cantilever beam with an equivalent prismatic beam stiffness. In this section, the validity of this approach is assessed.

Applicability Euler-Bernoulli

Euler-Bernoulli beam theory was applied to validate the tower and pontoon deflections. Applicability of the theory follows from cross-sectional and structural properties of the considered beam, which will indicate whether shear deformations have a considerable influence. In such case, Timoshenko beam theory is more suitable as shear deformations are no longer negligible. Euler-Bernoulli beam theory is valid when the following relation is satisfied:

$$\frac{EI}{\kappa L^2 AG} \ll 1 \qquad [3\text{-}93]$$

where κ is the Timoshenko shear coefficient, L is the structural length, A is the cross-sectional area and G is the shear modulus (79.3GPa for steel). For a hollow circular section [77], the Timoshenko shear coefficient is defined as:

$$\kappa = 6(1+\nu) * \frac{(1+m^2)^2}{(7+6\nu)(1+m^2)^2 + (20+12\nu)m^2} \qquad [3\text{-}94]$$

with $m = r_{out}/r_{in}$.

Since the tower deflections are larger, it is sufficient to apply this check only to the tower, as the tower is more likely to experience shear deformations. By substituting the equivalent bending stiffness of the tower, as obtained by the of matching maximum deflection, the tower length, the average tower cross sectional area and a Poisson ratio of 0.293 into Equation [3-93], the ratio is found as $\frac{EI_{eq,t}}{\kappa L^2 AG} \approx 0.002$, proving that Euler-Bernoulli beam theory is indeed applicable.

Equivalent Beam Stiffness

From modal analysis, performed in OrcaFlex, it is known that the fundamental natural frequency of the turbine is equal to $f_{0,OrcaFlex} = 0.467Hz$. This value is obtained by isolating only the tower, without consideration of the rest of the structure. If the turbine is considered as a prismatic cantilever beam with a lumped mass at its tip, the fundamental natural frequency can be estimated using the following expression [78]:

$$f_0 \approx \frac{1}{2\pi}\sqrt{\frac{3EI_{eq,t}}{(0.2235m_{tower} + m_{RNA})L^3}} \quad [3\text{-}95]$$

where the tower and RNA mass are 426te and 335te, respectively.

By substituting the equivalent bending stiffness of the tower, the fundamental natural frequency of the turbine can be found as:

$$f_0 = 0.458Hz$$

Although this value is close to the one that was found in OrcaFlex, it makes sense that the exact value is not found. This is due to the fact that Equation [3-95] is based on a prismatic beam, meaning that the beam mass is equally distributed along its axis, which is not the case.

Cantilever Beam Approximation

The analytically derived maximum deflections were found slightly lower than the maximum deflections from OrcaFlex. The expression used to calculate the maximum tip deflection (Equation [3-92]) was based on "clamped-free" boundary conditions (BCs), while the connection in OrcaFlex has a certain rotational stiffness, i.e. not fully clamped. For a cantilever beam that is supported by a rotational spring with spring stiffness k_r, the rotational BC at its supported end is $\phi(0) = M(0)/k_r$, in contrast to the fully clamped BC, which is $\phi(0) = 0$. By substituting these BCs in the Euler-Bernoulli differential equations (see Appendix H), the following expression is obtained for the maximum tip deflection:

$$u_{beam} = \frac{F_0 L^3}{3EI} + \frac{F_0 L^2}{k_r} \quad [3\text{-}96]$$

This expression proves that deflection of a beam supported by a rotational spring is always larger than a beam with a fully rigid connection. It is, however, too complex to derive the actual rotational spring stiffness analytically, as the total rotational spring k_r stiffness is influenced by the rotational stiffness of the tower-transition piece connection and bending of the pontoons and its connections with the transition piece.

4
MODEL VALIDATION

The following chapter is meant to demonstrate the validity of the modelling approach using OrcaFlex simulations and scale test data of an existing reference TLP. As certain geometric and static properties of the reference TLP are unknown, the first step is to determine missing properties by means of a reverse engineering approach. The concept is then modelled in OrcaFlex and validated using the experimental data, after which results from the OrcaFlex and Matlab are compared to prove the validity of the analytical model.

4.1 Reverse Engineering of Reference TLP

4.1.1 Global Dimensioning

The global dimensioning and static characteristics of the SBM TLP are approximated using illustrations and other technical information that was provided (see Section 2.7). Estimation of the main platform dimensions are based on geometric proportions, which are derived from a number of visual representations of the platform, shown in Figure 4-1. Here, the green, purple and orange braces are denoted as primary, whereas the blue and grey braces are labelled secondary. The resulting expressions for calculation of the global geometric parameters are shown in Equations [4-1] to [4-7].

Since the bracing system is said to be designed similar to jacket structures, the wall thickness of the braces are chosen according to typical values in practice. As a rule of thumb [79, p. 330], the bracing of bottom fixed offshore structures are designed according to the ratio $19t_{brace} \leq D_{brace} \leq 60t_{brace}$. Following this design rule, the wall thickness of the braces can be calculated using the expression in Equation [4-8].

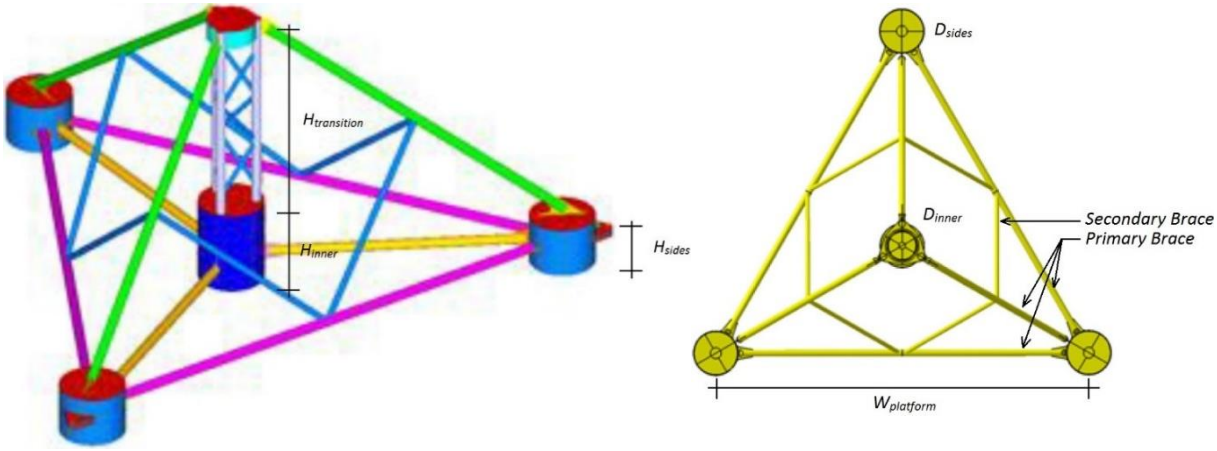

(a) (b)

Figure 4-1: Three-Dimensional (a) and Two-Dimensional (b) Representation of Reference TLP [72]

$$W_{platform} = \sqrt{3} \cdot R_{floater} \quad [4\text{-}1]$$

$$D_{sides} = \frac{1}{4.6} \cdot R_{floater} \quad [4\text{-}2]$$

$$D_{inner} = 0.94 \cdot D_{sides} \quad [4\text{-}3]$$

$$D_{brace,secondary} = 0.80 \cdot D_{brace,primary} \quad [4\text{-}4]$$

$$H_{transition} = \frac{10}{14.1} \cdot H_{floater} \quad [4\text{-}5]$$

$$H_{inner} = \frac{4.1}{14.1} \cdot H_{floater} \quad [4\text{-}6]$$

$$H_{sides} = \frac{2.5}{4.1} \cdot H_{inner} \quad [4\text{-}7]$$

$$t_{brace} = D_{brace,primary}/21 \quad [4\text{-}8]$$

Assuming that the virtual crossing point, which was stated to be slightly above hub height, is 5m above hub height, the static line angles α, line length L_0 and footprint breadth W_T can be derived using trigonometric ratios. Finally, the buoy wall thickness and the mooring line characteristics are derived from standard values in OrcaFlex (Line Type Wizard). The only geometric parameter that is yet unsolved is the primary brace diameter, which is considered too error sensitive to determine with visual estimation. This parameter, along with the dry mass of the platform and ballast volume in the side buoys during operational condition, are determined in a static weight analysis.

4.1.2 Static Weight Analysis

The dry mass of the total structure, including turbine, is calculated with Equation [4-9] and the dry mass of the platform is calculated using Equation [4-10]. See Section 2.7, Table 2-1 for the values of known parameters.

$$M_{tot} = M_{\nabla,op} - \frac{3F_{pre}\cos(\alpha)}{g} \quad [4\text{-}9]$$

$$M_p = M_{tot} - M_{tower} - M_{RNA} - M_{lines} \quad [4\text{-}10]$$

where $M_{\nabla,op}$ is the platform displaced mass during operational conditions, F_{pre} is the mooring line pretension, M_{tower} is the tower mass, M_{RNA} is the RNA mass and M_{lines} is the total dry mass of the mooring lines.

The wet mass of chain mooring, according to standard values in OrcaFlex, is 48kgm^{-1} per line. Moreover, since the transition piece in the platform is derived from swivel stacks employed in taut-moored FPSOs, which weighs up to 300t, an additional 200t of dry mass is added to platform to account for the weight of the transition piece (denoted with M_{trans}).

The remaining unknown parameters are solved using parametric expressions for the total mass of steel ($\rho_s = 7850\text{kgm}^{-3}$) of the TLP structure M_{steel} and the displaced mass during operational condition $\widetilde{M}_{\nabla,op}$, which are functions of the geometric parameters and ballast volume. The latter is equated to $M_{\nabla,op}$ to find a solution of the displaced volume including ballast.

$$M_{steel} = M_p - M_{trans} \quad [4\text{-}11]$$

$$\widetilde{M}_{\nabla,op} = V_{disp}\big|_{D=D_{op}} \cdot \rho_w \quad [4\text{-}12]$$

where V_{disp} is the displaced volume as a function of the draft D and D_{op} is the draft during operational conditions.

4.1.3 Verification of Parameters

Using the solution of this system of two equations, the pretension $\tilde{F}_{pre}$, the dry mass of the platform $\widetilde{M}_p$ and natural periods in surge $T_{n,1}$ and heave $T_{n,3}$ are derived (see Appendix I for derivations) and compared to their known values as a means of confirmation of the results. The resulting expressions are shown in Equation [4-13] to [4-15].

It was stated that the during load-out, the turbine is not installed, which means that the draft is based on the dry mass of the free-floating platform only. In this case, as the use of ballast water was only specified for operational conditions, the buoys are assumed to be completely buoyant. The restoring coefficients are derived from the EOMs by applying a small offset to the platform and calculating the resulting net force in the relevant direction.

Note that the hydrodynamic coefficients are unknown and cannot be derived from the provided information. Therefore, the magnitude of the added mass is chosen to match the known natural periods ($a_{33} = 0$, $a_{11} = 1.35M_{tot}$). It is also worth mentioning that the natural periods are based on fully rigid materials, whereas the provided heave natural period also includes structural influences. Structural deformations tend to decrease the tether loads in heave, making the system less stiff.

$$\tilde{F}_{pre} = g\frac{\widetilde{M}_{\nabla,op} - \widetilde{M}_p - M_{tower} - M_{RNA} - M_{lines}}{3\cos(\alpha)} \quad [4\text{-}13]$$

$$\widetilde{M}_p = V_{disp}\big|_{D=D_{lo}} \cdot \rho_w \quad [4\text{-}14]$$

$$T_{n,i} = 2\pi\sqrt{\frac{M_{tot} + a_{ii}}{C_{ii}}} \quad [4\text{-}15]$$

where D_{lo} is the draft during load-out, a_{ii} is the added mass in the ii-direction and C_{ii} are the stiffness of the system, shown in Equation [4-16] for surge and in Equation [4-17] for heave.

$$C_{11} = \frac{F_{pre}}{L_0} \cdot \left(2 + \sqrt{1 + \left(\frac{W_T}{d - D_{op}}\right)^2}\right) \quad [4\text{-}16]$$

$$C_{33} = \frac{3EA}{L_0} + \rho_w g A_{wp} \quad [4\text{-}17]$$

where W_T is the mooring line footprint breadth (radial distance chain connectors to anchor heads), d is the water depth, A_{wp} is the water piercing area and $EA = 2.525 \cdot 10^8\text{N}$ is the axial stiffness of the mooring lines (chains).

4.1.4 Results

The results are summarized in Table 4-1. For a detailed overview of dimensions and volumetric distribution of the structure, it is referred to Appendix I.

Table 4-1: Static Properties of Reference TLP

Parameter	SBM	Calculated	Unit
Total Mass	-	1770.2	t
Platform Mass	-	1239.7	t
Pretension per bundle	1560	1560	kN
Displaced Mass	2200	2214	t
Heave Natural Period	2.5	2.4	s
Surge Natural Period	45.0	45.0	s

4.2 OrcaFlex Model

Validation is performed using the motion and stress response in a fully rigid model of the SBM TLP in OrcaFlex (Figure 4-2), which was built using results from the reverse engineering exercise. The modelling approach was meant to keep the OrcaFlex model simple, while incorporating the properties that govern the behaviour of the system. The model includes four spar buoy elements representing the central buoy and three outer buoys, a surface-piercing buoy to represent the surface-piercing area, a lumped buoy at the CoG of the turbine (64m above tower base) to represent the mass of the turbine and three line elements to represent the mooring system.

The volumetric displacement of the model is composed of the submerged volumes of the five submerged buoys. The dimensions of the surface piercing buoy were based on the surface piercing area of the TLP during operational conditions and a length of 4m, of which half is submerged at system equilibrium. This buoy was given the mass of the transition piece. The diameters and masses of the remaining buoys were slightly adjusted, in comparison to the results of the previous

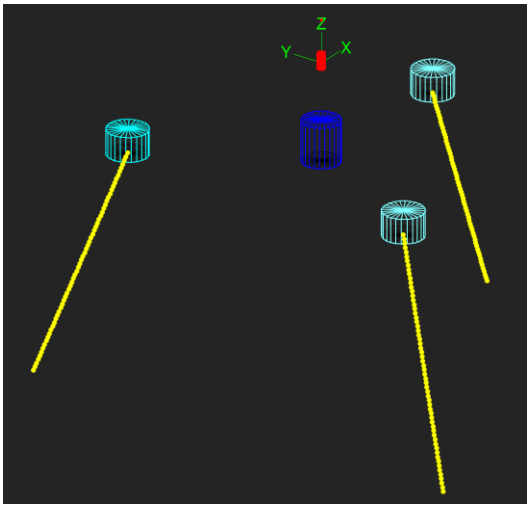

Figure 4-2: OrcaFlex Model of Reference TLP

section, in order to match the mass distribution and total displaced volume of the SBM design. Since the OrcaFlex model does not include the braces, the diameters of the buoys are increased while their heights are kept in accordance to the reverse-engineered values. The complete list of input values and geometric parameters that are utilized in the OrcaFlex model is included in Table I - 2, Appendix I.

4.3 Comparison with Scale Test Data

4.3.1 Methodology

The published scale test results of the reference TLP consists of a series of illustrations, in which the surge, heave and pitch RAOs are plotted against the wave period for different wave angles and reference positions on the structure. As summarized in Table 4-2, five different study cases have been distinguished, in which different wave heights and incident wave angles have been defined.

Analogous to this approach, the validation procedure of the OrcaFlex model was carried out by performing simulations using regular waves with varying wave heights, wave angles and wave periods between 5s and 30s with increments of 5s. Head waves are defined as 0-degree wave angles, meaning that positive wave angles are counter-clockwise from the negative X-axis. Thrust forces were modelled as a constant, concentrated force applied horizontally to the location of the turbine hub with varying angle w.r.t. the global X-axis. Currents have not been included in any of the cases. The resulting surge, heave, and pitch motion amplitudes are then divided by the wave amplitude to obtain the motion amplitude RAO value for each wave period.

Table 4-2: Study Cases for Which Scale Testing Data is Provided

	Case 1	Case 2	Case 3	Case 4	Case 5
DOF	Surge	Heave	Pitch	Surge	Surge
Wave Height [m]	4	4	4	1, 4, 16	4
Wave Angle [°]	0, 15, 30	0, 15, 30, 45, 60	0, 15, 30, 45, 60	0	0
Reference Location	Keel & nacelle	Nacelle	Keel	Keel	Keel
Thrust Force [kN]	0	0	0	0	0, 720 (0°), 720 (30°)

4.3.2 Results and Conclusion

A summary of the errors in each case is listed in Table 4-3 together with the dominant sources of error, in which the errors are defined as the calculated RAOs divided by published values and averaged over all wave periods. The calculated RAO plots and the validation data of the five considered cases, likewise in the form of illustrations, are presented in Appendix I.3.

Table 4-3: Average Difference in RAOs per Study Case

Case	RAO_{calc}/RAO	Source
1 (keel)	0.83	Wave periods ≤ 10s
1 (nacelle)	0.99	-
2	1.30	Wave periods ≤ 15s and increasing wave misalignments
3	0.74	Wave periods ≤ 10s
4	0.83	Wave periods ≤ 10s and wave period of 30s in case of 0.5m amplitude
5	0.84	Wave periods ≤ 10s and misaligned thrust forces at long waves

Overall, the OrcaFlex model predicted the motions and trends of the SBM TLP system well, considering the simplicity of the model and the yet unexploited possibilities for optimization. On average, the surge and pitch motions were, respectively, 13% and 26% lower than the provided data and the heave RAOs were roughly 30% higher than the SBM values. The trends of RAOs were all well matched, with most deviations at certain, specific wave periods. This may be due to dependency of the hydrodynamic coefficients to wave frequencies.

4.3.3 Discussion

Application of OrcaFlex as a validation tool, without additional diffraction analyses, inherently implies that one is limited to the Morison equation as wave force quantification method. This is not entirely in line with the practice in published reports, since the results included diffraction forces. Nevertheless, this approach was considered acceptable as the hydrodynamics of the SBM TLP are in the "Inertia and Drag" quadrant of Figure 3-7 (Section 3.2), indicating that the use of the Morison equation is justified. However, the relatively large errors in the heave and pitch RAOs could possibly be a consequence of excluding linear potential damping, which may have considerable influence on stiff DOFs with small velocity amplitudes. Moreover, with changes to the added mass coefficient, it was observed that the RAO values could be modified per wave frequency to match the SBM values. However, this procedure could not be justified since diffraction analysis was not performed.

It should also be noted that the accuracy of results in this study depend on the accuracy of the parameters calculated in the reverse engineering approach. Furthermore, the modelling of the structure in OrcaFlex was based on a simplified approach, in which the braced structure was disregarded and the system was modelled as entirely rigid. It is clear from publications that the SBM modelling included the braced structure and the overall structure included non-rigid components, particularly in the braces.

4.4 Validation of the Analytical Model

4.4.1 Methodology

Since the OrcaFlex model is now validated, the analytical model can likewise be (indirectly) validated by implementing the developed analytical model to the reference TLP and comparing the results between the two models. The validation process has been carried out using the 1-year extreme wave conditions, as was stated in the published reports [68] [72], combined with misaligned currents. Waves are considered regular and thrust and aerodynamic drag forces are disregarded. See Appendix I.4 for a detailed formulation of the underlying mathematical model, as applied to the reference TLP.

The platform's response is simulated the first 150 seconds and compared solely on the basis of motion outputs at the CoG of the structure. The errors are expressed in terms of RMSEs (Equation [3-89]), based on steady state conditions in order to omit possible errors due to non-physical start-up phenomena. Table 4-4 depicts a summary of the applied environmental conditions.

Table 4-4: Conditions Used for Validation Analysis

Parameter	Symbol	Value
Wave height	H_s	3.5m
Wave period	T_p	6.5s
Wave direction w.r.t. X-axis	μ_{wave}	30°
Current velocity at Water Plane	$U_{cur,wp}$	0ms^{-1}
Current velocity at Seabed	$U_{cur,sb}$	0ms^{-1}
Current direction w.r.t. X-axis	μ_{cur}	0°
Static Thrust Force	F_T	0kN

4.4.2 Results and Conclusions

The resulting RMSEs are presented in Table 4-5Table 3-6 and the visual comparisons of simulations are depicted in Figure 4-3. An overview of the rigid body natural modes, as calculated in OrcaFlex, is presented in Figure I - 1, Appendix I. Although the RMSEs are duration dependent and the obtained values may slightly converge further with longer simulations, from this short simulation, it can be concluded that the models exhibit almost identical behaviour when it comes to natural periods and are largely identical in motion simulations.

It should, however, be noted that the hydrodynamic coefficients are in both the OrcaFlex and analytical model not optimized to exactly mimic the published natural periods in all DOFs. As a result, a number of calculated natural periods show small dissimilarities w.r.t the given values. This optimization process does not contribute significantly to the validation of the analytical model is therefore omitted.

Table 4-5: Validation Results (Reference TLP)

	Natural Period (s)		Motion Response
DOF	Matlab	OrcaFlex	**Error (%)**
Surge	49.1	49.7	4.0
Sway	49.1	49.7	6.9
Heave	2.3	2.5	8.1
Roll	4.9	4.8	7.4
Pitch	4.9	4.8	9.1
Yaw	38.1	38.9	1.7

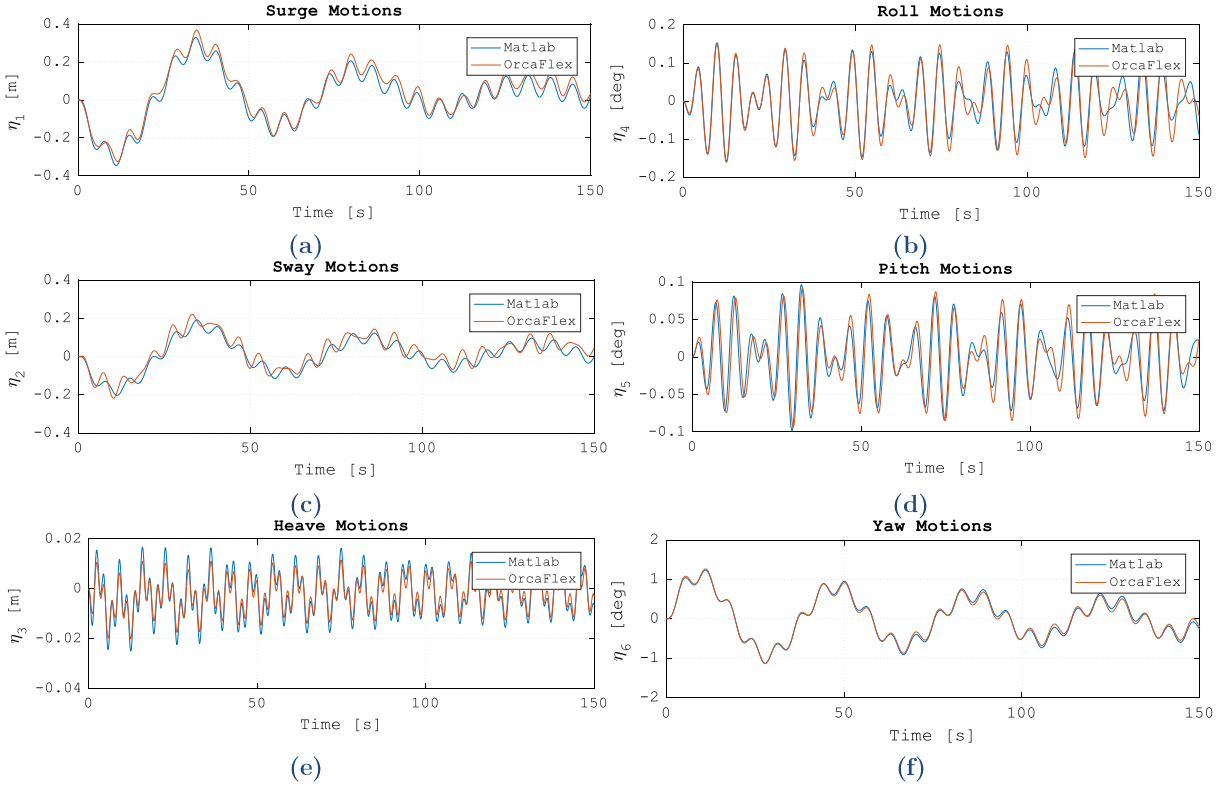

Figure 4-3: Time History of Motions of Reference TLP in Matlab and OrcaFlex

5
LINEARIZATION

The dynamic model of the WindFlo TLP was developed to simulate the actual system as detailed and accurate as possible. The consequence is that several nonlinear effects are included. This chapter is intended to investigate the influence of these phenomena by linearizing the system and identifying the differences in results with respect to the nonlinear model.

5.1 Introduction

5.1.1 Theoretical Background

In the first chapter of this report, it was determined that in order to evaluate the applicability of FD methods for the assessment of fatigue damage, the TD nonlinear model must be linearized. It is important to understand what is meant by "nonlinearities" and, therefore, which aspects of the EoMs must be linearized. As was mentioned in Section 2.6.2, a linear dynamic system is characterized by two properties:

1. All terms in the EoM depend linearly on the system variables (displacements, velocities and accelerations);
2. The mass, damping and stiffness matrix are symmetric.

If these conditions are met, a frequency-dependent transfer function matrix can be set up, such that the response in each DOF is determined by multiplication of the transfer function matrix with the external force vector (also in frequency domain). The latter is then the collection of all active forces that, independent of the system variables, transmit energy into the system. The transfer function is therefore independent of the external forces, which means that when it is referred to "nonlinearities", only the nonlinear dynamic effects of the system itself (i.e. nonlinear inertial, damping and restoring forces) are meant.

5.1.2 Linearization Approach

To perform linearization of the system, a distinction is made between primary and secondary nonlinearities. Primary nonlinearities include all force terms that have a nonlinear relationship with one or more system variables, being nonlinear rotation terms, mooring forces and forces with a quadratic velocity dependency. Secondary nonlinearities include all force terms that depend on cross-terms between motions, velocities and accelerations and/or cross-terms between different DOFs.

The general approach is that primary nonlinearities are linearized by assuming small velocity and displacement fluctuations around the equilibrium state of the system, while secondary nonlinearities are negated by approximating them as their mean values in the equilibrium state, assuming that fixation of such effects in the equilibrium state causes relatively small errors. The principle of the linearization method, therefore, strongly depends on the equilibrium state (equilibrium point), which stands for the average displacements, velocities and accelerations in all DOFs. In other words, in order to linearize the system, the "real" average displacement of the TLP must be estimated in advance for each sea state.

5.1.3 Prediction of System Equilibrium

The equilibrium point has the defining character that, when it serves as initial conditions, the system remains unchanged in the equilibrium point, provided that time-dependent force terms are not present. In other words, in the equilibrium state, all system's accelerations are zero and remain zero. Since the structure's displacements are limited through its mooring system, the mean velocities must be zero as well. The equilibrium point can, theoretically, be derived by substituting zeros for accelerations, velocities and external force terms in the EoMs, after which the system of equations can be solved for the remaining unknowns: the mean displacements.

However, analytical derivation of the equilibrium point is unsolvable due to the complexity of the EoMs. A more practical alternative, closely related to equilibrium condition, is the steady state condition, in which the static equilibrium has been reached but oscillations around the equilibrium may still occur. More specifically, an oscillating body is in its steady state when the mean accelerations and velocities are zero, with oscillations of displacements, velocities and acceleration around the mean deflection. Using this definition, the equilibrium point can be approximated numerically by determining the average displaced positions during steady state condition using a (short) simulation in the *nonlinear* model.

The equilibrium point is then found using Equation [5-1], in which the displacements are averaged over a number of wave periods to account for the expected dependency between motion periods and wave periods (i.e. longer waves require a longer duration for accurate approximation of the mean displacements). The steady state condition is then set to be reached when all mean accelerations have reached less than 1% of the maximum amplitude of the corresponding DOF (Equation [5-2]).

$$\underline{p}_0 = [\eta_{1,0} \quad \cdots \quad \eta_{6,0}]^T = \text{mean}([\eta_1 \quad \eta_2 \quad \eta_3 \quad \eta_4 \quad \eta_5 \quad \eta_6]^T)|_{t=t_{ss}\ldots t_{ss}+10T_p} \qquad [5\text{-}1]$$

$$\frac{\text{mean}(\eta_j)\big|_{t=0\ldots t_{ss}}}{\max(\eta_j) - \min(\eta_j)} \leq 0.01, \qquad j = 1 \ldots 6 \qquad [5\text{-}2]$$

where t_{ss} is the time at which steady state is reached and T_p is the spectral peak period.

5.2 Secondary Motion-Dependent Effects

5.2.1 Variable Submergence

A secondary motion-dependent phenomenon is the varying submerged volume due to the water piercing part of the central column, which was discussed in Section 3.2 and Section 3.5. By substituting the equilibrium point into Equation [3-29], the following expression is obtained:

$$\Delta V = A_{wp} \cdot \left(\xi\left(\eta_{1,0}, \eta_{2,0}, t\right) - \eta_{3,0}\right) \quad [5\text{-}3]$$

where $\eta_{1,0}$, $\eta_{2,0}$ and $\eta_{3,0}$ are the mean surge, sway and heave positions, respectively.

Since water level fluctuations are fixed, varying CoB and hydro- and aerodynamic drag areas of the segments in the vicinity of the MSL are fixed as well (Figure 3-18). As a result, the system variables η_1, η_2 and η_3 in Equations [B-37] and [B-39] (Appendix B) are replaced by $\eta_{1,0}$, $\eta_{2,0}$ and $\eta_{3,0}$, respectively. It should also be noted that, since the submerged value is a constant, the vertical buoyancy force (Equation [3-28]) and instantaneous distance from keel to the overall CoB (Equation [3-30]) are now constants as well. These and all other parameters discussed in this section must be constant in order to prevent nonlinear cross-terms, which is justified as long as the submerged volume and drag area do not deviate substantially from their mean values.

5.2.2 Wave Kinematics and Wind Shear

Both the wave kinematics (Equations [3-17] to [3-20]) and wind velocity (Equation [3-41]) depend on the instantaneous position of the structure w.r.t. the global coordinate frame, which induces nonlinear dependency on the system variables. To omit these effects, the equilibrium positions of all DOFs are substituted in the aforementioned equations. The assumption is that the influence of motions around the equilibrium state have negligible influence on motion dependent phase angles of the hydrodynamic forces and the height dependent wind velocity.

5.2.3 Motion Dependent Lever Arms

Recall that the rotational EoMs were based on moments around the CoG of the total structure in the translational coordinate frame, which were included in the force vectors defined in Section 3.5.3. Moments induced by hydrodynamic forces, mooring forces and turbine loads were defined in, respectively, Equations [3-55], [3-57] and [3-59]. These expressions depend on the distance from the total CoG to:

- CoBs of the submerged parts $\underline{p}_j$;
- Instantaneous position of the mooring line connectors $\underline{p}_{new,i}$;
- CoGs of the tower segments $\underline{p}_k$ and RNA $\underline{p}_{RNA}$.

Since these lever arms are taken w.r.t. translational coordinate frame, the distances depend on the rotational DOFs through multiplication of the rotation matrix $\boldsymbol{R}$ (see for example

Equation [3-31]). To prevent nonlinear cross-terms, the equilibrium positions are substituted in the rotation matrices ($\boldsymbol{R}|_{\underline{\eta}=\underline{p}_0}$) that are multiplied with the lever arms. By doing so, the lever arms are statically corrected to include the mean static orientations, which is justified if rotation amplitudes are small.

5.2.4 Instantaneous Orientations

As explained in Section 3.4 and 3.5, hydro- and aerodynamic drag areas are multiplied with $\boldsymbol{R}$ to account for the instantaneous orientation of the surfaces with respect to the flow direction and thrust forces and gyroscopic moments also depend on the orientation of the rotor plane. To prevent nonlinear cross-terms, the equilibrium positions are substituted in the rotation matrices of these forces. This approach implies that the loads are applied to a certain, statically orientated, portion of the body while the body's orientation w.r.t. the loads remains stationary throughout the simulation. This is justified if rotation amplitudes or the surfaces itself are small.

5.3 Nonlinear Rotations

5.3.1 Rotation Matrix

The rotation matrix $\boldsymbol{R}$, angular velocity matrix $\dot{\boldsymbol{R}}$ and angular acceleration matrix $\ddot{\boldsymbol{R}}$, all defined in Section 3.1.3, contain sinusoidal functions of the rotational DOFs and various cross-terms. To linearize these effects, it is assumed that rotations are small ($\leq 10°$), such that the following approximations hold:

$$\sin(\alpha) \approx \alpha \qquad [5\text{-}4]$$

$$\cos(\alpha) \approx 1 \qquad [5\text{-}5]$$

$$\alpha^2 \approx \dot{\alpha}^2 \approx \ddot{\alpha}^2 \approx \alpha \cdot \dot{\alpha} \approx \alpha \cdot \ddot{\alpha} \approx \dot{\alpha} \cdot \ddot{\alpha} \approx 0 \qquad [5\text{-}6]$$

in which α represents the amplitude of a rotational DOF.

By doing so, the linearized rotation matrix $\boldsymbol{R}^{(L)}$ can be formulated as in Equation [5-7] and the angular velocity and angular acceleration matrices are obtained by, respectively, the first and second order time differentiation of $\boldsymbol{R}^{(L)}$.

$$\boldsymbol{R}^{(L)} = \begin{bmatrix} 1 & -\eta_6 & \eta_5 \\ \eta_6 & 1 & -\eta_4 \\ -\eta_5 & \eta_4 & 1 \end{bmatrix} \qquad [5\text{-}7]$$

5.3.2 Hydrostatic Restoring Moments

In Section 3.2.5, the hydrostatic roll and pitch restoring moments were established according to Equations [3-26] and [3-27], respectively, for heeling angles up to $15°$. For rotation amplitudes smaller than $10°$, the previously mentioned simplifications can be applied to obtain the linearized roll and pitch restoring moments, as shown in Equations [5-8] and [5-9], respectively.

$$M_B^x = -\rho_w g(V_0 + \Delta V) \cdot \left(KB_{var} + \frac{I_t}{V_0 + \Delta V} - KG\right) \cdot \eta_4 \quad [5\text{-}8]$$

$$M_B^y = -\rho_w g(V_0 + \Delta V) \cdot \left(KB_{var} + \frac{I_t}{V_0 + \Delta V} - KG\right) \cdot \eta_5 \quad [5\text{-}9]$$

5.4 Mooring System

5.4.1 Identification of Nonlinearities

Formulation of mooring loads, derived in Section 3.3, Equation [3-35], are based on the instantaneous line lengths $L_{new,i}$ and the directional unit vector $\underline{\hat{L}}_i$, which are functions of the system variables through instantaneous position of the line connectors $\underline{P}_{new,i}$ (Equation [3-31]). The instantaneous line length $L_{new,i}$ is a nonlinear function, which means $\underline{\hat{L}}_i$ is also nonlinear and, therefore, the mooring loads are nonlinear as well. As a result, the mooring stiffness is displacement-dependent, meaning that the rate of change of restoring forces depend on the displaced position of the structure.

The nonlinear stiffness matrix $\boldsymbol{K}_{NL}$ and its elements, derived from the derivative of the mooring forces to the system variables, can be represented as in, respectively, Equations [5-10] and [5-11]. Nonlinearity of the stiffness matrix elements is demonstrated by plotting K_{ij} against η_j, which is presented in Figure J - 1, Appendix J.

$$\boldsymbol{K}_{NL}\left(\underline{\eta}\right) = \begin{bmatrix} K_{11} & 0 & 0 & K_{14} & K_{15} & 0 \\ 0 & K_{22} & 0 & K_{24} & 0 & 0 \\ K_{31} & K_{32} & K_{33} & K_{34} & K_{35} & K_{36} \\ 0 & K_{42} & 0 & K_{44} & 0 & 0 \\ K_{51} & 0 & 0 & K_{54} & K_{55} & 0 \\ 0 & K_{62} & 0 & K_{64} & 0 & K_{66} \end{bmatrix} \quad [5\text{-}10]$$

$$K_{ij} = \frac{\partial f_{moor,i}}{\partial \eta_j} \quad [5\text{-}11]$$

where $f_{moor,i}$ is the i^{th} element of the mooring force vector (defined in Equation [3-57]).

5.4.2 Linearization

The small perturbation method was used for the linearization of the mooring system, which is based on small fluctuations of the system variables around the equilibrium state (or operating point), as depicted in Figure 5-1. The basis of this approach is the first order Taylor series expansion, which is used to linearize the mooring forces around the equilibrium points.

The first order approximation of the mooring force vector $\underline{f}_{moor}^{(L)}$ is then established using Equation [5-12].

$$\underline{f}_{moor}^{(L)} = \underline{f}_{moor}\Big|_{\underline{\eta} = \underline{p}_0} + \sum_{j=1}^{6} \frac{\partial \underline{f}_{moor}}{\partial \eta_j}\Big|_{\underline{\eta} = \underline{p}_0} \cdot (\eta_j - \eta_{j,0}) \quad [5\text{-}12]$$

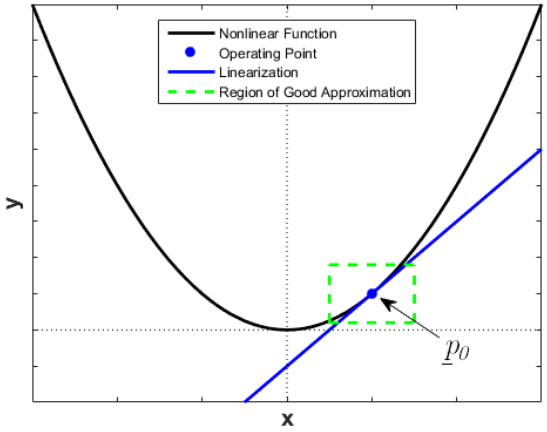

Figure 5-1: Applicability Small Perturbation Method

In order to find the elements of the linearized stiffness matrix, the differentiation in Equation [5-11] is applied to $\underline{f}_{moor}^{(L)}$, which results in the linear stiffness matrix as a function of $\underline{p}_0$. Results of this linearization procedure are demonstrated in Appendix J.2 and, as an example, the linearized stiffness matrix at zero equilibrium position is presented in Equation [5-13].

$$\boldsymbol{K}_L\left(\underline{p}_0 = \begin{bmatrix}0\\ \vdots \\ 0\end{bmatrix}\right) = \begin{bmatrix} 8.3\cdot10^5 & 0 & 0 & 0 & 2.5\cdot10^8 & 0 \\ 0 & 8.3\cdot10^5 & 0 & 2.5\cdot10^8 & 0 & 0 \\ 0 & 0 & 9.4\cdot10^7 & 0 & 0 & 0 \\ 0 & 2.5\cdot10^8 & 0 & 1.0\cdot10^{11} & 0 & 0 \\ 2.5\cdot10^8 & 0 & 0 & 0 & 1.0\cdot10^{11} & 0 \\ 0 & 0 & 0 & 0 & 0 & 4.8\cdot10^8 \end{bmatrix} \quad [5\text{-}13]$$

5.5 Quadratic Velocity Terms

5.5.1 Introduction

Quadratic velocity dependency applies to viscous friction forces, such as hydro- and aerodynamic drag, as well as rotor thrust forces. Hydrodynamic drag forces are part of the Morison equation, as discussed in Section 3.2, Equation [3-23]. Aerodynamic friction forces are exerted to the tower and RNA (in parked condition), as was formulated in Section 3.4, Equations [3-42] and [3-45], respectively. Finally, the rotor thrust forces were defined in Equation [3-48]. Symbols and terms that are unspecified in this paragraph can be revised in the paragraphs mentioned above.

For all of the abovementioned forces, only the components that depend on the structural (response) velocities need to be linearized, as the water/wind velocities generate external forces that do not depend on the system variables. To be able to linearize only the structural velocities, the force that depends on the relative velocity squared is approximated as the summation of the external force and quadratic damping term [80]. This approach is illustrated in Figure 5-2 and formulated in Equation [5-44]. The basis of this approximation is that cross terms between the wind/water velocity and structural velocities are negligible, which is only valid for small structural velocities w.r.t. wind/wave velocities.

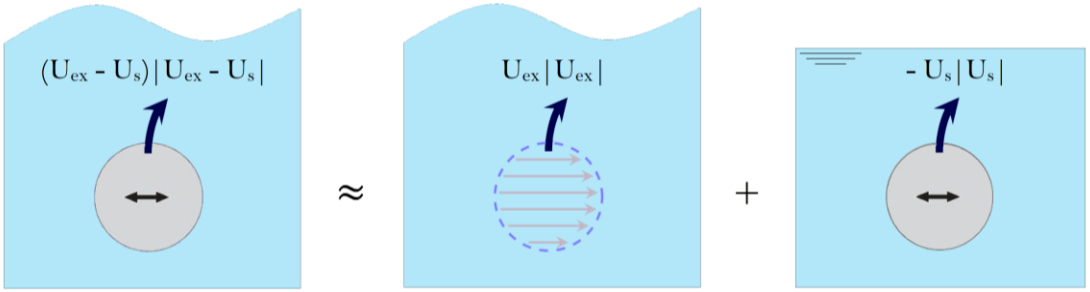

Figure 5-2: Approximation of Total Quadratic Velocity as Separate Quadratic Components

$$(\underline{U}_{ex} - \underline{U}_s) \circ |\underline{U}_{ex} - \underline{U}_s| \approx \underline{U}_{ex} \circ |\underline{U}_{ex}| - \underline{U}_s \circ |\underline{U}_s| \quad [5\text{-}14]$$

where $\underline{U}_{ex}$ is the total (mean and fluctuating) wind or water particle velocity and $\underline{U}_s$ is the structural velocity.

In order to approximate the quadratic structural velocities, three different methodologies have been applied, each discussed in the following sections. These linearization techniques are:

- The first-order Taylor series expansion;
- The Lorentz method;
- Stochastic linearization.

5.5.2 Taylor Series Linearization

Under the assumption that the structural velocity variations are small around the operating point, the Taylor series expansion can be applied to linearize the hydro- and aerodynamic drag and thrust forces. The linearized expressions of the hydrodynamic drag, aerodynamic tower drag, aerodynamic RNA drag and rotor thrust forces are depicted in, respectively, Equations [5-15] to [5-18]. One should also recall that, in the equilibrium state, it is assumed that all structural velocities are zero ($\underline{\dot{\eta}}_0 = [0 \quad \cdots \quad 0]^T$).

$$\underline{F}_{d,hyd}^{(L)} = \underline{F}_{d,hyd}\big|_{\underline{\eta}=\underline{p}_0} + \sum_{j=1}^{6} \left.\frac{\partial \underline{F}_{d,hyd}}{\partial \eta_j}\right|_{\underline{\eta}=\underline{p}_0} \cdot (\eta_j - \eta_{j,0}) + \sum_{j=1}^{6} \left.\frac{\partial \underline{F}_{d,hyd}}{\partial \dot{\eta}_j}\right|_{\underline{\eta}=\underline{p}_0} \cdot \dot{\eta}_j \quad [5\text{-}15]$$

$$\underline{F}_{aero}^{(L)} = \underline{F}_{aero}\big|_{\underline{\eta}=\underline{p}_0} + \sum_{j=1}^{6} \left.\frac{\partial \underline{F}_{aero}}{\partial \eta_j}\right|_{\underline{\eta}=\underline{p}_0} \cdot (\eta_j - \eta_{j,0}) + \sum_{j=1}^{6} \left.\frac{\partial \underline{F}_{aero}}{\partial \dot{\eta}_j}\right|_{\underline{\eta}=\underline{p}_0} \cdot \dot{\eta}_j \quad [5\text{-}16]$$

$$\underline{F}_{RNA,ex}^{(L)} = \underline{F}_{RNA,ex}\big|_{\underline{\eta}=\underline{p}_0} + \sum_{j=1}^{6} \left.\frac{\partial \underline{F}_{RNA,ex}}{\partial \eta_j}\right|_{\underline{\eta}=\underline{p}_0} \cdot (\eta_j - \eta_{j,0}) + \sum_{j=1}^{6} \left.\frac{\partial \underline{F}_{RNA,ex}}{\partial \dot{\eta}_j}\right|_{\underline{\eta}=\underline{p}_0} \cdot \dot{\eta}_j \quad [5\text{-}17]$$

$$F_T^{(L)} = F_T\big|_{\underline{\eta}=\underline{p}_0} + \sum_{j=1}^{6} \left.\frac{\partial F_T}{\partial \eta_j}\right|_{\underline{\eta}=\underline{p}_0} \cdot (\eta_j - \eta_{j,0}) + \sum_{j=1}^{6} \left.\frac{\partial F_T}{\partial \dot{\eta}_j}\right|_{\underline{\eta}=\underline{p}_0} \cdot \dot{\eta}_j \quad [5\text{-}18]$$

5.5.3 Lorentz Linearization

Lorentz linearization was originally developed for linearization of quadratic bottom friction due to one-dimensional tidal waves in shallow water [81], and was later successfully validated using experimental testing [82]. The basis of this approach is the assumption that the average energy dissipation over one (tidal) wave period is equal for the linearized and actual friction force, as formulated in Equation [5-19]. The solution to this equation yields an expression for an equivalent drag constant, which is shown in Equation [5-20].

$$\int_0^T F_d \cdot u \, dt = \int_0^T F_d^{(L)} \cdot u \, dt \qquad [5\text{-}19]$$

$$C_d^{(L)} = \frac{8u_a}{3\pi} C_d \qquad [5\text{-}20]$$

where:

- $F_d = \frac{1}{2}\rho C_d A \cdot u|u|$ is the nonlinear drag force as a function of the fluid density ρ, drag coefficient C_d and incident drag area A;
- $F_d^{(L)} = \frac{1}{2}\rho C_d^{(L)} A \cdot u$ is the linearized drag force;
- $u = u_a \sin(\omega t)$ is the harmonic velocity distribution with amplitude u_a.

Adjustments

The Lorentz method is valid for any type of loading that is quadratically dependent on a velocity term, which means it can also be used for quadratic damping. However, to apply the method, the structural velocities must agree with the assumptions on which the method is based, namely:

1. Zero mean velocity;
2. One-dimensional spatial distribution of the velocity;
3. Harmonic velocity fluctuations.

The first limitation is consistent with the assumptions that were used to obtain the equilibrium point, being zero mean velocities and accelerations. The second limitation is avoided by determining separate equivalent drag/thrust constants at the equilibrium positions of the RNA and {pontoon, tower} segments. Furthermore, a distinction is made between horizontal and vertical velocities, meaning that the equivalent drag constants also depend on the structural velocity direction.

The third condition is not met since the structural velocities are most likely non-harmonic. It is, therefore, not possible to define time-invariant amplitudes of the structural velocities in advance, which is required according to the conventional Lorentz method (see Equation [5-20]). To avoid this limitation, equivalent structural velocity amplitudes are predicted based on the velocity amplitudes of the frequency-dependent harmonic components of the wind/wave spectrum. More specifically, it is assumed that the average structural velocity amplitude is

proportional to the average velocity amplitude of the wind/wave input during the respective sea state, as formulated in Equation [5-21].

$$\underline{U}_s \circ \left|\underline{U}_s\right| \approx \underline{U}_s \circ \sum_{i=1}^{N_w} \frac{8}{3\pi} \cdot \frac{\underline{u}_{a,i}}{N_w} \qquad [5\text{-}21]$$

where $\underline{u}_{a,i}$ is the harmonic wind/wave velocity component corresponding to frequency i and N_w is the number of generated wind/wave components within the spectrum.

Application to Hydrodynamic Drag

The linearized drag component of the hydrodynamic force that is acting on submerged segment j is presented in Equation [5-22]. See Equation [3-54] for the nonlinear expression and for the definition of the parameters, it is referred to Section 3.2.2.

$$\underline{F}_{d,hyd,j}^{(L)} = \frac{\rho_w}{2} \cdot \underline{C}_{D,j} \circ \left[\boldsymbol{R}\right|_{\underline{\eta}=\underline{p}_0} \cdot \underline{A}_j\Big] \circ \left(\underline{U}_j \circ \left|\underline{U}_j\right| - \dot{\underline{P}}_j \circ \sum_{i=1}^{N_{waves}} \frac{8}{3\pi} \cdot \frac{\underline{u}_i}{N_{waves}} \right) \qquad [5\text{-}22]$$

in which $\underline{U}$ is the water particle velocity (defined in Equation [3-24]), $\dot{\underline{P}}_j$ is the structural velocity at segment j and $\underline{u}_i$ is the harmonic velocity amplitude corresponding to frequency i, determined using Equation [5-23].

$$\underline{u}_i = \begin{bmatrix} \omega_i a_i \cdot \dfrac{\cosh\left(k_i \cdot \left(d + z_{hyd,j}\right)\right)}{\sinh(k_i d)} \\ \omega_i a_i \cdot \dfrac{\cosh\left(k_i \cdot \left(d + z_{hyd,j}\right)\right)}{\sinh(k_i d)} \\ \omega_i a_i \cdot \dfrac{\sinh\left(k_i \cdot \left(d + z_{hyd,j}\right)\right)}{\sinh(k_i d)} \end{bmatrix} \qquad [5\text{-}23]$$

Application to Aerodynamic Forces

The linearized aerodynamic drag force acting on tower segment k, the aerodynamic RNA drag and rotor thrust forces are formulated in Equations [5-24], [5-25] and [5-26], respectively. For the nonlinear expressions and definition of the parameters, it is referred to Sections 3.4.3, 3.4.4 and 3.5.3.

$$\underline{F}_{aero}^{(L)} = \frac{1}{2}\rho_a \cdot \underline{C}_{D,k} \circ \left[\boldsymbol{R}\right|_{\eta=p_0} \cdot \underline{A}_k\Big] \circ \left(\underline{U}_{w,k} \circ \left|\underline{U}_{w,k}\right| - \dot{\underline{P}}_k \cdot \sum_{j=1}^{N_{turb}} \frac{8}{3\pi} \cdot \frac{u_{turb,j}}{N_{turb}} \right) \qquad [5\text{-}24]$$

$$\underline{F}_{RNA,ex}^{(L)} = \frac{1}{2}\rho_a \cdot C_{D,RNA} \circ \underline{A}_{RNA,ex}\Big|_{\eta=p_0} \circ \left(\underline{U}_{w,RNA} \circ \left|\underline{U}_{w,RNA}\right| - \dot{\underline{P}}_{RNA} \cdot \sum_{j=1}^{N_{turb}} \frac{8}{3\pi} \cdot \frac{u_{turb,j}}{N_{turb}} \right) \qquad [5\text{-}25]$$

$$F_T^{(L)} = \frac{1}{2}\rho_a \cdot C_T \cdot A_{RNA,op}^X \cdot \left(U_{w,RNA}^X \cdot \left|U_{w,RNA}^X\right| - \dot{P}_{RNA}^X \cdot \sum_{j=1}^{N_{turb}} \frac{8}{3\pi} \cdot \frac{u_{turb,j}}{N_{turb}} \right) \quad [5\text{-}26]$$

where $\underline{A}_{RNA,ex}\big|_{\eta=p_0}$ are the statically rotated rotor plane areas in parked conditions, calculated with:

$$\underline{A}_{RNA,ex}\big|_{\eta=p_0} = \boldsymbol{R}|_{\eta=p_0} \cdot \begin{bmatrix} A_{RNA,ex}^X & 0 & 0 \end{bmatrix}^T \quad [5\text{-}27]$$

5.5.4 Stochastic Linearization

For fatigue damage, the most influential property of the loading are its fluctuations around the mean. In that sense, linearization can also be based on finding the smallest difference between the standard deviation of the linearized force w.r.t. that of the actual force. This is the basis of the stochastic linearization method, which assumes that the quadratic velocity can be approximated as the multiplication of the velocity with a constant that is proportional to the standard deviation of the quadratic velocity [83]. The quadratic velocity can therefore be approached as in Equation [5-28].

$$|U| \cdot U \approx \alpha \cdot \mathrm{std}(U) \cdot U \quad [5\text{-}28]$$

where α is an iteratively determined constant and $\mathrm{std}(U)$ is the standard deviation of the velocity U, defined as:

$$\mathrm{std}(U) = \sqrt{\frac{1}{t_{sim}/\Delta t - 1} \sum_{i=1}^{t_{sim}/\Delta t} \left(U|_{t=t_i} - \mathrm{mean}(U) \right)^2} \quad [5\text{-}29]$$

The non-dimensional constant α is iteratively determined such that the approximation error is minimal [40]. Its initial value is commonly based on the statistical expectation value of the squared error between the actual and linearized velocity term, under the assumption that the velocity is a zero-mean Gaussian process. The minimum expected squared error is then analytically solved to determine the initial value of α (see for full derivation [83]):

$$\alpha_0 = \sqrt{8/\pi} \quad [5\text{-}30]$$

Adjustments

Similar to the Lorentz method, stochastic linearization is only valid for quadratic velocities with one-dimensional (independency of) spatial distribution. This limitation is, again, avoided by considering separate vectoral velocities at each section of the TLP and turbine. As was demonstrated in Equation [5-44], in order to linearize the structural velocities, the water/wind velocities and structural velocities need to be considered separately.

Linearization is then performed by assuming that the actual structural velocities are Gaussian distributed with known standard deviations, which are predicted in each direction and at each point in the structure using the short simulation that is also used for prediction of the equilibrium position. By doing so, the nonlinear velocity term can be approximated as follows:

$$\underline{U}_{s,NL} \circ \left|\underline{U}_{s,NL}\right| \approx \alpha \cdot \mathrm{std}\left(\underline{U}_{s,NL}\right) \circ \underline{U}_{s,L} \quad [5\text{-}31]$$

where $\underline{U}_{s,NL}$ and $\underline{U}_{s,L}$ are the structural velocity vectors according to the nonlinear and linear model, respectively.

Once the structural velocity is obtained from the nonlinear model, the subsequent step is to solve the linearized model using the initial value of α (α_0). Subsequently, using the obtained structural velocity of the linear model, the value of α can be updated based on the minimum RMSE between the quadratic and linearized structural velocity, as formulated in Equation [5-32].

$$\frac{\partial}{\partial \alpha}\mathrm{RMS}\left(\underline{U}_{s,NL} \circ \left|\underline{U}_{s,NL}\right| - \alpha \cdot \mathrm{std}\left(\underline{U}_{s,NL}\right) \circ \underline{U}_{s,L}\right) = 0 \quad [5\text{-}32]$$

The above described iterative process requires the linear model to be solved multiple times and the value of α to be determined for each point in the structure and in each direction. This operation would undermine the time-efficient character of the linearized method. It is, therefore, decided to only use α_0 in this thesis.

Application to Hydrodynamic Drag

The linearized drag force that is acting on submerged segment j is presented in Equation [5-33].

$$\underline{F}_{d,hyd,j}^{(L)} = \frac{\rho_w}{2} \cdot \underline{C}_{D,j} \circ \left[\boldsymbol{R}|_{\underline{\eta}=\underline{p}_0} \cdot \underline{A}_j\right] \circ \left(\underline{U}_j \circ \left|\underline{U}_j\right| - \alpha_0 \cdot \mathrm{std}\left(\underline{\dot{P}}_j\right) \circ \underline{\dot{P}}_j\right) \quad [5\text{-}33]$$

Application to Aerodynamic Forces

The linearized expressions of the aerodynamic tower drag, aerodynamic RNA drag and rotor thrust forces are depicted in, respectively, Equations [5-34] to [5-36].

$$\underline{F}_{aero}^{(L)} = \frac{1}{2}\rho_a \cdot \underline{C}_{D,k} \circ \left[\boldsymbol{R}|_{\eta=p_0} \cdot \underline{A}_k\right] \circ \left(\underline{U}_{w,k} \circ \left|\underline{U}_{w,k}\right| - \alpha_0 \cdot \mathrm{std}\left(\underline{\dot{P}}_k\right) \circ \underline{\dot{P}}_k\right) \quad [5\text{-}34]$$

$$\underline{F}_{RNA,ex}^{(L)} = \frac{1}{2}\rho_a \cdot C_{D,RNA} \circ \left[\boldsymbol{R}|_{\eta=p_0} \cdot \begin{bmatrix} A_{RNA,ex}^X & 0 & 0 \end{bmatrix}^T\right] \circ \left(\underline{U}_{w,RNA} \circ \left|\underline{U}_{w,RNA}\right| - \alpha_0 \cdot \mathrm{std}\left(\underline{\dot{P}}_{RNA}\right) \circ \underline{\dot{P}}_{RNA}\right) \quad [5\text{-}35]$$

$$F_T^{(L)} = \frac{1}{2}\rho_a \cdot C_T \cdot A_{RNA,op}^X \cdot \left(U_{w,RNA}^X \cdot \left|U_{w,RNA}^X\right| - \alpha_0 \cdot \mathrm{std}\left(\dot{P}_{RNA}^X\right) \cdot \dot{P}_{RNA}^X\right) \quad [5\text{-}36]$$

5.6 Selection of an Appropriate Linearization Method

5.6.1 Methodology

In the previous paragraphs, linearization of all nonlinear effects was discussed and three different methods were proposed with which the quadratic damping could be linearly approximated. With this, three different linearized models have been developed, in which the quadratic velocity terms are linearized based on the Taylor, Lorentz and stochastic linearization, each taking into account all other linearized effects (rotations, mooring system and secondary nonlinearities).

In this section, the performance of each linearized model is evaluated and compared based on differences w.r.t. the nonlinear model. On this basis, the best performing model is chosen with which, in the following paragraph, the influence of linearization on the long-term damage will be determined. The performance of the models are investigated on the basis of a 900s simulation of a sea-state that is representative for normal operational conditions, consisting of irregular waves combined with misaligned currents and stochastic wind velocities (Table 5-1). Stress and damage differences w.r.t. the nonlinear model are quantified based on the following criteria:

- The absolute difference in cubic weighted mean (CWM) stress range, averaged over all hotspots (Equation [5-37]);
- The absolute difference in damage, averaged over all hotspots (Equation [5-38]);
- The ratio of the nonlinear to linear model- based damage (D_{NL}/D_L), averaged over all hotspots.

$$\varepsilon_{CWM} = \text{mean}\left(\left|1 - \frac{\text{mean}\left(S_{NL,i}^3\right)}{\text{mean}\left(S_{L,i}^3\right)}\right|\right), \qquad i = \begin{matrix}P_1 \dots P_6 \\ T_1 \dots T_6\end{matrix} \tag{5-37}$$

$$\varepsilon_D = \text{mean}\left(\left|1 - \frac{D_{NL,i}}{D_{L,i}}\right|\right), \qquad i = \begin{matrix}P_1 \dots P_6 \\ T_1 \dots T_6\end{matrix} \tag{5-38}$$

where subscripts NL and L denote the nonlinear and linear simulation result, respectively.

Table 5-1: Conditions Used for Selection of Linearization Method

Parameter	Symbol	Value
Wave height	H_s	5.75m
Wave period	T_p	13.5s
Wave direction w.r.t. X-axis	μ_{wave}	45°
Current velocity at Water Plane	$U_{cur,wp}$	0.45ms^{-1}
Current velocity at Seabed	$U_{cur,sb}$	0ms^{-1}
Current direction w.r.t. X-axis	μ_{cur}	180°
Average Wind Speed (80m+MSL)	$u_{w,a}$	10.5ms^{-1}
Wind direction w.r.t. X-axis	μ_{wind}	0°

5.6.2 Results and Conclusions

The results are presented in Table 5-2 and visual comparisons of the linearized responses are depicted in Appendix J.3. Based on the results, it can be concluded that both in terms of absolute differences (ε_D), as well as in terms of conservativeness in damage prediction (D_{NL}/D_L), the stochastic linearization is the best performing method with regard to damage approximation. Therefore, the stochastic linearization method will be adopted hereafter.

Table 5-2: Difference w.r.t. Results in Nonlinear Model

		Taylor	Lorentz	Stochastic
ε_{CWM} [-]	**Pontoons**	0.67	0.70	0.39
	Mid-Section	1.28	0.49	0.78
ε_D [-]	**Pontoons**	0.79	0.74	0.52
	Mid-Section	4.09	0.89	0.86
D_{NL}/D_L [-]	**Pontoons**	0.72	0.67	0.48
	Mid-Section	4.89	1.42	0.14

5.6.3 Discussion

The linear to nonlinear model-based damage differences in the mid-section hotspots are relatively large compared to damage differences in the pontoon hotspots, indicating that the stress response at the mid-section is more sensitive to nonlinear aerodynamic damping compared to the sensitivity of the stress response in the pontoon hotspots to hydrodynamic damping. This is because the turbine loads and corresponding mid-section stresses are influenced to a greater extent by structural velocities than the stresses in the pontoon cross-sections, which are primarily influenced by mooring forces.

Due to poorly approximated stresses in the mid-section, the Taylor linearization has proven to be unsatisfactory. This shows that Taylor expansion of the nonlinear aerodynamic damping around zero structural velocity (in all DOFs) results in an underestimation of the damping. It has also become evident that the Lorentz method is unsuitable for fatigue damage approximations in an environment with stochastic wind velocities. This demonstrates that the accuracy of the equivalent structural velocity amplitude (the $\underline{u}_{a,i}$-term in Equation [5-21]), which was predicted based on the average wind velocity amplitude, has a major effect on the stress response.

Since the stochastic linearization is solely based on reproducing the velocity fluctuations, the approximated stress variations and fatigue damage are relatively accurate (small ε_{CWM} and ε_D-values). Unlike the other methods, stochastic linearization tends to underestimate the linear damping, which results in overestimation of stress ranges and subsequent damage response. Therefore, from a conservative design point of view, the stochastic method performs more favourable.

5.7 Influence of Nonlinearities on Long-Term Damage

5.7.1 Introduction

In this section, the influence of nonlinearities on the long-term fatigue damage is established by comparison of the long-term damage according to the nonlinear model to the long-term damage according to the linear model. The linear model is based on the stochastic linearization method for linearization of quadratic damping. According to DNV standards, an important limitation of the fatigue damage calculation method, as explained in Section 3.7.4, is that the *F*-class SN-curve is only applicable to principal stresses with angles up to 30° w.r.t. the normal line of the weld seam. In other words, when multiaxiality exceeds a certain limit, the applied SN-curve is no longer valid. Therefore, the presence of multiaxiality and its influence on the validity of the damage calculation method are analysed as well.

5.7.2 Methodology

In both the linear and nonlinear model, the long-term fatigue damage D_{tot} is represented by the weighted average of damage per sea state D_i and extrapolated from the simulation duration per sea state T_{sim} to the operational lifetime T_{life}. This is formulated in Equation [5-39]. The long-term fatigue damage analysis is based on 12 different sea states, selected in such a way that the fatigue governing conditions are captured as accurately as possible. The underlying methodological approach of selecting the sea states is presented in Appendix J.4 and the resulting sea states are depicted in Table 5-3.

$$D_{tot} = \frac{T_{life}}{T_{sim}} \cdot \sum_{i=1}^{N_{ss}} D_i \cdot \frac{n_{ss,i}}{\sum_{i=1}^{N_{ss}} n_{ss,i}} \qquad [5\text{-}39]$$

where $n_{ss,i}$ the number of occurrences of sea state i and N_{ss} is the number of sea states.

To assess the influence of multiaxiality, the principal stress directions in the pontoons and mid-section hotspots are calculated using, respectively, Equations [5-40] and [5-41] based on the nonlinear model. For definitions of the stress components, it referred to Paragraph 3.7.

$$\theta_p = \frac{1}{2}\tan^{-1}\left(\frac{2\tau_{xy,p}}{\sigma_{xx,p} - \sigma_{yy,p}}\right), \qquad p = P_1 \dots P_6 \qquad [5\text{-}40]$$

$$\theta_t = \frac{1}{2}\tan^{-1}\left(\frac{2\tau_{zy,t}}{\sigma_{zz,t} - \sigma_{yy,t}}\right), \qquad t = T_1 \dots T_6 \qquad [5\text{-}41]$$

Due to randomness in the stress response, it is possible that even during relatively mild sea states, the principal stress angles incidentally exceed 30°. The maximum principal stress direction during a time series is, therefore, not a representative upper/design value to base the applicability of the SN-curve. It is considered more appropriate to represent the design value as the 99th percentile (θ_{99}) during a time series, which denotes a value that is greater than 99% of the data.

Table 5-3: Sea States for Long Term Motion and Fatigue Analysis

Sea State Number	H_s	T_p	μ_{wave}	$u_{w,a}$	μ_{wind}	$U_{cur,wl}$	μ_{cur}	$n_{ss,i}$
1	0.75m	4.5s	0°	15.5ms^{-1}	0°	1.28ms^{-1}	180°	452
2	1.25m	5.5s	90°	15.5ms^{-1}	0°	1.28ms^{-1}	180°	546
3	1.75m	7.5s	90°	15.5ms^{-1}	0°	1.28ms^{-1}	180°	697
4	1.75m	6.5s	90°	15.5ms^{-1}	0°	1.28ms^{-1}	180°	339
5	2.75m	8.5s	45°	10.5ms^{-1}	0°	0.45ms^{-1}	180°	283
6	3.25m	9.5s	45°	10.5ms^{-1}	0°	0.45ms^{-1}	180°	296
7	3.75m	10.5s	45°	10.5ms^{-1}	0°	0.45ms^{-1}	180°	452
8	4.75m	11.5s	45°	10.5ms^{-1}	0°	0.45ms^{-1}	180°	269
9	5.25m	12.5s	45°	10.5ms^{-1}	0°	0.45ms^{-1}	180°	218
10	5.75m	13.5s	45°	10.5ms^{-1}	0°	0ms^{-1}	0°	168
11	7.75m	14.5s	45°	10.5ms^{-1}	0°	0ms^{-1}	0°	26
12	8.75m	15.5s	45°	25.5ms^{-1}	0°	0ms^{-1}	0°	10

5.7.3 Results and Conclusions

The long-term damage ratio at each hotspot, defined as the ratio of linear model-based long-term damage to nonlinear model based long-term damage ($D_{tot,L}/D_{tot,NL}$), including the 99th percentile of the principal stress directions are depicted in Table 5-4. A visual comparison of the damage response per sea state is represented in the form of histograms, as shown in Figure 5-3 and Figure 5-4 for, respectively, the pontoon and mid-section hotspots. For numerical values of stress and fatigue damage differences per sea state, the time history of the nonlinear and linear model results and the principal stress directions, it is referred to Appendix J.

The most important observations and main conclusions that can be drawn from the results of the long-term damage analysis are summarized in 4 key points, namely:

1. Non-Conservative Damage Approximation

In general, during sea states where multi-axial loading is prominent, the linear model underestimates the damage in the pontoon hotspots (see Figure 5-3). As a result, the long-term damage at hotspot P_4 is underestimated with 19% the w.r.t the nonlinear model. This observation suggests that multiaxiality has a negative influence on the accuracy of the linearization. However, the damage in hotspot P_3 during sea states 5 and 6 are also underestimated despite the fact that the load is virtually uniaxial. Further investigation is conducted in Paragraph 5.8.

2. Large Differences During Extreme Conditions

Damage differences are amplified during sea states 11 and 12, which is inevitable as extreme sea states induce large motion amplitudes and these in turn cause relatively large

errors in mooring forces. Depending on the equilibrium point, the linearized mooring stiffness can then overestimate or underestimate forces (see for example Figure J - 2). In addition, due to increased structural velocities, differences between quadratic and linear damping will also increase. Nevertheless, errors during extreme conditions have little influence on the long-term damage differences, since such sea states are rare.

3. Overestimation of Turbine Loads

The linear model-based damage is in each of the mid-section hotspots (T_1 to T_6) and during all sea states conservative w.r.t. the damage according to the nonlinear model. Overestimation of the damage by the linear model is due to underestimation of the linearized aerodynamic damping, as was explained in Section 5.6.3.

4. Large Principal Stress Directions

During certain sea states, the principal stress directions exceed 30° in hotspots P_4, T_1, T_2 and T_6, meaning that the F-class SN-curve is not applicable to these cases. Possible implications for the reliability of the linearization method have been investigated in Paragraph 5.8.

Table 5-4: Long-Term Damage Ratios and Principle Stress Directions Per Sea State

	Pontoon Hotspots						Mid-Section Hotspots					
	P_1	**P_2**	**P_3**	**P_4**	**P_5**	**P_6**	**T_1**	**T_2**	**T_3**	**T_4**	**T_5**	**T_6**
$D_{tot,L}/D_{tot,NL}$	2.82	1.81	1.10	0.81	2.63	1.05	2.01	1.97	1.92	2.31	2.72	1.81
Sea State	**Design Values of Principle Stress Direction θ_{99} [°]**											
1	1.1	0.2	0.0	8.1	0.7	1.1	1.2	0.3	0.0	0.2	0.0	43.6
2	1.1	0.2	0.5	8.1	0.7	1.0	1.2	0.5	0.8	0.3	0.0	43.6
3	1.6	0.3	0.7	8.3	0.3	0.9	1.3	0.6	1.2	0.9	0.1	43.5
4	1.4	0.2	0.7	8.2	0.5	1.0	1.3	0.7	1.2	0.8	0.1	43.6
5	1.6	0.9	6.9	27.3	1.0	0.2	2.4	0.8	0.6	0.8	1.0	43.5
6	1.6	0.9	8.7	30.7	1.6	0.5	2.4	0.9	0.7	0.8	0.9	43.3
7	1.7	0.9	11.2	33.7	2.1	0.8	2.4	0.8	0.7	0.7	0.9	43.1
8	2.2	1.2	15.1	35.5	2.4	1.1	2.5	0.9	0.8	0.6	0.7	43.0
9	2.6	1.6	15.5	34.3	2.5	1.2	2.6	0.9	0.8	0.5	0.7	42.9
10	3.0	1.7	17.7	34.9	2.8	1.3	2.9	0.9	0.9	0.4	0.6	42.8
11	3.6	2.8	24.1	36.1	3.2	1.7	3.6	1.2	1.3	2.1	0.4	42.5
12	5.6	2.7	5.5	3.9	4.8	3.6	32.3	34.2	16.8	11.9	12.8	18.7

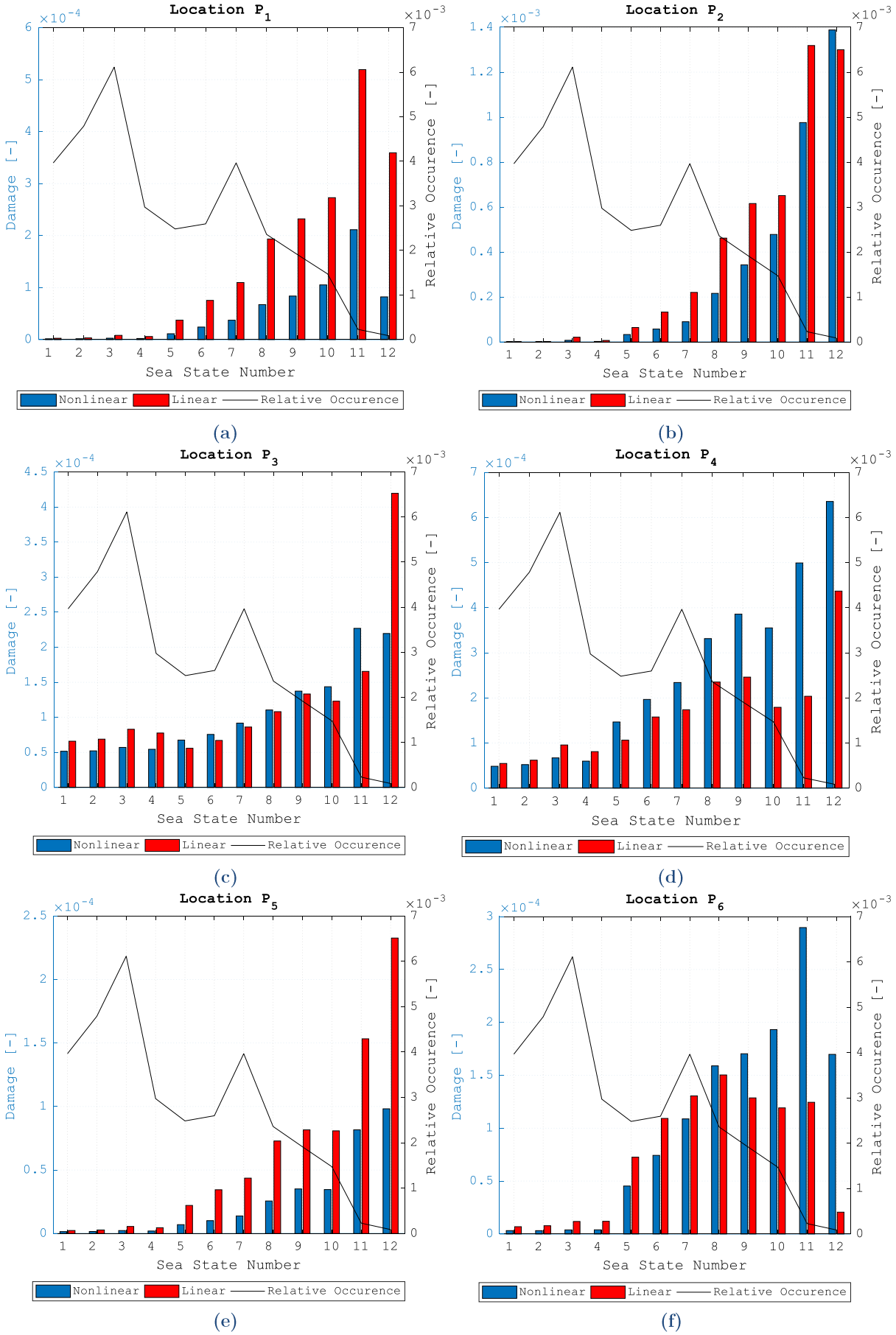

Figure 5-3: Damage Per Sea State at the Pontoon Hotspots

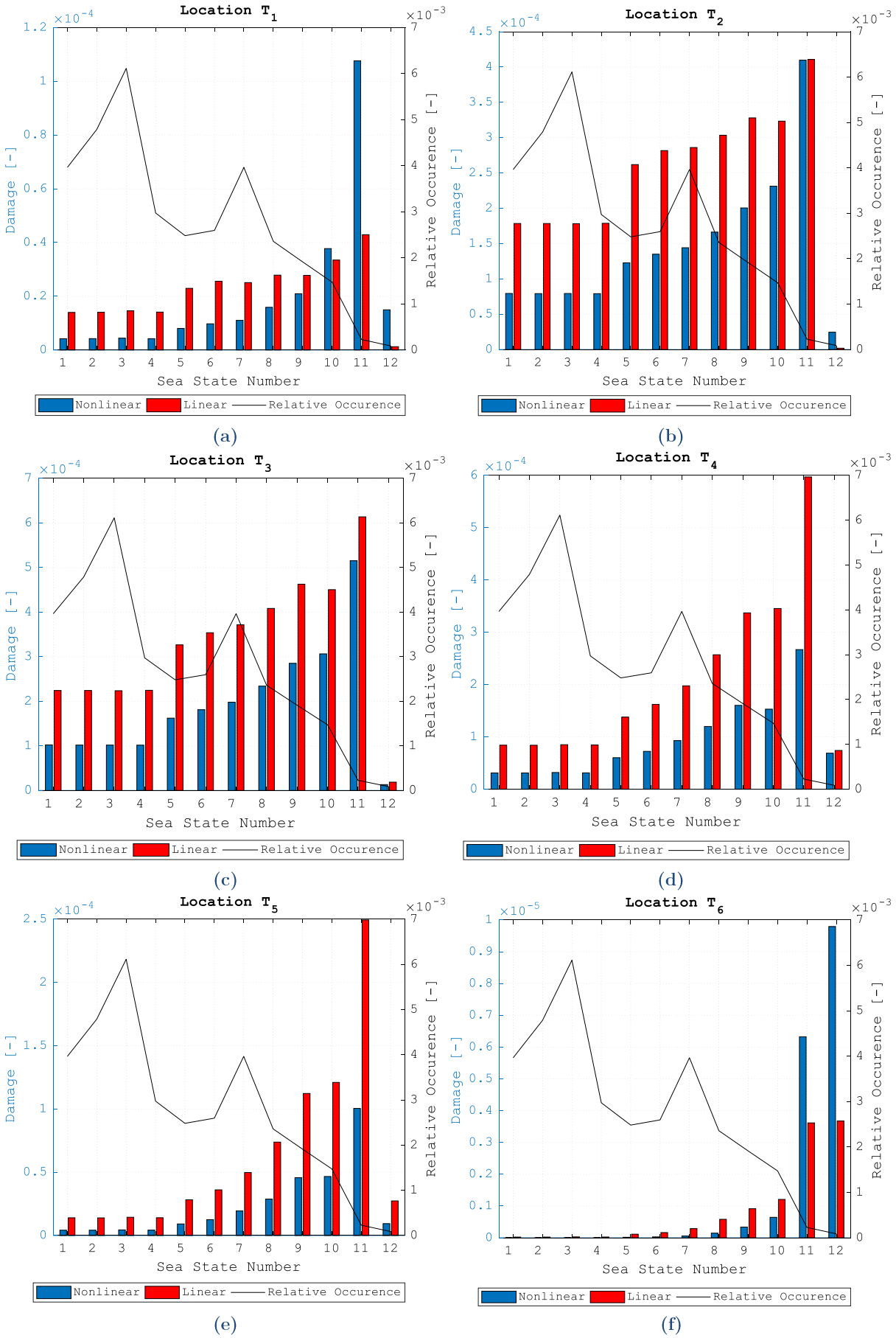

Figure 5-4: Damage Per Sea State at the Mid-Section Hotspots

5.8 Discussion

5.8.1 Validity of Linearization Approach

Before the results and observations from the previous chapter are discussed, the general validity of the linearization process is examined by (i) numerically reaffirming the linearity of the linearized system, (ii) evaluating the physical correctness of the numerically determined equilibrium point and (iii) investigating the influence of principal stress directions greater than 30° on the performance of the linear model.

i. Linearity of the System

Linearity of the system is demonstrated by solving the response of the linearized model to a sinusoidal point load. The results (see Appendix J.8) demonstrated that the steady state response can be described by a sinusoidal function with nearly zero phase shift w.r.t. the applied force, proving that the system is linear. It should be noted, however, that the ratio of external force amplitude to response amplitude can only be constant at all time instants (i.e. exactly zero phase differences at all times) if the stiffness matrix is diagonal. This is not the case since there are linear couplings between the DOFs, which must be decoupled by means of modal analysis. Due to time constraints, this procedure has been omitted.

ii. Validity of Equilibrium Point

According to Gros [84] and Ajjarapu [85], non-unique steady state solutions of complex dynamic systems may occur as a result of chaotic response. Such solutions are characterized by their sensitivity to the initial conditions. Therefore, to confirm that the numerically obtained equilibrium point $\underline{p_0}$ is a unique, physically correct solution, the motion response and subsequent values of $\underline{p_0}$ are solved for different initial conditions using the nonlinear model. The results, shown in Appendix J.9, demonstrate that the equilibrium position is independent of the initial conditions and is therefore a unique, physical solution.

iii. Validity of SN-Curve

The results in Table 5-4 demonstrated the presence of cases in which the design values of the principal stress directions exceed the prescribed 30°. Therefore, for these specific cases, the appropriateness of the applied *F*-class SN-curve is investigated by recalculating the damage using a SN-curve that is compatible with angles of 30° to 45°. According to DNV [86], the SN-curve that is suited for such cases is the *E*-class SN-curve, with values of m_i and C_i as defined as in Equation [5-42], a reference thickness of 25mm and a thickness exponent k of 0.20.

$$C_i = \begin{cases} 10^{11.610}, & m_i = 3 \; and \; \tilde{S}_i \geq 74.1\text{MPa} \\ 10^{15.350}, & m_i = 5 \; and \; \tilde{S}_i < 74.1\text{MPa} \end{cases} \quad [5\text{-}42]$$

The above expressions are applied to the combinations of hotspots and sea states where it was found that $\theta_{99} \geq 30°$, after which the long-term damage is recalculated with Equation [5-39]. As a result, the *E*-curve based long-term damage at hotspots P_4 and T_6 are decreased with, respectively, 31% and 45% compared to the long-term damage according to the *F*-curve. Since the method proposed by DNV is based on the assumption that the damage reduces for increasing angles of the principal stress direction, it is not surprising that the damage according to the *F*-curve ($\theta \leq 30°$) is conservative in comparison to damage based on the *E*-curve ($30° \leq \theta \leq 45°$). Differences between the linear and nonlinear model-based damage are not affected when the *E*-curve is incorporated for the relevant sea states, as it is applied to both the linear and nonlinear model. Therefore, application of different SN-curves may only be beneficial in terms of improving the reliability of the damage values itself and does not affect the performance of the linearization.

Although not directly applicable to the WindFlo TLP, it should be noted that if stress ranges are accumulated in the vicinity of the transition value of the SN-curve (where the two slopes coincide), larger differences between linear and non-linear method can arise. A small linearization-induced difference in the stress range can then cause the damage to be calculated on a different slope of the SN-curve. One must, therefore, be aware of the transition value in the slope of the selected SN-curve.

5.8.2 Reasons Behind Damage Underestimation

As mentioned in Section 5.7.3, the damage according to the linear model is underestimated in hotspot P_4 when compared to the damage calculated with the nonlinear model. This occurs mostly when multiaxiality is observed, but also in two cases where the loads are almost uniaxial. The reason for the damage underestimation is two-fold, being:

i. Stress Ranges in the HCF Range

During operational conditions, roughly 95% of the stress ranges are typically in the HCF range (below 65.8MPa). Since the SN-curve in this region is characterized by an inverse slope of 5, small differences in the stress range induce large damage difference.

ii. Limitations of Principal Stress Approach

In section 3.7.4, it was explained that the stress component used for the fatigue calculation is the first or second principal stress, depending on which has the largest absolute mean value. Since the one of the two normal components of the stress tensor is always much larger than the other, the minima of the first principal stress and maxima of the second principal stress are cut off at the zero-line. Or, mathematically (see Section 3.7.3 for definitions of stress components):

$$\sigma_I \geq 0, \qquad |\sigma_{xx,p}| \gg |\sigma_{yy,p}| \text{ or } |\sigma_{zz,t}| \gg |\sigma_{yy,t}| \qquad [5\text{-}43]$$

$$\sigma_{II} \leq 0, \qquad |\sigma_{xx,p}| \gg |\sigma_{yy,p}| \text{ or } |\sigma_{zz,t}| \gg |\sigma_{yy,t}| \qquad [5\text{-}44]$$

The consequence of choosing either the first or second principal stress is that the damage induced by peaks across the zero-line are neglected, which is unjustifiable when the amplitudes of the numerically smaller principal stress component are not negligible. Therefore, the limitation of choosing either of the two components is that the other component must remain (nearly) zero, which leads to the restriction formulated in Equation [3-45]. This expression proves that, in conditions where multiaxiality occurs, prediction of fatigue damage based on one of the principal stress components is only justified when the product of the two normal components is positive and larger than the shear stress squared.

$$\tau_{xy}^2 \leq \sigma_{xx} \cdot \sigma_{yy} \qquad [5\text{-}45]$$

As far as the adequacy of linearization is concerned, the choice in stress component for the calculation of damage does not necessarily cause differences with respect to the nonlinear model. However, linearization induces a shift in the mean principal stress at the pontoon cross-sections and since the average value is in some cases close to zero, more of the first principal stress minima will cross the zero-line and will therefore be disregarded. This inevitably causes an underestimation of the damage w.r.t. the nonlinear model. This is clearly visible in the case of hotspot P_3 during sea state 5 ($\theta_{99} = 6.9°$), as depicted in Figure 5-5. In conclusion, prediction of the fatigue damage and comparison of linear and nonlinear model-based damage is only reliable if multi-axial stresses are incorporated adequately.

Note: it has also been determined that applying a second iteration value of α for each sea state (see Appendix J.10) yields almost no improvement in the accuracy of the linearized model. This is to be expected as the hydrodynamic damping is typically small and hardly affected the mean stresses.

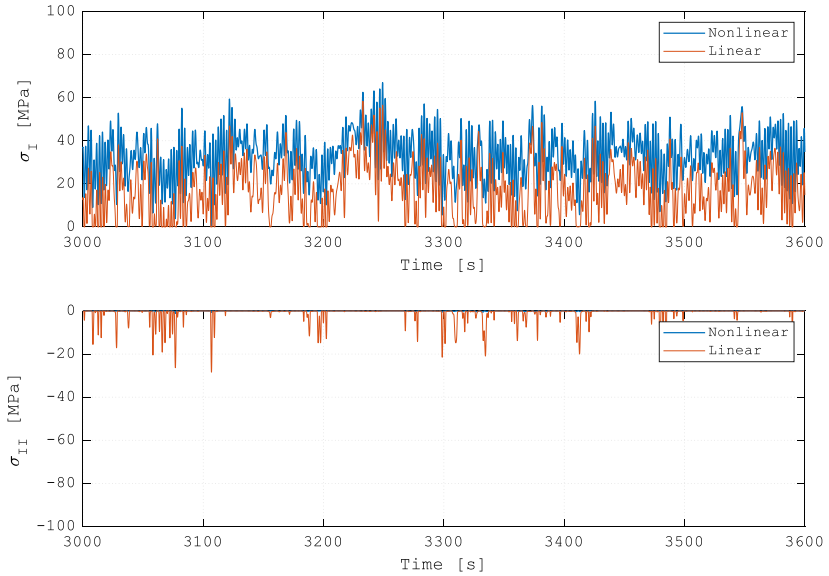

Figure 5-5: Principle Stress Response at Hotspot P_3 During Sea State 5

5.8.3 Damage Differences According to Uniaxial Loading

In the previous section, it was concluded that in the case of multi-axial loading, the choice of the fatigue-relevant stress component prevents the adequacy of the linearization method to be proven. Therefore, for the purpose of confirmation, the shear stresses and minor normal stresses ($\sigma_{yy,p}$ and $\sigma_{yy,t}$) have been omitted and the damage has been determined again, resulting in the damage differences in Table 5-5. For a visual representation of the damage differences per sea state (in the form of histograms), it is referred to Appendix J.11.

Table 5-5: Long-Term Damage Ratios (Uniaxial Loading)

	Pontoon Hotspots						Mid-Section Hotspots					
	$\mathbf{P_1}$	$\mathbf{P_2}$	$\mathbf{P_3}$	$\mathbf{P_4}$	$\mathbf{P_5}$	$\mathbf{P_6}$	$\mathbf{T_1}$	$\mathbf{T_2}$	$\mathbf{T_3}$	$\mathbf{T_4}$	$\mathbf{T_5}$	$\mathbf{T_6}$
$D_{tot,L}/D_{tot,NL}$	2.86	2.02	1.94	1.65	2.66	1.20	1.62	1.88	1.97	2.29	2.66	0.52

Unsurprisingly, the main differences w.r.t. the results with incorporation of multi-axial loads occurs in hotspots P_4 and T_6, where the largest principal stress directions were observed. Other damage ratios have remained nearly the same, confirming that in these cases, the stress response was indeed nearly uniaxial. The long-term damage underestimation in T_6 is a result of increasing damage underestimation for sea states with wave heights of 4m and higher, which is due to small inaccuracies in the stress response. What distinguishes this hotspot is its location compared to the turbine loads. Since wind velocities are in all sea states applied to the positive X-axis, there is a small lever-arm of the aerodynamic loads relative to T_6, which produces relatively small normal stresses. As a result, when wave conditions become harsher, structural velocities, nonlinear rotations and secondary nonlinearities become more influential. Small deviations in the stress response, which are inevitable, will then induce a large damage ratio as the stress ranges are all in the HCF range.

5.8.4 Influence and Incorporation of Multiaxiality

Since it was concluded that the damage calculation method (both in the linear and nonlinear model) is unreliable when multi-axial loading occurs, in the current section, an attempt has been made to resolve this limitation by calculating the fatigue damage using the instantaneous maximum value between first and second principal values instead of choosing either of the two components throughout a whole simulation. By doing so, the stress ranges are based on the numerically largest value between the first and second principal stress in each time step (Equation [5-46]), which represents the difference between the maximum tension on one principal plane and maximum compression on the other principal plane (see Figure 5-6 for further clarification).

$$\sigma_{eff}(t) = \begin{cases} \sigma_I(t), & \sigma_I(t) \geq |\sigma_{II}(t)| \\ \sigma_{II}(t), & \sigma_I(t) < |\sigma_{II}(t)| \end{cases} \quad [5\text{-}46]$$

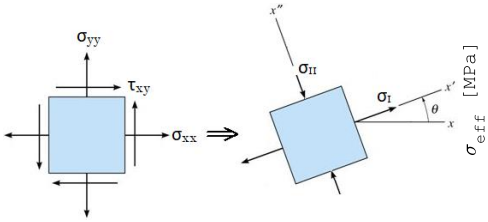

Figure 5-6: Visual Representation of First and Second Principle Stress

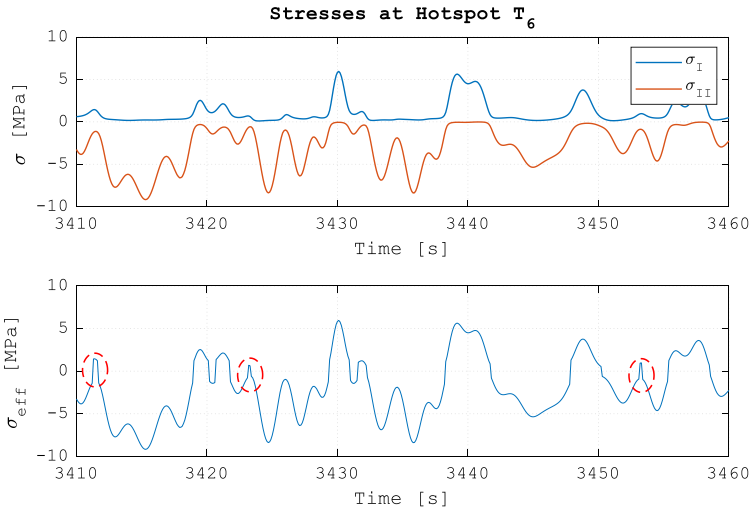

Figure 5-7: Erroneous Stress Peaks due to Non-Proportionality

Since this is done both in the linear and nonlinear model, the damage difference can be calculated regardless of whether multi-axial loads occur. However, due to out-of-phase shear and normal stresses (non-proportionality), first and second principal stresses will be locally out of phase, which generates erroneous peaks. Especially when the absolute values of the first and second principal stresses are in close proximity, fatigue damage is overestimated by the presence of such peaks. This effect is clearly visible for the response in hotspot T_6 during sea state 6, as shown in Figure 5-7. Therefore, due to non-proportionalities, this method is not suitable.

5.8.5 Importance of Non-Proportionality

It has become clear that non-proportional multiaxiality limits the applicability of the linearization method to only uniaxial load conditions. Furthermore, as mentioned in Section 2.5.2, in the presence of non-proportional multi-axial loads, application of uniaxial-based approach can lead to non-conservative results. It is, therefore, important to determine the extent to which non-proportional loading is present at the specific hotspots and sea states for which multi-axial loading is prominent ($\theta_{99} \geq 30°$).

The presence of non-proportionality is identified by visualization of the shear stress as a function of the corresponding normal stress per hotspot. Since fully proportional loading is characterized by a constant ratio between normal and shear stresses, the contour enclosed by the normal-shear stress relationship is a flat, straight line. In cases where relatively large non-proportionalities occur, the contour becomes increasingly wide and scattered. The results for the mid-section hotspots (T_2 and T_6) and pontoon hotspot (P_4) are presented in Figure 5-8 and Figure 5-9, respectively.

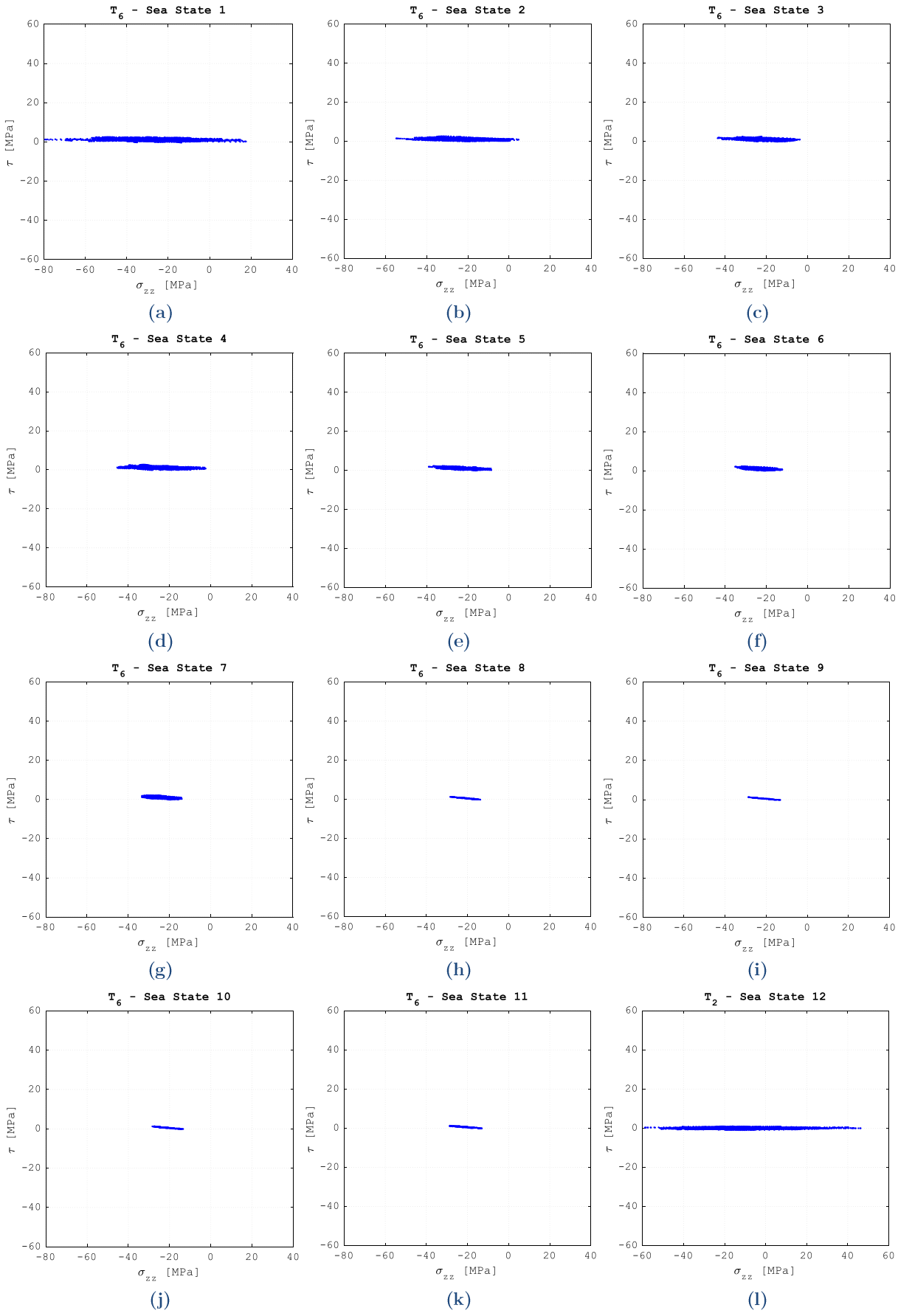

Figure 5-8: Visual Representation of Non-Proportionality at Mid-Section Hotspots

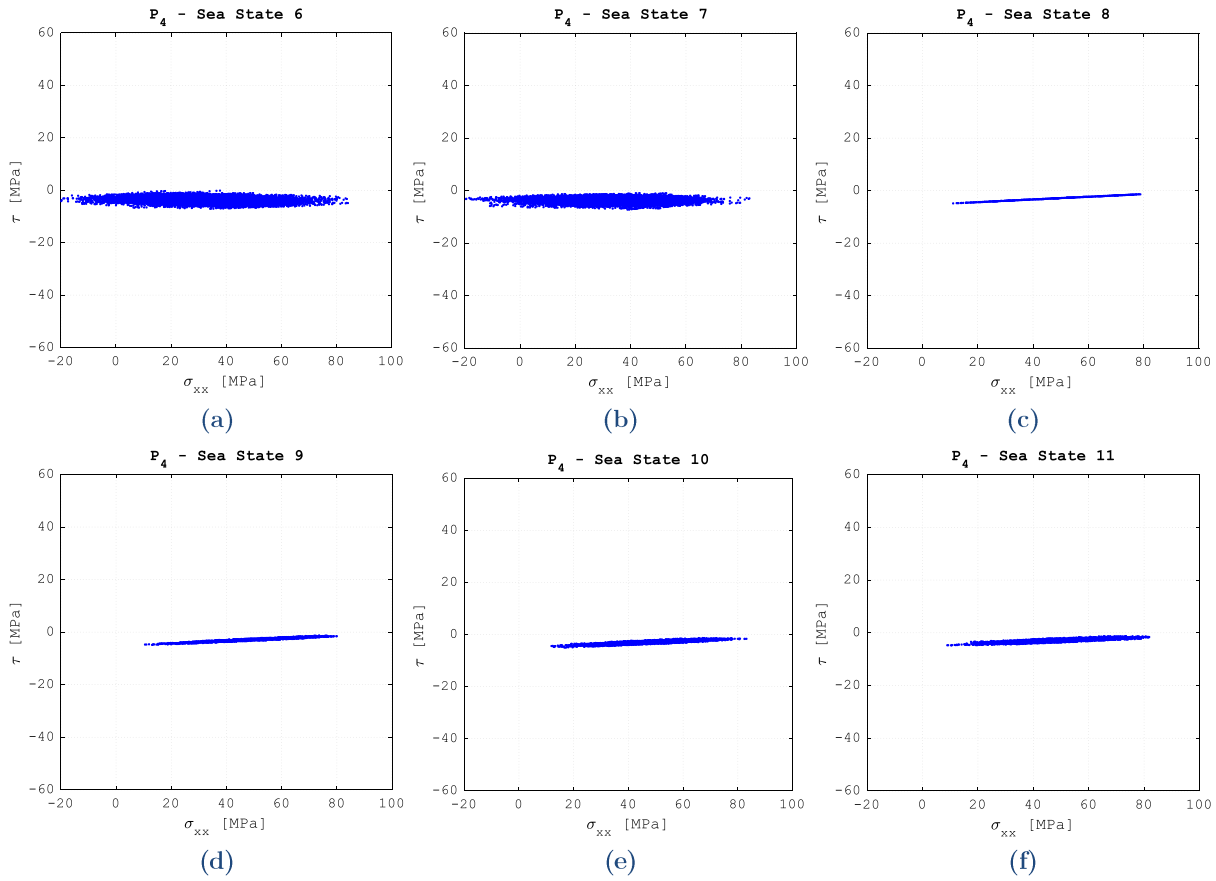

Figure 5-9: Visual Representation of Non-Proportionality at Pontoon Hotspots

Although a quantitative criterion could not be established with which the degree of non-proportionality could be derived from the results, it is possible to qualitatively assess whether non-proportionality can be a potential source of inaccuracies in the damage calculation. It can be deduced that the graphs do not all represent a thin line, which is an indication that non-proportional multi-axiality is present to a certain extent. This is particularly noticeable for sea states 6 and 7 in hotspot P_4, implying that the prevalent sea states may induce non-proportional multiaxial loading in at least one hotspot. As the influence of multi-axiality in combination with non-proportional loading is not known and the linearization method is only applicable to uniaxial or fully proportional multi-axial loads, from a design point of view, it is more reasonable to adopt a conservative approach regarding fatigue damage calculations. Especially in hotspots where the damage according to the linear model is, due to relatively small stress response, prone to underestimations, it is advisable to apply more stringent safety factors.

Note that a direct relationship between Figure 5-8 and Figure 5-9 and the corresponding angles of the principal stress directions cannot be derived, since these are also influenced by stress components normal to the x'-z' plane (see Equation [5-40] and Figure 3-28). For simplicity, these influences are not included in the figures.

6
CONCLUSIONS AND RECOMMENDATIONS

The following chapter is meant to recapitulate the findings that were presented in this thesis and draw conclusions regarding the development and validation of the solution method, which was discussed in Chapters 3 and 4, and its performance in identifying the influences of nonlinearities on the fatigue damage, as was investigated in Chapter 5. The final part of this chapter aims to reflect on the shortcomings of the research and to provide recommendations with which the limitations can be addressed.

6.1 Summary

The aim of this thesis was to evaluate the influence of non-linear hydrodynamic response on the fatigue damage of a TLP-type FOWT, taking into account aerodynamic coupling effects. Hence, a method has been developed with which the rigid-body motions, stress and fatigue damage response are determined in time domain, with the incorporation of:

- Morison-based hydrodynamic forces;
- Hydrostatic forces;
- Quasi-static mooring forces;
- Aerodynamic friction forces;
- Rotor thrust forces;
- Gyroscopic moments.

The dynamics are described by means of a system of coupled 6DOF-EoM and solved in Matlab using a built-in ODE-solver, after which the validity of the method is confirmed by comparing the motion and stress response with simulation results obtained from OrcaFlex models. The validation and verification procedure showed that the developed method accurately describes the rigid-body motions and stress response. On the other hand, it has been shown that flexibility in the tower can induce structural vibrations and increased stress amplitudes at the mid-section hotspots.

Finally, a method has been proposed to linearize the dynamics of the developed, analytical model. For linearization of quadratic damping, three different methods have been proposed, after which the best performing method is determined by means of a comparative study. Subsequently, using the fully linearized model, the difference in long-term damage w.r.t. the nonlinear model is calculated and the influence of multiaxiality is investigated.

6.2 Conclusions

Based on validation and verification results, it can be concluded that the incorporated phenomena and the level of accuracy with which they are described is sufficient to accurately embody the rigid-body dynamics and stress response of the WindFlo TLP. The exact influence of flexibility on the long-term fatigue damage, however, remains unknown.

Regarding the effects of nonlinearities on the fatigue damage of the WindFlo TLP, it can be concluded that a linear approach is suitable for the approximation of the long-term damage in the pontoon hotspots. However, in mid-section hotspots with relatively low stress response, the long-term damage is underestimated by 48% due to the high sensitivity of the damage to differences in the stress response. Conservative safety factors should, therefore, be applied to the damage in such hotspots when they are calculated by a linear approach. In general, the damage in sea states with wave height lower than 7.75m are accurately described by the linearized model and, in the case of mid-section hotspots with relatively low stress response, the damage is underestimated for wave heights of 3.75m and higher. The presence of multiaxiality and non-proportionality has been demonstrated for a number of hotspots and during both operational and extreme conditions, but it has not been possible to capture their combined influences on the damage.

Finally, it has been determined that the damage calculation method in this thesis is only applicable to uniaxial or proportional multi-axial loads. In the latter case, the instantaneous, numerically largest value between the first and second principal stress must then be used for the determination of the fatigue damage. The method can thus be used for the purpose of obtaining initial sizing and comparing design alternative in early design stages.

6.3 Recommendations for Further Work

In this thesis a number of aspects have been omitted which, on the basis of observations from results and literature research, have been regarded as important phenomena concerning fatigue damage in general and the applicability of linear approach. These are summarized below:

- The coupled pitch/tower bending and roll/tower bending modes of the TLPWT system could not be predicted due to the rigid-body assumption. This can be added to the model with two additional DOFs representing the fore-aft and side-to-side motions of the tower. The corresponding EoMs can be derived based on a single beam element using Euler-Bernoulli beam theory.
- Advanced modelling of turbine control system is of great importance for fatigue assessment of TLPWTs, since control system-induced vibrations are highly dynamic and interacting with platform loads. Furthermore, 1P and 3P vibrations and torsional stresses due to yaw error also require further investigation.

- Follow-up investigation regarding multiaxiality is required to develop a stress component that can be applied to the developed method in case of non-proportional multi-axial loading.
- Investigation on the influence of higher order wave theories and diffraction analyses are required to determine whether these effects are rightfully ignored
- The influence of time-varying wave direction on the fatigue damage response must be further assessed.
- The linearized, time domain EoMs must be decoupled and transformed into frequency domain in order to be used efficiently.

BIBLIOGRAPHY

[1] S. Shafiee and E. Topal, "When will fossil fuel reserves be diminished?," *Energy Policy Journal,* vol. 2009, no. 37, p. 9, 2008.

[2] "Statistics Explained," Eurostat, June 2017. [Online]. Available: http://ec.europa.eu/eurostat/statistics-explained/index.php/Renewable_energy_statistics. [Accessed 17 Sep 2017].

[3] N. Harding, A. Bertossa and J. Sandon, "Metocean study for Dounreay Tri," Renewable Energy Systems Ltd, 2016.

[4] R. James and M. C. Ros, "Floating Offshore Wind: Market and Technology Review," The Carbon Trust, 2015.

[5] R. J. Brooks and A. Tobias, "Choosing the Best Model: Level of Detail, Complexity and Model Performance," *Mathl. Comput. Modelling,* vol. 24, no. 4, pp. 1-14, 1996.

[6] MathWorks, *Matlab,* 9.1.0.441655 ed., Natick, Massachusetts: MathWorks Inc., 2016.

[7] "Orcina," Orcina Ltd, Daltongate, Cumbria, 2016.

[8] . L. H. Holthuijsen, Waves in Oceanic and Coastal Waters, Cambridge: CAMBRIDGE UNIVERSITY PRESS, 2007.

[9] J. Rodney, M. Sobey, P. Goodwin, Thieke and Westberg, "APPLICATION OF STOKES, CNOIDAL, AND FOURIER WAVE THEORIES," in *Journal of Waterway, Port, Coastal, and Ocean Engineering*, 1987.

[10] J. Journée and W. Massie, OFFSHORE HYDROMECHANICS, Delft: Delft University of Technology, 2008.

[11] E. E. Bachynski and T. Moan, "HYDRODYNAMIC MODELING OF TENSION LEG PLATFORM WIND TURBINES," in *International Conference on Ocean, Offshore and Arctic Engineering*, Nantes, 2013.

[12] C. Wehmeyer, F. Ferri, M. T. Andersen and R. R. Pedersen, "Hybrid Model Representation of a TLP Including Flexible Topsides in Non-Linear Regular Waves," *Energies,* vol. 2014, no. 7, pp. 5047-5064, 2014.

[13] I. Young, Wind Generated Ocean Waves, Kidlington, Oxford: ELSEVIER SCIENCE Ltd , 1999.

[14] M. Karimirad, Q. Meissonnier, Z. Gao and T. Moan, "Hydroelastic code-to-code comparison for a tension leg spar-type floating wind turbine".

[15] S. Chandrasekaran and A. Jain, "Dynamic behaviour of square and triangular offshore tension leg platforms under regular wave loads," *Ocean Engineering,* vol. 2002, no. 29, pp. 279-313, 2000.

[16] J. Yang, M. A. Sanjuán and H. Liu, "Vibrational subharmonic and superharmonic resonances," Elsevier, Xuzhou, 2015.

[17] DET NORSKE VERITAS (DNV), "GLOBAL PERFORMANCE ANALYSIS OF DEEPWATER FLOATING STRUCTURES," DET NORSKE VERITAS (DNV), 2010.

[18] J. Manwell, J. McGowan and A. Rogers, Wind Energy Explained – Theory, Design and Application, John Wiley & Sons Ltd, 2002.

[19] T. v. Kármán, "Progress in the Statistical Theory of Turbulence," in *Proceedings of the National Academy of Sciences of the United States of America*, PASADENA, 1948.

[20] J. Kaimal, J. Wyngaard, Y. Izumi and O. Coté, "Spectral characteristics of surface-layer turbulence," *Quarterly Journal Of The Royal Meteorological Society,* vol. 98, no. 417, pp. 563-589, 1972.

[21] J. Jia, Essentials of Applied Dynamic Analysis, Vienna: Springer, 2014.

[22] H. Namik and K. Stol, "Individual Blade Pitch Control of a Floating Offshore Wind Turbine on a Tension Leg Platform," *AIAA Aerospace Sciences Meeting,* vol. 48, pp. 4 - 7, 2010.

[23] D. Duckwitz and M. Shan, "Active tower damping and pitch balancing - design, simulation and field test," *Journal of Physics: Conference Series,* 2012.

[24] O. Matsushita , M. Tanaka , H. Kanki , M. Kobayashi and P. Keogh , Vibrations of Rotating Machinery - Volume 1, Tokyo : Springer, 2017.

[25] R. Lupton, "Frequency-domain modelling of floating wind turbines," University of Cambridge, Cambridge, 2014.

[26] C. Jensen, "Numerical Simulation of Gyroscopic Effects in Ansys," Aalborg University, Aalborg, 2011.

[27] D. Matha, T. Fischer, M. Kuhn and J. Jonkman, "Model Development and Loads Analysis of a Wind Turbine on a Floating Offshore Tension Leg Platform," National Renewable Energy Laboratory (NREL), Stockholm, 2010.

[28] E. E. Bachynski, M. I. Kvittem, C. Luan and T. Moan, "Wind-Wave Misalignment Effects on Floating Wind Turbines: Motions and Tower Load Effects," *Journal of Offshore Mechanics and Arctic Engineering,* p. 12, 2014.

[29] Z. Demirbilek, "Design formulae for offset, set down and tether loads of a tension leg platform (TLP)," *Ocean Engineering,* vol. 5, no. 17, pp. 517-523, 1990.

[30] I. Senjanovic, M. Tomic, N. Hadzic, "Formulation of consistent nonlinear restoring stiffness for dynamic analysis of tension leg platform and its influence on response," University of Zagreb, Zagreb, 2012.

[31] M. R. Tabeshpour and R. Shoghi, "Comparison between linear and nonlinear models for surge motion of TLP," IAU, Tehran, 2012.

[32] V. BAPAT and P. SRINIVASAN, "EFFECT OF STATIC DEFLECTION ON NATURAL FREQUENCY OF NON-LINEAR SPRING MASS SYSTEM BY DIRECT LINEARIZATION METHOD," Indian Institute of Science, Bangalore, 1968.

[33] M. Hall, B. Buckham and C. Crawford, "Evaluating the importance of mooring line model fidelity in floating offshore wind turbine simulations," *Wind Energy,* vol. 2014, no. 17, p. 1835–1853, 2013.

[34] W.-t. Hsu, K. P. Thiagarajan and L. Manuel, "Extreme mooring tensions due to snap loads on a floating offshore wind turbine system," Elsevier, Orono, 2017.

[35] G. Stabile, "A Reduced Order Model for the Dynamics of Long Flexible Cylinders in an offshore environment," University of Braunschweig, 2016.

[36] E. E. Bachynski and T. Moan, "Ringing loads on tension leg platform wind turbines," Elsevier, Trondheim, 2013.

[37] M. Shen, Z. Hu and G. Liu, "Dynamic response and viscous effect analysis of a TLP-type floating wind turbine using a coupled aero-hydro-mooring dynamic code," *Renewable Energy,* vol. 2016, no. 99, pp. 800-812, 2017.

[38] T. Matsui, Y. Sakoh and T. Nozu, "Second-order sum-frequency oscillations of tension-leg platforms: prediction and measurement," *Applied Ocean Research,* vol. 1993, no. 15, pp. 107-118, 1993.

[39] R. Bishop and W. Price , Hydroelasticity of ships, Cambridge : Cambridge University Press, 1979.

[40] T. Finn, "Hydroelasticity of a large floating wind turbine platform," KTH ROYAL INSTITUTE OF TECHNOLOGY, STOCKHOLM, 2014.

[41] J. Schijve, Fatigue of Structures and Materials, Springer, 2009.

[42] D. Radaj, C. Sonsino and W. Fricke, Fatigue assessment of welded joints by local approaches, Cambridge: Woodhead Publishing, 2006.

[43] T. Lassen and N. Récho, Fatigue Life Analyses of Welded Structures, Chippenham, Wiltshire: ISTE Ltd, 2006.

[44] J. H. den Besten, "Fatigue resistance of welded joints in aluminium high-speed craft: A TOTAL STRESS CONCEPT," Delft University of Technology, Delft, 2015.

[45] C. Hartsuijker, "Toegepaste mechanica," Academic Service, 2001.

[46] V. Radhakrishnan, "Multiaxial fatigue — An overview," *Sadhana,* 1995.

[47] C. Riess and M. Obermayr, "The non-proportionality of local stress paths in engineering applications," Frattura ed Integrità Strutturale, 2016.

[48] V. Anes, L. Reis and M. de Freitas, "On the assessment of multiaxial fatigue damage under variable amplitude loading," Frattura ed Integrità Strutturale, 2016.

[49] Y. Wang, "Estimation of fatigue lifetime for selected metallic materials under multiaxial variable amplitude loading," Frattura ed Integrità Strutturale, Nanjing, 2016.

[50] C. Ronchei, A. Carpinteri, G. Fortese, A. Spagnoli, S. Vantadori, M. Kurek and T. Łagoda, "Life estimation by varying the critical plane orientation in the modified Carpinteri-Spagnoli criterion," Frattura ed Integrità Strutturale, Parma, 2016.

[51] M. Kurek and T. Łagoda, "Determination of the critical plane orientation depending on the fatigue curves for bending and torsion," Frattura ed Integrità Strutturale, Opole, Poland, 2016.

[52] N. R. Gates and A. Fatemi, "Interaction of shear and normal stresses in multiaxial fatigue damage analysis," Frattura ed Integrità Strutturale, 2016.

[53] M. Margetin, R. Ďurka and V. Chmelko, "Multiaxial fatigue criterion based on parameters from torsion and axial S-N curve," Frattura ed Integrità Strutturale, 2016.

[54] T. I. Marin, "Fatigue Analysis of the Column-Pontoon Connection in a Semi-Submersible Floating Wind Turbine," Delft University of Technology, Delft, 2014.

[55] P. van Lieshout, H. den Besten and M. Kaminski, "Comparative study of multiaxial fatigue methods applied to welded joints in marine structures," Frattura ed Integrità Strutturale, 2016.

[56] P. Dong, Z. Wei and J. K. Hong, "A path-dependent cycle counting method for variable-amplitude multi-axial loading," *International Journal of Fatigue,* vol. 2010, no. 32, p. 720–734, 2010.

[57] A. Robertson, J. Jonkman, F. Vorpahl and W. Popko, "Offshore Code Comparison Collaboration Continuation Within IEA Wind Task 30: Phase II Results Regarding a Floating Semisubmersible Wind System," National Renewable Energy Laboratory (NREL), Oak Ridge, 2014.

[58] T. Burton, D. Sharpe, N. Jenkins and E. Bossanyi, "WIND ENERGY Handbook," John Wiley and Sons, 2011.

[59] J. E. Withee, "Fully Coupled Dynamic Analysis of a Floating Wind Turbine System," Massachusetts Institute of Technology, Massachusetts , 2004.

[60] D. Matha, "Model Development and Loads Analysis of an Offshore Wind Turbine on a Tension Leg Platform, with a Comparison to Other Floating Turbine Concepts," Cole Boulevard, Golden, Colorado, 2009.

[61] J. Jonkman and P. Sclavounos, "Development of Fully Coupled Aeroelastic and Hydrodynamic Models for Offshore Wind Turbines," in *ASME Wind Energy Symposium*, Reno, Nevada, 2006.

[62] W. O. Schiehlen, Advanced multibody system dynamics : simulation and software tools, Boston : Kluwer Academic, 1993.

[63] V. S. Anishchenko , T. E. Vadivasova and G. I. Strelkova , Deterministic Nonlinear Systems: A Short Course, Cham : Springer , 2014 .

[64] A. Metrikine and A. Vrouwenvelder, Dynamics of Structures, Delft: Delft University of Technology.

[65] J. Jonkman, "Dynamics Modeling and Loads Analysis of an Offshore Floating Wind Turbine," National Renewable Energy Laboratory (NREL), Battelle, 2007.

[66] E. E. Bachynski and T. Moan, "Linear and Nonlinear Analysis of Tension Leg Platform Wind Turbines," in *International Offshore and Polar Engineering Conference*, Rhodes, 2012.

[67] M. I. Kvittem and T. Moan, "Frequency Versus Time Domain Fatigue Analysis of a Semisubmersible Wind Turbine Tower," NTNU, Trondheim, 2015.

[68] C. Melis, F. Caille, T. Perdrizet, Y. Poirette and P. Bozonnet, "A NOVEL TENSION-LEG APPLICATION FOR FLOATING OFFSHORE WIND: TARGETING LOWER NACELLE MOTIONS," in *35th International Conference on Ocean, Offshore and Arctic Engineering (OMAE2016)*, Busan, South Korea, 2016.

[69] F. Adam, T. Myland, F. Dahlhaus and J. Großmann, "SCALE TESTS OF THE GICON - TLP FOR WIND TURBINES," in *33rd International Conference on Ocean, Offshore and Arctic Engineering (OMEA2014)*, San Francisco, California, USA, 2014.

[70] R. Zamora-Rodriguez, P. Gomez-Alonso, J. A. Lopez, P. Dinoi, V. De-Diego-Martin, A. N. Simos and A. S. Iglesias, "MODEL SCALE ANALYSIS OF A TLP FLOATING OFFSHORE WIND TURBINE," in *33rd International Conference on Ocean, Offshore and Arctic Engineering (OMAE2014)*, San Francisco, California, USA, 2014.

[71] j. Jonkman, S. Butterfield, W. Musial and G. Scott, "Definition of a 5-MW Reference Wind Turbine for Offshore System Development," Narional Renewable Energy Laboratory (NREL), Golden, Colorado, 2009.

[72] C. Melis, C. Bauduin, A. Wattez and A. Newport, "Adapting Tension Leg Technology to Provide an Economical Solution for Floating Wind Power," in *Offshore Technology Conference (OTC)*, Houston, Texas, USA, 2016.

[73] W. Bateman, V. Katsardi and C. Swan, "Extreme Ocean Waves Part I: The practical application of fully nonlinear wave modelling," Department of Civil Engineering, Imperial College, London, 2011.

[74] M. Lewisa, S. Neilla, P. Robinsa, M. Hashemi and S. Ward, "Characteristics of the velocity profile at tidal-stream energy sites," *Renewable Energy,* vol. 2017, no. 114, pp. 258-272, 2017.

[75] DET NORSKE VERITAS (DNV), "DNV-RP-C205: ENVIRONMENTAL CONDITIONS AND ENVIRONMENTAL LOADS," DET NORSKE VERITAS, 2010.

[76] ASTM, "ASTM Standard E 1049: Standard Practices for Cycle Counting in Fatigue Analysis," ASTM International, West Conshohocken, 2011.

[77] SaECaNet, "SaECaNet - Science and Engineering Cafe on the Net," [Online]. Available: https://www.saecanet.com/Calculation_data/000158_000240_kappa.html. [Accessed 10 10 2017].

[78] Department of Electronics and Electrical Engineering, "Sakshat Virtual Labs," IIT GUWAHATI, 2011. [Online]. Available: http://iitg.vlab.co.in/?sub=62&brch=175&sim=1078&cnt=1. [Accessed 10 10 2017].

[79] S. K. Chakrabarti, "Handbook of Offshore Engineering," 2005.

[80] O. T. GUDMESTAD and J. J. CONNOR, "Linearization methods and the influence of current on the nonlinear hydrodynamic drag force," Statoil, Stavanger, Norway.

[81] H. A. Lorentz, "Verslag van de Staatscommissie," ALGEMEENE LANDSDRUKKERIJ, 's-GRAVENHAGE, 1926.

[82] G. M. Terra, W. J. van de Berg and L. R. Maas, "Experimental verification of Lorentz' linearization procedure for quadratic friction," *Fluid Dynamics Research,* vol. 2005, no. 36, pp. 175-188, 2005.

[83] Det Norske Veritas, "SESAM User Manual Wadam - Wave Analysis by Diffraction and Morison Theory," Det Norske Veritas, Høvik, 2010.

[84] C. Gros, "Complex and Adaptive Dynamical Systems," Springer, Switzerland, 2015.

[85] V. Ajjarapu, "Computational techniques for voltage stability assessment and control," Springer, 2007.

[86] Det Norske Veritas, "DNVGL-RP-C203: Fatigue design of offshore steel structures," DNVGL, 2016.

[87] Loughborough University, "Numerical Initial Value Problems," in *HELM (Helping Engineers Learn Mathematics)*, Loughborough, Loughborough University, 2008, p. 84.

[88] World Heritage Encyclopedia, "World eBook Library," World Library Foundation, 2002. [Online]. Available: http://www.worldlibrary.in/articles/Stiff_equation. [Accessed 1 10 2017].

[89] L. F. Shampine and S. Thompson, "Scholarpedia," 2014. [Online]. Available: http://www.scholarpedia.org/article/Stiff_systems. [Accessed 10 2017].

[90] E. E. Bachynski, "Design and Dynamic Analysis of Tension Leg Platform Wind Turbines," 2014.

[91] T.-T. Tran and D.-H. Kim, "The platform pitching motion of floating offshore wind turbine: A preliminary unsteady aerodynamic analysis," *Journal of Wind Engineering and Industrial Aerodynamics,* vol. 2015, p. 17, 2015.

[92] S. Marcacci, "CleanTechnica," 8 May 2013. [Online]. Available: https://cleantechnica.com/2013/05/08/offshore-wind-industry-will-become-e130-billion-annual-market-by-2020/. [Accessed 15 12 2017].

[93] "GICON," GICON, 10 May 2017. [Online]. Available: http://www.gicon.de/en/aktuelles/nachrichtenliste-aktuell/newsdetails/archive/2017/may/10/article/gicon-and-glosten-are-joining-forces-for-tlp-offering.html. [Accessed 15 Dec 2017].

[94] M. Anders, "Developing Offshore Floating Wind Turbines: The Tension-Leg-Buoy Design," Norwegian University of Life Sciences, Ås, 2016.

[95] Y. Zhao, J. Yang and Y. He, "Preliminary Design of a Multi-Column TLP Foundation for a 5-MW Offshore Wind Turbine," Energies, Shanghai, 2012.

[96] B. Le Méhauté, An introduction to hydrodynamics and water waves, New York: Springer, 1976.

[97] M. O. L. Hansen, Aerodynamics of Wind Turbines, London: Earthscan, 2008.

APPENDIX A

WindFlo TLP Design

A.1 Platform Specifications

The complete overview of geometric parameters is depicted in Figure A - 3, along with a top view of the platform in Figure A - 1, denoted with "*section A*", and a cross sectional view of the pontoons at section B[4] is shown in Figure A - 2. Values of relevant design parameters are listed Table A - 1[5].

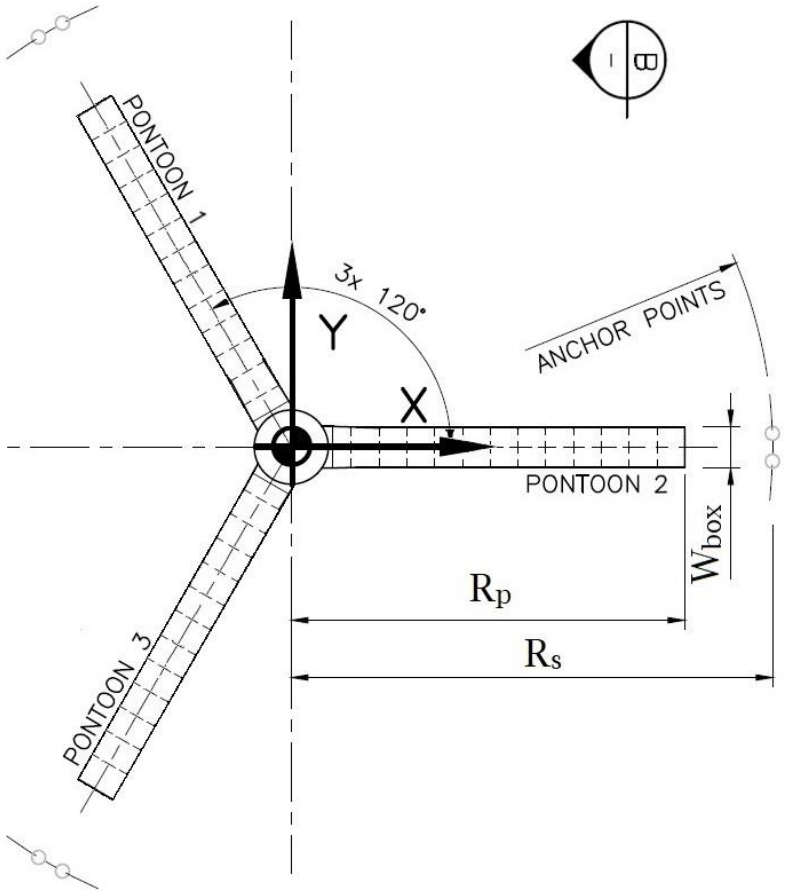

Figure A - 1: Platform Top View (Section "A" view)

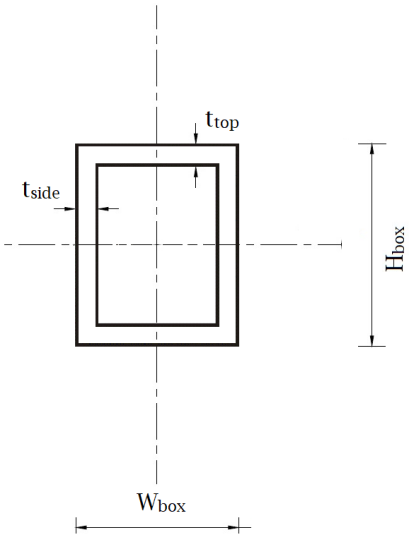

Figure A - 2: Pontoon Cross Section View (Section "B" view)

[4] Note that section B is not drawn to scale.

[5] Global- and local dimensioning of the WindFlo TLP, as well as the mooring configuration and turbine dimensions are designed on the basis of motion performance and ULS analysis, performed by Bluewater parallel to the research in this paper. Dimensions presented in this section are based on the last known version, obtained on October 10, 2017.

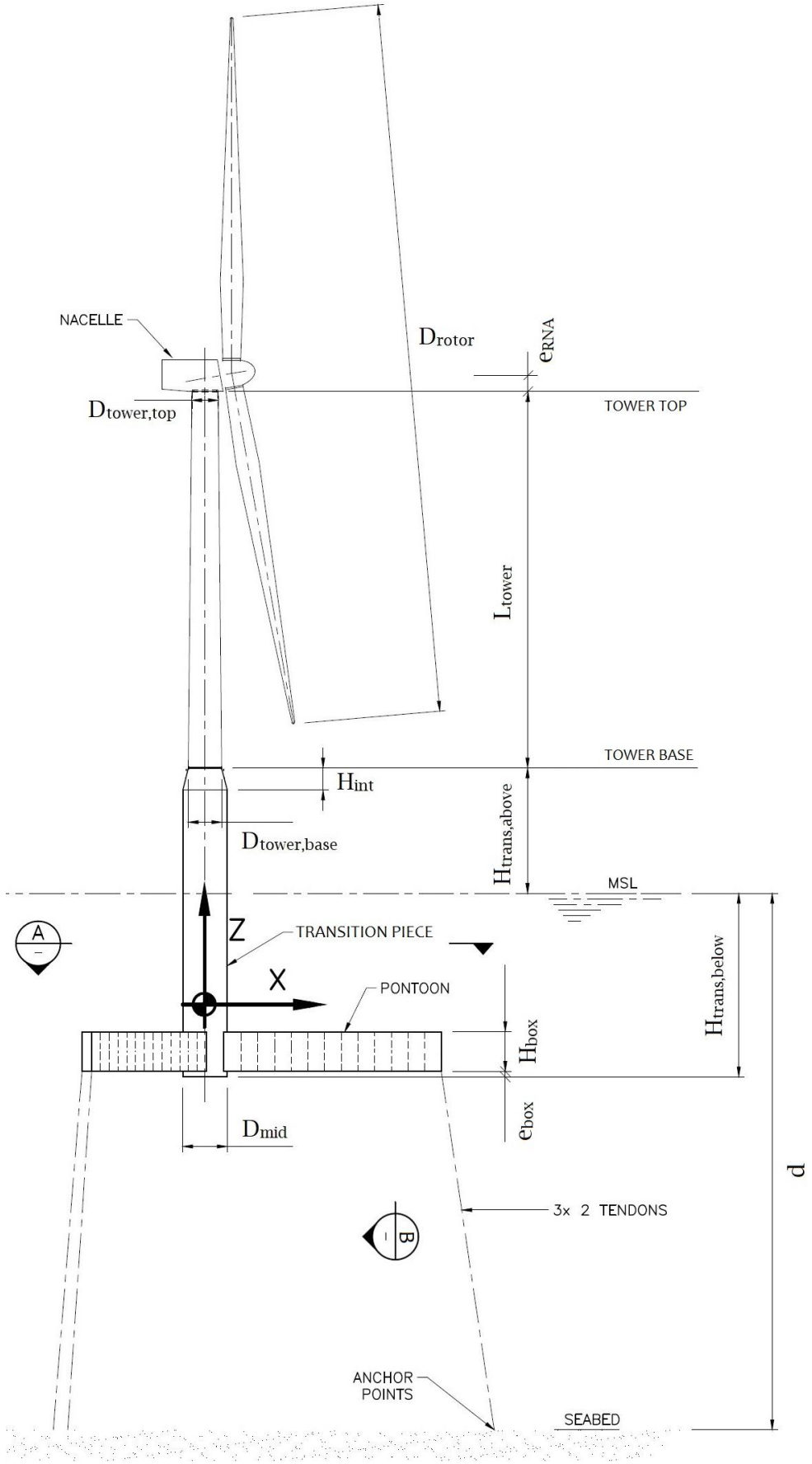

Figure A - 3: WindFlo TLP - Parametric Representation

Table A - 1: Principle Parameters Associated With Design of WindFlo TLP

Parameter	Symbol	Unit	Value
Water Depth	d	m	94
Transition Piece Height (below MSL/draft)	$H_{trans,below}$	m	27
Transition Piece Height (above MSL)	$H_{trans,above}$	m	5.6
Central Column Diameter	D_{mid}	m	6
Central Column Thickness	t_{mid}	mm	62.4
Vertical Distance Keel to Pontoon Bottom	e_{box}	m	0.5
Vertical Eccentricity Mooring Line Attachment	e_M	m	2.5
Pontoon Height	H_{box}	m	5
Pontoon Width	W_{box}	m	5
Pontoon Length	L_{box}	m	44.5
Radius Centre to Tendon Connections	R_P	m	47.5
Radius Centre to Anchor Points	R_S	m	55.4
Pontoon Top and Bottom Plate Thickness	t_{top}	mm	50
Pontoon Side Plate Thickness	t_{side}	mm	25
Platform Mass	M_p	t	2725
Total Displacement	M_{disp}	t	4193
Pretension (total)	$F_{T,0}$	kN	14400
Drag Constants Pontoon	$\underline{C}_{D,p}$	-	$[1.2 \quad 1.2 \quad 0.5]^T$
Drag Constants Mid-Section & Transition Piece	$\underline{C}_{D,mid}$	-	$[1.2 \quad 1.2 \quad 0.5]^T$
Added Mass Pontoon	$\underline{C}_{a,p}$	-	$[1.0 \quad 1.0 \quad 1.0]^T$
Added Mass Mid-Section & Transition Piece	$\underline{C}_{a,mid}$	-	$[1.0 \quad 1.0 \quad 1.0]^T$
Mass Moments of Inertia TLP (About CoG)	$\underline{J}_{TLP}$	tm^2	$[6.17 \quad 6.17 \quad 5.00]^T \cdot 10^5$
Cross Sectional Area of Pontoons	$A^x_{pontoon}$	m^2	0.51
Cross Sectional Area of Pontoons (Longitudinal)	$A^y_{pontoon}$	m^2	7.35
Enclosed Area of Pontoons	$A^{enc}_{pontoon}$	m^2	24.58
Second Moments of Area Pontoon Cross-Section	$\underline{I}_{pontoon}$	m^4	$[2.79 \quad 0.91 \quad 4.72]^T$
Cross Sectional Area of Mid-section	A_{mid}	m^2	1.24
Second Moments of Area Mid-section Cross-Section	$\underline{I}_{mid}$	m^4	$[2.90 \quad 2.90 \quad 5.16]^T$
Elasticity Modulus	E	GPa	212
Pontoon Connection Stiffness with Transition Piece About x, y and z Axes of Pontoon CoG	$\underline{k}_{r,p}$	kNm/rad	$[4.88 \quad 4.88 \quad 10^6]^T \cdot 10^7$

A.2 Turbine Specifications

As a starting point, design of the WindFlo TLP was based on the NREL offshore 5MW baseline wind turbine, which is thoroughly specified by Jonkman et al. [71]. Relevant properties of the RNA are listed in Table A - 2 and tower properties are presented in Table A - 3. Figure A - 4 depicts the distribution of the tower diameter, as a function of its position w.r.t. the tower base.

Table A - 2: RNA Parameters

Parameter	Symbol	Unit	Value
Rotor Diameter	D_{rotor}	m	126
Vertical Distance Bottom of Main Bearing to RNA CoG	$e_{v,RNA}$	m	1.75
Horizontal Distance Turbine Yaw Axis to RNA CoG	$e_{h,RNA}$	m	1.87
RNA mass	M_{RNA}	t	330
Cut-in Rotor Speed	ω_{in}	rpm	6.9
Rated Rotor Speed	ω_r	rpm	12.1
Cut-in Wind Speed	U_{in}	ms^{-1}	3
Cut-out Wind Speed	U_{out}	ms^{-1}	25
RNA Drag Area in Parked Conditions	$A^X_{RNA,ex}$	m^2	122.9
RNA Drag Constant in Parked Conditions	$C_{D,RNA}$	-	0.25
Mass Moments of Inertia of RNA (About CoG)	$\underline{J}_{RNA}$	tm^2	$[2.94 \quad 5.50 \cdot 10^4 \quad 2.94]^T$
Blade Mass Moment of Inertia (w.r.t. root)	$J_{P,blade}$	tm^2	11776

Table A - 3: Tower Specifications

Parameter	Symbol	Unit	Value
Tower Base Diameter	$D_{tower,base}$	m	6.0
Tower Top Diameter	$D_{tower,top}$	m	4.7
Tower Height	L_{tower}	m	67
Average Tower Wall Thickness	t_{tower}	mm	54
Tower Mass	M_{tower}	t	347
Drag Constants Tower	$\underline{C}_{D,t}$	-	$[1.2 \quad 1.2 \quad 0]^T$
Mass Moments of Inertia of Tower About x, y and z Axes of Tower CoG	$\underline{J}_t$	tm^2	$[1.58 \quad 1.58 \cdot 10^5 \quad 0.03]^T$
Tower Connection Stiffness with Transition Piece About x, y and z Axes of Tower CoG	$\underline{k}_{r,t}$	kNm/rad	$[9.74 \quad 9.74 \cdot 10^7 \quad 10^6]^T$

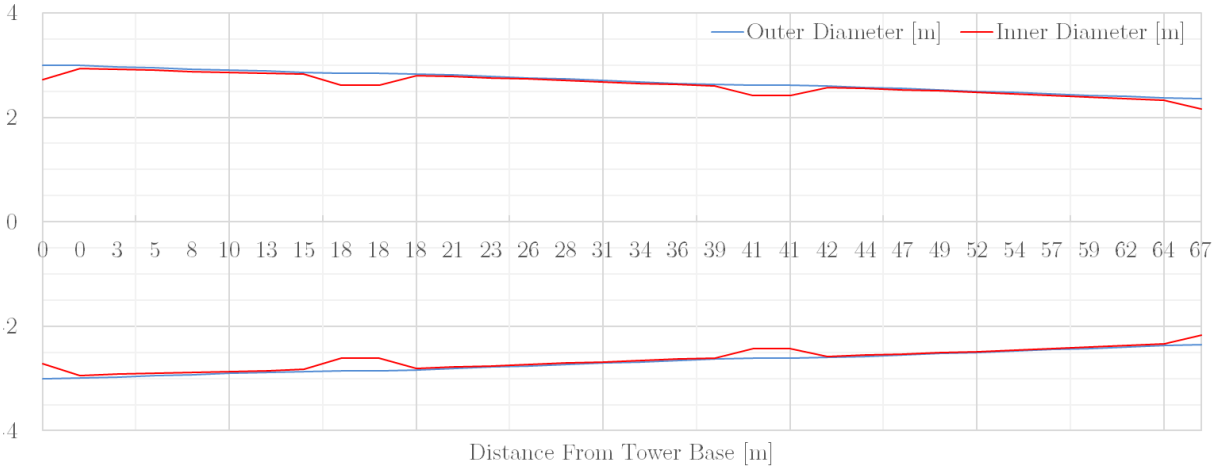

Figure A - 4: Distribution of Tower Diameter Along Longitudinal Axis

Thrust Coefficient C_T

Preliminary assessment on the power production of the 5MW turbine, including active pitch control system, shows a certain relationship between the thrust coefficient C_T and wind speed at nacelle height, depicted in Table A - 4. Note that these values were obtained based on a bottom-fixed platform and for 90° angle of attack (wind stream normal to blade chord).

In order to create a continuous dependency of the thrust coefficient C_T to the mean wind velocity at RNA level $\tilde{u}_{w,a}$, the thrust coefficient values are fitted with a 10th degree polynomial, as shown in Figure A - 5. Note that the curve fitted C_T function (Equation [A-1]) is, much like the original values, only valid in the wind velocity range of 3.5 to 25ms^{-1}.

$$C_T = 2.4546 \cdot 10^{-11} \cdot \tilde{u}_{w,a}^{10} - 3.7240 \cdot 10^{-9} \cdot \tilde{u}_{w,a}^{9} + 2.3919 \cdot 10^{-7} \cdot \tilde{u}_{w,a}^{8} - 8.4456 \cdot 10^{-6} \cdot \tilde{u}_{w,a}^{7} + 1.7798 \cdot 10^{-4} \cdot \tilde{u}_{w,a}^{6} - 0.0023 \cdot \tilde{u}_{w,a}^{5} + 0.0170 \cdot \tilde{u}_{w,a}^{4} - 0.068 \cdot \tilde{u}_{w,a}^{3} + 0.1158 \cdot \tilde{u}_{w,a}^{2} - 0.0546 \cdot \tilde{u}_{w,a} + 0.9687 \quad \text{[A-1]}$$

where $\tilde{u}_{w,a} = u_{w,a} \cdot \left(1 + 5.73 \cdot 10^{-2} \cdot \sqrt{1 + 0.148 \cdot |u_{w,a}|} \cdot \ln\left(z_w|_{Z=Z_{RNA}}/H\right)\right)$.

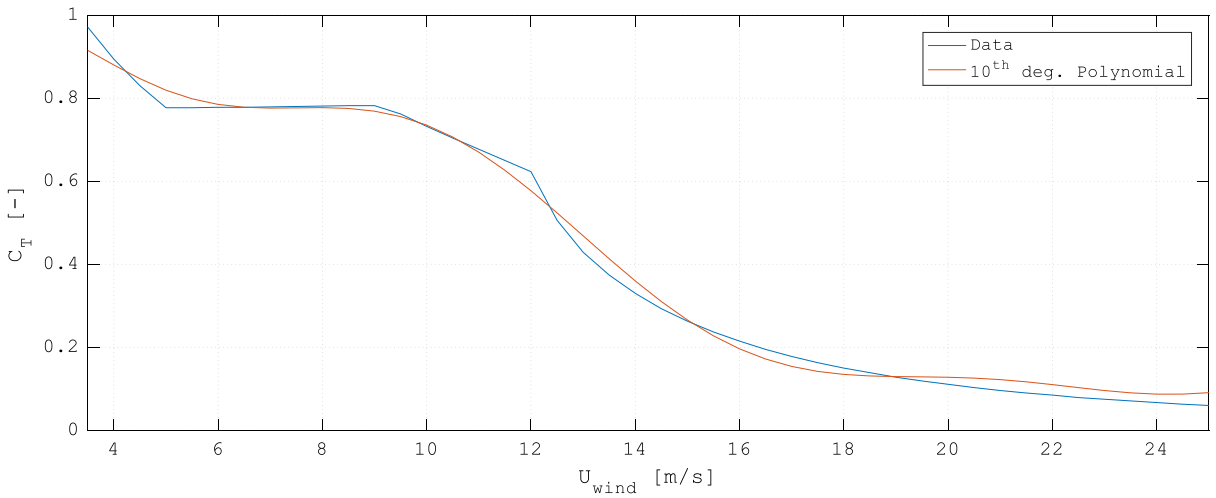

Figure A - 5: Thrust Coefficient

Table A - 4: Guaranteed Power Curve (Dounreay Conditions)

Wind Speed (ms^{-1})	C_T	Wind Speed (ms^{-1})	C_T
3.5	0.971	14.5	0.293
4	0.894	15	0.263
4.5	0.83	15.5	0.237
5	0.777	16	0.215
5.5	0.777	16.5	0.195
6	0.778	17	0.178
6.5	0.778	17.5	0.163
7	0.779	18	0.15
7.5	0.78	18.5	0.139
8	0.781	19	0.128
8.5	0.782	19.5	0.119
9	0.782	20	0.111
9.5	0.762	20.5	0.103
10	0.732	21	0.096
10.5	0.704	21.5	0.09
11	0.677	22	0.085
11.5	0.65	22.5	0.079
12	0.623	23	0.075
12.5	0.506	23.5	0.071
13	0.429	24	0.067
13.5	0.374	24.5	0.063
14	0.33	25	0.06

RNA Drag Coefficients in Parked Condition

Drag coefficients of rotors and nacelle during parked conditions, shown in Table A - 5, have been determined by Jonkman et al. [71] and used to calculate the drag area and weighted average drag constant $C_{D,RNA}$ of the RNA according to Equation [A-2] and [A-3], respectively.

$$A_{RNA,ex}^{X} = \sum_{i=1}^{17} L_i \cdot t_i + \frac{\pi}{4} D_{Nacelle}^2 \quad [A\text{-}2]$$

$$C_{D,RNA} = \frac{\sum_{i=1}^{17} L_i \cdot t_i \cdot C_{D,i} + \frac{\pi}{4} D_{Nacelle}^2 \cdot C_{D,Nacelle}}{A_{RNA,ex}^{X}} \quad [A\text{-}3]$$

where L_i, t_i and $C_{D,i}$ are, respectively, the length, thickness and aerodynamic drag coefficient of segment i of the rotor blade. And $D_{Nacelle}$ and $C_{D,Nacelle}$ are the diameter and drag coefficient of the nacelle, respectively.

Table A - 5: Drag Coefficients for Sub-parts of the RNA

Structural Part i	**Length L_i**	**Thickness t_i**	**$C_{D,i}$**
Rotor segment 1	2.7	0.64	0.5
Rotor segment 2	2.7	0.69	0.5
Rotor segment 3	2.7	0.75	0.35
Rotor segment 4	4.1	0.82	0.0113
Rotor segment 5	4.1	0.84	0.0094
Rotor segment 6	4.1	0.80	0.0094
Rotor segment 7	4.1	0.76	0.0087
Rotor segment 8	4.1	0.72	0.0065
Rotor segment 9	4.1	0.67	0.0065
Rotor segment 10	4.1	0.63	0.0057
Rotor segment 11	4.1	0.59	0.0057
Rotor segment 12	4.1	0.54	0.0052
Rotor segment 13	4.1	0.50	0.0052
Rotor segment 14	4.1	0.45	0.0052
Rotor segment 15	2.7	0.42	0.0052
Rotor segment 16	2.7	0.38	0.0052
Rotor segment 17	2.7	0.26	0.0052
Nacelle (diameter)	3.0	-	1.2

APPENDIX B

Parametric Discretization of WindFlo TLP Geometry

B.1 Platform and Turbine Mass

Discretization of Platform Mass

Segmentation of pontoon masses is based on equal subdivision of the total pontoon mass. The total platform mass is given by Equation [B-1], where the mass of the permanently submerged part of the central column is denoted with m_{mid}.

$$m_p = \sum_{i=1}^{3N_{box}} m_{box,i} + m_{mid} \quad \text{[B-1]}$$

where

$$m_{box,k} = \frac{m_{box}}{N_{box}},\ k = 1 \dots 3N_{box} \quad \text{[B-2]}$$

Discretization of Turbine and Transition Piece Mass

Distribution of mass segments of transition piece and tower is based on volumetric distribution of a cone-shaped geometry. Note that "transition piece" denotes the topmost and middle sections of the submerged parts of the central column. The total turbine mass is given by Equation [B-3].

$$m_{turbine} = \sum_{i=2}^{N_{tower}+5} m_{t,i} \quad \text{[B-3]}$$

where

$$m_{t,i} = \begin{cases} m_{mid}, & i = 1 \\ a_i * m_{trans}, & i = 2 \dots 4 \\ a_i * m_{tower}, & i = 5 \dots N_{tower} + 4 \\ m_{RNA}, & i = N_{tower} + 5 \end{cases} \quad \text{[B-4]}$$

$$a_i = \begin{cases} \frac{V_{trans,i}}{V_{trans,tot}}, & i = 2 \dots 4 \\ \frac{V_{tower,i}}{V_{tower,tot}}, & i = 5 \dots N_{tower} + 4 \end{cases} \quad \text{[B-5]}$$

and the volumetric distribution of tower $V_{tower,i}$ and transition piece $V_{trans,i}$ is based on the cone-shape geometries:

$$V_{trans,i} = \frac{\pi H_{trans,i}}{12}\left(D_{trans}(z_{i,base})^2 + D_{trans}(z_{i,base})D_{trans}(z_{i,top}) + D_{trans}(z_{i,top})^2\right) \quad \text{[B-6]}$$

$$V_{tower,i} = \frac{\pi H_{tower,i}}{12 V_{tower}} \left(D_{tower}(z_{i,base})^2 + D_{tower}(z_{i,base}) D_{tower}(z_{i,top}) + D_{tower}(z_{i,top})^2 \right) \quad \text{[B-7]}$$

with

$$V_{trans,tot} = \frac{\pi H_{trans}}{12} \left(D_{mid}^2 + D_{mid} D_{trans,top} + D_{trans,top}^2 \right) \quad \text{[B-8]}$$

$$V_{tower,tot} = \frac{\pi H_{tower}}{12} \left(D_{tower,base}^2 + D_{tower,base} D_{tower,top} + D_{tower,top}^2 \right) \quad \text{[B-9]}$$

$$D_{trans}(z') = D_{mid} - \frac{D_{mid} - D_{trans,top}}{H_{trans}} z' \quad \text{[B-10]}$$

$$D_{tower}(z') = D_{tower,base} - \frac{D_{tower,base} - D_{tower,top}}{H_{tower} + e_{v,RNA}} z' \quad \text{[B-11]}$$

B.2 Mass Moments of Inertia

Platform and Turbine

The mass moments of inertia are calculated using discretized lumped mass segments for structural elements with an eccentricity w.r.t. the reference point (O_G). Standard closed-form expressions are used for the mass moments of inertia of structural components around their local CoG-fixed axis frames.

Mass moments of inertia of lumped masses around an arbitrary axis is calculated using the parallel axis theorem.

$$\underline{J} = \underline{J}_{TLP} + \underline{J}_{RNA} + \underline{J}_t + \sum_{k=1}^{N_{box} N_{leg}} m_{box,k} * \underline{r_{box,k}} + \sum_{i=1}^{N_{tower}+5} m_{t,i} * \underline{r_{t,i}} \quad \text{[B-12]}$$

with

$$\underline{r_{box,k}} = \begin{bmatrix} Y_{CoG,box,k}^2 + Z_{CoG,box,k}^2 \\ X_{CoG,box,k}^2 + Z_{CoG,box,k}^2 \\ X_{CoG,box,k}^2 + Y_{CoG,box,k}^2 \end{bmatrix} \quad \text{[B-13]}$$

$$\underline{r_{t,i}} = \begin{bmatrix} Y_{CoG,t,i}^2 + Z_{CoG,t,i}^2 \\ X_{CoG,t,i}^2 + Z_{CoG,t,i}^2 \\ X_{CoG,t,i}^2 + Y_{CoG,t,i}^2 \end{bmatrix} \quad \text{[B-14]}$$

The radial distances from global coordinate system (CoG) to the centre of box segments $L_{leg,k}$ is calculated using:

$$L_{leg,k} = \begin{cases} R_p - \frac{L_{box}}{2N_{box}}, & k = 1, N_{box}+1, 2N_{box}+1 \\ L_{leg,k-1} - \frac{L_{box}}{N_{box}}, & k = 2 \dots N_{box}, N_{box}+2 \dots 2N_{box}, 2(N_{box}+1) \dots N_{legs} N_{box} \end{cases} \quad \text{[B-15]}$$

where

$$L_{box} = R_p - \frac{D_{mid}}{2} \quad \text{[B-16]}$$

Rotor plane

The mass moment of inertia of the rotor blades, as used for calculating gyroscopic moments, is approximated as the summation of the polar moments of inertia of each blade.

$$I_{disk} = N_{blades} I_{p,blade} \quad \text{[B-17]}$$

B.3 Mooring Configuration

Static Coordinates of Mooring Line Connectors

The static mooring configuration is characterized by the coordinate vectors in Equations [B-18], [B-19] and [B-20], representing the coordinates of the static position of the mooring line connectors between mooring line 1, 2 and 3 and their corresponding pontoon, respectively.

$$P_{0,1} = \begin{bmatrix} -R_p/2 \\ \sqrt{3}R_P/2 \\ -KG + e_{bot} + e_{box} \end{bmatrix} \quad \text{[B-18]}$$

$$P_{0,2} = \begin{bmatrix} R_p \\ 0 \\ -KG + e_{bot} + e_{box} \end{bmatrix} \quad \text{[B-19]}$$

$$P_{0,3} = \begin{bmatrix} -R_p/2 \\ -\sqrt{3}R_P/2 \\ -KG + e_{bot} + e_{box} \end{bmatrix} \quad \text{[B-20]}$$

Static Coordinates of Mooring Line Connectors

The mooring configuration is also characterized by the coordinate vectors in Equations [B-21], [B-22] and [B-23], which represent the coordinates of the static position of the anchor points of mooring line 1, 2 and 3, respectively.

$$SB_1 = P_{0,1} + \begin{bmatrix} -W_T/2 \\ \sqrt{3}W_T/2 \\ -H_T \end{bmatrix} \quad \text{[B-21]}$$

$$SB_2 = P_{0,2} + \begin{bmatrix} W_T \\ 0 \\ -H_T \end{bmatrix} \quad \text{[B-22]}$$

$$SB_3 = P_{0,3} - \begin{bmatrix} W_T/2 \\ \sqrt{3}W_T/2 \\ H_T \end{bmatrix} \quad \text{[B-23]}$$

where

$$H_T = d - T_{mean} + e_{bot} + e_{box} \quad \text{[B-24]}$$

and

$$W_T = R_S - R_P \quad \text{[B-25]}$$

B.4 Discretization of Centre of Gravity

Pontoon Segments

The CoGs of each pontoon segment are described by Equation [B-26].

$$CoG_{box,k} = \begin{bmatrix} X_{CoG,box,k} \\ Y_{CoG,box,k} \\ Z_{CoG,box,k} \end{bmatrix}, \qquad k = 1 \dots N_{legs}N_{box} \tag{B-26}$$

where

$$X_{CoG,box,k} = \begin{cases} -\dfrac{L_{leg,k}}{2}, & k = 1 \dots N_{box} \\ L_{leg,k}, & k = N_{box}+1 \dots 2N_{box} \\ -\dfrac{L_{leg,k}}{2}, & k = 2N_{box}+1 \dots N_{legs}N_{box} \end{cases} \tag{B-27}$$

$$Y_{CoG,box,k} = \begin{cases} \dfrac{\sqrt{3}}{2}L_{leg,k}, & k = 1 \dots N_{box} \\ 0, & k = N_{box}+1 \dots 2N_{box} \\ -\dfrac{\sqrt{3}}{2}L_{leg,k}, & k = 2N_{box}+1 \dots N_{legs}N_{box} \end{cases} \tag{B-28}$$

$$Z_{CoG,box,k} = -KG + e_{bot} + \frac{H_{box}}{2} \tag{B-29}$$

Central Column and Turbine Segments

The CoGs of the central column and turbine segments are described by Equation [B-30].

$$CoG_{t,i} = \begin{bmatrix} X_{CoG,t,i} \\ Y_{CoG,t,i} \\ Z_{CoG,t,i} \end{bmatrix} = \begin{cases} [0 \quad 0 \quad -KG + KG_{t,i}]^T, & i = 1 \dots N_{tower}+4 \\ [e_{x,RNA} \quad 0 \quad -KG + KG_{t,i}]^T, & i = N_{tower}+5 \end{cases} \tag{B-30}$$

where

$$H_{t,i} = \begin{cases} H_{mid}, & i = 1 \\ \dfrac{H_{trans}}{3}, & i = 2 \dots 4 \\ \dfrac{H_{tower}}{N_{tower}}, & i = 5 \dots N_{tower}+4 \\ 0, & i = N_{tower}+5 \end{cases} \tag{B-31}$$

$$KG_{t,i} = \begin{cases} \dfrac{H_{mid}}{2}, & i = 1 \\ KG_{t,i-1} + \dfrac{H_{t,i-1} + H_{t,i}}{2}, & i = 2 \dots N_{tower}+5 \end{cases} \tag{B-32}$$

B.5 Discretization of Centre of Buoyancy

Pontoon Segments

The CoBs of each pontoon segment are equal to their CoGs:

$$CoB_{box,k} = CoG_{box,k} \quad \text{[B-33]}$$

Submerged Parts of Central Column

To prevent fluctuating water level- induced contact problem, the top submerged part of the central column is not subdivided in multiple sections for the calculation of hydrodynamic forces. Therefore, the CoBs of the middle and upper part of the central column are described by Equation [B-34] and [B-35], respectively.

$$CoB_{t,1} = \begin{bmatrix} CoB_{mid}^{x} \\ CoB_{mid}^{z} \\ CoB_{mid}^{z} \end{bmatrix} = \begin{bmatrix} 0 \\ 0 \\ Z_{CoG,t,1} \end{bmatrix} \quad \text{[B-34]}$$

$$CoB_{t,2} = \begin{bmatrix} CoB_{trans}^{x} \\ CoB_{trans}^{y} \\ CoB_{trans}^{z} \end{bmatrix} = \begin{bmatrix} 0 \\ 0 \\ -KG + H_{mid} + CoB_{trans}(t) \end{bmatrix} \quad \text{[B-35]}$$

where

$$CoB_{trans} = \frac{H_{trans,BelowWL}(t)}{4} \frac{\left(R_{base}^2 + 3R_{WL}^2 + 2R_{base}R_{WL}\right)}{R_{base}^2 + R_{WL}^2 + R_{base}R_{WL}} \quad \text{[B-36]}$$

and

$$H_{trans,BelowWL}(t) = T_{mean} + \xi(\eta_1, \eta_2, t) - \eta_3 - H_{mid} \quad \text{[B-37]}$$

$$R_{WL} = \frac{D_{trans,WL}(t)}{2} \quad \text{[B-38]}$$

$$D_{trans,WL}(t) = D_{trans}(T_{mean} - H_{mid}) + \frac{D_{mid} - D_{trans,top}}{H_{trans}} * (\xi(\eta_1, \eta_2, t) - \eta_3) \quad \text{[B-39]}$$

B.6 Discretization of Drag Areas

Pontoon Segments

The static drag areas in the direction of the global axes are described by Equation [B-40].

$$\begin{bmatrix} A_{box,k}^{x} \\ A_{box,k}^{y} \\ A_{box,k}^{z} \end{bmatrix} = \begin{cases} \left[\frac{H_{box}L_{box}\sqrt{3}}{2N_{box}} \quad \frac{H_{box}L_{box}}{2N_{box}} \quad \frac{W_{box}L_{box}}{N_{box}}\right]^T, & k = 2 \dots N_{box} + 1, 2N_{box} + 2 \dots N_{legs}(N_{box} + 1) \\ \left[0 \quad \frac{H_{box}L_{box}}{N_{box}} \quad \frac{W_{box}L_{box}}{N_{box}}\right]^T, & k = N_{box} + 1 \dots 2N_{box} \end{cases} \quad \text{[B-40]}$$

Submerged Parts of Central Column

To prevent fluctuating water level- induced contact problem, the top part of the transition piece is not subdivided in multiple sections for the calculation of hydrodynamic forces.

$$A_{mid,1} = \begin{bmatrix} D_{mid}H_{mid} \\ D_{mid}H_{mid} \\ \pi D_{mid}^2/4 \end{bmatrix} \quad [B\text{-}41]$$

$$A_{mid,2} = \begin{bmatrix} A^x_{trans,below} \\ A^y_{trans,below} \\ 0 \end{bmatrix} \quad [B\text{-}42]$$

with

$$A^x_{trans,below} = A^y_{trans,below} = \frac{\left(D_{trans,base} + D_{trans,WL}\right)}{2} * H_{trans,BelowWL}(t) \quad [B\text{-}43]$$

Wind Drag Areas

All areas subjected to wind drag are defined in Equation [B-44].

$$A_{wind} = \begin{cases} \begin{bmatrix} A^x_{trans,above} & A^y_{trans,above} & 0 \end{bmatrix}^T, & j = 1 \\ \begin{bmatrix} H_{t,j+3} * D_t(z_{t,j}) & H_{t,j+3} * D_t(z_{t,j}) & 0 \end{bmatrix}^T, & j = 2 \dots N_{tower} \\ 0, & j = N_{tower} + 1 \end{cases} \quad [B\text{-}44]$$

where

$$A^x_{trans,above} = A^y_{trans,above} = \frac{\left(D_{trans,WL} + D_{trans,top}\right)}{2} * H_{trans,AboveWL}(t) \quad [B\text{-}45]$$

$$H_{trans,AboveWL}(t) = H_{trans} - H_{trans,BelowWL}(t) \quad [B\text{-}46]$$

$$z_{t,j} = \frac{H_{tower}}{N_{tower}} * (j - 1.5), \qquad j = 2 \dots N_{tower} \quad [B\text{-}47]$$

APPENDIX C

Wind and Wave Spectra

C.1 Wave Spectrum

As was shown in Section 3.2.2, the superposition principle is characterized by a wave spectrum $S(\omega)$, which is the probability distribution of the wave energy for a given sea state. In other words, it defines how much energy is accumulated within a frequency bin that corresponds to a certain wave amplitude. According to met-ocean studies [3], the wave spectrum that corresponds well with the wave characteristics at the Dounreay site is the JONSWAP spectrum, as depicted in Equation [C-1].

$$S(\omega) = (1 - 0.287 \ln \gamma) * S_{PM}(\omega) * \gamma^{\exp\left(-\frac{1}{2}\left(\frac{\omega-\omega_p}{\sigma\omega_p}\right)^2\right)} \quad [C\text{-}1]$$

where:

- $\gamma = 2$ is the dimensionless peak shape factor;
- $S_{PM}(\omega) = \frac{5}{16} H_s^2 \omega_p^4 \omega^{-5} \, exp\left(-\frac{5}{4}\left(\frac{\omega}{\omega_p}\right)^{-4}\right)$ is the Pierson-Moskowitz spectrum;
- $\omega_p = 2\pi/T_p$ is the peak frequency [rad/s];
- H_s is the significant wave height [m];
- $\sigma = \begin{cases} 0.07 \text{ for } \omega \leq \omega_p \\ 0.09 \text{ for } \omega \geq \omega_p \end{cases}$ is the spectral width parameter.

The wave number of each wave component is determined using the dispersion relationship, as shown in Equation [C-2]:

$$\omega_i^2 = g k_i \tanh(k_i d) \quad [C\text{-}2]$$

The frequency dependent wave amplitudes of each wave component are determined by discrete integration of the wave spectral density function $S(\omega)$ over a uniformly distributed frequency interval $[\omega_{min}, \omega_{max}]$ with constant frequency resolution $\Delta\omega$, as shown in Equation [C-3].

$$a_i = \sqrt{2S(\omega_i)\Delta\omega} \quad [C\text{-}3]$$

The frequency resolution is chosen such, that repetition of the time signal is avoided:

$$\Delta\omega = (\omega_{max} - \omega_{min})/N_{wave} = \pi/T_{sim} \quad [C\text{-}4]$$

where T_{sim} is the duration of the time signal.

C.2 Wind Spectrum

Frøya spectral density function for frequency *f*:

$$S(f) = \frac{320 * \left(\frac{U_{W0}}{U_{ref}}\right)^2 * \left(\frac{z}{z_{ref}}\right)^{0.45}}{\left(1 + \tilde{f}^n\right)^{\frac{5}{3n}}}$$

Where:

- U_{W0} is the 1h wind speed at z_{ref};
- $z_{ref} = 10\text{m}$ is the reference elevation above sea level;
- z is the elevation above sea level, taken as the RNA level;
- U_{ref} = 10ms^{-1} is a reference wind speed;
- $\tilde{f} = 172 * f * \left(\frac{z}{z_{ref}}\right)^{\frac{2}{3}} * \left(\frac{U_{W0}}{U_{ref}}\right)^{-\frac{3}{4}}$
- *f* is the frequency in Hertz over the range [0.00167Hz, 0.5Hz]. This means that $\omega_{turb,min} = 2\pi \cdot 0.00167$ and $\omega_{turb,max} = \pi$;
- n = 0.468 is a non-dimensional coefficient.

The spectral density function is discretized along a uniform frequency interval from $\omega_{turb,min}$ to $\omega_{turb,max}$ with constant frequency resolution $\Delta\omega_{turb}$. The constant frequency resolution is chosen such, that repetition of the time signal is avoided.

$$\Delta\omega_{turb} = \left(\omega_{turb,max} - \omega_{turb,min}\right)/N_{turb} = \pi/T_{sim} \quad \text{[C-5]}$$

where N_{turb} is the number of wind turbulence components and T_{sim} is the duration of the time signal.

APPENDIX D

Applicability of Linear Wave Theory

D.1 Nonlinear Wave Theories for Long Term Wave Conditions - Sea States

In the following analysis, the significant wave heights H_s and spectral peak periods T_s, provided in met-ocean studies [3], are used to determine for each sea state whether waves within the sea states are applicable to linear wave theory. The linear wave limit, the upmost threshold for which linear wave theory is applicable, and water depth classifications are determined based on Figure 3-5. The results are shown in Table D - 1. Note that boxes denoted with a zero correspond to sea states that are non-existent.

D.2 Nonlinear Wave Theories for Short Term Wave Conditions - Individual Waves

In the following analysis, average yearly occurring individual waves with wave height H and wave period T, provided in met-ocean studies [3], are used to determine for each individual wave whether it is applicable to linear wave theory. The linear wave limit, breaking wave limit and water depth classifications are determined based on Figure 3-5. The results are shown in Table D - 2. Note that boxes denoted with a zero correspond to sea states that are non-existent.

Table D - 1: Applicability Linear Wave Theory Based on Sea States

Hs [m]		Tp [s]																							
From	To	From	3	4	5	6	7	8	9	10	11	12	13	14	15	16	17	18	19	20	21	22	23	24
0	0.5	0.00208	0.001258	0.000842	0.000603	0.000453	0.000353	0.000282	0.000231	0.000193	0.000163	0.00014	0.000121	0.000106	9.36E-05	8.32E-05	0	0	0	0	0	0	0	0
0.5	1	0.006241	0.003775	0.002527	0.00181	0.001359	0.001058	0.000847	0.000693	0.000578	0.000489	0.000419	0.000364	0.000318	0.000281	0.00025	0.000223	0.000201	0.000182	0.000165	0.000151	0.000138		
1	1.5	0	0.006292	0.004212	0.003016	0.002265	0.001764	0.001412	0.001156	0.000963	0.000815	0.000699	0.000606	0.00053	0.000468	0.000416	0.000372	0.000335	0.000303	0.000276	0.000252	0.000231		
1.5	2	0	0	0.005897	0.004222	0.003171	0.002469	0.001977	0.001618	0.001349	0.001142	0.000979	0.000848	0.000743	0.000655	0.000582	0.000521	0.000469	0.000424	0.000386	0.000352	0		
2	2.5	0	0	0	0.005429	0.004077	0.003175	0.002541	0.00208	0.001734	0.001468	0.001258	0.001091	0.000955	0.000842	0.00075	0.00067	0.000603	0.000546	0.000496	0			
2.5	3	0	0	0	0	0.006635	0.004984	0.00388	0.003106	0.002543	0.00212	0.001794	0.001538	0.001333	0.001167	0.00103	0.000915	0.000819	0.000737	0.000667	0			
3	3.5	0	0	0	0	0	0.00589	0.004585	0.003671	0.003005	0.002505	0.00212	0.001818	0.001576	0.001379	0.001217	0.001082	0.000968	0.000871	0.000788	0			
3.5	4	0	0	0	0	0	0	0.005291	0.004236	0.003467	0.00289	0.002446	0.002097	0.001818	0.001591	0.001404	0.001248	0.001117	0.001005	0				
4	4.5	0	0	0	0	0	0	0	0.0048	0.00393	0.003276	0.002773	0.002377	0.002061	0.001803	0.001591	0.001415	0.001266	0.001139	0				
4.5	5	0	0	0	0	0	0	0	0.005365	0.004392	0.003661	0.003099	0.002657	0.002303	0.002015	0.001779	0.001581	0.001415	0.001273	0				
5	5.5	0	0	0	0	0	0	0	0	0.004854	0.004047	0.003425	0.002936	0.002545	0.002228	0.001966	0.001747	0.001564	0.001407	0.001273	0			
5.5	6	0	0	0	0	0	0	0	0.006495	0.005316	0.004432	0.003751	0.003216	0.002788	0.00244	0.002153	0.001914	0.001713	0.001541	0				
6	6.5	0	0	0	0	0	0	0	0	0.004817	0.004077	0.003496	0.00303	0.002652	0.00234	0.00208	0.001862	0.001675	0					
6.5	7	0	0	0	0	0	0	0	0	0	0.004404	0.003775	0.003273	0.002864	0.002527	0.002247	0.00201	0.00181	0					
7	7.5	0	0	0	0	0	0	0	0	0	0	0.00473	0.004055	0.003515	0.003076	0.002715	0.002413	0.002159	0.001944	0				
7.5	8	0	0	0	0	0	0	0	0	0	0	0.005056	0.004335	0.003757	0.003288	0.002902	0	0	0	0				
8	8.5	0	0	0	0	0	0	0	0	0	0	0	0.004614	0.004	0.0035	0.003089	0	0	0	0				
8.5	9	0	0	0	0	0	0	0	0	0	0	0	0	0.004242	0.003713	0	0.002912	0	0	0				
9	9.5	0	0	0	0	0	0	0	0	0	0	0	0	0	0.003925	0.003463	0	0	0	0				
9.5	10	0	0	0	0	0	0	0	0	0	0	0	0	0.004727	0	0.003651	0	0	0	0				
10	10.5	0	0	0	0	0	0	0	0	0	0	0	0	0	0	0	0.003412	0	0	0				
10.5	11	0	0	0	0	0	0	0	0	0	0	0	0	0	0	0	0.003578	0	0	0				
11	11.5	0	0	0	0	0	0	0	0	0	0	0	0	0	0	0	0.003745	0	0	0				
11.5	12	0	0	0	0	0	0	0	0	0	0	0	0	0	0	0	0.003911	0	0	0				
12	12.5	0	0	0	0	0	0	0	0	0	0	0	0	0	0	0	0.004077	0	0	0				
12.5	13	0	0	0	0	0	0	0	0	0	0	0	0	0	0	0	0.004244	0	0	0				
13	13.5	0	0	0	0	0	0	0	0	0	0	0	0	0	0	0	0.00441	0	0	0				
13.5	14	0	0	0	0	0	0	0	0	0	0	0	0	0	0	0	0.004577	0	0	0				
14	14.5	0	0	0	0	0	0	0	0	0	0	0	0	0	0	0	0.004743	0	0	0				
14.5	15	0	0	0	0	0	0	0	0	0	0	0	0	0	0	0	0.00491	0	0	0				
15	15.5	0	0	0	0	0	0	0	0	0	0	0	0	0	0	0	0.005076	0	0	0				

Linear Wave Limit d/(gT^2) =	0.002	0.002	0.002	0.002	0.002	0.0018	0.0018	0.0017	0.0016	0.0015	0.0014	0.0014	0.0012	0.0012	0.001	0.001	0.001	0.0007	0.0007	0.0007	0.0007
	0.8	0.5	0.3	0.2	0.2	0.1	0.1	0.09	0.07	0.06	0.05	0.05	0.04	0.04	0.03	0.03	0.03	0.02	0.02	0.02	0.02

Deep Water Waves

Intermediate Water Waves

Legend

Linear

Nonlinear

Table D - 2: Applicability Linear Wave Theory Based on Individual Waves

Wave Period [s]	1	2	3	4	5	6	7	8	9	10	11	12	13	14	15	16	17	18	19	20	21	22	23	24	25	26	27	28	29
Height [m]	2	3	4	5	6	7	8	9	10	11	12	13	14	15	16	17	18	19	20	21	22	23	24	25	26	27	28	29	30
0 0.5	0.006371	0.016989	0.055747	0.043833	0.0269	0.015082	0.008362	0.004405	0.002548	0.001474	0.001062	0.000803	0.00052	0.00034	0.000199	0.000176	0.000157	0.000141	0.000127	5.78E-05	5.27E-05	4.82E-05	4.42E-05	4.08E-05	3.77E-05	3.5E-05	3.25E-05	3.03E-05	2.83E-05
0.5 1	0	0.008495	0.02867	0.061162	0.048845	0.031205	0.017919	0.010382	0.005352	0.003159	0.002124	0.001357	0.00078	0.00068	0.000597	0.000265	0.000236	0.000212	0.000191	0.000173	0.000158	0.000145	0.000133	0.000122	0.000113	0.000105	9.75E-05	9.09E-05	8.49E-05
1 1.5	0	0.014158	0.007964	0.030581	0.038934	0.028605	0.017919	0.011012	0.006371	0.004212	0.002655	0.001508	0.0013	0.000566	0.000498	0.000441	0.000393	0.000353	0.000319	0.000289	0.000263	0.000241	0.000221	0.000204	0.000188	0.000175	0.000163	0.000152	0.000142
1.5 2	0	0	0.011149	0.014271	0.024776	0.021844	0.016724	0.011012	0.006352	0.002949	0.002478	0.001656	0.00091	0.000793	0.000697	0.000617	0.000551	0.000494	0.000446	0.000405	0.000369	0.000337	0.00031	0.000285	0.000264	0.000245	0.000228	0.000212	0.000198
2 2.5	0	0	0.014335	0.009174	0.012742	0.018723	0.014335	0.008495	0.004587	0.003791	0.001593	0.001357	0.00117	0.001019	0.000896	0.000794	0.000708	0.000635	0.000573	0.00052	0.000474	0.000434	0.000398	0.000367	0.000339	0.000315	0.000293	0.000273	0.000255
2.5 3	0	0	0.001752	0.011213	0.007787	0.011442	0.00876	0.006922	0.005607	0.003317	0.001947	0.001659	0.00143	0.001246	0.001095	0.00097	0.000865	0.000777	0.000701	0.000636	0.000579	0.00053	0.000487	0.000449	0.000415	0.000385	0.000358	0.000333	0.000311
3 3.5	0	0	0	0.013252	0.009203	0.006761	0.010353	0.00818	0.003313	0.002738	0.002301	0.00196	0.00169	0.001472	0.001294	0.001146	0.001023	0.000918	0.000828	0.000751	0.000684	0.000626	0.000575	0.00053	0.00049	0.000454	0.000423	0.000394	0.000368
3.5 4	0	0	0	0.015291	0.010618	0.007801	0.005973	0.004719	0.003823	0.003159	0.002655	0.002262	0.00195	0.001699	0.001493	0.001323	0.00118	0.001059	0.000956	0.000867	0.00079	0.000723	0.000664	0.000612	0.000565	0.000524	0.000488	0.000455	0.000425
4 4.5	0	0	0	0.017329	0.012034	0.008841	0.006769	0.005349	0.004332	0.003579	0.003009	0.002563	0.00221	0.001925	0.001692	0.001499	0.001337	0.0012	0.001083	0.000982	0.000895	0.000819	0.000752	0.000693	0.00064	0.000593	0.000553	0.000515	0.000481
4.5 5	0	0	0	0	0.01345	0.009882	0.007566	0.005978	0.004842	0.004002	0.003362	0.002865	0.00247	0.002152	0.001891	0.001675	0.001494	0.001341	0.00121	0.001098	0.001	0.000915	0.000841	0.000775	0.000716	0.000664	0.000618	0.000576	0.000538
5 5.5	0	0	0	0	0.014866	0.010922	0.008362	0.006607	0.005352	0.004423	0.003716	0.003167	0.00273	0.002379	0.002091	0.001852	0.001652	0.001482	0.001338	0.001214	0.001106	0.001012	0.000929	0.000856	0.000792	0.000734	0.000683	0.000636	0.000595
5.5 6	0	0	0	0	0.016282	0.011962	0.009158	0.007236	0.005861	0.004844	0.00407	0.003468	0.00299	0.002605	0.00229	0.002028	0.001809	0.001624	0.001465	0.001329	0.001211	0.001108	0.001018	0.000938	0.000867	0.000804	0.000748	0.000697	0.000651
6 6.5	0	0	0	0	0.017697	0.013002	0.009955	0.007865	0.006371	0.005265	0.004424	0.00377	0.003251	0.002832	0.002489	0.002205	0.001966	0.001765	0.001593	0.001445	0.001316	0.001204	0.001106	0.001019	0.000942	0.000874	0.000813	0.000758	0.000708
6.5 7	0	0	0	0	0.019113	0.014042	0.010751	0.008495	0.006881	0.005687	0.004778	0.004071	0.003511	0.003058	0.002688	0.002381	0.002124	0.001906	0.00172	0.00156	0.001422	0.001301	0.001195	0.001101	0.001018	0.000944	0.000878	0.000818	0.000765
7 7.5	0	0	0	0	0	0.015082	0.011548	0.009124	0.00739	0.006108	0.005132	0.004373	0.003771	0.003285	0.002887	0.002557	0.002281	0.002047	0.001848	0.001676	0.001527	0.001397	0.001283	0.001182	0.001093	0.001014	0	0	0
7.5 8	0	0	0	0	0	0.016123	0.012344	0.009753	0.0079	0.006529	0.005486	0.004675	0.004031	0.003511	0.003086	0.002734	0.002438	0.002188	0.001975	0.001791	0.001632	0.001493	0.001372	0.001264	0	0	0	0	0
8 8.5	0	0	0	0	0	0.017163	0.01314	0.010382	0.00841	0.00695	0.00584	0.004976	0.004291	0.003738	0.003285	0.00291	0.002596	0.00233	0.002102	0.001907	0.001738	0.0159	0	0	0	0	0	0	0
8.5 9	0	0	0	0	0	0.018203	0.013937	0.011012	0.008919	0.007371	0.006194	0.005278	0.004551	0.003964	0.003484	0.003086	0.002753	0.002471	0.00223	0.002023	0	0	0	0	0	0	0	0	0
9 9.5	0	0	0	0	0	0	0.014733	0.011641	0.009429	0.007793	0.006548	0.005579	0.004811	0.004191	0.003683	0.003263	0.00291	0.002612	0.002357	0	0	0	0	0	0	0	0	0	0
9.5 10	0	0	0	0	0	0	0.015529	0.01227	0.009939	0.008214	0.006902	0.005881	0.005071	0.004417	0.003882	0.003439	0.003068	0.002753	0	0	0	0	0	0	0	0	0	0	0
10 10.5	0	0	0	0	0	0	0.016326	0.012899	0.010449	0.008635	0.007256	0.006183	0.005331	0.004644	0.004081	0.003615	0.003225	0	0	0	0	0	0	0	0	0	0	0	0
10.5 11	0	0	0	0	0	0	0.017122	0.013529	0.010958	0.009056	0.00761	0.006484	0.005591	0.00487	0.004281	0.003792	0	0	0	0	0	0	0	0	0	0	0	0	0
11 11.5	0	0	0	0	0	0	0.017919	0.014158	0.011468	0.009478	0.007964	0.006786	0.005851	0.005097	0.00448	0	0	0	0	0	0	0	0	0	0	0	0	0	0
11.5 12	0	0	0	0	0	0	0	0.014787	0.011978	0.009899	0.008318	0.007087	0.006111	0.005323	0.004679	0	0	0	0	0	0	0	0	0	0	0	0	0	0
12 12.5	0	0	0	0	0	0	0	0.015416	0.012487	0.01032	0.008672	0.007389	0.006371	0.00555	0	0	0	0	0	0	0	0	0	0	0	0	0	0	0
12.5 13	0	0	0	0	0	0	0	0.016046	0.012997	0.010741	0.009026	0.007669	0.006631	0	0	0	0	0	0	0	0	0	0	0	0	0	0	0	0
13 13.5	0	0	0	0	0	0	0	0.016675	0.013507	0.011163	0.00938	0.007992	0.006891	0	0	0	0	0	0	0	0	0	0	0	0	0	0	0	0
13.5 14	0	0	0	0	0	0	0	0	0.014016	0.011584	0.009734	0.008294	0	0	0	0	0	0	0	0	0	0	0	0	0	0	0	0	0
14 14.5	0	0	0	0	0	0	0	0	0.014526	0.012005	0.010087	0.008595	0	0	0	0	0	0	0	0	0	0	0	0	0	0	0	0	0
14.5 15	0	0	0	0	0	0	0	0	0	0.015036	0.012426	0.010441	0	0	0	0	0	0	0	0	0	0	0	0	0	0	0	0	0
15 15.5	0	0	0	0	0	0	0	0	0	0	0.012847	0	0	0	0	0	0	0	0	0	0	0	0	0	0	0	0	0	0

Breaking Wave Limit (Deep)	0.0227	0.0227	0.0227	0.0227	0.0227	0.0227	0.0227	0.0227	0.0227																				
Linear Wave Limit	0.002	0.002	0.002	0.002	0.002	0.002	0.002	0.0018	0.0018	0.0017	0.0016	0.0015	0.0014	0.0014	0.0012	0.0012	0.001	0.001	0.0007	0.0007	0.0007	0.0007	0.0007	0.0007	0.0003	0.0003	0.0003	0.0003	0.0003
d/(gT ^ 2) =	4	2	0.8	0.5	0.3	0.2	0.2	0.1	0.1	0.09	0.07	0.06	0.05	0.05	0.04	0.04	0.04	0.03	0.03	0.03	0.02	0.02	0.02	0.02	0.02	0.01	0.01	0.01	0.01

Deep Water Waves

Intermediate Water Waves

Legend

= Linear

= NonLinear

= Breaking

APPENDIX E

Main Characteristics of Applied ODE Solvers

Numerous methods have been developed to solve ODEs using different numerical schemes. ODE solvers, here denoted by f_{ODE}, are distinguished based on the numerical method that is applied to compose the algorithm. In this section, the main characteristics of a number of numerical methods will be clarified.

E.1 Explicit Versus Implicit Methods

The distinction between explicit and implicit solvers are based on the conditions that are used to calculate the solution at any time step. More specifically, if the state of the system at time instant t_{i+1} is only based on the solution in the previous step(s), the method is explicit:

$$\boldsymbol{q}_{i+1} = f_{ODE}(\boldsymbol{q}_i) + O(\Delta t^{\epsilon}) \quad \text{[E-1]}$$

where ϵ is the order of the local truncation error.

If the state of the system at time instant t_{i+1} is also based on the solution in the current step, the method is implicit:

$$\boldsymbol{q}_{i+1} = f_{ODE}(\boldsymbol{q}_i, \boldsymbol{q}_{i+1}) + O(\Delta t^{\epsilon}) \quad \text{[E-2]}$$

E.2 Order of Truncation Error

The local truncation error $O(\Delta t^{\epsilon})$ is a direct result of the fact that all numerical methods are discretised approximations of the analytical solution, based on a Taylor-series expansion. The order to which the expansion is taken determines the accuracy of the approximated solution at each time step. The order of this error is called the local truncation error; the higher the order, the lower the local errors. As an example, the generic problem as shown in Equation [E-3] will be elaborated using the Forward Euler method. To find the local truncation error, the Taylor series expansion (TSE) of the arbitrary function $x(t)$ is applied near the time instant t_i and evaluated at the following time step $t_{i+1} = t_i + \Delta t$. Since the Forward Euler method is a first order method, the TSE is applied until the 2nd order:

$$x(t_{i+1}) = x(t_i) + \frac{t_{i+1} - t_i}{1!} * \left.\frac{\partial x}{\partial t}\right|_{t=t_i} + O(\Delta t^2) \quad \text{[E-3]}$$

Rewriting this expression in discretized manner, the approximation of $x(t)$ at t_{i+1} can be found using the state of the system during the previous time step. The velocity of $x(t)$ at t_{i+1} is approximated by deriving the expression in Equation [E-4] to time:

$$x_{i+1} = x_i + \Delta t \dot{x}_i + O(\Delta t^2) \quad \text{[E-4]}$$

$$\dot{x}_{i+1} = \dot{x}_i + \Delta t \ddot{x}_i + O(\Delta t^2) \quad \text{[E-5]}$$

where the acceleration can be calculated using the generic form of the EOM: $\ddot{x}_i = m^{-1}\left(-c\dot{x}_i - kx_i + F(t_i)\right)$.

In this case, the ODE solver function can be represented as:

$$f_{ODE}(\boldsymbol{q}_i) = \begin{bmatrix} x_i + \Delta t \dot{x}_i \\ \dot{x}_i + \Delta t * m^{-1}\left(-c\dot{x}_i - kx_i + F(t_i)\right) \end{bmatrix} \quad \text{[E-6]}$$

Accumulation of errors at a time instant t^* after the start of simulation is called the global truncation error (GTE) and its order can be calculated using the following relation:

$$GTE = \frac{t^*}{\Delta t} * O(\Delta t^{\epsilon}) \quad \text{[E-7]}$$

$$\epsilon_{global} = \epsilon - 1 \quad \text{[E-8]}$$

E.3 Time Stepping

Other integration schemes approximate the solution by truncating the TSE at higher order or by applying adaptive time stepping. The latter is a method to minimize the local error by varying Δt at each time step to match the acceptable error magnitude, besides increasing ϵ for the complete simulation. The purpose of such procedure is to achieve accuracy with minimum computational effort.

E.4 Linear Multi-Step Versus Runge-Kutta Methods

In general, numerical methods can be categorized in two groups: Linear multi-step solvers and Runge-Kutta solvers. Although many variations exist of both groups, only those methods will be discussed that are integrated in the Matlab ODE solvers.

Linear multi-step methods

Linear multi-step methods approximate the solution as a *weighted summation* of the solutions at a number of previous time steps. These methods are distinguished by the number of steps, whether the solver is explicit or implicit and the coefficients that are multiplied with the function values. In implicit linear multi-step methods, not only solutions at previous time steps are used, but also the solution at the current time instant. Implicit linear-multistep solvers include, amongst others, the Adams-Moulton methods, the trapezoidal rule and the

Backward Differentiation Formulas (BDFs). Examples of explicit linear multi-step methods are the Euler method and Adams-Bashforth method. A mathematical representation of the explicit linear multi-step method is shown in Equation [E-9] and the implicit variant is represented by Equation [E-10]:

$$\boldsymbol{q}_{i+1} = f_{ODE}(\boldsymbol{q}_{i-M+1}, \boldsymbol{q}_{i-M+2}, \dots, \boldsymbol{q}_i) + O(\Delta t^{\epsilon}) \ , for\ M = 1,2,3 \dots \infty \quad [E\text{-}9]$$

$$\boldsymbol{q}_{i+1} = f_{ODE}(\boldsymbol{q}_{i-M+1}, \boldsymbol{q}_{i-M+2}, \dots, \boldsymbol{q}_{i+1}) + O(\Delta t^{\epsilon}) \ , for\ M = 1,2,3 \dots \infty \quad [E\text{-}10]$$

where the integer M represents the maximum number of steps that are used to calculate the solution at time step t_{i+1}. If $M = 1$, the method is called a single-step or one-step method.

An explicit linear 3-step solver is visually represented in Figure E - 1:

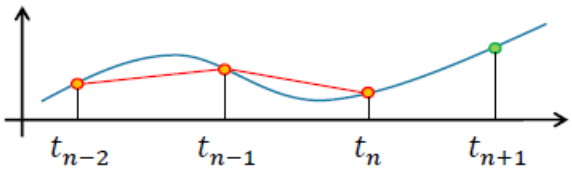

Figure E - 1: An Explicit Linear 3-Step Solver

The classical Runge-Kutta method

The classical Runge-Kutta method evaluates solutions at *4 intermediate steps* between the current step and the adjacent step. At each consecutive intermediate step, the new value and increment are calculated, after which the value of the intermediate step is recalculated based on the new increment. This procedure is continued four times, until the neighbouring time step is reached. A visual representation of this procedure for the solution between time steps 0 and 1 is shown in Figure E - 2. A mathematical representation of the solution scheme is given in Equation [E-11], from which can be seen that the RK4 method is a single-step method with local truncation order of 5.

$$\boldsymbol{q}_{i+1} = f_{ODE}(\boldsymbol{q}_i) + O(\Delta t^5) \quad [E\text{-}11]$$

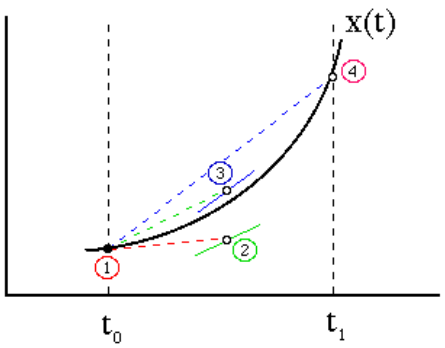

Figure E - 2: Runge-Kutta Algorithm

E.5 Predictor-Corrector Algorithms

It is often necessary for implicit linear multi-step methods to implement a so-called predictor-corrector method. From Equation [E-10], it is clear that the unknown value $\boldsymbol{q_{i+1}}$ appears at both the right-hand side as well as the left-hand side of the equation. The predictor-corrector algorithm is an efficient technique to get around this difficulty.

This feature uses an explicit method to obtain a first, rough estimate of the curve. Subsequently, an implicit method is applied to refine the predicted value. This procedure can be repeated several times, depending on the code and the allowed error tolerance [87].

E.6 Stiff Versus Non-Stiff Problems

Generally, stiff problems can be described as differential equations, consisting of terms that can cause numerical instability unless the time step size is extremely small. According to J.D. Lambert [88], the following definition of stiffness can be applied:

> *"If a numerical method with a finite region of absolute stability, applied to a system with any initial conditions, is forced to use in a certain interval of integration a steplength which is excessively small in relation to the smoothness of the exact solution in that interval, then the system is said to be stiff in that interval."*

When solving ODEs numerically, it is expected that the time step size is taken smaller in regions where the increment of the curve is relatively large, in order to restrain the magnitude of errors. When solving stiff problems, it may occur that although the curve shows minor variation, the numerical method requires time step sizes that are unacceptably small. This phenomenon is a computational property that relates to the interaction of the applied numerical method with the considered ODE. Although not necessarily, explicit methods are generally used to solve non-stiff problems. Stiff problems are almost always easier solved by implicit codes compared to explicit solvers. One must therefore assure that the solver is suitable for the problem [89].

APPENDIX F

Formulation of Sectional Stresses

F.1 Sectional Forces in Pontoon 1

The cross-sectional normal force, shear force in the local y-axis and shear force in the local z-axis in pontoon 1 are depicted in Equations [F-1], [F-2] and [F-3], respectively. The cross-sectional moments about the local x-, y- and z-axis in pontoon 1 are expressed as shown in Equations [F-4], [F-5] and [F-6].

$$N_1 = \sum_{i=1}^{N_{box}} \left(\frac{\sqrt{3}}{2} \left(F_{hyd,i}^{Y} + F_{in,i}^{Y} \right) - \frac{1}{2} \left(F_{hyd,i}^{X} + F_{in,i}^{X} \right) \right) + \frac{\sqrt{3}}{2} F_{T,1}^{Y} - \frac{1}{2} F_{T,1}^{X} P_{h,1} W_{box} H_{box} \quad \text{[F-1]}$$

$$V_{y,1} = \sum_{i=1}^{N_{box}} \left(\frac{\sqrt{3}}{2} \left(F_{hyd,i}^{X} + F_{in,i}^{X} \right) + \frac{1}{2} \left(F_{hyd,i}^{Y} + F_{in,i}^{Y} \right) \right) + \frac{\sqrt{3}}{2} F_{T,1}^{X} + \frac{1}{2} F_{T,1}^{Y} \quad \text{[F-2]}$$

$$V_{z,1} = \sum_{i=1}^{N_{box}} \left(F_{hyd,i}^{Z} + F_{in,i}^{Z} \right) + F_{T,1}^{Z} + P_{v,1} L_{box} W_{box} \quad \text{[F-3]}$$

$$M_{x,1} = -K_t \cdot \left(\frac{1}{2} \eta_4 + \frac{\sqrt{3}}{2} \eta_5 \right) + e_M \cdot \left(\frac{\sqrt{3}}{2} F_{T,1}^{X} + \frac{1}{2} F_{T,1}^{Y} \right) \quad \text{[F-4]}$$

$$M_{y,1} = -\left(\sum_{i=1}^{N_{box}} \left(r_i - \frac{D_{mid}}{2} \right) \cdot \left(F_{hyd,i}^{Z} + F_{in,i}^{Z} \right) + F_{T,1}^{Z} \cdot L_{box} + \frac{1}{2} P_{v,1} L_{box}^2 W_{box} \right) \quad \text{[F-5]}$$

$$M_{z,1} = -\left(\sum_{i=1}^{N_{box}} \left(r_i - \frac{D_{mid}}{2} \right) \cdot \left(\frac{\sqrt{3}}{2} \left(F_{hyd,i}^{X} + F_{in,i}^{X} \right) + \frac{1}{2} \left(F_{hyd,i}^{Y} + F_{in,i}^{Y} \right) \right) + \left(\frac{\sqrt{3}}{2} F_{T,1}^{X} + \frac{1}{2} F_{T,1}^{Y} \right) \cdot L_{box} \right) \quad \text{[F-6]}$$

where:

- i is the number of the discretized body;
- N_{box} is the number of pontoon segments per pontoon;
- $\underline{F}_{in,i}$ is the inertial force vector of segment i;
- r_i is the perpendicular distance from the position of the cross-section to the CoG of segment i;
- e_M is the eccentricity of the mooring forces with the centroid of the pontoon cross-section.

F.2 Sectional Forces in Pontoon 2

The cross-sectional normal force, shear force in the local y-axis and shear force in the local z-axis in pontoon 2 are depicted in Equations [F-7], [F-8] and [F-9], respectively. The cross-sectional moments about the local x-, y- and z-axis in pontoon 2 are expressed as shown in Equations [F-10], [F-11] and [F-12].

$$N_2 = \sum_{i=N_{box}+1}^{2N_{box}} \left(F_{hyd,i}^X + F_{in,i}^X\right) + F_{T,2}^X + P_{h,2} W_{box} H_{box} \quad \text{[F-7]}$$

$$V_{y,2} = \sum_{i=N_{box}+1}^{2N_{box}} \left(F_{hyd,i}^Y + F_{in,i}^Y\right) + F_{T,2}^Y \quad \text{[F-8]}$$

$$V_{z,2} = \sum_{i=N_{box}+1}^{2N_{box}} \left(F_{hyd,i}^Z + F_{in,i}^Z\right) + F_{T,2}^Z + P_{v,2} L_{box} W_{box} \quad \text{[F-9]}$$

$$M_{x,2} = -K_t \cdot \eta_4 + e_M \cdot F_{T,2}^Y \quad \text{[F-10]}$$

$$M_{y,2} = -\left(\sum_{i=N_{box}+1}^{2N_{box}} \left(r_i - \frac{D_{mid}}{2}\right) \cdot \left(F_{hyd,i}^Z + F_{in,i}^Z\right) + F_{T,2}^Z \cdot L_{box} + \frac{1}{2} P_{v,2} L_{box}^2 W_{box} \right) \quad \text{[F-11]}$$

$$M_{z,2} = -\left(\sum_{i=N_{box}+1}^{2N_{box}} \left(r_i - \frac{D_{mid}}{2}\right) \cdot \left(F_{hyd,i}^Y + F_{in,i}^Y\right) + F_{T,2}^Y \cdot L_{box} \right) \quad \text{[F-12]}$$

F.3 Sectional Forces in Pontoon 3

The cross-sectional normal force, shear force in the local y-axis and shear force in the local z-axis in pontoon 3 are depicted in Equations [F-13], [F-14] and [F-15], respectively. The cross-sectional moments about the local x-, y- and z-axis in pontoon 3 are expressed as shown in Equations [F-16], [F-17] and [F-18].

$$N_3 = -\sum_{i=2N_{box}+1}^{3N_{box}} \left(\frac{\sqrt{3}}{2}\left(F_{hyd,i}^Y + F_{in,i}^Y\right) + \frac{1}{2}\left(F_{hyd,i}^X + F_{in,i}^X\right) \right) + \frac{\sqrt{3}}{2} F_{T,3}^Y + \frac{1}{2} F_{T,3}^X + P_{h,3} W_{box} H_{box} \quad \text{[F-13]}$$

$$V_{y,3} = \sum_{i=2N_{box}+1}^{3N_{box}} \left(\frac{1}{2}\left(F_{hyd,i}^Y + F_{in,i}^Y\right) - \frac{\sqrt{3}}{2}\left(F_{hyd,i}^X + F_{in,i}^X\right) \right) + \frac{1}{2} F_{T,3}^Y - \frac{\sqrt{3}}{2} F_{T,3}^X \quad \text{[F-14]}$$

$$V_{z,3} = \sum_{i=2N_{box}+1}^{3N_{box}} \left(F_{hyd,i}^Z + F_{in,i}^Z\right) + F_{T,3}^Z + P_{v,3} L_{box} W_{box} \quad \text{[F-15]}$$

$$M_{x,3} = -K_t \cdot \left(\frac{1}{2}\eta_4 - \frac{\sqrt{3}}{2}\eta_5 \right) + e_M \cdot \left(\frac{1}{2} F_{T,3}^Y - \frac{\sqrt{3}}{2} F_{T,3}^X \right) \quad \text{[F-16]}$$

$$M_{y,3} = -\left(\sum_{i=2N_{box}+1}^{3N_{box}} \left(r_i - \frac{D_{mid}}{2} \right) \cdot \left(F_{hyd,i}^{Z} + F_{in,i}^{Z} \right) + F_{T,3}^{Z} \cdot L_{box} + \frac{1}{2} P_{v,3} L_{box}^2 W_{box} \right) \quad \text{[F-17]}$$

$$\begin{aligned} M_{z,3} = -\Bigg(\sum_{i=2N_{box}+1}^{3N_{box}} \left(r_i - \frac{D_{mid}}{2} \right) \cdot \left(\frac{1}{2} \left(F_{hyd,i}^{Y} + F_{in,i}^{Y} \right) - \frac{\sqrt{3}}{2} \left(F_{hyd,i}^{X} + F_{in,i}^{X} \right) \right) \\ + \left(\frac{1}{2} F_{T,3}^{Y} - \frac{\sqrt{3}}{2} F_{T,3}^{X} \right) \cdot L_{box} \Bigg) \end{aligned} \quad \text{[F-18]}$$

F.4 Sectional Forces in Central Column

The cross-sectional normal force, shear force in the local y-axis and shear force in the local z-axis in the central column are depicted in Equations [F-19], [F-20] and [F-21], respectively. The cross-sectional moments about the local x-, y- and z-axis in the central column are expressed as shown in Equations [F-22], [F-23] and [F-24].

$$\begin{aligned} N_t = \sum_{i=1}^{N_{tower}} \left(F_{aero,i}^{Z} + F_{in,i}^{Z} \right) + F_{hyd,trans}^{Z} + F_{in,trans}^{Z} + F_{in,RNA}^{Z} + F_{RNA}^{Z} + P_{v,mid} \\ \cdot \frac{1}{4} \pi D_{mid}^2 \end{aligned} \quad \text{[F-19]}$$

$$V_{x,t} = \sum_{i=1}^{N_{tower}} \left(F_{aero,i}^{X} + F_{in,i}^{X} \right) + F_{hyd,trans}^{X} + F_{in,trans}^{X} + F_{in,RNA}^{X} + F_{RNA}^{X} \quad \text{[F-20]}$$

$$V_{y,t} = \sum_{i=1}^{N_{tower}} \left(F_{aero,i}^{Y} + F_{in,i}^{Y} \right) + F_{hyd,trans}^{Y} + F_{in,trans}^{Y} + F_{in,RNA}^{Y} + F_{RNA}^{Y} \quad \text{[F-21]}$$

$$\begin{aligned} M_{x,t} = \sum_{i=1}^{N_{tower}} -\left(Z_{CoG,i} + KG + H_{mid} \right) \cdot \left(F_{aero,i}^{Y} + F_{in,i}^{Y} \right) \\ - \left(Z_{CoB,trans} + KG + H_{mid} \right) \cdot F_{hyd,trans}^{Y} \\ - \left(Z_{CoG,trans} + KG + H_{mid} \right) \cdot F_{in,trans}^{Y} \\ - \left(Z_{CoG,RNA} + KG + H_{mid} \right) \cdot \left(F_{in,RNA}^{Y} + F_{RNA}^{Y} \right) \end{aligned} \quad \text{[F-22]}$$

$$\begin{aligned} M_{y,t} = \sum_{i=1}^{N_{tower}} \left(Z_{CoG,i} + KG + H_{mid} \right) \cdot \left(F_{aero,i}^{X} + F_{in,i}^{X} \right) \\ + \left(Z_{CoB,trans} + KG + H_{mid} \right) \cdot F_{hyd,trans}^{X} \\ + \left(Z_{CoG,trans} + KG + H_{mid} \right) \cdot F_{in,trans}^{X} \\ + \left(Z_{CoG,RNA} + KG + H_{mid} \right) \cdot \left(F_{in,RNA}^{X} + F_{RNA}^{X} \right) - e_{x,RNA} \\ \cdot \left(F_{in,RNA}^{Z} + F_{RNA}^{Z} \right) + M_{gyro}^{Y} \end{aligned} \quad \text{[F-23]}$$

$$M_{z,t} = M_{gyro}^{Z} \quad \text{[F-24]}$$

where:

- i is the number of the discretized tower segment;
- N_{tower} is the number of tower segments;

- $\underline{F}_{in,RNA}$ and $\underline{F}_{in,trans}$ are the inertial force vector of the RNA and submerged parts of the central column, respectively;
- V_{trans} and m_{trans} are, respectively, the displaced volume and dry mass of the submerged parts of the central column;
- $m_{turbine}$ is the total mass of the turbine;
- H_{mid} is the height of the mid-section;
- $e_{x,RNA}$ is the eccentricity of the RNA-CoG in the X-direction w.r.t. to the CoG of the total structure.

F.5 Sectional Stresses

The method of determining the sectional stresses was introduced in Section 3.7 and in this section, further elaborations will be presented. The normal stresses and shear stress in the pontoons, as introduced before, are as shown in Equations [F-25] to [F-27].

$$\sigma_{x,j} = \frac{N_j}{A^x_{s,box}} + \frac{M_{z,j} \cdot y_{max}}{I_{z,box}} + \frac{M_{y,j}}{I_{y,box}} \cdot \frac{H_{box}}{2} \quad [F\text{-}25]$$

$$\sigma_{y,j} = P_{h,j} \cdot \frac{H_{box} L_{box}}{A^y_{s,box}} \quad [F\text{-}26]$$

$$\tau_{xy,j} = \frac{V_{z,j} Q_z}{I_{z,box} \cdot t_{top}} + \frac{V_{y,j} Q_y}{I_{y,box} \cdot t_{top}} + \frac{M_{x,j}}{2A_{in,box} \cdot t_{top}} \quad [F\text{-}27]$$

where the cross-sectional distance along the local y-axis is given by:

$$y_{max} = \begin{cases} 0, & Hotspots \left\{P_{1,i}, P_{2,i}, P_{3,i}\right\} \\ \frac{W_{box}}{2}, & Hotspots \left\{P_{1,ii}, P_{2,ii}, P_{3,ii}\right\} \end{cases} \quad [F\text{-}28]$$

The first moments of the area at the locations where the shear stress is calculated are derived using Equations [F-29] and [F-30].

$$Q_z = A_{Vz} \cdot \frac{H_{box} - t_{top}}{2} \quad [F\text{-}29]$$

$$Q_y = A_{Vy} \cdot \frac{W_{box} - t_{side}}{2} \quad [F\text{-}30]$$

where

$$A_{Vz} = \begin{cases} 0, & Hotspots \left\{P_{1,i}, P_{2,i}, P_{3,i}\right\} \\ \frac{1}{2} W_{box} t_{top}, & Hotspots \left\{P_{1,ii}, P_{2,ii}, P_{3,ii}\right\} \end{cases} \quad [F\text{-}31]$$

and

$$A_{Vy} = \begin{cases} \frac{H_{box} \cdot t_{side} + \left(\frac{W_{box}}{2} - \frac{3}{2} \cdot t_{side}\right) \cdot t_{top}}{2}, & Hotspots \left\{P_{1,i}, P_{2,i}, P_{3,i}\right\} \\ \frac{H_{box} \cdot t_{side}}{2}, & Hotspots \left\{P_{1,ii}, P_{2,ii}, P_{3,ii}\right\} \end{cases} \quad [F\text{-}32]$$

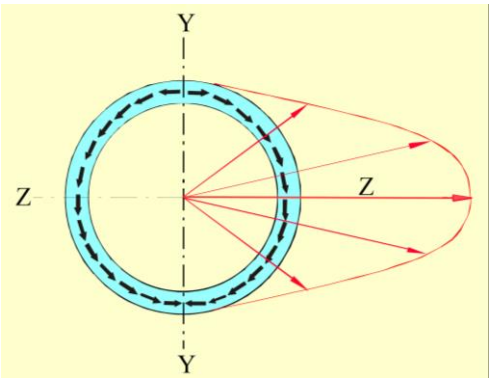

Figure F - 1: Shear Stress Distribution in a Thin-Walled Cylinder

The normal stresses and shear stress in the cross-section of the mid-section are, as introduced before, shown in Equations [F-33] to [F-35].

$$\sigma_{z,t} = \frac{N_t}{A_{s,t}} + \frac{M_{x,t}}{I_{x,t}} \cdot \frac{D_{mid}}{2} \cdot \cos(\alpha) + \frac{M_{y,t}}{I_{y,t}} \cdot \frac{D_{mid}}{2} \cdot \sin(\alpha) \quad \text{[F-33]}$$

$$\sigma_{y,t} = -P_{h,mid} \cdot \left(\frac{D_{mid}^2 + D_{mid,in}^2}{D_{mid}^2 - D_{mid,in}^2} \right) \quad \text{[F-34]}$$

$$\tau_{zy,t} = \frac{2 \cdot V_{x,t} \cdot \sin(\alpha)}{\pi D_{mid} t_{mid}} + \frac{2 \cdot V_{y,t} \cdot \cos(\alpha)}{\pi D_{mid} t_{mid}} + \frac{M_{z,t}}{J_t} \cdot \frac{D_{mid}}{2} \quad \text{[F-35]}$$

where α denotes the position along the cross section of the mid-section. this dependency on the angle α is clearly visible when considering, for example, the shear stress distribution in a thin-walled cylinder due to an arbitrary shear force, as shown in Figure F - 1.

APPENDIX G

Verification Results WindFlo TLP

G.1 Rigid Body Natural Modes

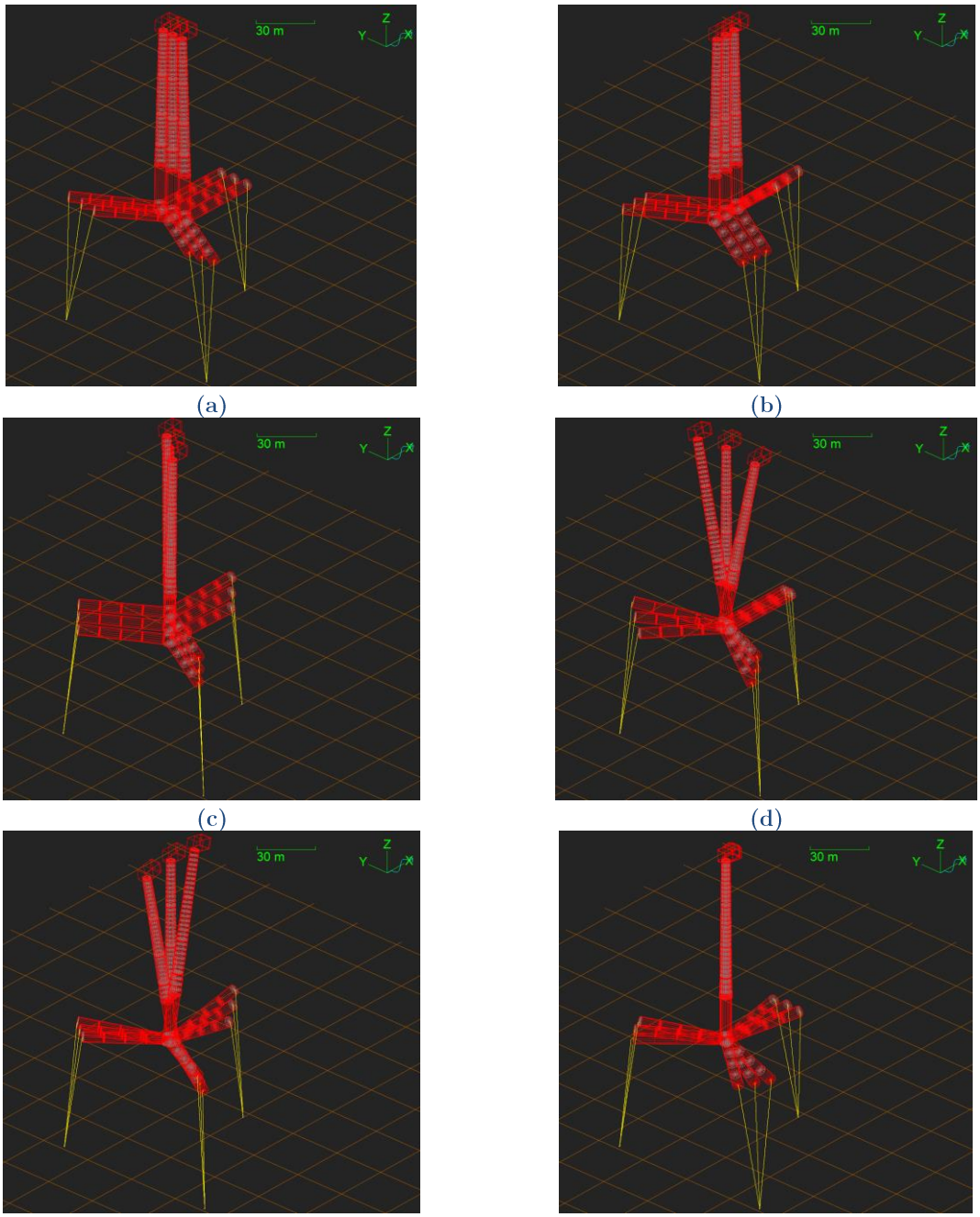

(a) (b) (c) (d) (e) (f)

Figure G - 1: Rigid Body Natural Modes of WindFlo TLP

G.2 Motion Response

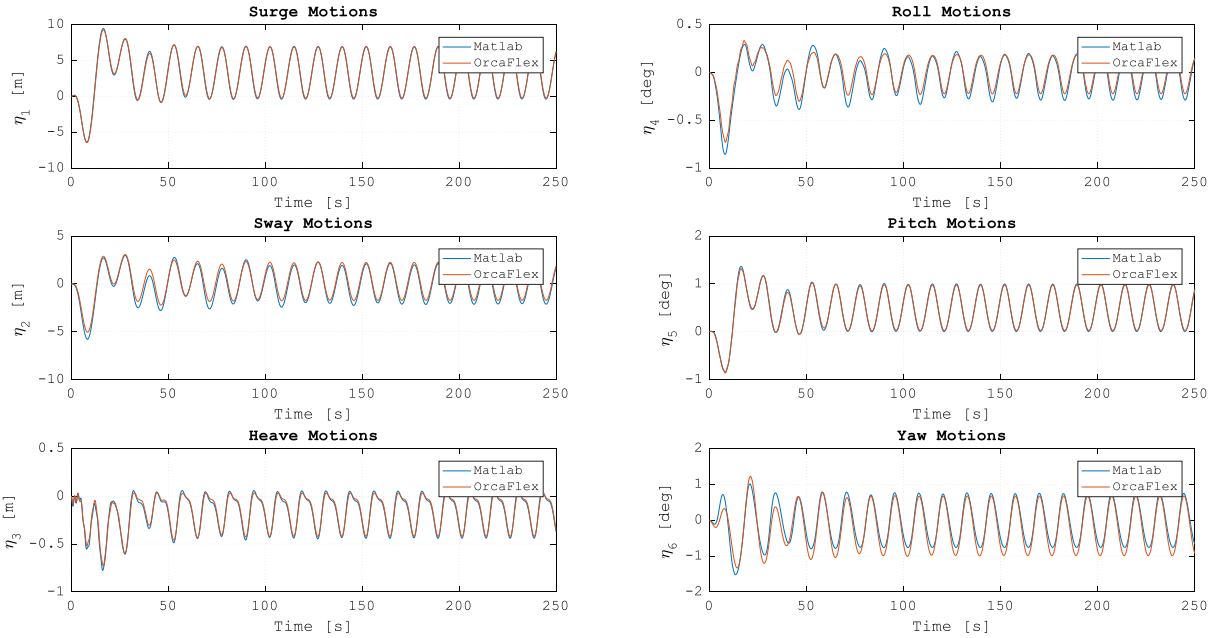

Figure G - 2: Displacements

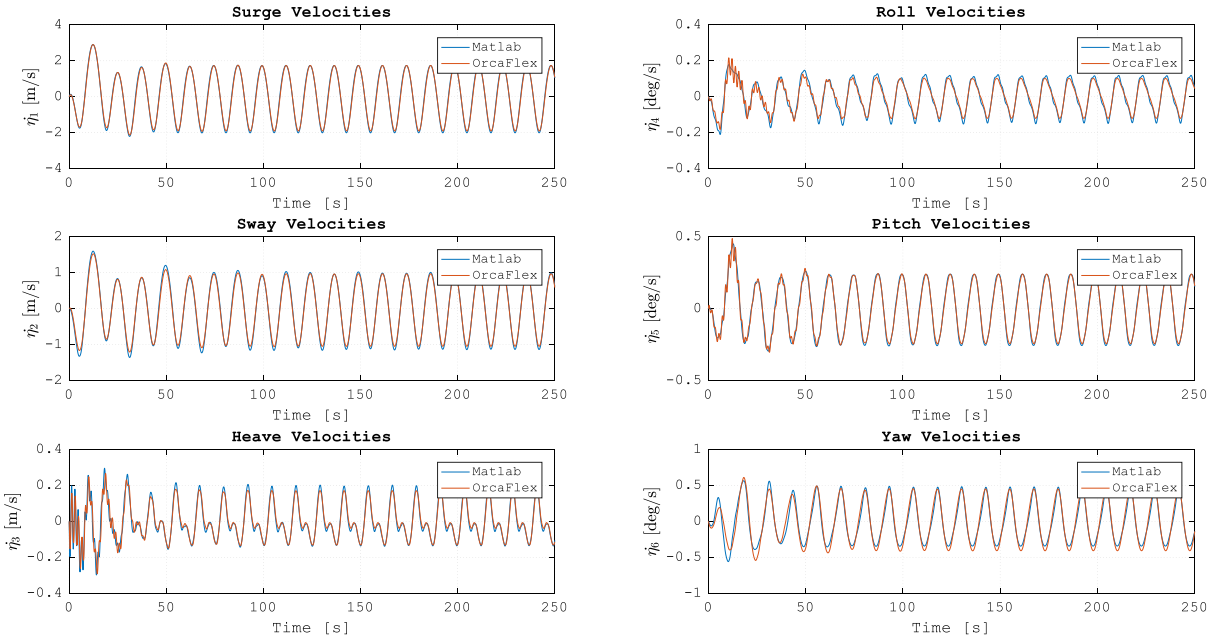

Figure G - 3: Velocities

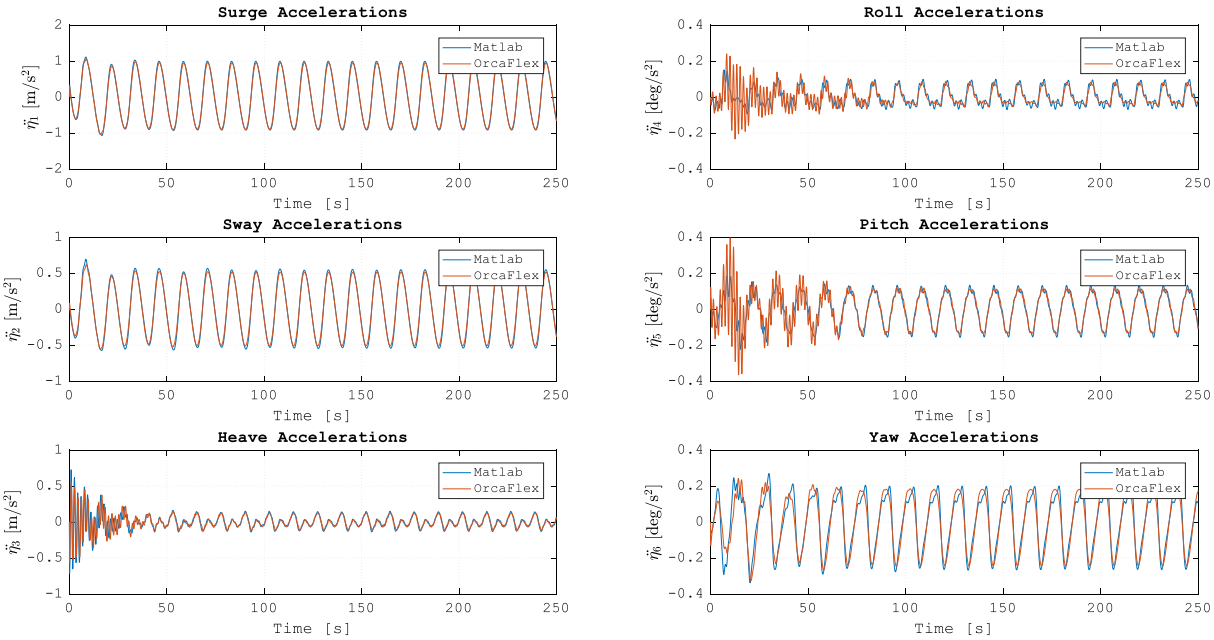

Figure G - 5: Accelerations

G.3 Mooring Load Response

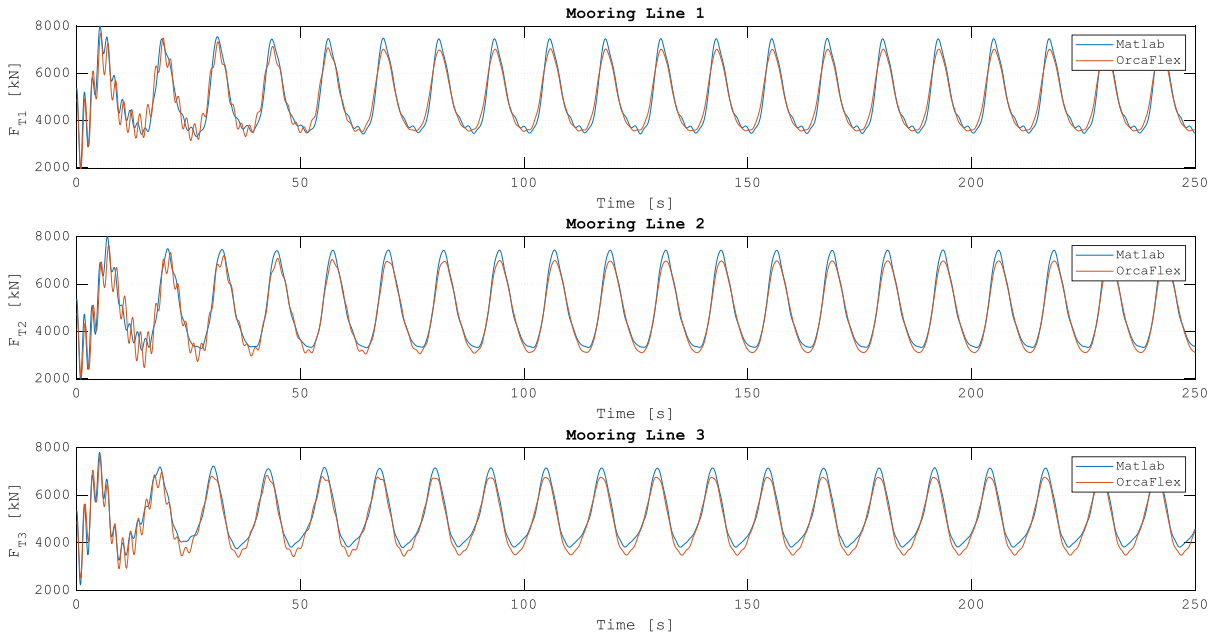

Figure G - 4: Mooring Loads

G.4 Verification of Normal Stress Response

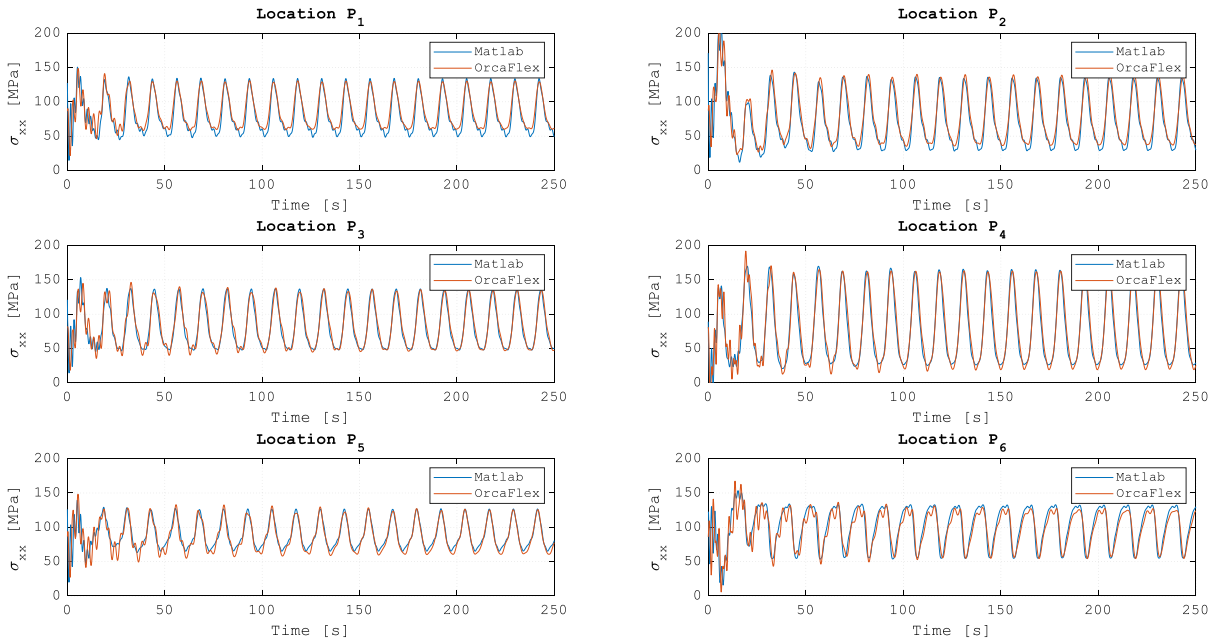

Figure G - 6: Axial Stresses at Pontoon Hotspots

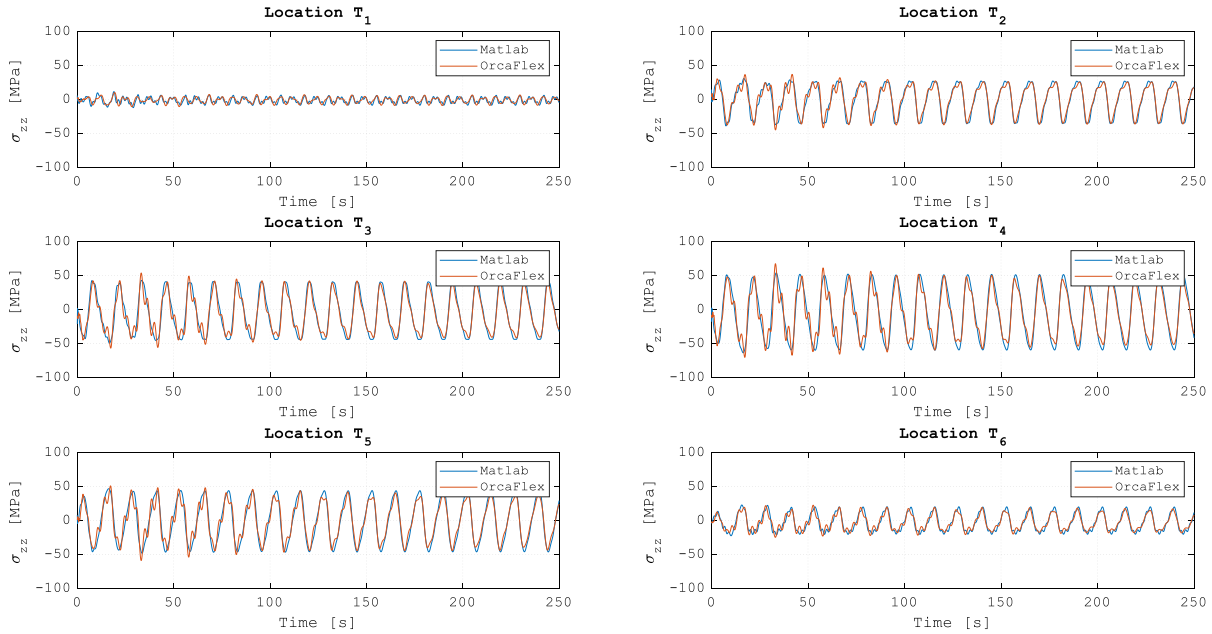

Figure G - 7: Axial Stresses at Mid-Section Hotspots

G.5 Verification of Shear Stress Response

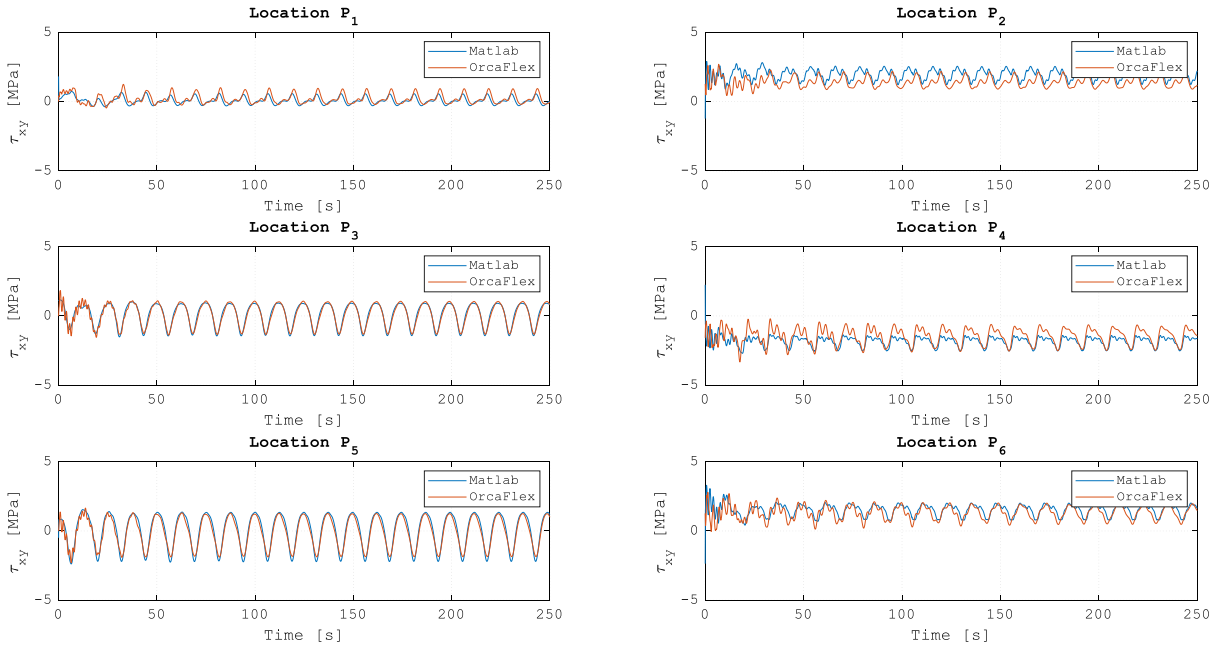

Figure G - 8: Shear Stresses at Pontoon Hotspots

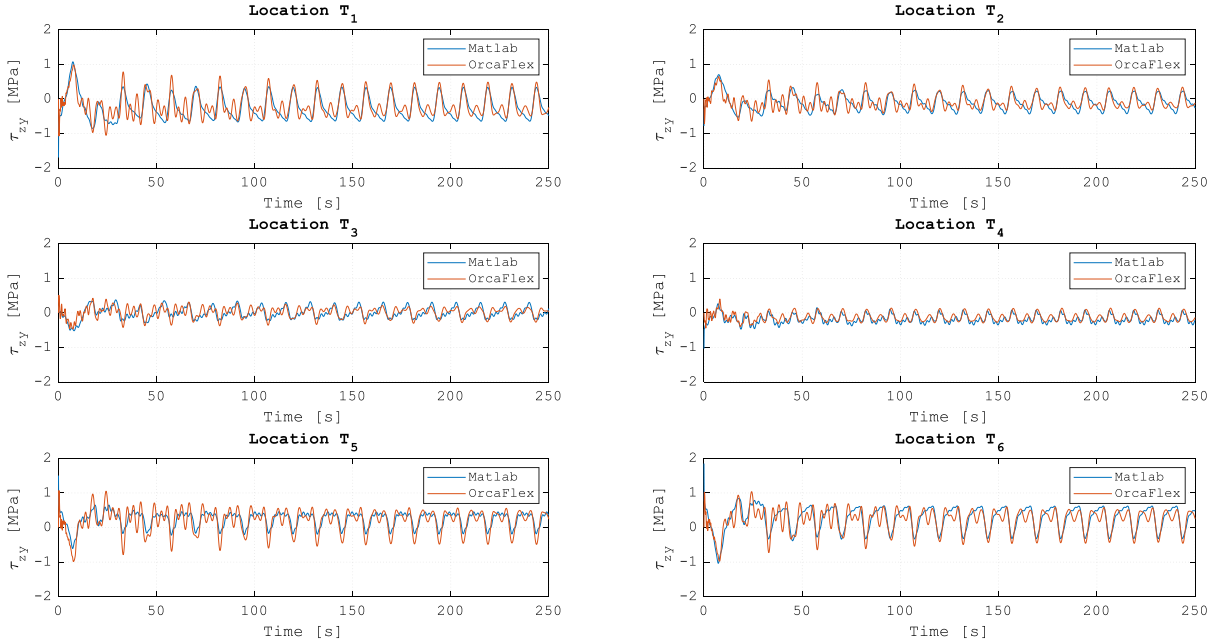

Figure G - 9: Shear Stresses at Mid-Section Hotspots

APPENDIX H

Derivations and Additional Results Flexibility Analysis

H.1 Derivation of Equivalent Tower Stiffness

The second moment of inertia of the tower varies along the longitudinal axis of the tower s, as a function of the local outer diameter and wall thickness according to the following expression:

$$I_p(s) = \frac{\pi}{4}\left(\left(\frac{D_{out}(s)}{2}\right)^4 - \left(\frac{D_{in}(s)}{2}\right)^4\right) \quad \text{[H-1]}$$

The distribution of the wall thickness is not fully continuous along s, and as a result, the second moment of inertia is non-continuously distributed as well. However, for the global deformation of the tower, a polynomial fit is considered to be sufficiently accurate. The actual and polynomial fitted second moment of inertia are plotted in Figure H - 1, in which the fitted polynomial is expressed as:

$$I_{zz,fit}(s) = 10.765 - 0.0005s^3 + 0.0359s^2 - 0.9447s \quad \text{[H-2]}$$

Assuming fully homogenous tower material, the equivalent out-of-plane bending stiffness of the tower is found by equating the maximum tip deflection according to an equivalent cantilever beam to the solution obtained by solving the Euler-Bernoulli differential equations for beam deformation. This approach involves solving the fourth spatial derivative of the beam deflection, given by Equation [H-3]. The result is a system of four equations with four unknowns.

Figure H - 1: Tower Second Moment of Inertia

$$\frac{d^2}{ds^2}\left(EI_{zz,fit}(s)\frac{d^2w}{ds^2}\right) = q(s) \quad \text{[H-3]}$$

$$V(s) = -\int q(s)ds + C_1 \quad \text{[H-4]}$$

$$M(s) = \int V(s)ds + C_2 \quad \text{[H-5]}$$

$$\phi(s) = \frac{1}{EI_{zz,fit}(s)}\int M(s)\,ds + C_3 \quad \text{[H-6]}$$

$$w(s) = -\int \phi(s)\,ds + C_4 \quad \text{[H-7]}$$

where, in this case, $q(s) = 0$.

Using the boundary conditions of a cantilever beam $w(0) = \phi(0) = M(L_{tower}) = 0$ and $V(L_{tower}) = F_0$, the following continuous expression for maximum deflection is obtained:

$$w_{max} = w(L_{tower}) = -\int_0^{L_{tower}} \frac{F_0}{EI_{zz,fit}(s)}\left(\frac{s^2}{2} - s\right)ds \quad \text{[H-8]}$$

By equating the resulting expression to the maximum tip deflection of an equivalent cantilever beam, the equivalent prismatic cantilever beam bending stiffness of the tower is found as:

$$EI_{eq,t} = 3.645 * 10^{11} Nm^2$$

H.2 Additional Simulation Results

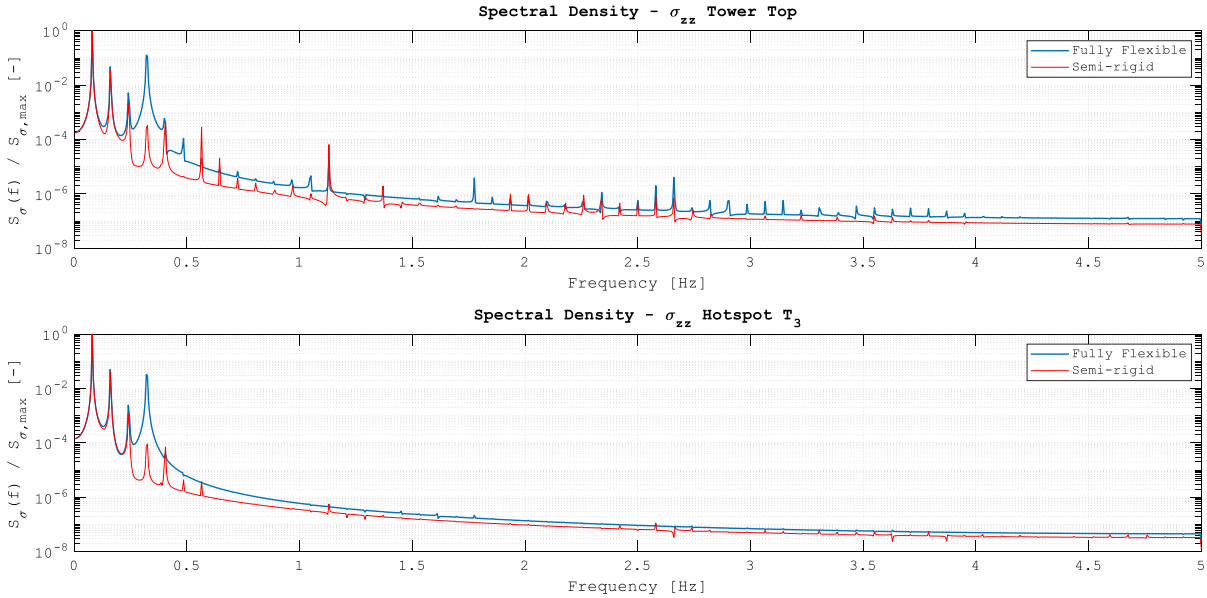

Figure H - 2: Comparison Stress PSDs of Fully Flexible and Semi-Rigid Model

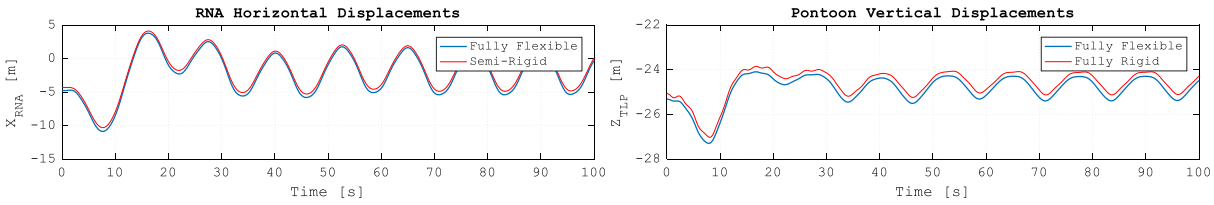

(a) (b)

Figure H - 3: Rigid and Flexible Body Displacements at RNA (a) and Pontoon Tip (b)

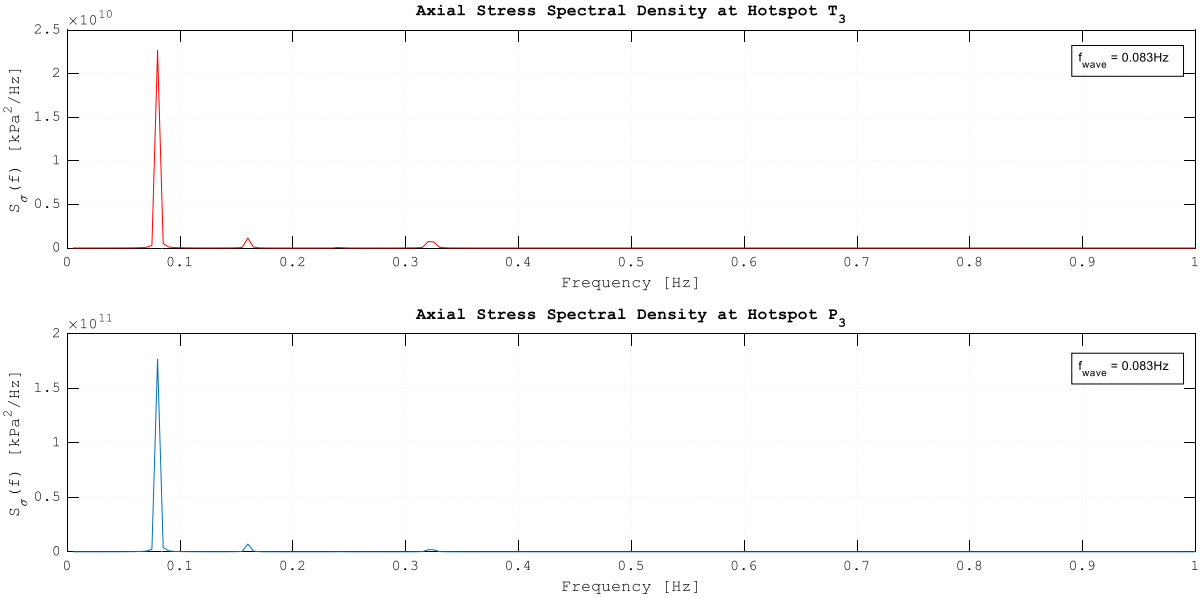

Figure H - 4: Stress PSDs on Linear Scale

APPENDIX I

Modelling of the Reference TLP

I.1 Detailed Geometric Description

In Table I - 1, a detailed overview is provided of the results of the reverse engineering approach discussed in Section 4.1.

Table I - 1: Reverse Engineering Results

Parameter	Symbol	Value	Unit
Platform width	$W_{platform}$	77.9	m
Diameter middle buoy	D_{inner}	9.1	m
Diameter side buoys	D_{sides}	9.8	m
Height middle buoy	H_{inner}	10.2	m
Height side buoys	H_{sides}	6.2	m
Height transition piece	$H_{transition}$	24.8	m
Length green braces	$L_{greenBrace}$	49.4	m
Length purple braces	$L_{purpleBrace}$	68.2	m
Length orange braces	$L_{orangeBrace}$	35.2	m
Length blue braces	$L_{blueBrace}$	27.6	m
Primary brace diameter	$D_{brace,primary}$	700	mm
Secondary brace diameter	$D_{brace,secondary}$	560	mm
Wall thickness buoys	t_{buoys}	60	mm
Brace wall thickness	t_{brace}	33.4	mm
Static Line length	L_0	59.1	m
Footprint breadth	W_T	21.5	m
Static Line angle	α	21.4	°
Water piercing area	A_{wp}	2.7	m^2
Displaced Volume Per Leg (maximum)	$\nabla_{leg,max}$	541.8	m^3
Displaced Volume Per Leg (operational)	$\nabla_{leg,op}$	492.3	m^3
Displaced Volume Middle Buoy	∇_{mid}	668.7	m^3
Keel to centre of gravity	KG	34.9	m
Keel to centre of buoyancy (operational)	KB	6.32	m
Platform Mass (double check)	$\widetilde{M}_p$	1225.2	t

I.2 Detailed Description of the SBM OrcaFlex Model

In Table I - 2, a detailed overview is provided of the parameters used as input for the SBM OrcaFlex model, discussed in Section 4.2.

Table I - 2: Input Parameters Modelling of Reference TLP

Parameter	Value	Unit
Water depth	80	m
Surface piercing buoy diameter	1.89	m
Surface piercing buoy length {submerged, total}	2, 4	m
Central buoy diameter	9.26	m
Central buoy height	10.2	m
Side buoy diameter	9.97	m
Side buoy height	6.2	m
Length from floater centre to end of side buoys	45	m
Draft	25	m
CoG of system (from keel)	32.7	m
Mass of Surface piercing buoy	522	t
Mass of Side buoy	277.3	t
Mass of Central buoy	393.3	t
Total mass of substructure	1225.2	t
Total mass of complete system (incl. turbine)	1747.2	t
Mass Moment of Inertia Surface piercing buoy {x, y, z}	365, 365, 382	tm^2
Mass Moment of Inertia Central buoy {x, y, z}	6857, 6857, 6914	tm^2
Mass Moment of Inertia Side buoy {x, y, z}	3713, 3713, 5650	tm^2
Static Mooring Line Angle	21.4	°
Static Mooring Line Length	63.64	m
Mooring Line diameter	0.05	m
Mooring Line Weight in air (chain)	0.055	tm^{-1}
Pretension {total, individual bundle}	4680, 1560	kN
Drag area Surface piercing buoy {normal, axial}	3.78, 2.81	m^2
Drag area Central buoy {normal, axial}	94.45, 67.35	m^2
Drag area Side buoys {normal, axial}	61.81, 78.07	m^2
Drag coefficients Surface piercing buoy {normal, axial}	0.6, 3.5	-
Drag coefficients Central buoy {normal, axial}	0.6, 3.5	-
Drag coefficients Side buoys {normal, axial}	0.6, 3.5	-
Added mass coefficients Surface piercing buoy {normal, axial}	1.35, 0	-
Added mass coefficients Central buoy {normal, axial}	1.35, 0	-
Added mass coefficients Side buoys {normal, axial}	1.35, 0	-

I.3 Results of RAO Validation with Published Data

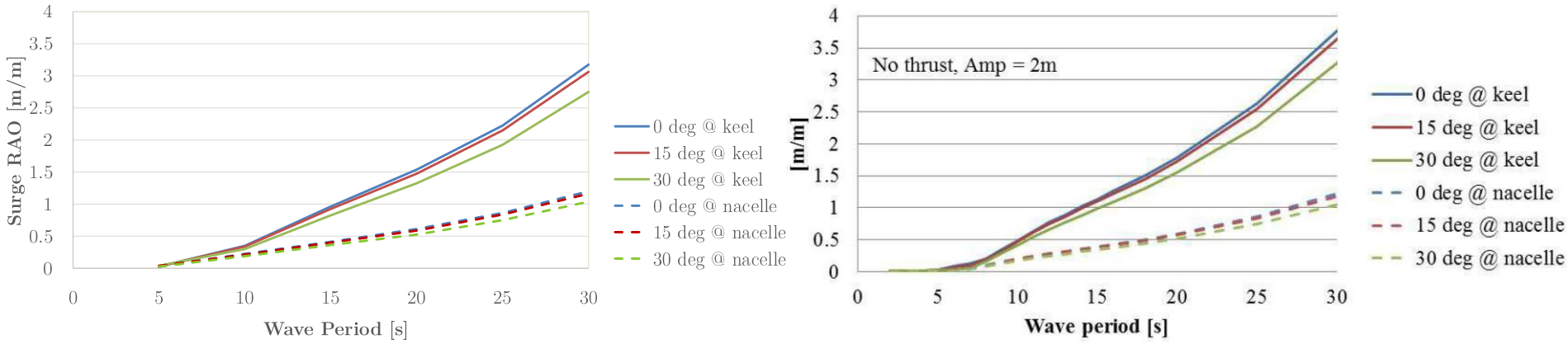

(a) (b)

Figure I - 1: Calculated (a) and Reference (b) Values of Motion RAOs for Case 1

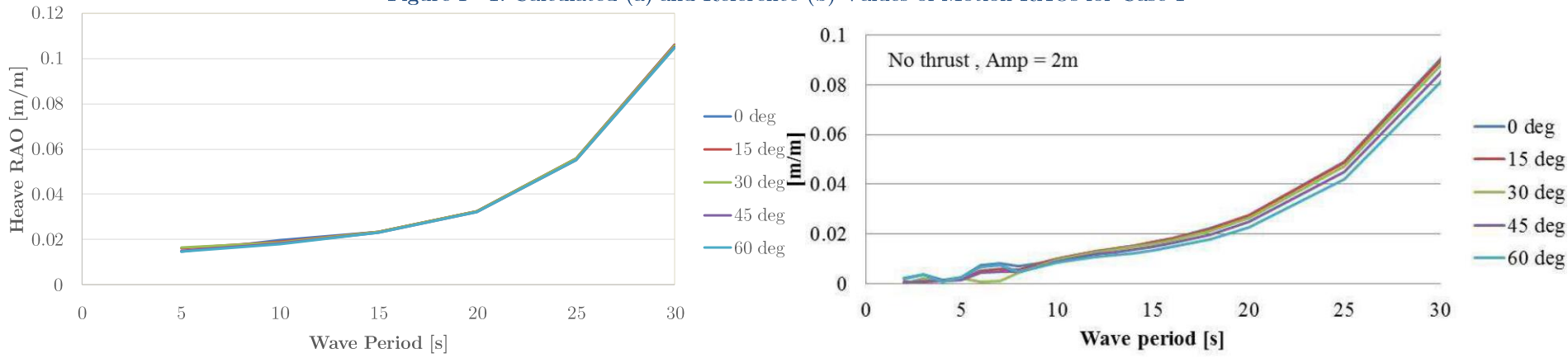

(a) (b)

Figure I - 2: Calculated (a) and Reference (b) Values of Motion RAOs for Case 2

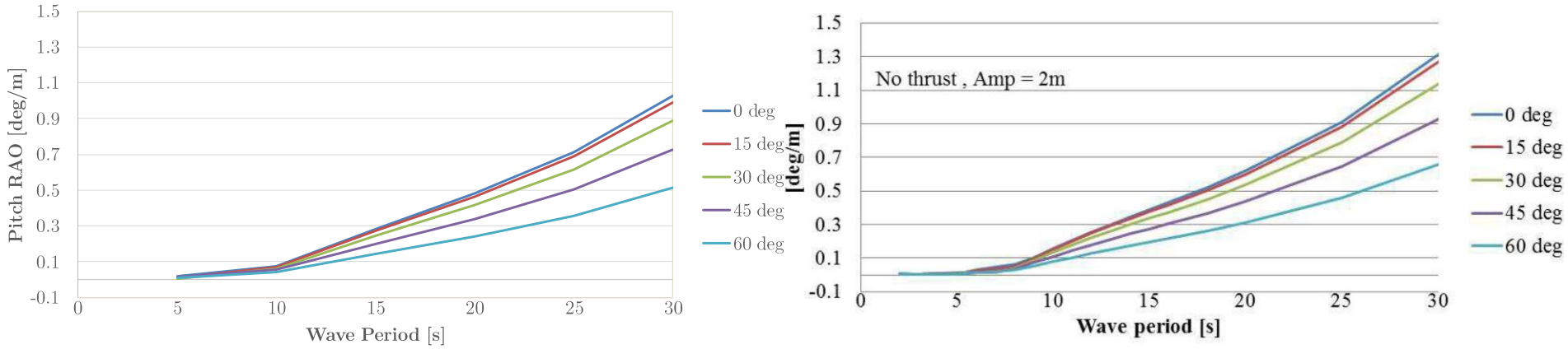

(a) (b)

Figure I - 3: Calculated (a) and Reference (b) Values of Motion RAOs for Case 3

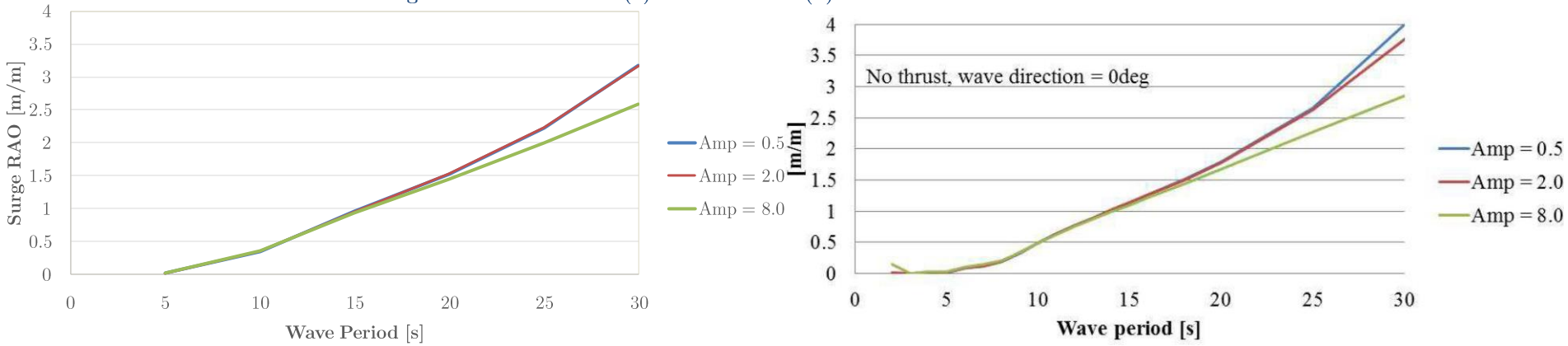

(a) (b)

Figure I - 4: Calculated (a) and Reference (b) Values of Motion RAOs for Case 4

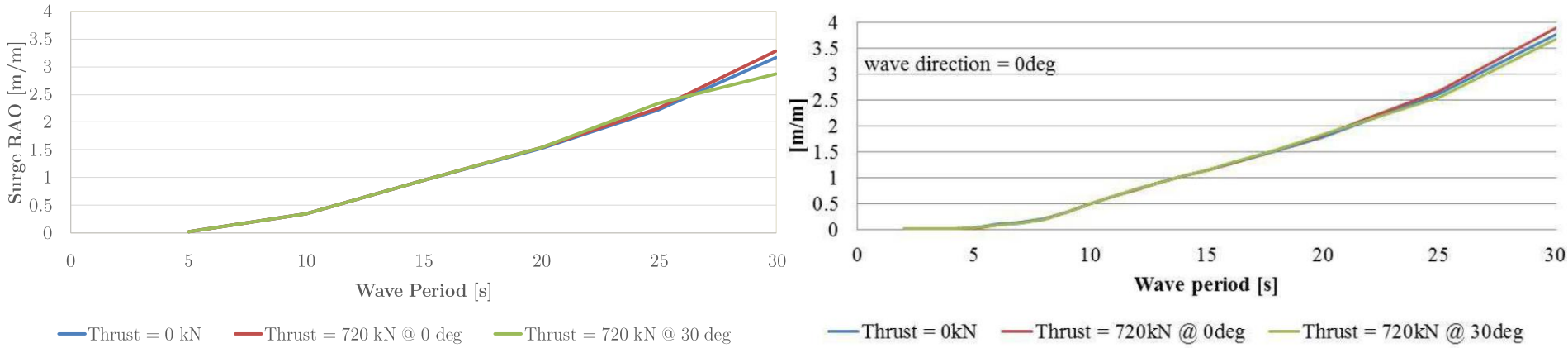

(a) (b)

Figure I - 5: Calculated (a) and Reference (b) Values of Motion RAOs for Case 5

I.4 Implementation of Analytical Model to Reference TLP

Introduction

The 3D model that was developed in Chapter 3 is implemented to obtain the 3D motions (η_1, η_2, η_3, η_4, η_5, η_6) of the SBM TLP. The model set-up is presented below:

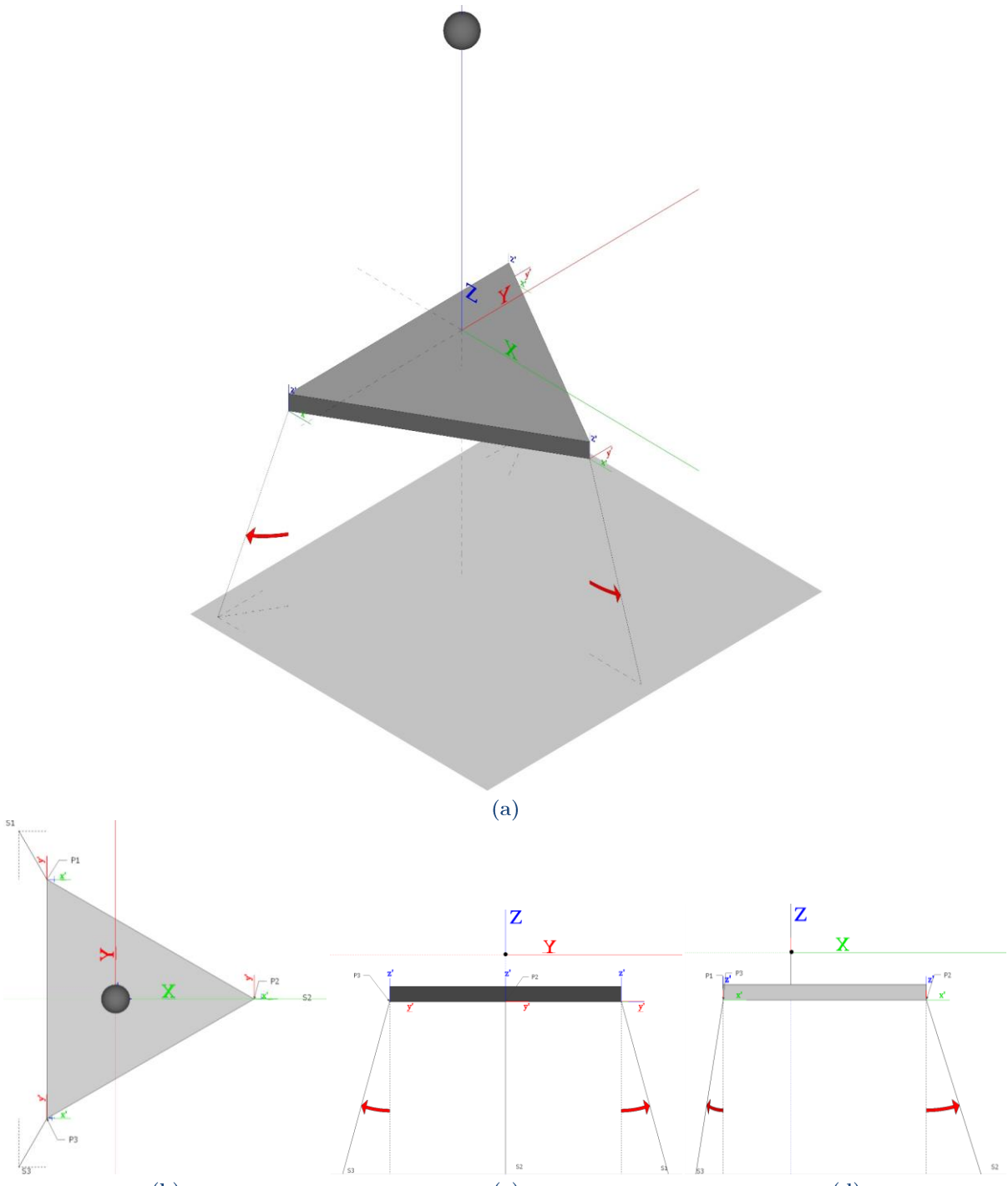

(a)

(b) (c) (d)

Figure I - 6: SBM Model in Matlab

Axis Conventions

Origin of global coordinate system in the CoG, which is also the rotation pivot point. Description of axis conventions is provided in Table I - 3. The wave kinematics are described using the expressions as introduced in Chapter 3.

Table I - 3: Axis Conventions Analytical Model (SBM TLP)

Parameter	Symbol	Origin	Positive direction
Surge	η_1	CoG(0)	Right
Sway	η_2	CoG(0)	Right
Heave	η_3	CoG(0)	Up
Roll	η_4	CoG(0)	According to right hand rule
Pitch	η_5	CoG(0)	Opposite to right hand rule
Yaw	η_6	CoG(0)	According to right hand rule
Coordinates of tendon attachment points	$X_{P,i}\ X_{S,i}, X_{P,i,new}$ $Y_{P,i}, Y_{S,i}, Y_{P,i.new}$ $Z_{P,i}, Z_{S,i}, Z_{P,i.new}$	CoG(0)	According to positive directions about CoG(0)
Lever arms w.r.t. displaced CoG at time t	$a_{x,P,i}, a_{y,P,i},$ $a_{z,P,i}, X_{CoB,i},$ $Y_{CoB,i}, Z_{CoB,i}$	CoG(t)	According to positive directions about CoG(0)
Displacements at tendon-platform attachment i w.r.t. static position.	$\Delta X_i, \Delta Y_i, \Delta Z_i$	$P_i(0)$	According to positive directions about CoG(0)
Tendon angle at attachment points w.r.t. static position	α_i	$P_i(t)$	Any
Tendon Force	$F_{T,i}$	$P_i(t)$	Tensile force
Vertical position water particle w.r.t. wave crest at given point	$z_{CoB,i}$	MSL $+ \xi_3(x_i, y_i, t)$	Up
Rotation angle w.r.t. positive X direction	$\mu_{wave}, \mu_{wind},$ μ_{cur}, μ_{RNA}	CoG(0)	Counter clockwise
Location of CoB of buoy i	$X'_{KB_i}, Y'_{KB_i}, Z'_{KB_i}$	CoG(t)	According to positive directions about CoG(0)
Location of hub CoG	$X'_{hub}, Y'_{hub}, Z'_{hub}$	CoG(t)	According to positive directions about CoG(0)

Mass and Mass Moment of Inertia

$$m_p = m_{platform} + \frac{L_{tower} - Z_t}{L_{tower}} * m_{tower} \quad \text{[I-1]}$$

$$m_{RNA} = m_{rotors} + m_{hub} + \frac{Z_t}{L_{tower}} * m_{tower} \quad \text{[I-2]}$$

Assumptions

- Inertia loads of turbine are approximated as single lumped mass;
- Time dependent buoyancy due to heave motions and wave submergence are included;
- Platform mass moment of inertia approximated based on an equilateral triangle with an equivalent surface area: $I_5 = \frac{\sqrt{3}}{288} A_{top} m_p$

Formulation of Equations of Motion

EOM_{surge}:

$$F_{D,p}^{x} + F_{w}^{x} + F_{add}^{x} + F_{in,t}^{x} - \sum F_{T_i} * \mathrm{H}_i^{x} = \ddot{\eta}_1 m_{tot} \quad \text{[I-3]}$$

EOM_{sway}:

$$F_{D,p}^{y} + F_{w}^{y} + F_{add}^{y} + F_{in,t}^{y} - \sum F_{T_i} * \mathrm{H}_i^{y} = \ddot{\eta}_2 m_{tot} \quad \text{[I-4]}$$

EOM_{heave}:

$$F_B + F_{B,var}^{z} + F_{D,p}^{z} + F_{add}^{z} + F_{in,t}^{z} - \sum F_{T_i} * \mathrm{H}_i^{z} = \ddot{\eta}_3 m_{tot} \quad \text{[I-5]}$$

EOM_{roll}:

$$-M_s^{yz} + M_{hyd}^{yz} + M_{hub}^{yz} - \sum F_{T,i} * \mathrm{H}_i^{z} * a_{y,P,i} + \sum F_{T,i} * \mathrm{H}_i^{y} * a_{z,P,i} = \ddot{\eta}_4 I_{4,p} \quad \text{[I-6]}$$

EOM_{pitch}:

$$-M_s^{xz} + M_{hyd}^{xz} + M_{hub}^{xz} - \sum F_{T,i} * \mathrm{H}_i^{z} * a_{x,P,i} + \sum F_{T,i} * \mathrm{H}_i^{x} * a_{z,P,i} = \ddot{\eta}_5 I_{5,p} \quad \text{[I-7]}$$

EOM_{yaw}:

$$M_{hyd}^{xy} + M_{hub}^{xy} - \sum F_{T,i} * \mathrm{H}_i^{y} * a_{x,P,i} + \sum F_{T,i} * \mathrm{H}_i^{x} * a_{y,P,i} = \ddot{\eta}_6 I_{6,p} \quad \text{[I-8]}$$

Formulation of Lever Arms and Distances

Connection points of tendons to platform are denoted with P_1, P_2 and P_3, representing the left, middle and right point respectively. Similarly, anchoring positions of the tendons are denoted with S_1, S_2 and S_3, representing the left, middle and right anchoring point. All static parameters are listed below:

$$H_T = d - T_{mean} \quad \text{[I-9]}$$

$$W_T = \frac{R_P * H_T}{Z_{hub} + z_{cross} + T_{mean}} \quad \text{[I-10]}$$

$$Y_P = \begin{bmatrix} Y_{P,1} \\ Y_{P,2} \\ Y_{P,3} \end{bmatrix} = W_{platform} \begin{bmatrix} 0.5 \\ 0 \\ -0.5 \end{bmatrix} \quad \text{[I-11]}$$

$$Z_P = \begin{bmatrix} Z_{P,1} \\ Z_{P,2} \\ Z_{P,3} \end{bmatrix} = -KG \begin{bmatrix} 1 \\ 1 \\ 1 \end{bmatrix} \quad \text{[I-12]}$$

$$Y_S = \begin{bmatrix} Y_{S,1} \\ Y_{S,2} \\ Y_{S,3} \end{bmatrix} = Y_P + \frac{W_T}{2} \begin{bmatrix} \sqrt{3} \\ 0 \\ -\sqrt{3} \end{bmatrix} \quad \text{[I-13]}$$

$$Z_S = \begin{bmatrix} Z_{S,1} \\ Z_{S,1} \\ Z_{S,1} \end{bmatrix} = Z_P - H_T \quad \text{[I-14]}$$

$$X_P = \begin{bmatrix} X_{P,1} \\ X_{P,2} \\ X_{P,3} \end{bmatrix} = R_p \begin{bmatrix} -0.5 \\ 1 \\ -0.5 \end{bmatrix} \quad \text{[I-15]}$$

$$X_S = \begin{bmatrix} X_{S,1} \\ X_{S,2} \\ X_{S,3} \end{bmatrix} = X_P + W_T \begin{bmatrix} -0.5 \\ 1 \\ -0.5 \end{bmatrix} \quad \text{[I-16]}$$

$$L_{0,i} = \sqrt{\left(X_{S,i} - X_{P,i}\right)^2 + \left(Y_{S,i} - Y_{P,i}\right)^2 + \left(Z_{S,i} - Z_{P.i}\right)^2} \quad \text{[I-17]}$$

$$Z_{t,0} = z_{hub,WL} + T_{mean} - KG \quad \text{[I-18]}$$

$$A_{wp} = \left(\frac{\pi}{4} 1.55^2\right) \quad \text{[I-19]}$$

Rotation matrices:

$$R_{tot}(\eta_6, \eta_5, \eta_4) = \boldsymbol{R} \quad \text{[I-20]}$$

Parameters w.r.t. displaced CoG at time t:

$$P_i' = \begin{bmatrix} X_i' \\ Y_i' \\ Z_i' \end{bmatrix} = \boldsymbol{R} * \begin{bmatrix} X_{P,i} \\ Y_{P,i} \\ Z_{P,i} \end{bmatrix} \quad \text{[I-21]}$$

$$\dot{P}_i' = \dot{\boldsymbol{R}} * \begin{bmatrix} X_{P,i} \\ Y_{P,i} \\ Z_{P,i} \end{bmatrix} \quad \text{[I-22]}$$

$$\ddot{P}_i' = \ddot{\boldsymbol{R}} * \begin{bmatrix} X_{P,i} \\ Y_{P,i} \\ Z_{P,i} \end{bmatrix} \quad \text{[I-23]}$$

$$\begin{bmatrix} a_{x,P,i} \\ a_{y,P,i} \\ a_{z,P,i} \end{bmatrix} = P_i' \quad \text{[I-24]}$$

$$CoB_{P,i}^{rot} = \begin{bmatrix} X_{CoB,i} \\ Y_{CoB,i} \\ Z_{CoB,i} \end{bmatrix} = \boldsymbol{R} * \begin{bmatrix} X_{P,i} \\ Y_{P,i} \\ Z_{P,i} + KB_i \end{bmatrix} \quad \text{[I-25]}$$

$$P_{hub}' = \begin{bmatrix} X_{hub}' \\ Y_{hub}' \\ Z_{hub}' \end{bmatrix} = \boldsymbol{R} * \begin{bmatrix} 0 \\ 0 \\ Z_{t,0} \end{bmatrix} \quad \text{[I-26]}$$

$$\dot{P}_{hub}' = \dot{\boldsymbol{R}} * \begin{bmatrix} 0 \\ 0 \\ Z_{t,0} \end{bmatrix} \quad \text{[I-27]}$$

$$\ddot{P}_{hub}' = \ddot{\boldsymbol{R}} * \begin{bmatrix} 0 \\ 0 \\ Z_{t,0} \end{bmatrix} \quad \text{[I-28]}$$

Parameters w.r.t. static position CoG:

$$P_{new} = \begin{bmatrix} X_{P,i,new} \\ Y_{P,i,new} \\ Z_{P,i,new} \end{bmatrix} = \begin{bmatrix} \eta_1 \\ \eta_2 \\ \eta_3 \end{bmatrix} + P_i' \quad \text{[I-29]}$$

$$\Delta P = \begin{bmatrix} \Delta X_{P,i} \\ \Delta Y_{P,i} \\ \Delta Z_{P,i} \end{bmatrix} = \begin{bmatrix} X_{P,i,new} \\ Y_{P,i,new} \\ Z_{P,i,new} \end{bmatrix} - \begin{bmatrix} X_{P,i} \\ Y_{P,i} \\ Z_{P,i} \end{bmatrix} \quad \text{[I-30]}$$

$$\Delta \dot{P} = \begin{bmatrix} \dot{\eta}_1 \\ \dot{\eta}_2 \\ \dot{\eta}_3 \end{bmatrix} + \dot{P}_i' \quad \text{[I-31]}$$

$$\Delta \ddot{P} = \begin{bmatrix} \ddot{\eta}_1 \\ \ddot{\eta}_2 \\ \ddot{\eta}_3 \end{bmatrix} + \ddot{P}_i' \quad \text{[I-32]}$$

Other time dependent parameters:

$$L_{new,i} = \sqrt{\left(X_{S,i} - X_{P,i,new}\right)^2 + \left(Y_{S,i} - Y_{P,i,new}\right)^2 + \left(Z_{S,i} - Z_{P.i,new}\right)^2} \quad \text{[I-33]}$$

$$\begin{bmatrix} \mathrm{H}_i^x \\ \mathrm{H}_i^y \\ \mathrm{H}_i^z \end{bmatrix} = \frac{1}{L_{new}} \begin{bmatrix} X_{P,i,new} - X_{S,i} \\ Y_{P,i,new} - Y_{S,i} \\ Z_{P,i,new} - Z_{S,i} \end{bmatrix} \quad \text{[I-34]}$$

$$\alpha_i = \tan^{-1}\left(\frac{\sqrt{\left(X_{S,i} - X_{P,i,new}\right)^2 + \left(Y_{S,i} - Y_{P,i,new}\right)^2}}{Z_{P.i,new} - Z_{S,i}}\right) \quad \text{[I-35]}$$

$$Z = Z_i - T_{mean} - \xi(X_i, Y_i, t) + KG \quad \text{[I-36]}$$

$$[X_i \quad Y_i \quad Z_i]^T = \boldsymbol{R} * [0 \quad 0 \quad z_i]^T + [\eta_1 \quad \eta_2 \quad \eta_3]^T \quad \text{[I-37]}$$

Derivation of Forces

Derivation of wind forces:

$$\underline{F_w} = \frac{1}{2}\rho_a \left(\underline{U_{hub}} \circ \left|\underline{U_{hub}}\right| \circ \underline{A_{wind}} * C_{D,hub} + \underline{U_{tower}} \circ \left|\underline{U_{tower}}\right| * \left(Z'_{hub} + \eta_3 - \xi_v(0,0,t)\right) * D_{tower,avg} * C_{D,tower}\right) \quad \text{[I-38]}$$

$$P_{RNA} = \begin{bmatrix} x_{RNA} \\ y_{RNA} \\ z_{RNA} \end{bmatrix} = \boldsymbol{R} * \begin{bmatrix} D_{RNA}/2 \\ 0 \\ D_{RNA}/2 \end{bmatrix} \quad \text{[I-39]}$$

$$\underline{A_{wind}} = \begin{bmatrix} A_{wind}^x \\ A_{wind}^y \\ A_{wind}^z \end{bmatrix} = \begin{cases} \pi \begin{bmatrix} x_{RNA} * z_{RNA} \\ y_{RNA} * z_{RNA} \\ x_{RNA} * y_{RNA} \end{bmatrix}, & operational\ conditions \\ \boldsymbol{R} * 3A_{blade}, & extreme\ conditions \end{cases} \quad \text{[I-40]}$$

$$U_{hub} = \begin{bmatrix} U_{hub}^x \\ U_{hub}^y \\ U_{hub}^z \end{bmatrix} = \begin{bmatrix} cos(\mu_{wind}) \\ sin(\mu_{wind}) \\ 0 \end{bmatrix} U_{wind}(Z_t) - \begin{bmatrix} \dot{\eta}_1 \\ \dot{\eta}_2 \\ 0 \end{bmatrix} + \begin{bmatrix} \dot{X}'_{hub} \\ \dot{Y}'_{hub} \\ 0 \end{bmatrix} \quad \text{[I-41]}$$

$$U_{tower} = \begin{bmatrix} U_{tower}^x \\ U_{tower}^y \\ U_{tower}^z \end{bmatrix} = \begin{bmatrix} cos(\mu_{wind}) \\ sin(\mu_{wind}) \\ 0 \end{bmatrix} U_{wind}\left(\frac{Z_t}{2}\right) - \begin{bmatrix} \dot{\eta}_1 \\ \dot{\eta}_2 \\ 0 \end{bmatrix} + \frac{Z_t}{2} * \begin{bmatrix} cos(\eta_5)\dot{\eta}_5 \\ cos(\eta_4)\dot{\eta}_4 \\ 0 \end{bmatrix} \quad \text{[I-42]}$$

Derivation of hydrodynamic drag forces:

$$\underline{F_{D,p,i}} = \frac{1}{2}\rho_w * U_{hyd,i} \circ \left|U_{hyd,i}\right| \circ \boldsymbol{R} \begin{bmatrix} A_{D,i}^x \\ A_{D,i}^y \\ A_{D,i}^z \end{bmatrix} \circ \begin{bmatrix} C_{D,platform}^x \\ C_{D,platform}^y \\ C_{D,platform}^z \end{bmatrix} \quad \text{[I-43]}$$

$$F_{D,p} = \begin{bmatrix} F_{D,p}^x \\ F_{D,p}^y \\ F_{D,p}^z \end{bmatrix} = \sum_{i=1}^{N} \underline{F_{D,p,i}} \quad \text{[I-44]}$$

$$U_{hyd,i} = \begin{bmatrix} U_{hyd,i}^x \\ U_{hyd,i}^y \\ U_{hyd,i}^z \end{bmatrix} = \begin{bmatrix} cos(\mu_{cur}) \\ sin(\mu_{cur}) \\ 0 \end{bmatrix} U_{cur}(z_i) + \begin{bmatrix} cos(\mu_{wave}) \\ sin(\mu_{wave}) \\ 1 \end{bmatrix} \circ \begin{bmatrix} \dot{\xi}_h(X_i', Y_i', Z_i', t) \\ \dot{\xi}_h(X_i', Y_i', Z_i', t) \\ \dot{\xi}_v(X_i', Y_i', Z_i', t) \end{bmatrix} - \begin{bmatrix} \Delta\dot{X}_i \\ \Delta\dot{Y}_i \\ \Delta\dot{Z}_i \end{bmatrix} \quad \text{[I-45]}$$

[I-46]

Derivation of rotational inertia forces:

$$F_{int} = \begin{bmatrix} F_{in,t}^x \\ F_{in,t}^y \\ F_{in,t}^z \end{bmatrix} = F_{gyro} + m_{hub}\ddot{P}'_{hub} \quad \text{[I-47]}$$

Derivation of hydrodynamic inertia forces:

$$F_{add} = \begin{bmatrix} F_{add}^x \\ F_{add}^y \\ F_{add}^z \end{bmatrix} = \sum_{i=1}^{N} \underline{F_{add,i}} \quad \text{[I-48]}$$

$$F_{add,i} = \begin{bmatrix} cos(\mu_{wave}) \\ sin(\mu_{wave}) \\ 1 \end{bmatrix} \circ \begin{bmatrix} (a_{11,i} + m_{disp,i}) \\ (a_{22,i} + m_{disp,i}) \\ (a_{33,i} + m_{disp,i}) \end{bmatrix} \circ \begin{bmatrix} \ddot{\xi}_h(X_i', Y_i', Z_i', t) \\ \ddot{\xi}_h(X_i', Y_i', Z_i', t) \\ \ddot{\xi}_v(X_i', Y_i', Z_i', t) \end{bmatrix} - \begin{bmatrix} a_{11,i} \\ a_{22,i} \\ a_{33,i} \end{bmatrix} \circ \Delta\ddot{P} \quad \text{[I-49]}$$

$$\begin{bmatrix} a_{11,i} \\ a_{22,i} \\ a_{33,i} \end{bmatrix} = \begin{bmatrix} C_{a11} \\ C_{a22} \\ C_{a33} \end{bmatrix} * m_{disp,i} \quad \text{[I-50]}$$

Derivation of tendon forces:

$$F_B = g * \left(m_{disp} - m_{tot}\right) \quad \text{[I-51]}$$

$$F_{T_i} = \frac{L_{new} - L_0}{L_0} * EA_{chain} + \frac{F_B + F^z_{B,var}}{3 * H^z_i} \quad \text{[I-52]}$$

$$F^z_{B,var} = \rho_w g \Delta V \quad \text{[I-53]}$$

$$\Delta V = A_{wp} * (\xi_3(0,0,t) - \eta_3) \quad \text{[I-54]}$$

$$KB(t) = \frac{V_{sub} KB_0 + \frac{\Delta V^2}{2A_{wp}}}{V_{sub} + \Delta V} \quad \text{[I-55]}$$

Derivation of moments around Y, including influence of time-varying buoyancy due to mean wave submergence.

$$M_s = \begin{bmatrix} M_s^{yz} \\ M_s^{xz} \\ M_s^{xy} \end{bmatrix} = \rho_w g (V_{sub} + \Delta V) * \begin{bmatrix} KB(t) + \frac{I_t}{\nabla_0}\left(1 + \frac{1}{2} tan(\eta_4)^2\right) - KG \\ KB(t) + \frac{I_t}{\nabla_0}\left(1 + \frac{1}{2} tan(\eta_5)^2\right) - KG \\ 0 \end{bmatrix} \circ \begin{bmatrix} sin(\eta_4) \\ sin(\eta_5) \\ 0 \end{bmatrix} \quad \text{[I-56]}$$

$$M^{yz}_{hub} = -Z^{rotated}_t(t) * \left(F^y_{in,t} + F^y_w\right) + Y^{rotated}_t(t) * F^z_{in,t} \quad \text{[I-57]}$$

$$M^{xz}_{hub} = -Z^{rotated}_t(t) * \left(F^x_{in,t} + F^x_w\right) + X^{rotated}_t(t) * F^z_{in,t} \quad \text{[I-58]}$$

$$M^z_{hub} = -Y^{rotated}_t(t) * \left(F^x_{in,t} + F^x_w\right) + X^{rotated}_t(t) * \left(F^y_{in,t} + F^y_w\right) \quad \text{[I-59]}$$

$$M_{hyd} = \begin{bmatrix} M^{yz}_{hyd} \\ M^{xz}_{hyd} \\ M^{xy}_{hyd} \end{bmatrix} = \sum_{i=1}^{N} \begin{bmatrix} -Z_{CoB,i}\left(F^y_{D,p,i} + F^y_{add,i}\right) + Y_{CoB,i}\left(F^z_{D,p,i} + F^z_{add,i}\right) \\ -Z_{CoB,i}\left(F^x_{D,p,i} + F^x_{add,i}\right) + X_{CoB,i}\left(F^z_{D,p,i} + F^z_{add,i}\right) \\ -Y_{CoB,i}\left(F^x_{D,P,i} + F^x_{add,i}\right) + X_{CoB,i}\left(F^y_{D,P,i} + F^y_{add,i}\right) \end{bmatrix} \quad \text{[I-60]}$$

I.5 Derivation of Natural Periods

Analytical expressions for natural periods of surge, heave and pitch are directly derived from the EoMs of the two-dimensional dynamic system. In all cases, nonlinear restoring forces are linearized under the assumption of infinitely small displacements and mooring angles. The natural periods are derived based on the assumption of zero external forces, zero added mass and zero drag. This means that the average wave amplitude is also zero:

$$\xi_a = C_{D,i} = C_{a,ii} = 0 \quad \text{[I-61]}$$

Surge Natural Period

Assuming infinitely small surge displacement ($n_1 \ll 1$), no displacements in other DOFs ($\eta_3 = \eta_5 = 0$) and zero external forces, the EoM for surge becomes as shown in Equation [I-62].

$$\ddot{\eta}_1 m_{tot} = -\sum_{i=1}^{3} F_{T_i} * \sin(\alpha_i) \approx -g\left(\rho_w \nabla_0 - m_{dry}\right) \cdot \frac{\eta_1}{L_m} \quad \text{[I-62]}$$

Which leads to the following expression for the restoring coefficient:

$$C_{11} = \frac{-\ddot{\eta}_1 m_{tot}}{\eta_1} = \frac{g(\rho_w \nabla_0 - m_{dry})}{L_m} \quad \text{[I-63]}$$

$$T_{0,\eta_1} = 2\pi \sqrt{\frac{m_{tot}}{C_{11}}} = 2\pi \sqrt{\frac{m_{tot} L_m}{g(\rho_w \nabla_0 - m_{dry})}} \quad \text{[I-64]}$$

Note that the restoring coefficient is identical to the spring constant of a simple pendulum. This approximation holds as long the small-angle approximation is valid, which is roughly for $\eta_1 < 0.17 L_m$. For surge amplitudes larger than this value, interactions with other DOFs start to play a role, i.e. horizontal forces due to other DOFs appear in the EOM.

Heave Natural Period

Assuming infinitely small heave displacement ($n_3 \ll 1$), no displacements in other DOFs ($\eta_1 = \eta_5 = 0$) and zero external forces, the EoM for surge becomes as shown in Equation [I-65].

$$\ddot{\eta}_3 m_{tot} = -\rho_w g A_{wp} \eta_3 - \sum_{i=1}^{3} \frac{\Delta L_i}{L_m} * EA * \cos(\alpha_i) \approx -\rho_w g A_{wp} \eta_3 - 3\frac{\eta_3}{L_m} EA \quad \text{[I-65]}$$

Which leads to the following expression for the restoring coefficient:

$$C_{33} = \frac{-\ddot{\eta}_3 m_{tot}}{\eta_3} = \frac{3EA}{L_m} + \rho_w g A_{wp} \quad \text{[I-66]}$$

$$T_{0,\eta_3} = 2\pi \sqrt{\frac{m_{tot}}{C_{33}}} = 2\pi \sqrt{\frac{m_{tot}}{\frac{3EA}{L_m} + \rho_w g A_{wp}}} \quad \text{[I-67]}$$

I.6 Rigid Body Natural Modes of Reference TLP

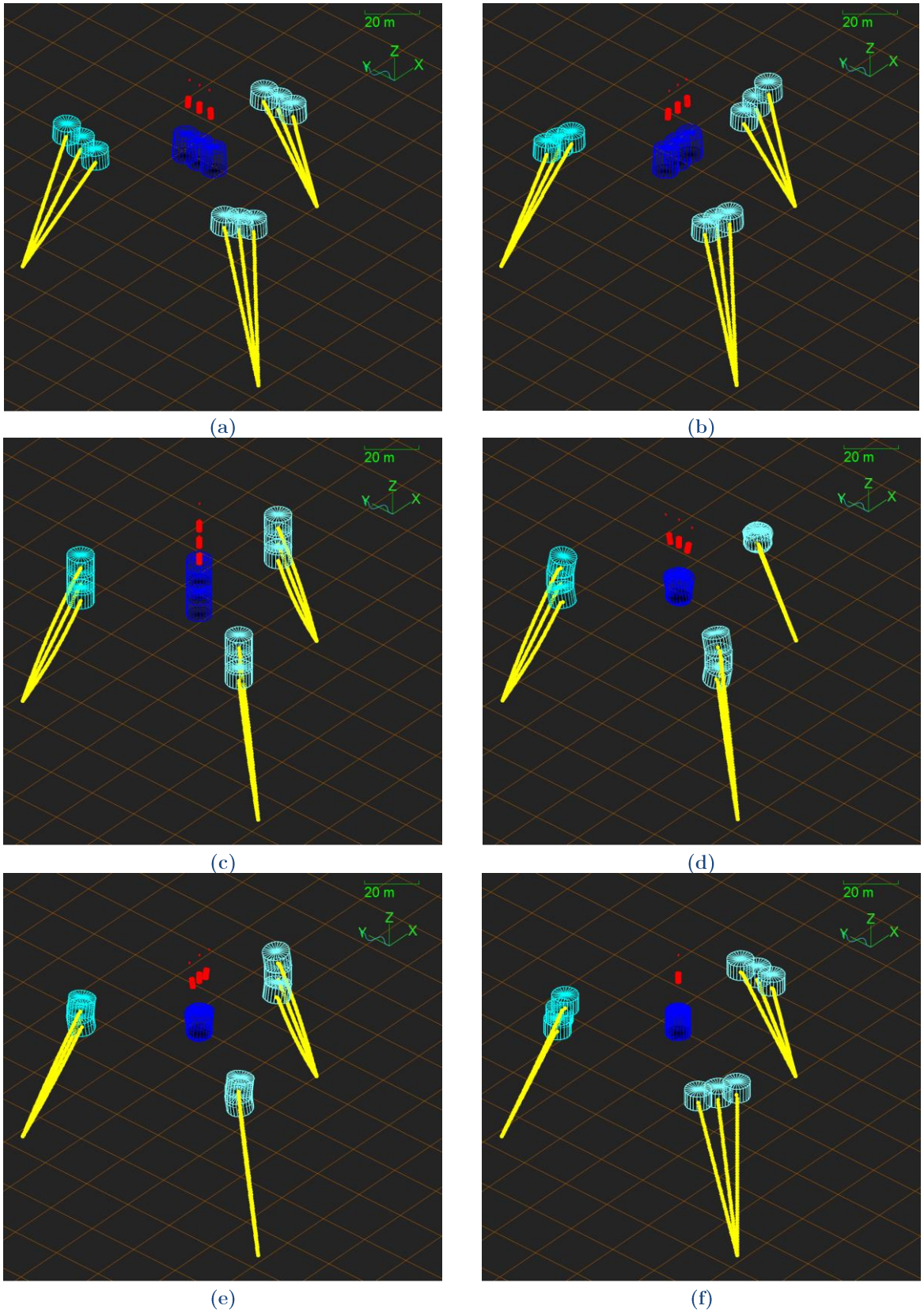

Figure I - 7: Rigid Body Natural Modes of Reference TLP

APPENDIX J

Linearization Approach

J.1 Identification of Nonlinearities Mooring Stiffness

In Figure J - 1, an overview is provided of the non-zero elements of the nonlinear stiffness matrix.

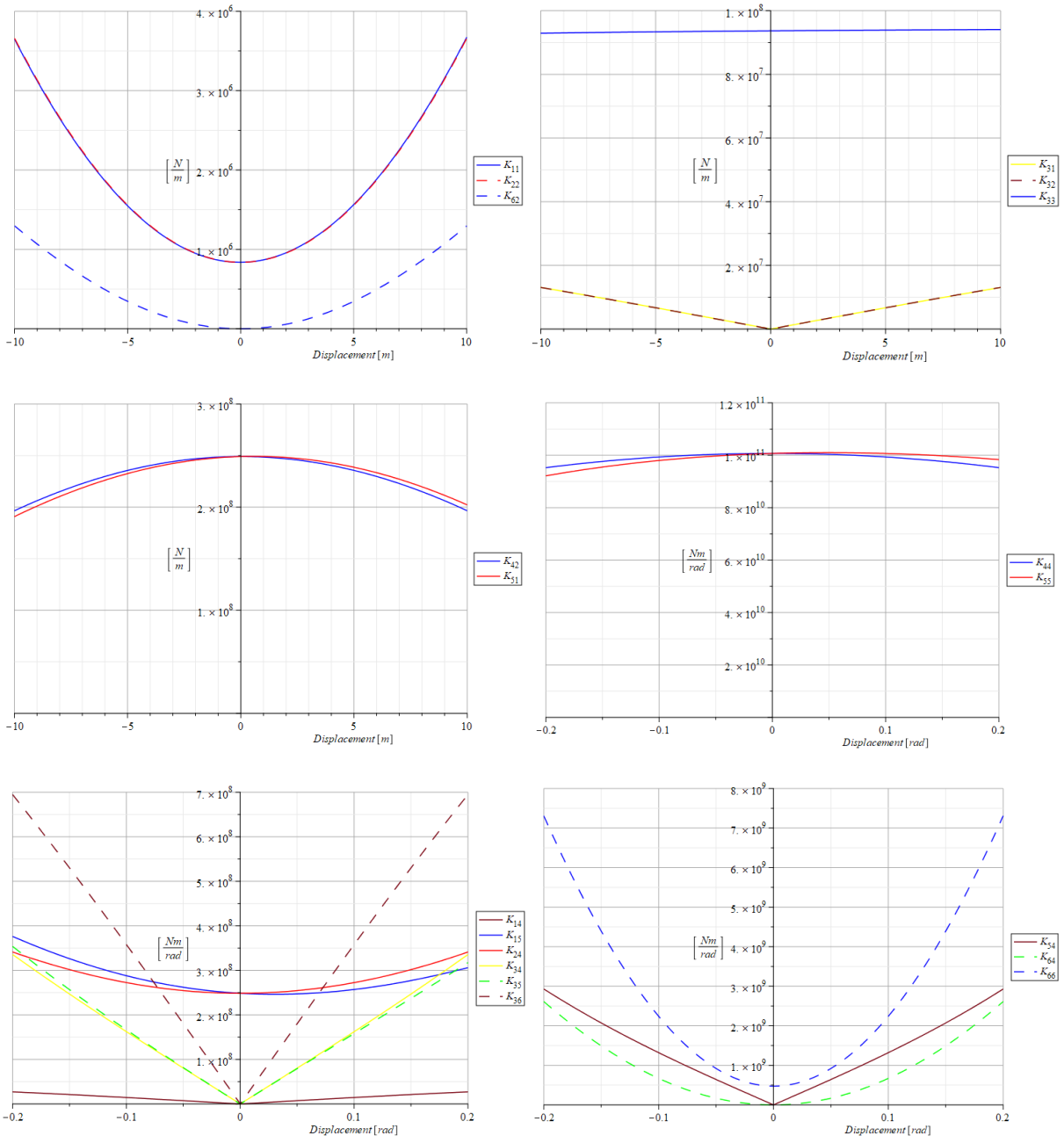

Figure J - 1: Nonlinear Distribution of Mooring Stiffness

J.2 Linearized Mooring Forces

In Figure J - 2, the linear and nonlinear mooring forces in each DOF are plotted as a function of the DOF itself, while keeping the other DOFs at their equilibrium state. This, essentially, represents the decoupled diagonal elements of the linearized stiffness matrix. This example was based on the equilibrium point $\underline{p}_0 = [1.434 \quad -0.010 \quad -0.015 \quad 0 \quad 0.004 \quad 0]^T$.

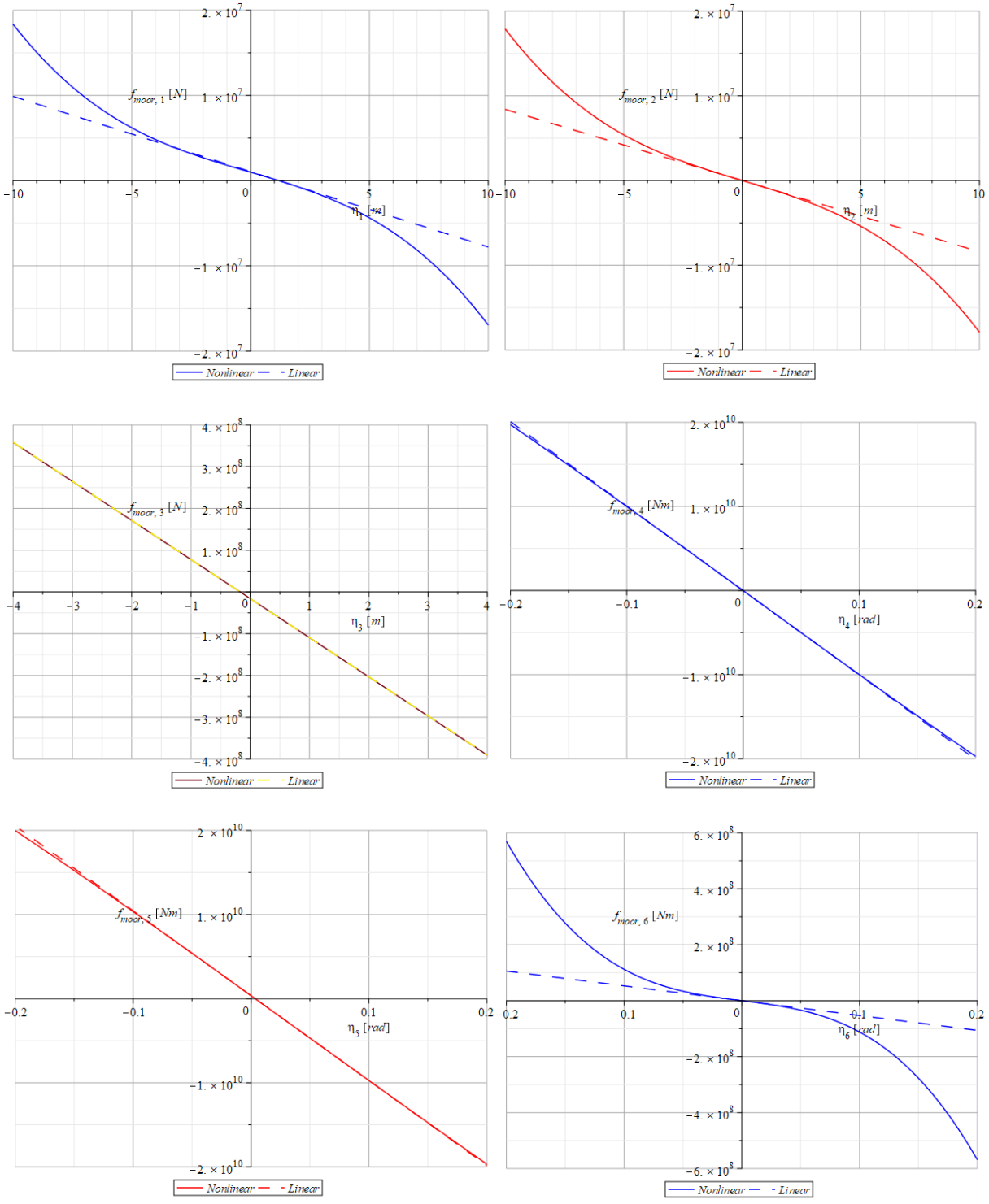

Figure J - 2: Linear Approximations of Mooring Stiffness

J.3 Comparison of Linearization Methods

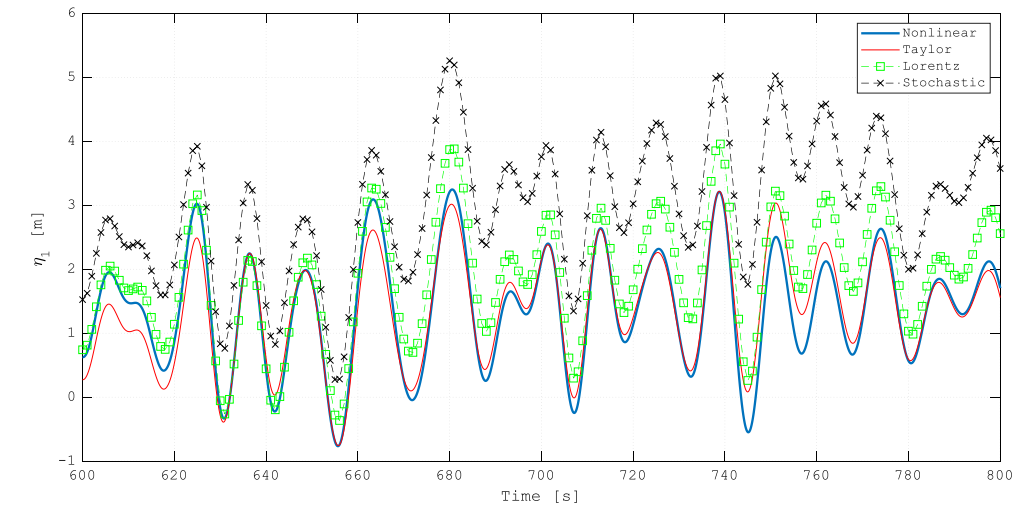

(a)

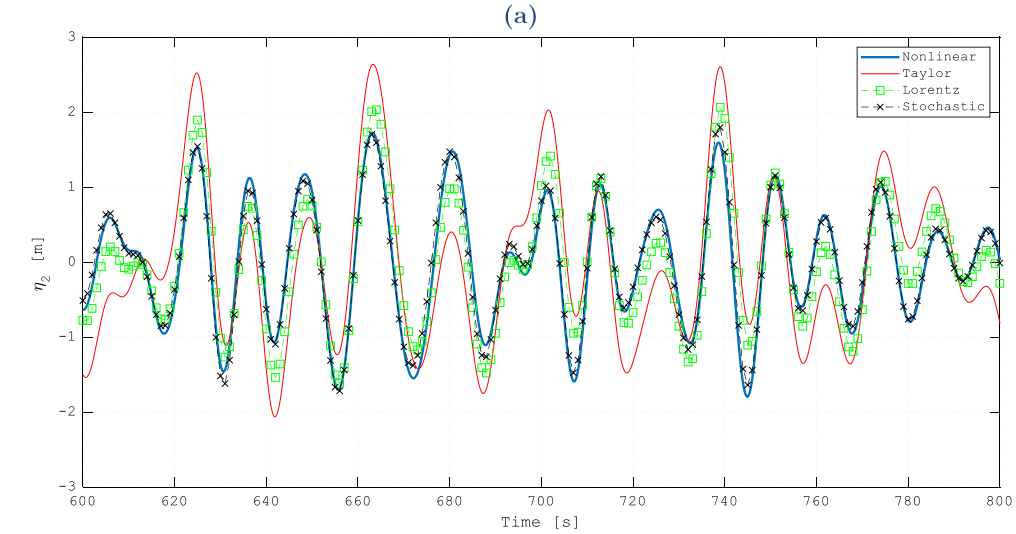

(b)

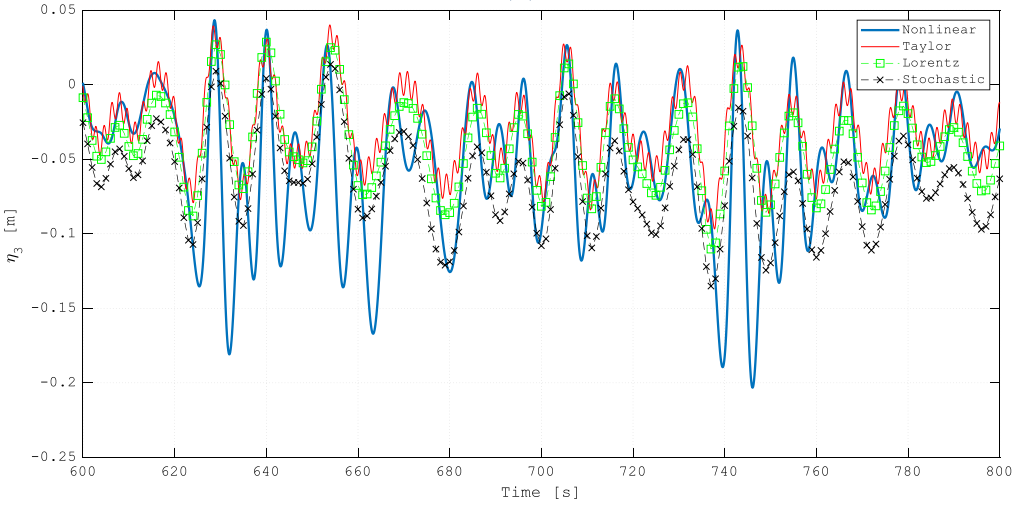

(c)

Figure J - 3: Displacements in Surge (a), Sway (b) and Heave (c)

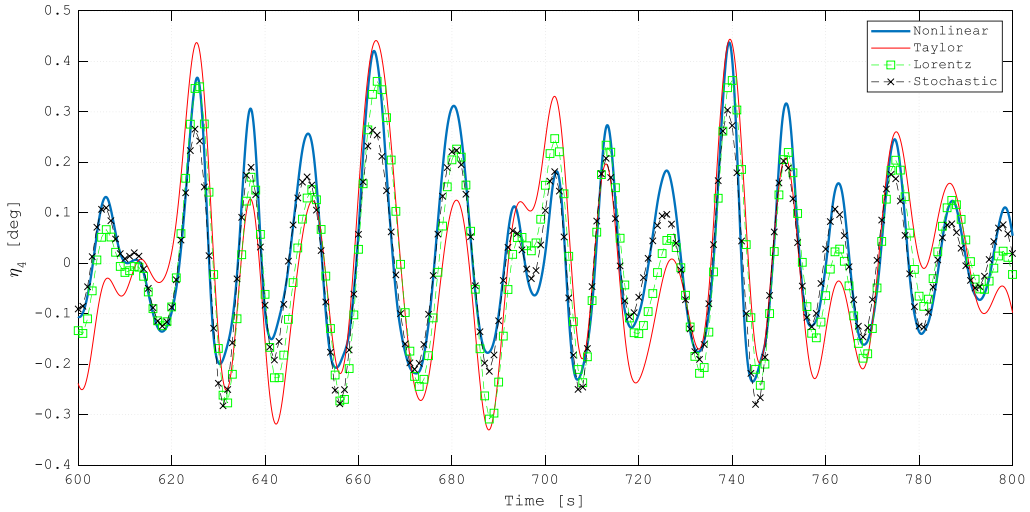

(a)

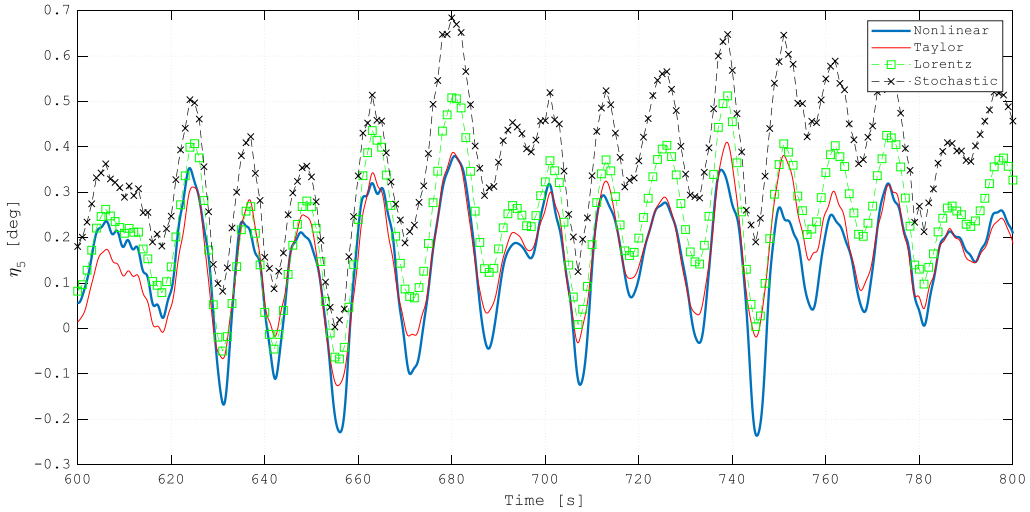

(b)

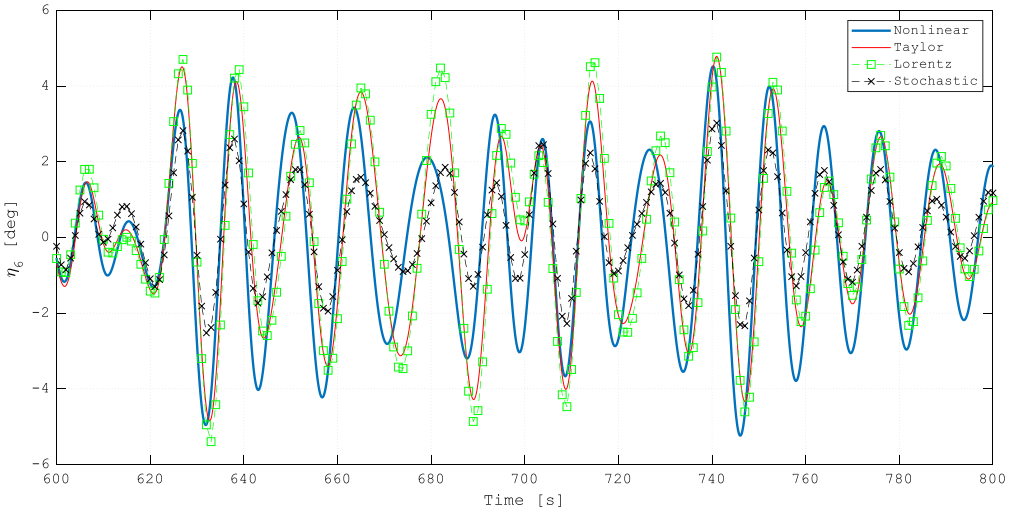

(c)

Figure J - 4: Displacements in Roll (a), Pitch (b) and Yaw (c)

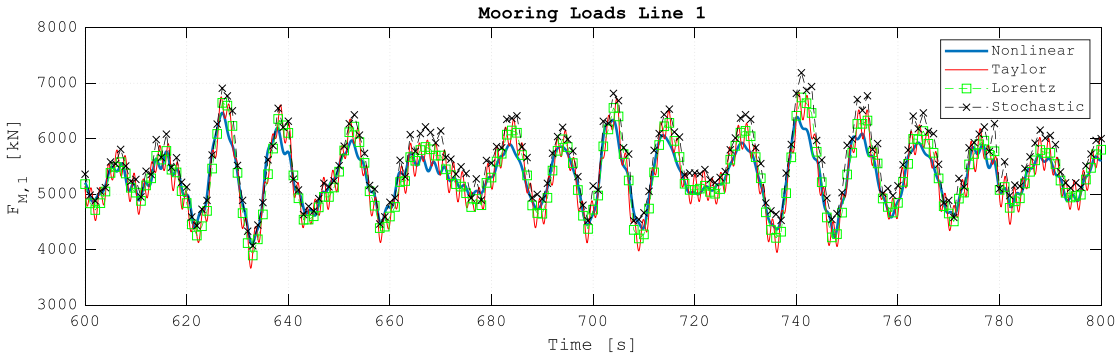

Figure J - 5: Mooring Load Response

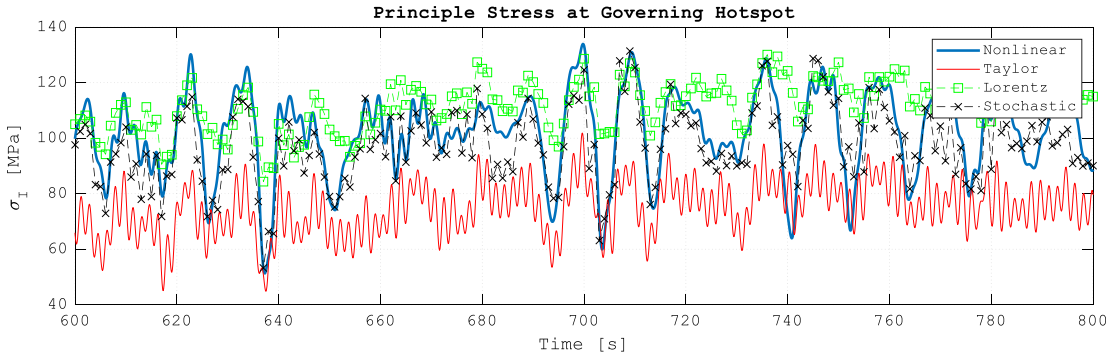

Figure J - 6: Principle Stress Response at Governing Hotspot

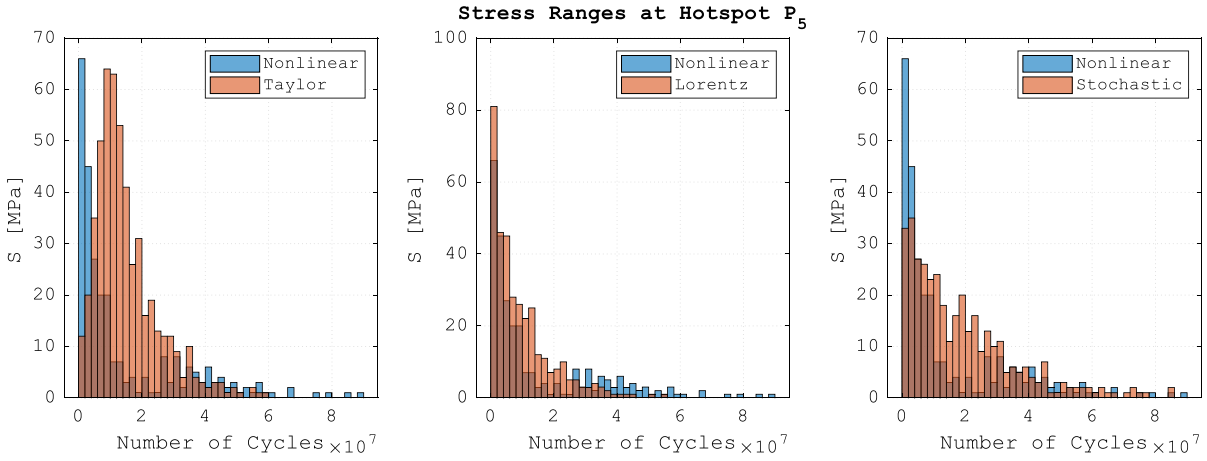

Figure J - 7: Stress Range Diagrams at Hotspot P_5

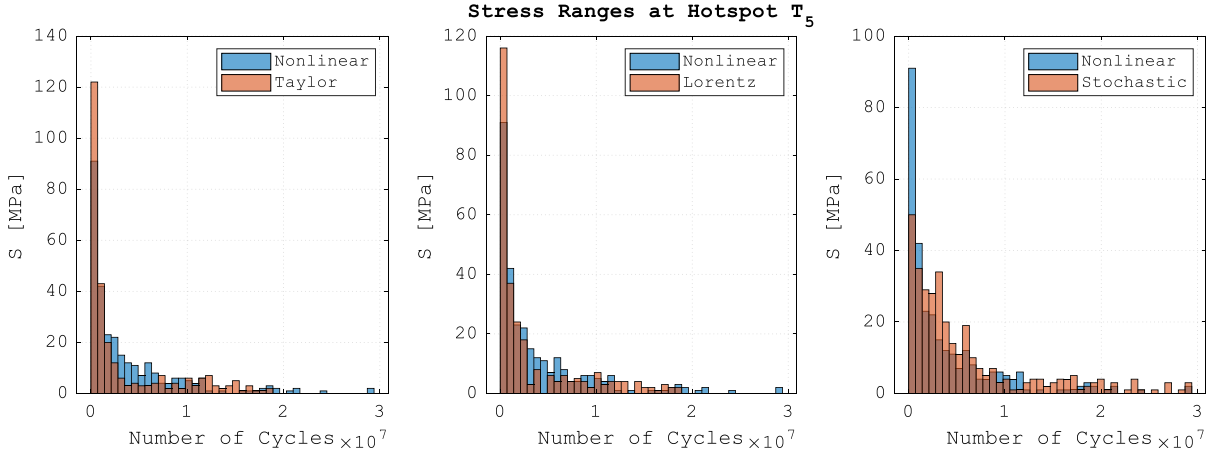

Figure J - 8: Stress Range Diagrams at Hotspot T_5

J.4 Sea States for Long Term Fatigue Analysis

Fatigue damage is analysed on the basis of twelve different sea states ($N_{ss} = 12$), selected in such a way that the long-term operational conditions are resembled as accurately as possible. The sea states are selected from the met-ocean data, by assuming that the damage during each sea state is proportional to the stress range cubed:

$$D_i \propto S_i^3 \qquad \text{[J-1]}$$

where D_i and S_i are the damage and representative stress range during sea state i, respectively.

If, for this selection procedure, the influence of wind, nonlinear mooring loads and multi-axiality are disregarded, one can also assume that the stress range is linearly proportional to the wave load:

$$S_i \propto F_{wave,i} \qquad \text{[J-2]}$$

where $F_{wave,i}$ is the representative wave force amplitude during sea state i.

The total wave load is a sum of the hydrodynamic drag and inertia force, which are proportional to the wave height H_{wave} and wave period T_{wave} through the water particle velocity U_{wave} and acceleration $\dot{U}_{wave}$. Hence, by distinguishing drag and inertia dominated regimes, the relationships in Equation [J-3] are found. These expressions can then form a direct, *qualitative* relationship between fatigue damage D_i and characteristic wave height and period during a sea state i, as depicted in Equation [J-4].

$$F_{wave} \propto \begin{cases} U_{wave}^2 \propto (H_{wave}/T_{wave})^2, & \text{drag dominated conditions} \\ \dot{U}_{wave} \propto H_{wave}/T_{wave}^2, & \text{inertia dominated conditions} \end{cases} \qquad \text{[J-3]}$$

$$D_i \propto \begin{cases} \left(H_{s,i}/T_{p,i}\right)^6, & \text{drag dominated conditions} \\ \left(H_{s,i}/T_{p,i}^2\right)^3, & \text{inertia dominated conditions} \end{cases} \qquad \text{[J-4]}$$

where $H_{s,i}$ and $T_{p,i}$ are, respectively, the significant wave height and peak period.

The relationship in Equation [J-4] is then applied to each sea state in the met-ocean data and multiplied with the respective number of occurrence to obtain an indication value of the damage per sea state ($D_i \cdot n_{ss,i}$). The twelve wave conditions that correspond to the highest indication values are selected. Both drag dominated (sea states with bold outlines in Table J - 1) and inertia dominated (sea states with bold outlines in Table J - 2) conditions are considered, together with the corresponding governing wave directions (Table J - 3). The sea states also include three different wind and current velocities with the corresponding prevailing directions (Table J - 4 and Table J - 5).

Table J - 1: Governing Sea States for Drag Dominated Fatigue Damage

	Tp [s]																				
Hs [m]	From	3	4	5	6	7	8	9	10	11	12	13	14	15	16	17	18	19	20	21	22	23
From	To	4	5	6	7	8	9	10	11	12	13	14	15	16	17	18	19	20	21	22	23	24
0	0.5	2.61E-09	5.45E-10	1.58E-10	2.62E-10	2.71E-10	2.38E-10	9.27E-11	6.01E-11	2.1E-11	4.81E-12	1.52E-12	8.11E-13	1.58E-13	6.79E-15	3.34E-14	0	0	0	0	0	0
0.5	1	8.05E-08	**2.01E-07**	5.08E-08	2.87E-08	6.32E-08	5.19E-08	2.42E-08	1.29E-08	5.18E-09	1.74E-09	6.24E-10	2.18E-10	9.47E-11	2.99E-11	2.16E-11	5.82E-12	2.15E-12	1.55E-12	3.75E-13	2.85E-13	1.1E-13
1	1.5	0	1.18E-07	**3.38E-07**	1.49E-07	1.64E-07	1.79E-07	1.07E-07	7.63E-08	3.56E-08	1.15E-08	4.87E-09	1.52E-09	5.71E-10	2.48E-10	2.08E-10	4.15E-11	1.9E-11	7.39E-12	6.94E-13	3.96E-13	1.02E-13
1.5	2	0	0	5.94E-08	**2.11E-07**	**1.84E-07**	2.2E-07	1.52E-07	1.52E-07	8.12E-08	2.83E-08	1.3E-08	4.76E-09	1.71E-09	4.5E-10	3.55E-10	8.09E-11	3.16E-11	1.33E-11	4.28E-12	1.09E-12	0
2	2.5	0	0	0	5.7E-08	1.03E-07	2.03E-07	2.02E-07	1.78E-07	1.27E-07	5.18E-08	2.48E-08	9.79E-09	4.22E-09	1.28E-09	7.83E-10	1.74E-10	8.72E-11	1.88E-11	2.02E-12	0	0
2.5	3	0	0	0	4.84E-09	2.36E-08	1.37E-07	1.87E-07	1.99E-07	1.4E-07	6.53E-08	3.44E-08	1.52E-08	4.67E-09	1.17E-09	1.01E-09	2.46E-10	9.62E-11	1.23E-11	0	0	0
3	3.5	0	0	0	0	3.38E-09	2.95E-08	1.21E-07	1.97E-07	1.46E-07	7.35E-08	4.39E-08	1.7E-08	6.43E-09	2.03E-09	1.53E-09	2.55E-10	1.59E-10	2.43E-11	0	0	0
3.5	4	0	0	0	0	0	6.13E-09	4.59E-08	1.56E-07	1.39E-07	8.31E-08	3.68E-08	2.02E-08	9.07E-09	2.38E-09	1.51E-09	3E-10	6.73E-11	0	0	0	0
4	4.5	0	0	0	0	0	0	8.24E-09	7.34E-08	1.33E-07	8.67E-08	4.3E-08	2.1E-08	1.18E-08	2.8E-09	1.43E-09	5.04E-10	9.8E-11	0	0	0	0
4.5	5	0	0	0	0	0	0	1.28E-09	2.53E-08	1.09E-07	9.12E-08	4.49E-08	2.16E-08	9.49E-09	3.87E-09	2.36E-09	7.74E-10	4.45E-10	0	0	0	0
5	5.5	0	0	0	0	0	0	0	6.63E-09	4.83E-08	7.25E-08	4.66E-08	1.3E-08	1.14E-08	2.39E-09	3.84E-09	1.11E-09	2.08E-10	5.13E-11	0	0	0
5.5	6	0	0	0	0	0	0	2.27E-09	1.24E-09	1.8E-08	3.67E-08	4.63E-08	1.11E-08	7.82E-09	2.73E-09	2.5E-09	6.24E-10	2.12E-10	0	0	0	0
6	6.5	0	0	0	0	0	0	0	0	5.56E-09	1.24E-08	3.57E-08	1.61E-08	5.25E-09	2.65E-09	8.95E-10	1.07E-10	3.12E-10	0	0	0	0
6.5	7	0	0	0	0	0	0	0	0	0	7.07E-09	1.56E-08	1.13E-08	4.86E-09	1.87E-09	1.41E-09	1.35E-10	3.43E-10	0	0	0	0
7	7.5	0	0	0	0	0	0	0	0	0	2.63E-09	6.07E-09	9.71E-09	5.3E-09	1.49E-09	1.4E-09	8.34E-11	6.08E-11	0	0	0	0
7.5	8	0	0	0	0	0	0	0	0	0	1.07E-09	8.09E-09	1.14E-08	3.24E-09	6.07E-10	0	0	0	0	0	0	0
8	8.5	0	0	0	0	0	0	0	0	0	0	2.44E-09	6.89E-09	2.49E-09	1.22E-09	0	0	0	0	0	0	0
8.5	9	0	0	0	0	0	0	0	0	0	0	0	6.32E-10	4.24E-09	0	6.14E-10	0	0	0	0	0	0
9	9.5	0	0	0	0	0	0	0	0	0	0	0	0	1E-09	6.88E-10	0	0	0	0	0	0	0
9.5	10	0	0	0	0	0	0	0	0	0	0	0	1.75E-09	0	8.06E-10	0	0	0	0	0	0	0
10	10.5	0	0	0	0	0	0	0	0	0	0	0	0	0	0	3.29E-10	0	0	0	0	0	0
10.5	11	0	0	0	0	0	0	0	0	0	0	0	0	0	0	3.79E-10	0	0	0	0	0	0
11	11.5	0	0	0	0	0	0	0	0	0	0	0	0	0	0	1.3E-09	0	0	0	0	0	0
11.5	12	0	0	0	0	0	0	0	0	0	0	0	0	0	0	1.49E-09	0	0	0	0	0	0
12	12.5	0	0	0	0	0	0	0	0	0	0	0	0	0	0	1.68E-09	0	0	0	0	0	0
12.5	13	0	0	0	0	0	0	0	0	0	0	0	0	0	0	1.9E-09	0	0	0	0	0	0
13	13.5	0	0	0	0	0	0	0	0	0	0	0	0	0	0	2.13E-09	0	0	0	0	0	0
13.5	14	0	0	0	0	0	0	0	0	0	0	0	0	0	0	2.38E-09	0	0	0	0	0	0
14	14.5	0	0	0	0	0	0	0	0	0	0	0	0	0	0	2.65E-09	0	0	0	0	0	0
14.5	15	0	0	0	0	0	0	0	0	0	0	0	0	0	0	2.94E-09	0	0	0	0	0	0
15	15.5	0	0	0	0	0	0	0	0	0	0	0	0	0	0	3.25E-09	0	0	0	0	0	0

Table J - 2: Governing Sea States for Inertia Dominated Fatigue Damage

	Tp [s]																				
Hs [m]	From	3	4	5	6	7	8	9	10	11	12	13	14	15	16	17	18	19	20	21	22	23
From	To	4	5	6	7	8	9	10	11	12	13	14	15	16	17	18	19	20	21	22	23	24
0	0.5	4.08E-11	8.51E-12	2.48E-12	4.09E-12	4.24E-12	3.71E-12	1.45E-12	9.4E-13	3.29E-13	7.52E-14	2.37E-14	1.27E-14	2.47E-15	1.06E-16	5.22E-16	0	0	0	0	0	0
0.5	1	3.4E-08	8.5E-08	2.14E-08	1.21E-08	2.67E-08	2.19E-08	1.02E-08	5.46E-09	2.19E-09	7.32E-10	2.63E-10	9.19E-11	4E-11	1.26E-11	9.13E-12	2.45E-12	9.09E-13	6.52E-13	1.58E-13	1.2E-13	4.63E-14
1	1.5	0	2.3E-07	6.6E-07	2.9E-07	3.21E-07	3.49E-07	2.1E-07	1.49E-07	6.95E-08	2.24E-08	9.52E-09	2.96E-09	1.11E-09	4.84E-10	4.05E-10	8.1E-11	3.71E-11	1.44E-11	1.36E-12	7.74E-13	1.99E-13
1.5	2	0	0	3.19E-07	1.13E-06	9.87E-07	1.18E-06	8.14E-07	8.13E-07	4.35E-07	1.51E-07	6.99E-08	2.55E-08	9.16E-09	2.41E-09	1.9E-09	4.34E-10	1.7E-10	7.13E-11	2.3E-11	5.83E-12	0
2	2.5	0	0	0	6.49E-07	1.17E-06	2.32E-06	2.3E-06	2.03E-06	1.44E-06	5.9E-07	2.83E-07	1.12E-07	4.81E-08	1.46E-08	8.92E-09	1.99E-09	9.94E-10	2.15E-10	2.3E-11	0	0
2.5	3	0	0	0	1.01E-07	4.9E-07	**2.85E-06**	3.9E-06	4.13E-06	2.9E-06	1.36E-06	7.15E-07	3.16E-07	9.71E-08	2.43E-08	2.1E-08	5.11E-09	2E-09	2.56E-10	0	0	0
3	3.5	0	0	0	0	1.16E-07	1.01E-06	**4.16E-06**	6.76E-06	5.01E-06	2.52E-06	1.51E-06	5.84E-07	2.21E-07	6.97E-08	5.25E-08	8.77E-09	5.45E-09	8.36E-10	0	0	0
3.5	4	0	0	0	0	0	3.23E-07	2.42E-06	**8.23E-06**	7.32E-06	4.38E-06	1.94E-06	1.06E-06	4.78E-07	1.26E-07	7.98E-08	1.58E-08	3.55E-09	0	0	0	0
4	4.5	0	0	0	0	0	0	6.33E-07	5.63E-06	1.02E-05	6.65E-06	3.3E-06	1.61E-06	9.06E-07	2.15E-07	1.1E-07	3.87E-08	7.52E-09	0	0	0	0
4.5	5	0	0	0	0	0	0	1.37E-07	2.71E-06	**1.17E-05**	9.77E-06	4.81E-06	2.32E-06	1.02E-06	4.14E-07	2.53E-07	8.29E-08	4.76E-08	0	0	0	0
5	5.5	0	0	0	0	0	0	0	9.59E-07	6.99E-06	**1.05E-05**	6.74E-06	1.88E-06	1.64E-06	3.46E-07	5.56E-07	1.6E-07	3.01E-08	7.42E-09	0	0	0
5.5	6	0	0	0	0	0	0	4.31E-07	2.37E-07	3.43E-06	6.98E-06	**8.8E-06**	2.11E-06	1.49E-06	5.18E-07	4.75E-07	1.19E-07	4.04E-08	0	0	0	0
6	6.5	0	0	0	0	0	0	0	0	1.36E-06	3.02E-06	8.72E-06	3.94E-06	1.28E-06	6.48E-07	2.18E-07	2.61E-08	7.61E-08	0	0	0	0
6.5	7	0	0	0	0	0	0	0	0	0	2.17E-06	4.8E-06	3.48E-06	1.5E-06	5.76E-07	4.33E-07	4.14E-08	1.06E-07	0	0	0	0
7	7.5	0	0	0	0	0	0	0	0	0	1E-06	2.31E-06	3.7E-06	2.02E-06	5.68E-07	5.32E-07	3.18E-08	2.32E-08	0	0	0	0
7.5	8	0	0	0	0	0	0	0	0	0	4.98E-07	3.77E-06	**5.32E-06**	1.51E-06	2.83E-07	0	0	0	0	0	0	0
8	8.5	0	0	0	0	0	0	0	0	0	0	1.37E-06	3.87E-06	1.4E-06	6.85E-07	0	0	0	0	0	0	0
8.5	9	0	0	0	0	0	0	0	0	0	0	0	4.24E-07	**2.84E-06**	0	4.11E-07	0	0	0	0	0	0
9	9.5	0	0	0	0	0	0	0	0	0	0	0	0	7.92E-07	5.45E-07	0	0	0	0	0	0	0
9.5	10	0	0	0	0	0	0	0	0	0	0	0	1.62E-06	0	7.47E-07	0	0	0	0	0	0	0
10	10.5	0	0	0	0	0	0	0	0	0	0	0	0	0	0	3.54E-07	0	0	0	0	0	0
10.5	11	0	0	0	0	0	0	0	0	0	0	0	0	0	0	4.71E-07	0	0	0	0	0	0
11	11.5	0	0	0	0	0	0	0	0	0	0	0	0	0	0	1.86E-06	0	0	0	0	0	0
11.5	12	0	0	0	0	0	0	0	0	0	0	0	0	0	0	2.41E-06	0	0	0	0	0	0
12	12.5	0	0	0	0	0	0	0	0	0	0	0	0	0	0	3.1E-06	0	0	0	0	0	0
12.5	13	0	0	0	0	0	0	0	0	0	0	0	0	0	0	3.94E-06	0	0	0	0	0	0
13	13.5	0	0	0	0	0	0	0	0	0	0	0	0	0	0	4.96E-06	0	0	0	0	0	0
13.5	14	0	0	0	0	0	0	0	0	0	0	0	0	0	0	6.19E-06	0	0	0	0	0	0
14	14.5	0	0	0	0	0	0	0	0	0	0	0	0	0	0	7.67E-06	0	0	0	0	0	0
14.5	15	0	0	0	0	0	0	0	0	0	0	0	0	0	0	9.43E-06	0	0	0	0	0	0
15	15.5	0	0	0	0	0	0	0	0	0	0	0	0	0	0	1.15E-05	0	0	0	0	0	0

Table J - 3: Prevailing Wave Directions for Selected Sea States

Hs [m]		Direction w.r.t. N (°)							
From	To	0	45	90	135	180	225	270	315
0	0.5	23.0%	0.4%	1.1%	0.4%	0.0%	0.0%	53.6%	21.1%
0.5	1	33.9%	0.4%	1.6%	0.4%	0.1%	0.1%	**43.0%**	20.7%
1	1.5	**38.8%**	0.3%	1.5%	0.2%	0.0%	0.0%	35.0%	24.1%
1.5	2	**38.8%**	0.2%	1.1%	0.1%	0.0%	0.0%	28.4%	31.5%
2	2.5	36.6%	0.1%	0.3%	0.0%	0.0%	0.0%	21.1%	41.8%
2.5	3	33.7%	0.1%	0.0%	0.0%	0.0%	0.0%	16.3%	**49.8%**
3	3.5	30.3%	0.0%	0.0%	0.0%	0.0%	0.0%	10.3%	**59.7%**
3.5	4	30.0%	0.0%	0.0%	0.0%	0.0%	0.0%	7.9%	**61.7%**
4	4.5	26.8%	0.0%	0.0%	0.0%	0.0%	0.0%	6.2%	66.5%
4.5	5	21.6%	0.0%	0.0%	0.0%	0.0%	0.0%	3.7%	**75.4%**
5	5.5	24.7%	0.0%	0.0%	0.0%	0.0%	0.0%	1.2%	**74.1%**
5.5	6	20.0%	0.0%	0.0%	0.0%	0.0%	0.0%	4.4%	**75.6%**
6	6.5	29.2%	0.0%	0.0%	0.0%	0.0%	0.0%	0.0%	66.7%
6.5	7	23.1%	0.0%	0.0%	0.0%	0.0%	0.0%	7.7%	84.6%
7	7.5	25.0%	0.0%	0.0%	0.0%	0.0%	0.0%	0.0%	62.5%
7.5	8	25.0%	0.0%	0.0%	0.0%	0.0%	0.0%	0.0%	**75.0%**
8	8.5	33.3%	0.0%	0.0%	0.0%	0.0%	0.0%	0.0%	66.7%
8.5	9	0.0%	0.0%	0.0%	0.0%	0.0%	0.0%	0.0%	**100.0%**
9	9.5	0.0%	0.0%	0.0%	0.0%	0.0%	0.0%	0.0%	0.0%
9.5	10	0.0%	0.0%	0.0%	0.0%	0.0%	0.0%	0.0%	100.0%
10	10.5	0.0%	0.0%	0.0%	0.0%	0.0%	0.0%	0.0%	0.0%
10.5	11	0.0%	0.0%	0.0%	0.0%	0.0%	0.0%	0.0%	0.0%
11	11.5	0.0%	0.0%	0.0%	0.0%	0.0%	0.0%	0.0%	0.0%
11.5	12	0.0%	0.0%	0.0%	0.0%	0.0%	0.0%	0.0%	0.0%
12	12.5	0.0%	0.0%	0.0%	0.0%	0.0%	0.0%	0.0%	0.0%
12.5	13	0.0%	0.0%	0.0%	0.0%	0.0%	0.0%	0.0%	0.0%
13	13.5	0.0%	0.0%	0.0%	0.0%	0.0%	0.0%	0.0%	0.0%
13.5	14	0.0%	0.0%	0.0%	0.0%	0.0%	0.0%	0.0%	0.0%
14	14.5	0.0%	0.0%	0.0%	0.0%	0.0%	0.0%	0.0%	0.0%
14.5	15	0.0%	0.0%	0.0%	0.0%	0.0%	0.0%	0.0%	0.0%
15	15.5	0.0%	0.0%	0.0%	0.0%	0.0%	0.0%	0.0%	0.0%

Table J - 4: Prevailing Wind Directions for Selected Sea States

Wind	Direction w.r.t. N (°)								
Velocity									
[m/s]	0	45	90	135	180	225	270	315	All
0	10.2%	6.2%	8.8%	15.2%	11.4%	15.3%	19.4%	13.6%	100.0%
1	10.1%	6.1%	8.7%	15.1%	11.3%	15.2%	19.3%	13.5%	99.0%
2	9.8%	5.9%	8.4%	14.8%	11.1%	14.9%	19.0%	13.2%	97.0%
3	9.2%	5.4%	8.1%	14.4%	10.6%	14.5%	18.7%	12.7%	94.0%
4	8.5%	4.8%	7.6%	13.9%	9.9%	13.9%	18.2%	12.0%	89.0%
5	7.6%	4.0%	7.1%	13.3%	9.2%	13.2%	17.6%	11.1%	83.0%
6	6.7%	3.4%	6.5%	12.4%	8.2%	12.2%	16.8%	10.0%	76.0%
7	5.8%	2.6%	5.8%	11.3%	7.1%	10.9%	15.9%	8.8%	68.0%
8	4.9%	2.0%	5.0%	10.0%	5.9%	9.5%	14.7%	7.5%	59.0%
9	4.1%	1.5%	4.1%	8.6%	4.6%	7.8%	13.3%	6.3%	50.0%
10	3.4%	1.1%	3.2%	7.0%	3.4%	6.2%	**11.8%**	5.2%	41.0%
11	2.8%	0.8%	2.2%	5.4%	2.4%	5.0%	10.3%	4.4%	33.0%
12	2.2%	0.6%	1.5%	4.2%	1.6%	4.0%	8.9%	3.7%	27.0%
13	1.7%	0.5%	1.0%	3.0%	1.1%	3.2%	7.5%	3.0%	21.0%
14	1.3%	0.4%	0.7%	2.1%	0.8%	2.5%	6.3%	2.4%	16.0%
15	1.1%	0.3%	0.4%	1.4%	0.5%	1.9%	**5.0%**	1.9%	13.0%
16	0.8%	0.2%	0.3%	1.0%	0.4%	1.4%	4.0%	1.5%	9.0%
17	0.6%	0.1%	0.2%	0.6%	0.2%	1.0%	3.1%	1.2%	7.0%
18	0.4%	0.1%	0.1%	0.4%	0.1%	0.7%	2.5%	0.8%	5.0%
19	0.3%	0.0%	0.1%	0.2%	0.1%	0.5%	1.9%	0.6%	4.0%
20	0.2%	0.0%	0.0%	0.1%	0.1%	0.4%	1.4%	0.5%	3.0%
21	0.2%	0.0%	0.0%	0.1%	0.0%	0.3%	1.0%	0.3%	2.0%
22	0.1%	0.0%	0.0%	0.0%	0.0%	0.2%	0.7%	0.2%	1.0%
23	0.1%	0.0%	0.0%	0.0%	0.0%	0.1%	0.5%	0.2%	1.0%
24	0.1%	0.0%	0.0%	0.0%	0.0%	0.1%	0.3%	0.1%	1.0%
25	0.0%	0.0%	0.0%	0.0%	0.0%	0.1%	**0.2%**	0.1%	0.0%
26	0.0%	0.0%	0.0%	0.0%	0.0%	0.0%	0.2%	0.0%	0.0%
27	0.0%	0.0%	0.0%	0.0%	0.0%	0.0%	0.1%	0.0%	0.0%
28	0.0%	0.0%	0.0%	0.0%	0.0%	0.0%	0.1%	0.0%	0.0%
29	0.0%	0.0%	0.0%	0.0%	0.0%	0.0%	0.0%	0.0%	0.0%
30	0.0%	0.0%	0.0%	0.0%	0.0%	0.0%	0.0%	0.0%	0.0%
31	0.0%	0.0%	0.0%	0.0%	0.0%	0.0%	0.0%	0.0%	0.0%
32	0.0%	0.0%	0.0%	0.0%	0.0%	0.0%	0.0%	0.0%	0.0%
33	0.0%	0.0%	0.0%	0.0%	0.0%	0.0%	0.0%	0.0%	0.0%

Table J - 5: Prevailing Current Directions for Selected Sea States

Current		Direction w.r.t. N (°)											
Velocity [m/s]		0	30	60	90	120	150	180	210	240	270	300	330
From	To	30	60	90	120	150	180	210	240	270	300	330	360
0	0.1	0.51%	0.49%	0.49%	0.51%	0.47%	0.42%	0.42%	0.43%	0.43%	0.47%	0.50%	0.52%
0.1	0.2	1.08%	1.12%	1.34%	1.47%	1.22%	1.05%	0.98%	0.97%	1.12%	1.38%	1.46%	1.28%
0.2	0.3	1.24%	1.36%	1.72%	2.34%	2.02%	1.45%	1.05%	1.04%	1.59%	2.03%	2.20%	1.71%
0.3	0.4	0.84%	0.97%	2.11%	3.34%	2.54%	1.26%	0.54%	0.58%	1.32%	2.24%	2.45%	1.55%
0.4	0.5	0.38%	0.52%	1.94%	**3.75%**	2.86%	0.76%	0.29%	0.29%	0.78%	2.00%	2.08%	0.94%
0.5	0.6	0.09%	0.16%	1.22%	3.54%	2.36%	0.49%	0.09%	0.11%	0.39%	1.06%	1.45%	0.40%
0.6	0.7	0.01%	0.04%	0.55%	2.75%	1.93%	0.20%	0.02%	0.02%	0.16%	0.48%	0.76%	0.13%
0.7	0.8	0.00%	0.00%	0.11%	1.61%	1.12%	0.05%	0.00%	0.00%	0.04%	0.14%	0.26%	0.02%
0.8	0.9	0.00%	0.00%	0.04%	0.73%	0.51%	0.01%	0.00%	0.00%	0.01%	0.05%	0.04%	0.00%
0.9	1	0.00%	0.00%	0.01%	0.26%	0.21%	0.00%	0.00%	0.00%	0.00%	0.00%	0.00%	0.00%
1	1.1	0.00%	0.00%	0.00%	0.07%	0.07%	0.00%	0.00%	0.00%	0.00%	0.00%	0.00%	0.00%
1.1	1.2	0.00%	0.00%	0.00%	0.00%	0.01%	0.00%	0.00%	0.00%	0.00%	0.00%	0.00%	0.00%
1.2	1.3	0.00%	0.00%	0.00%	**0.00%**	0.00%	0.00%	0.00%	0.00%	0.00%	0.00%	0.00%	0.00%
1.3	1.4	0.00%	0.00%	0.00%	0.00%	0.00%	0.00%	0.00%	0.00%	0.00%	0.00%	0.00%	0.00%
1.4	1.5	0.00%	0.00%	0.00%	0.00%	0.00%	0.00%	0.00%	0.00%	0.00%	0.00%	0.00%	0.00%
1.5	1.6	0.00%	0.00%	0.00%	0.00%	0.00%	0.00%	0.00%	0.00%	0.00%	0.00%	0.00%	0.00%
1.6	1.7	0.00%	0.00%	0.00%	0.00%	0.00%	0.00%	0.00%	0.00%	0.00%	0.00%	0.00%	0.00%
1.7	1.8	0.00%	0.00%	0.00%	0.00%	0.00%	0.00%	0.00%	0.00%	0.00%	0.00%	0.00%	0.00%
1.8	1.9	0.00%	0.00%	0.00%	0.00%	0.00%	0.00%	0.00%	0.00%	0.00%	0.00%	0.00%	0.00%
1.9	2	0.00%	0.00%	0.00%	0.00%	0.00%	0.00%	0.00%	0.00%	0.00%	0.00%	0.00%	0.00%

J.5 Differences in Stress and Damage Response Per Sea State

The stress and fatigue response per sea state are summarized in Table J - 6 and Table J - 7. Here, the differences between the nonlinear and linear model are expressed in terms of:

- the normalized RMSEs of the maximum principal stresses;
- the absolute difference in cubic weighted mean stress range ε_{CWM} (Equation [5-37]);
- the damage ratio (D_L/D_{NL}) between the linear and nonlinear simulation.

Table J - 6: Difference Linear vs. Nonlinear Results per Sea State for Pontoon Hotspots

		Sea State Number											
Hotspot		**1**	**2**	**3**	**4**	**5**	**6**	**7**	**8**	**9**	**10**	**11**	**12**
Stress RMSE [%]	P_1	20	20	19	19	17	14	15	12	13	13	11	9
	P_2	22	22	19	20	33	27	28	22	21	20	18	12
	P_3	20	20	19	21	23	22	23	20	18	20	16	9
	P_4	20	19	19	19	19	18	18	15	17	17	18	9
	P_5	14	13	13	13	15	12	13	11	11	12	11	8
	P_6	43	41	42	39	12	11	9	9	9	13	11	8
ε_{CWM} [-]	P_1	0.9	0.8	0.5	0.6	0.4	0.4	0.4	0.4	0.4	0.4	0.4	0.2
	P_2	1.2	0.9	0.5	0.6	0.6	0.5	0.4	0.4	0.5	0.7	0.6	1.0
	P_3	0.9	0.9	0.8	0.8	1.1	1.1	1.0	1.0	1.0	1.1	1.3	0.5
	P_4	1.0	0.9	0.8	0.9	1.2	1.1	1.1	1.2	1.3	1.7	2.0	1.5
	P_5	0.9	0.8	0.6	0.7	0.5	0.5	0.5	0.4	0.5	0.5	0.5	0.3
	P_6	0.7	0.6	0.5	0.5	0.7	0.7	0.8	1.0	1.1	1.3	1.9	5.1
D_L/D_{NL} [-]	P_1	1.7	2.0	3.1	2.8	3.3	3.1	2.9	2.9	2.8	2.6	2.5	4.4
	P_2	1.0	1.4	2.9	2.9	1.9	2.3	2.4	2.1	1.8	1.4	1.4	0.9
	P_3	1.3	1.3	1.5	1.4	0.8	0.9	0.9	1.0	1.0	0.9	0.7	1.9
	P_4	1.1	1.2	1.4	1.4	0.7	0.8	0.7	0.7	0.6	0.5	0.4	0.7
	P_5	1.6	1.7	2.4	2.3	3.2	3.4	3.1	2.8	2.3	2.3	1.9	2.4
	P_6	2.2	2.5	3.1	3.1	1.6	1.5	1.2	0.9	0.8	0.6	0.4	0.1

Table J - 7: Difference Linear vs. Nonlinear Results per Sea State for Mid-Section Hotspots

		Sea State Number											
Hotspot		**1**	**2**	**3**	**4**	**5**	**6**	**7**	**8**	**9**	**10**	**11**	**12**
Stress RMSE [%]	$\mathbf{T_1}$	26	26	26	26	28	28	28	25	25	22	16	12
	$\mathbf{T_2}$	26	26	26	26	28	28	29	26	24	25	19	8
	$\mathbf{T_3}$	1	1	1	1	2	3	3	1	1	1	1	11
	$\mathbf{T_4}$	2	2	2	2	2	1	1	1	2	2	3	4
	$\mathbf{T_5}$	26	26	26	27	27	26	26	23	21	21	18	7
	$\mathbf{T_6}$	20	20	19	18	9	10	11	11	12	11	10	12
$\boldsymbol{\varepsilon_{CWM}}$ [-]	$\mathbf{T_1}$	0.6	0.6	0.6	0.6	0.6	0.6	0.6	0.8	0.9	1.1	2.1	17.0
	$\mathbf{T_2}$	0.6	0.6	0.6	0.6	0.5	0.5	0.5	0.6	0.6	0.7	1.0	5.6
	$\mathbf{T_3}$	0.5	0.6	0.5	0.6	0.5	0.5	0.6	0.6	0.6	0.7	0.8	0.8
	$\mathbf{T_4}$	0.5	0.6	0.6	0.6	0.5	0.5	0.5	0.5	0.5	0.5	0.4	1.0
	$\mathbf{T_5}$	0.6	0.6	0.6	0.6	0.5	0.5	0.5	0.5	0.5	0.5	0.4	0.6
	$\mathbf{T_6}$	0.2	0.2	0.3	0.2	0.3	0.4	0.4	0.4	0.5	0.6	1.1	1.2
D_L/D_{NL} [-]	$\mathbf{T_1}$	3.3	3.3	3.3	3.3	2.9	2.6	2.3	1.8	1.3	0.9	0.4	0.0
	$\mathbf{T_2}$	2.2	2.3	2.2	2.3	2.1	2.1	2.0	1.8	1.6	1.4	1.0	0.1
	$\mathbf{T_3}$	2.2	2.2	2.2	2.2	2.0	2.0	1.9	1.7	1.6	1.5	1.2	1.4
	$\mathbf{T_4}$	2.7	2.7	2.7	2.7	2.3	2.2	2.1	2.1	2.1	2.3	2.2	1.1
	$\mathbf{T_5}$	3.3	3.3	3.3	3.3	3.1	2.9	2.6	2.6	2.5	2.6	2.5	2.9
	$\mathbf{T_6}$	15.9	15.6	11.1	13.9	6.6	5.6	5.1	4.0	2.7	1.9	0.6	0.4

J.6 Time History Results Linear and Nonlinear Model

The influence of nonlinearities is visualized for extreme conditions (sea state 12) based on the TD results of the motions, mooring loads and principal stresses. The results are shown below .

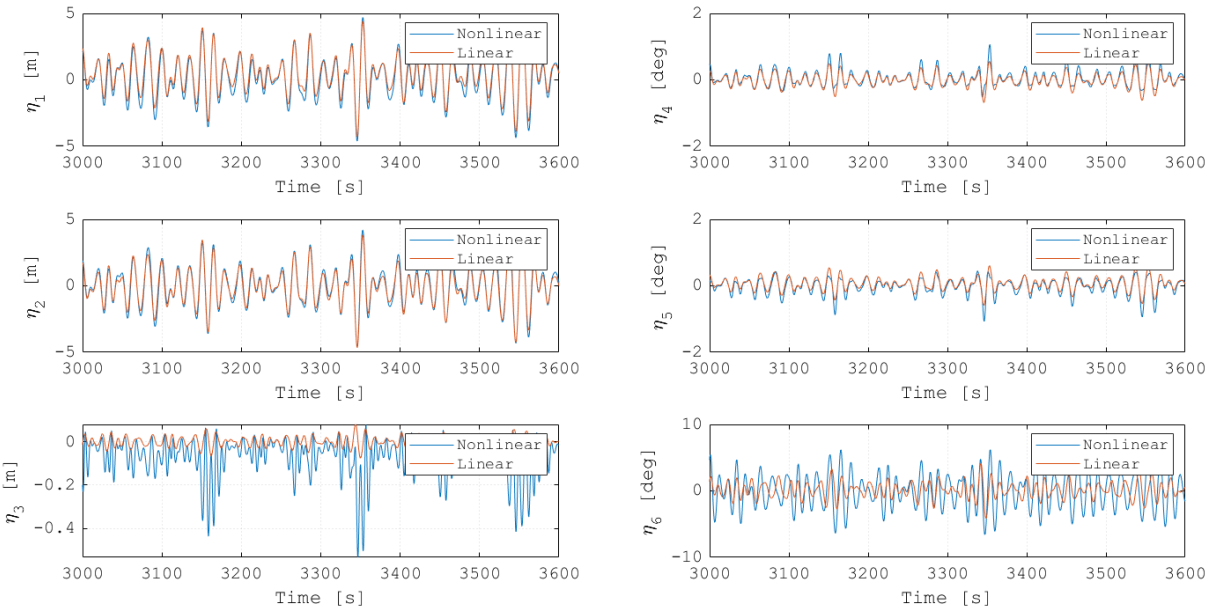

Figure J - 9: Nonlinear and Linearized Displacements

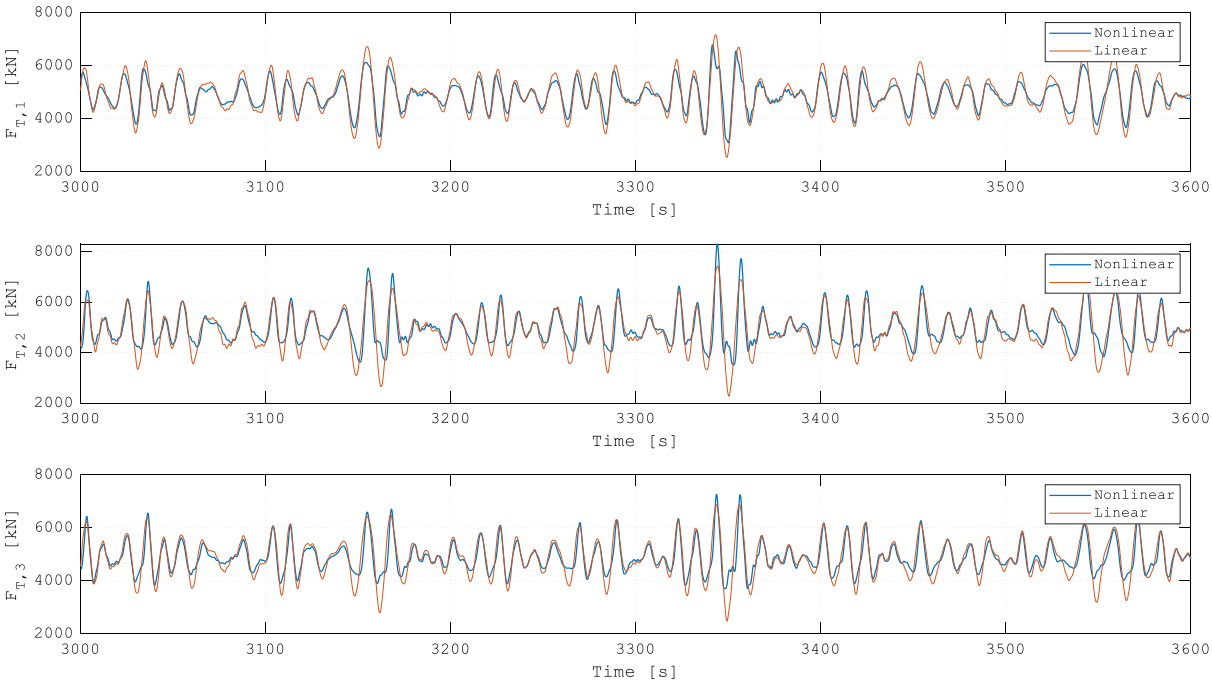

Figure J - 10: Nonlinear and Linearized Mooring Loads

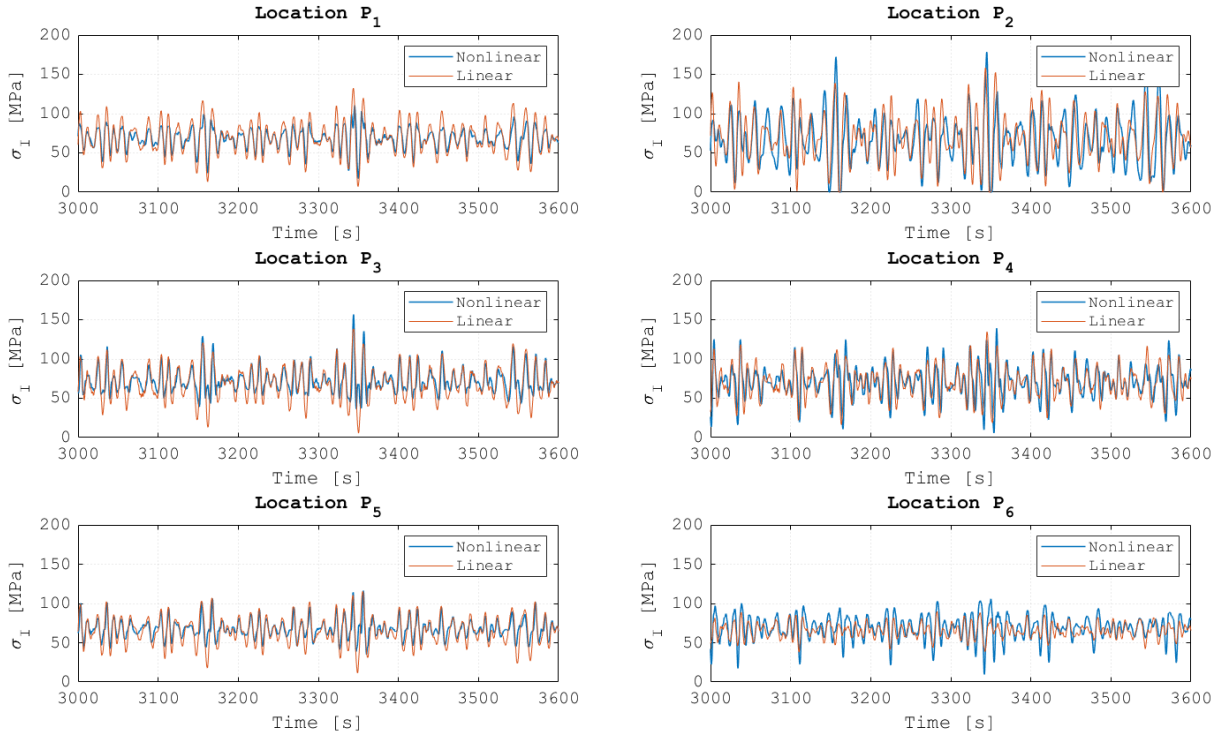

(a)

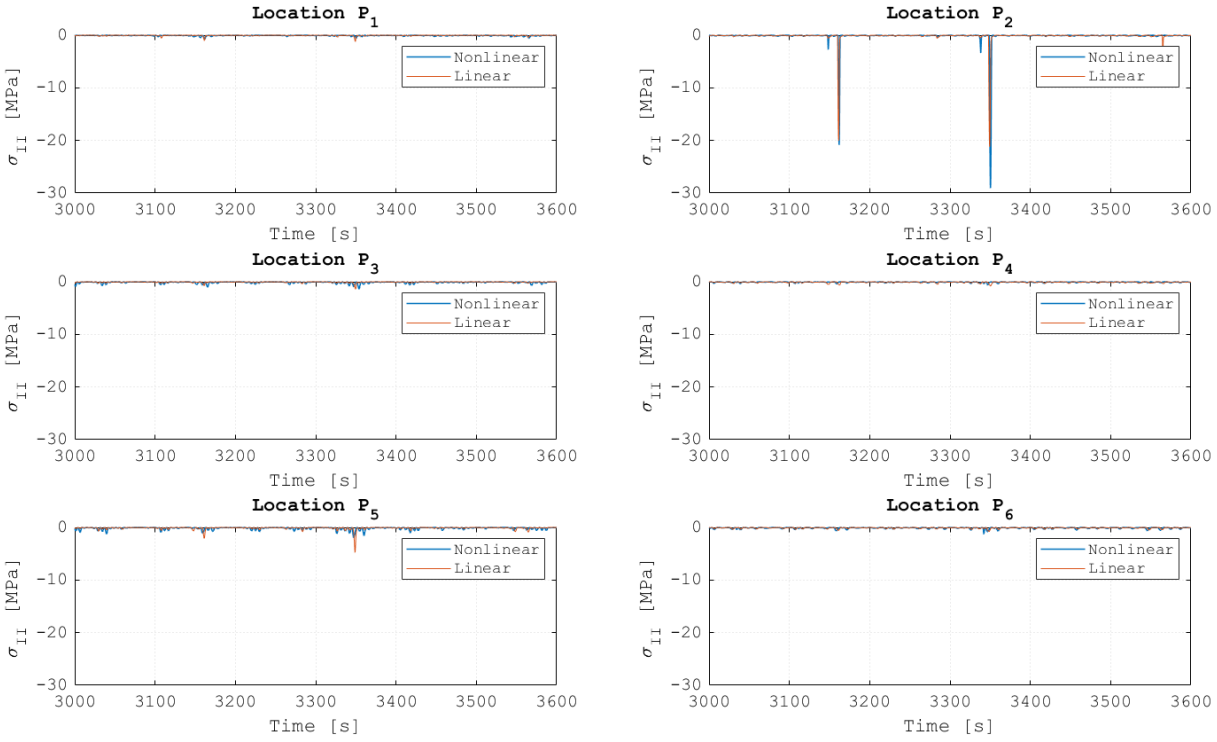

(b)

Figure J - 11: Nonlinear and Linearized First (a) and Second (b) Principle Stresses at the Pontoon Hotspots

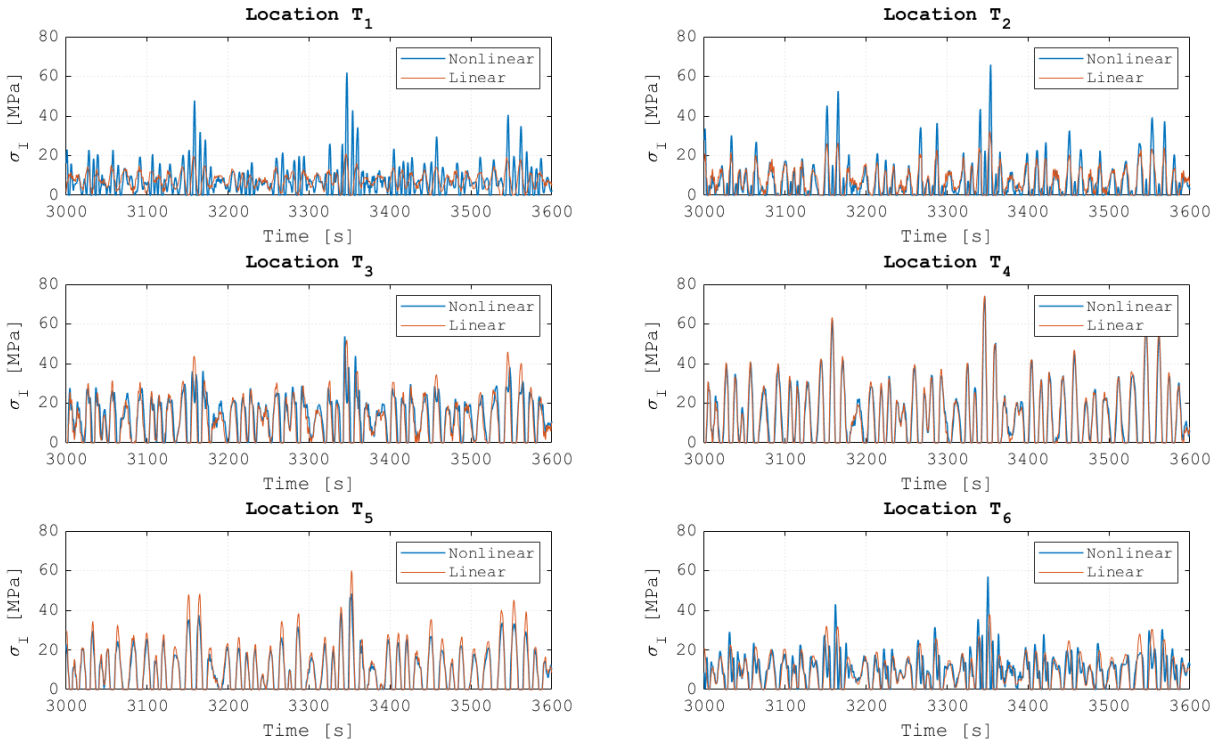

(a)

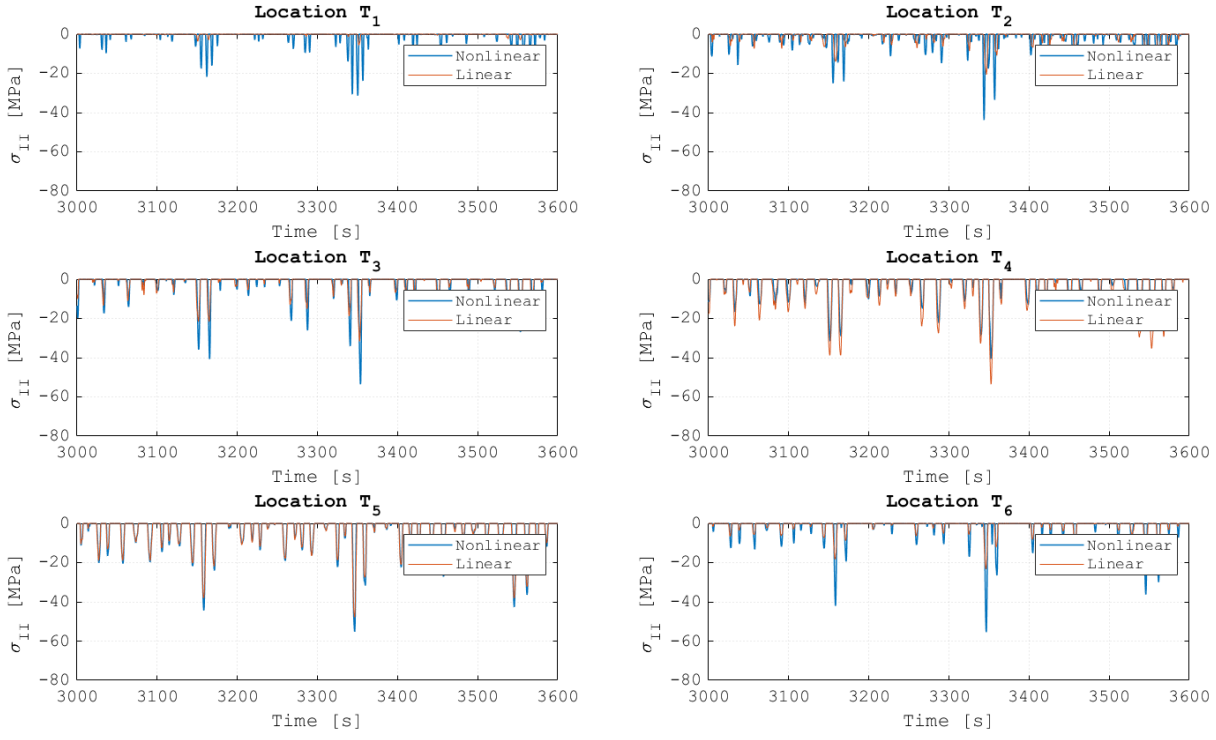

(b)

Figure J - 12: Nonlinear and Linearized First (a) and Second (b) Principle Stresses at the Mid-Section Hotspots

J.7 Principal Stress Directions (Nonlinear Model)

In Figure J - 13, the presence of multiaxiality is visualized by plotting the principal stress directions in TD for conditions during which large multiaxial loading was observed (sea state 8).

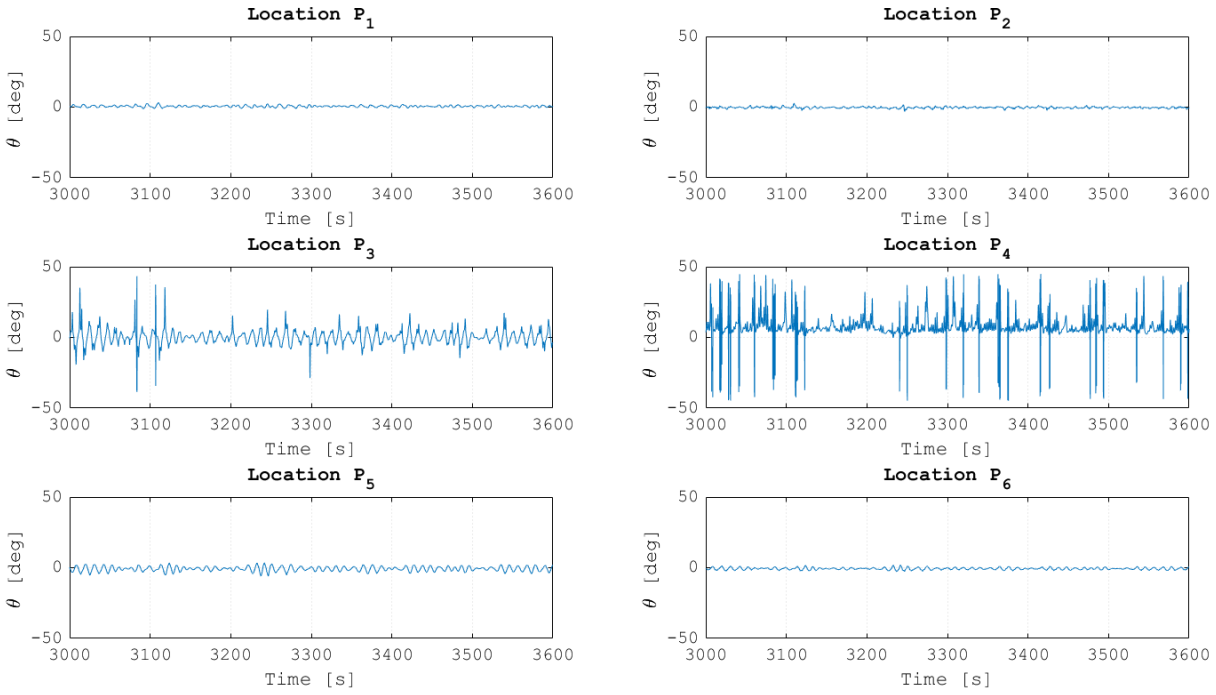

(a)

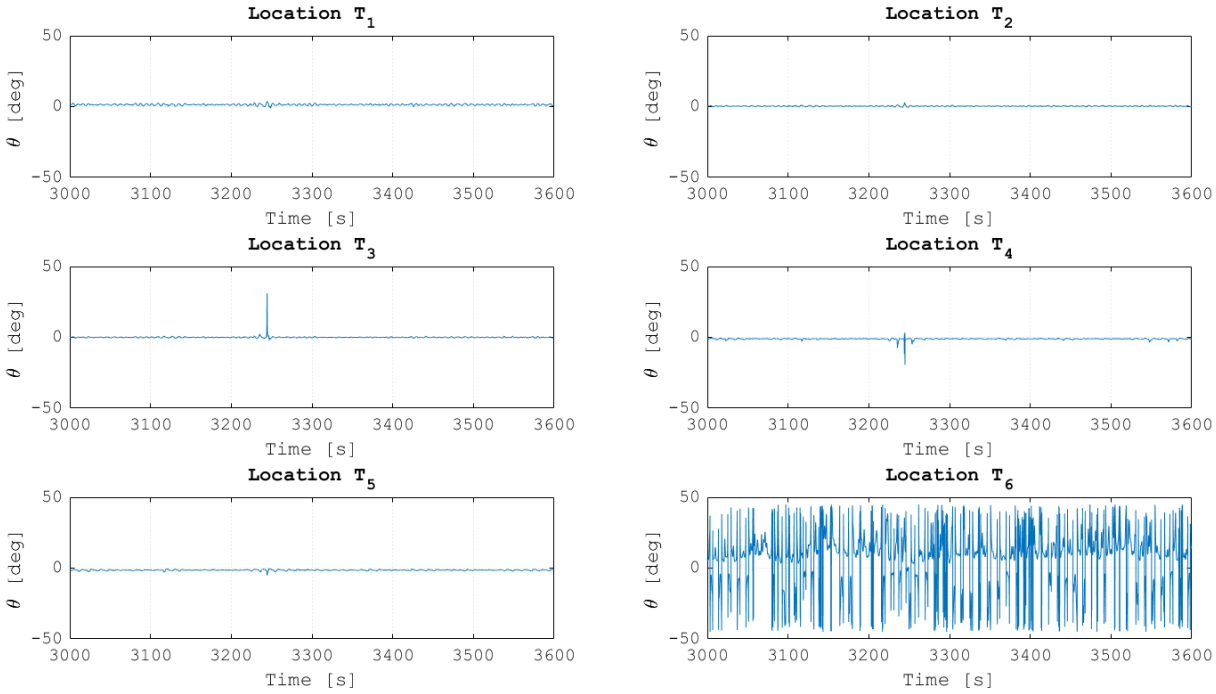

(b)

Figure J - 13: Principle Stress Directions at the Pontoon (a) and Mid-Section (b) Hotspots According to the Nonlinear Model

J.8 Numerical Confirmation of Linearity

To prove the linearity of the linearized model, the system's response is solved, based on a single sinusoidal point load, applied to the CoG of the structure in the direction of each DOF and in absence of waves, currents and wind. The mooring system is linearized around an arbitrary non-zero equilibrium point: $\underline{p_0} = [1.434 \quad -0.010 \quad -0.015 \quad 0 \quad 0.004 \quad 0]^T$.

As depicted in Figure J - 14, the steady state response is a sinusoidal function with a (nearly) fixed amplitude ratio w.r.t. the applied force, indicating that the response is linear.

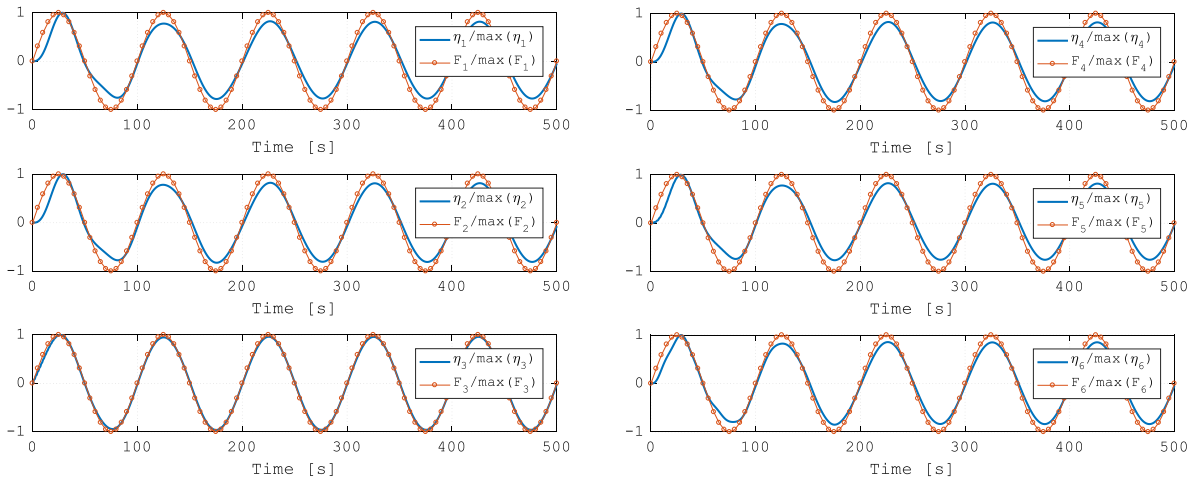

Figure J - 14: Motion Response Linearized Model to Sinusoidal Point Load

J.9 Validity of Equilibrium Point

To confirm that the linearization approach is valid and the numerically obtained equilibrium point is a unique solution, the response to the environmental conditions in Table 5-1 are simulated for varying initial displacements in the X-direction. The resulting values of $\underline{p_0}$, as a function of the initial displacement, are shown in Figure J - 15. The results demonstrate that the equilibrium position is independent of the initial conditions and is therefore a unique, physical solution. The slight variations in the solution are a consequence of differences in the transient response, causing the steady state solution to be reached at different time instants. This effect diminishes when the simulation duration is increased.

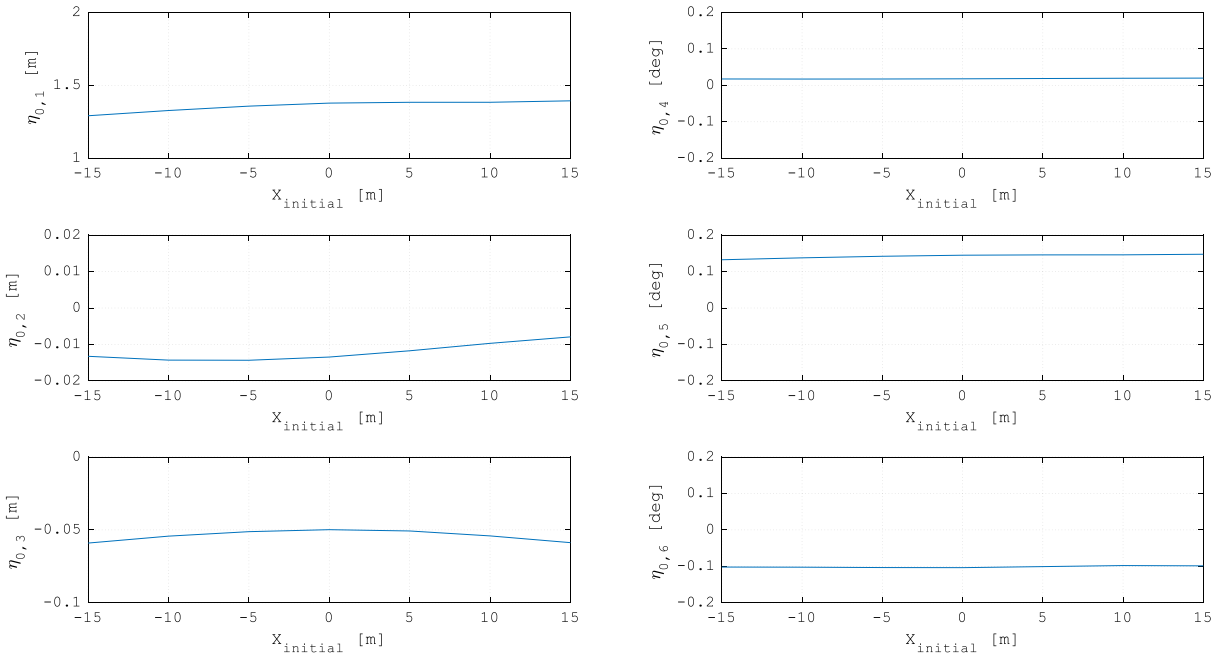

Figure J - 15: Equilibrium Position as a Function of Initial Conditions

J.10 Validity of Initial α-Value

By applying Equation [5-32], the second iteration value of α can be found for each sea state. Although the value of α should be considered separately for each DOF, as was explained in Section 5.5.4, it is decided to use a single value. Therefore, the surge velocities are considered as a basis of determining the updated values. The results are shown in Table J - 8. In Figure J - 16, it is shown that the use of the updated value of α, in the case where the updated value deviates most from the initial value, hardly improves the linear velocity approximation.

Table J - 8: Updated Values of α Per Sea State

Sea State	1	2	3	4	5	6	7	8	9	10	11	12
$\alpha^2 \pi$	9.8	8.3	7.7	7.9	7.8	7.5	6.6	4.4	4.4	4.4	4.4	9.2

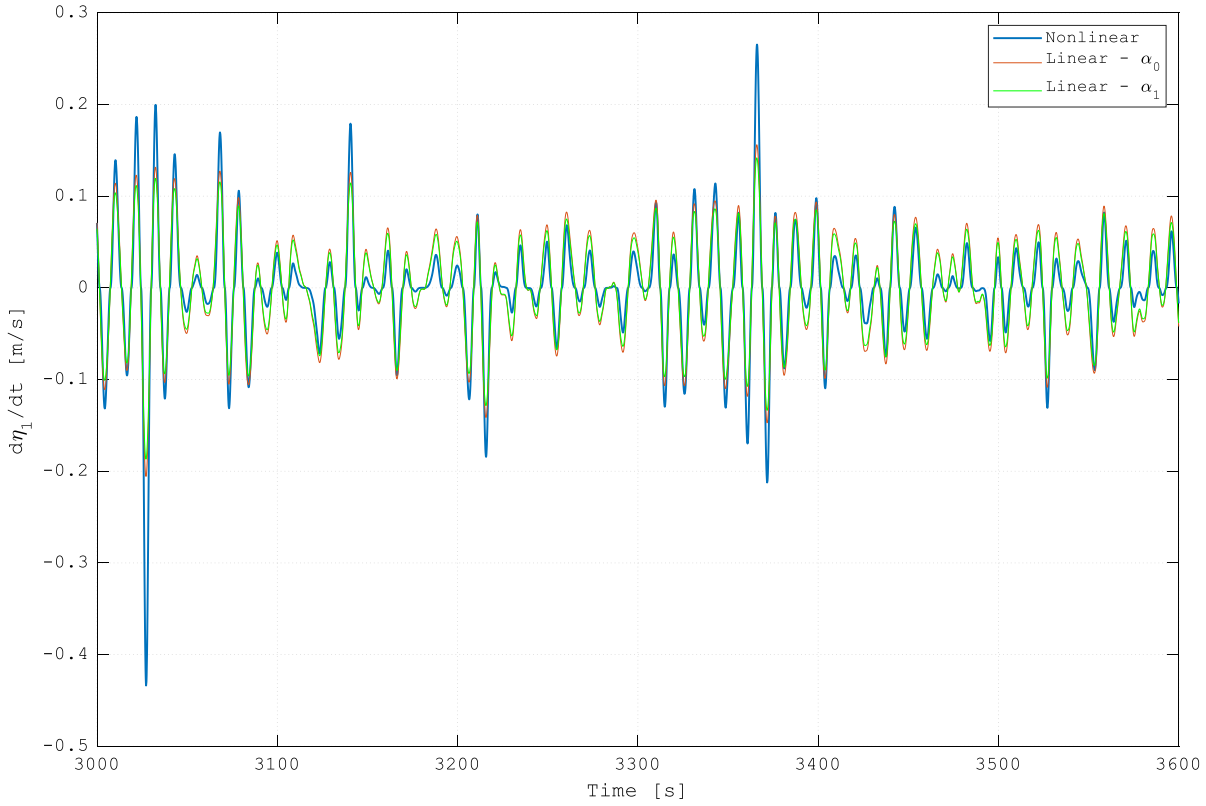

Figure J - 16: Comparison Linearized Structural Velocity for Updated Value of α

J.11 Damage Per Sea State for Uniaxial Load Approximation

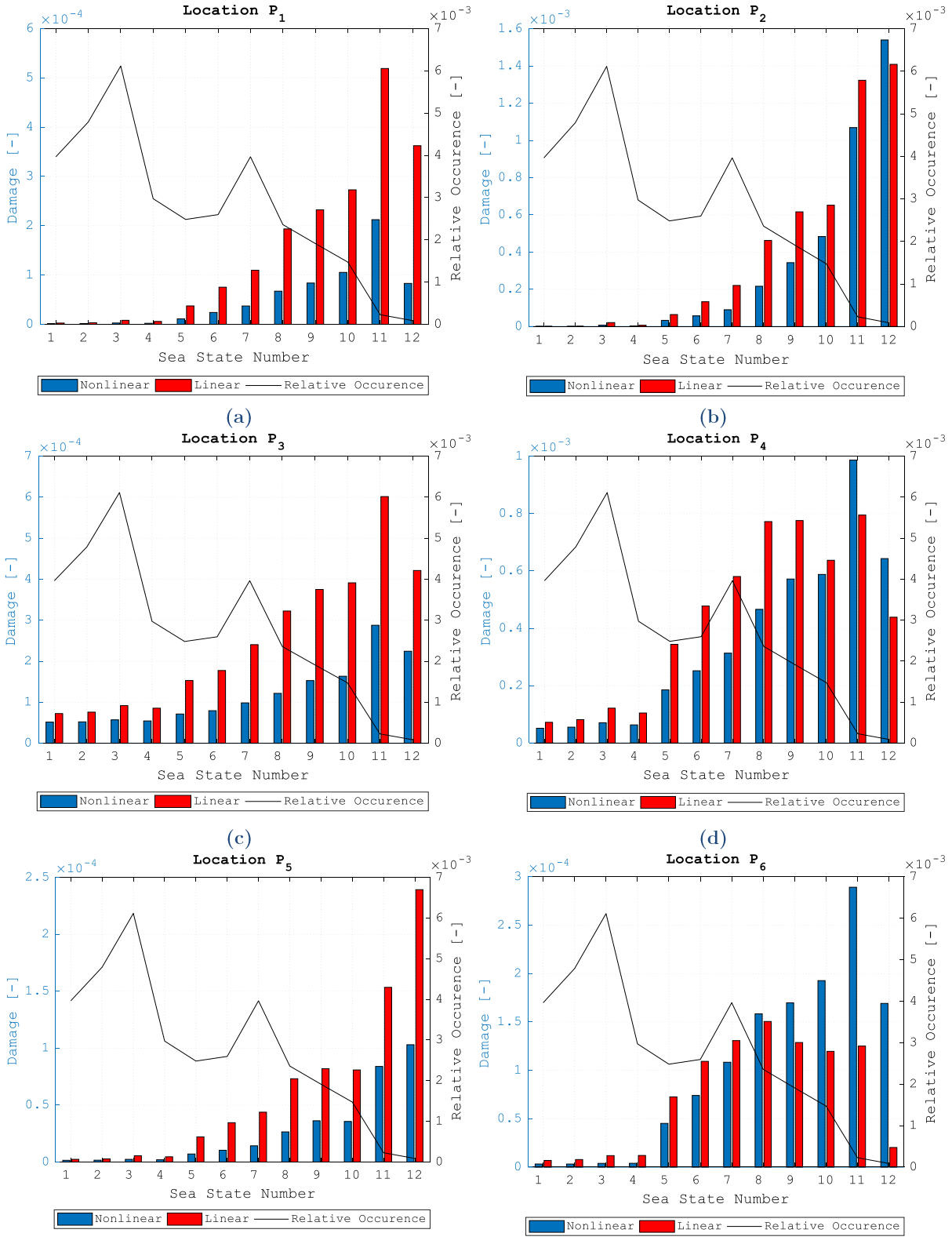

Figure J - 17: Damage Per Sea State at the Pontoon Hotspots (Uniaxial)

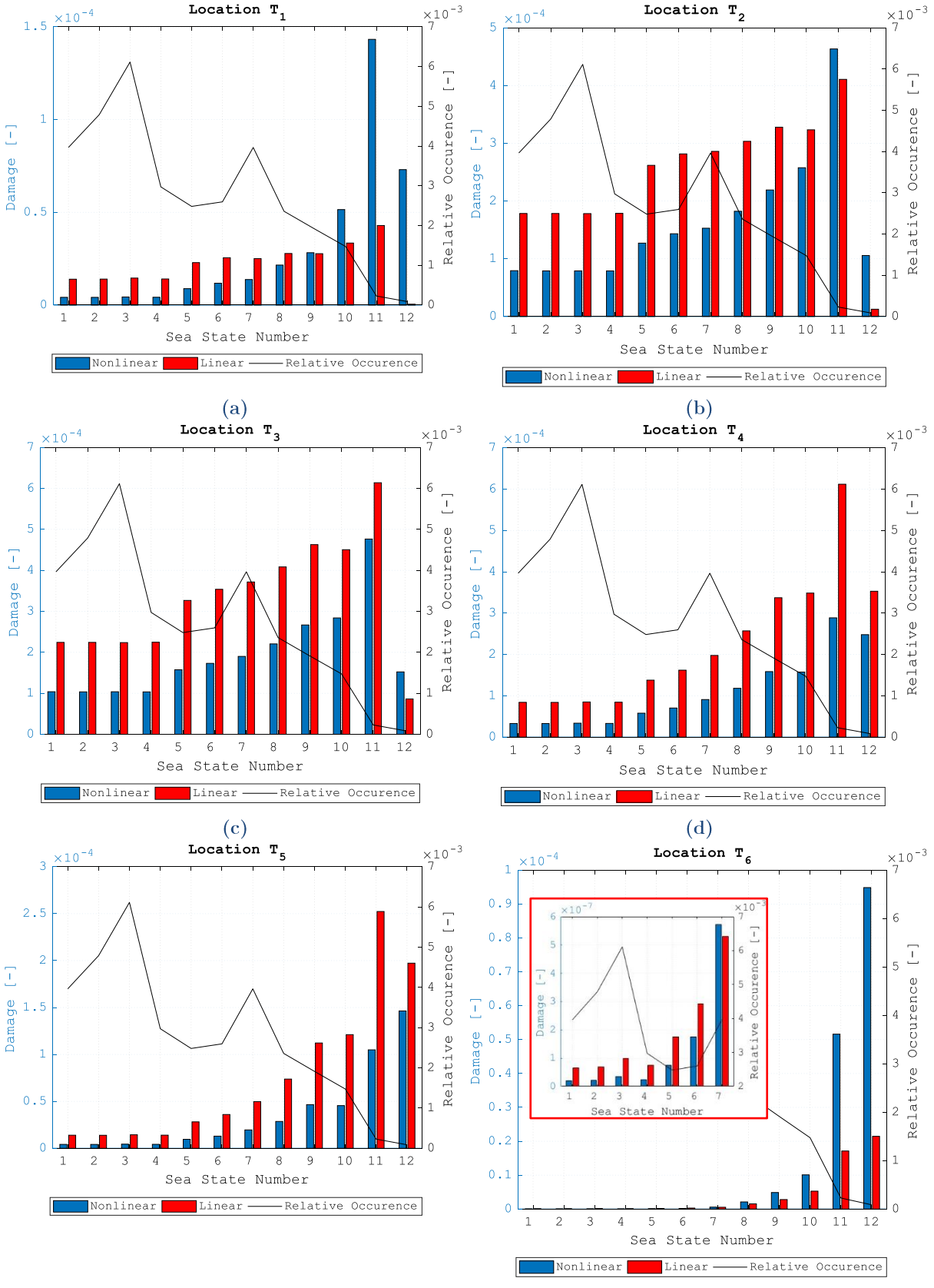

Figure J - 18: Damage Per Sea State at the Pontoon Hotspots (Uniaxial)